Electronic Thesis and Dissertation Repository

12-11-2015 12:00 AM

Silver Nanoparticle Transport Through Soil: Illuminating the Governing Pore-Scale Processes

Ian L. Molnar
The University of Western Ontario

Supervisor
Dr. Denis O'Carroll
The University of Western Ontario Joint Supervisor
Dr. Jason Gerhard
The University of Western Ontario

Follow this and additional works at: https://ir.lib.uwo.ca/etd

Part of the Environmental Engineering Commons, and the Hydrology Commons

Recommended Citation

SILVER NANOPARTICLE TRANSPORT THROUGH SOIL:
ILLUMINATING THE GOVERNING PORE-SCALE PROCESSES
(Thesis format: Integrated Article)

by

Ian Louis <u>Molnar</u>

Graduate Program in Civil and Environmental Engineering

A thesis submitted in partial fulfillment
of the requirements for the degree of
Doctor of Philosophy

The School of Graduate and Postdoctoral Studies
The University of Western Ontario
London, Ontario, Canada

Abstract

Engineered nanoparticles are widely used and will eventually be released to the subsurface environment and contaminate groundwater resources. However, the transport of engineered nanoparticles through soil is currently not well understood and cannot be modelled in any fundamental manner, placing groundwater resources at risk from nanoparticle contamination. This inability to accurately simulate transport is due to a lack of experimental information on nanoparticle interactions in the pore spaces of real soils.

This thesis illuminates the pore-scale processes governing silver nanoparticle transport through soil. In addition, it examines the influence of surface chemistry and grain/pore distributions on those processes. For the first study, a method was developed and validated which employs Synchrotron X-ray Computed Microtomography (SXCMT) to experimentally quantify changing concentrations of silver nanoparticles, both spatially and temporally, within real soil pore spaces during transport. For the second study, the SXCMT imaging method was employed to experimentally investigate the role of pore-scale processes on silver nanoparticle transport through different soils representing different surface chemistries and grain distributions. The experiments found that nanoparticle transport and retention is significantly impacted by small regions of low fluid velocity near grain-grain contacts (termed 'immobile zones'). For the third study, the experimental SXCMT datasets from the second study were coupled with Computational Fluid Dynamics to estimate the pore-scale nanoparticle mass flux and flow rates. The estimated distributions of mass flux and flow rates suggested that the current approach to modelling nanoparticle retention was incapable of considering mass flow in the centers of soil pores, rendering it unable to accurately predict the rate at which nanoparticles will be retained by soil.

Overall, this thesis presents the first experimental datasets of pore-scale nanoparticle concentrations during transport. These previously unobtainable datasets provided the first direct confirmation of 'immobile zones' and their contribution to anomalous nanoparticle transport behaviour. In addition, they provided some of the first evidence as to why current modelling approaches are unable to predict nanoparticle retention rates.

Keywords

Co-Authorship Statement

The thesis was written in accordance with the guidelines and regulations for an Integrated Article format stipulated by the School of Graduate and Postdoctoral Studies at the University of Western Ontario. The candidate designed, conducted and analyzed all of the experimental and numerical modelling work in this thesis under the supervision of Dr. Denis O'Carroll and Dr. Jason Gerhard. The underlying methodology for the synchrotron studies in this work were developed in conjunction with Dr. Clinton Willson and Dr. Kyungmin Ham. The analysis and interpretation of the synchrotron data was completed by the candidate in collaboration with Dr. Clinton Willson and Dr. Mark Rivers. In addition, the literature review, while primarily written by the candidate, was written in collaboration with Drs. William Johnson, Clinton Willson, Jason Gerhard, and Denis O'Carroll. Full details for all chapters given below.

Chapter 2: Literature Review: Predicting colloid transport through saturated porous media: A critical review

Molnar, I. L., W. P. Johnson, J. I. Gerhard, C. S. Willson, and D. M. O'Carroll (2015), Predicting colloid transport through saturated porous media: A critical review, *Water Resources Research*, 51(50th anniversary special collection), 6804-6845.

Contributions:

Ian Molnar: primary author/writer, developed outline, reviewed/revised chapter, coordinated the other collaborators/co-authors.

Denis O'Carroll and Jason Gerhard: invited to submit manuscript to special journal edition, reviewed/revised chapter.

William Johnson: Assisted in outline development, reviewed/revised chapter. In the published version of this chapter, Dr. Johnson was the primary writer of the section *Mechanistic Simulations: Unfavorable Conditions* and co-writer of the section *Upscaling from pore to continuum scale.* Both of these sections have been removed from the main body of the thesis and appear instead within the Appendices 7.3 and 7.4.

Clinton Willson: Reviewed/revised chapter. In the published version of this chapter, Dr. Willson was the primary writer of the section *Opportunities in Imaging and X-Ray Computed Microtomography.* This section has been removed from the main body of the thesis and appears instead within the Appendix 7.4.4.

Chapter 3: A Method for Obtaining Silver Nanoparticle Concentrations Within a Porous Medium via Synchrotron X-Ray Computed Microtomography

Molnar, I. L., C. S. Willson, D. M. O'Carroll, M. L. Rivers, and J. I. Gerhard (2014), Method for Obtaining Silver Nanoparticle Concentrations within a Porous Medium via Synchrotron X-ray Computed Microtomography, *Environmental Science and Technology*., 48(2), 1114-1122.

Contributions:

Ian Molnar: primary author/writer, helped create and refine the experimental methodology, planned and conducted experiments at the synchrotron light source, conducted all laboratory analyses, synthesized nanoparticles, interpreted and analyzed the collected data.

Denis O'Carroll: assisted in methodology development and data interpretation, reviewed and revised chapter.

Jason Gerhard: assisted in methodology development and data interpretation, reviewed and revised chapter.

Clinton Willson: Supplied the initial idea for the work and assisted in experimental methodology development and data interpretation, reviewed and revised chapter.

Mark Rivers: Assisted in experimental methodology development and interpretation of data, reviewed/revised chapter.

Chapter 4: The impact of immobile zones on the transport and retention of nanoparticles in porous media

Molnar, I. L., J. I. Gerhard, C. S. Willson, and D. M. O'Carroll (2015), The impact of immobile zones on the transport and retention of nanoparticles in porous media, *Water Resources Research.* doi: 10.1002/2015WR017167

Contributions:

Ian Molnar: primary author/writer, planned and conducted experiments at the synchrotron light source, conducted all laboratory analyses and numerical modelling work, synthesized nanoparticles, interpreted and analyzed the collected data.

Denis O'Carroll: Assisted in data interpretation, reviewed and revised chapter.

Jason Gerhard: Assisted in data interpretation, reviewed and revised chapter.

Clinton Willson: Assisted in data interpretation, reviewed and revised chapter.

Chapter 5: The impact of pore geometry and fluid velocity on the transport of nanoparticles in porous media

Contributions:

Ian Molnar: primary author/writer, planned and conducted experiments at the synchrotron light source, conducted all laboratory analyses and numerical modelling work, synthesized nanoparticles, interpreted and analyzed the collected data.

Denis O'Carroll: Assisted in data interpretation, reviewed and revised chapter.

Jason Gerhard: Assisted in data interpretation, reviewed and revised chapter.

Clinton Willson: Assisted in data interpretation, reviewed and revised chapter.

'My name is Ozymandias, king of kings:

Look on my works, ye Mighty, and despair!'

- Percy Bysshe Shelley, *Ozymandias*

Acknowledgments

Any work as large and complex as a dissertation requires the help and support of a large number of people, too many to list here. So to everyone who has supported and helped me over the years, thank you so much. There are a number of people who deserve a special acknowledgement for the role they have played in helping this project come to fruition:

First and foremost, Dr.'s Denis O'Carroll and Jason Gerhard have been more than just supervisors and advisors, they have been mentors and infinitely patient over the many years we have worked together. Thank you, thank you, thank you. Thank you for all of your patience, for everything you saw in me when we first started, for giving me this opportunity and dragging me through to completion. Dr. Clinton Willson, thank you for agreeing to come on board and help guide us through the ins and outs of x-ray microtomography. And thank you, as well, for inviting me to Louisiana for a semester and for staying with us through to the end; it has been a pleasure working with you and a lot of fun (although I still do not know anything about sports).

A number of engineering staff members have also helped with this project, and with my graduate studies, over the years: Tim Stephens, Caitlin Marshall, Stephanie Laurence, Whitney Barrett and everyone down at EFS. Thank you for your help and guidance over the years! I have pestered each and every one of you with questions over the years and you have patiently answered each one (and sorry for flooding the labs repeatedly).

All the members of RESTORE, past and present, have had an outstanding impact on my work and my life. You guys are a family, warm and welcoming, and have been a major source of my inspiration and drive over the years. Specifically I would like to thank Dr. Cjestmir de Boer, Dr. Rory Hadden, Dr. Kevin Mumford, Dr. Magdalena Krol, Stephanie Drake, Geremy Camps-Roach, Erin Cullen, Stephanie MacPhee, Xueying Liu, Ahmed Chowdhury, Jessica Barker and Alex Hockin for their close friendships and help.

Chris Kocur, I blame you for my decision to enter graduate school and stick around for a PhD. It has been a ton of fun being a student with you from 2003 – 2015, and it will be a ton more fun as we become research comrades-in-arms. I am proud to call you a true friend, and doubly proud that you stood up with me at my wedding, thank you!

To my 'non-research' friends Nathan Newport and Chris Course, thank you for accepting the fact that there were going to be months when you just would not see or hear from me due to grad school craziness. Nathan, thank you for listening to my endless discussions about what exactly I was trying to muddle through in my computer scripts and still agreeing to be the best man at my wedding.

Sarah and Adam Charron: You are the best family any person can hope to have. Thank you for continuing to be patient with me, and love me, through all these years. James Charron, you are going to read this someday and I want to tell you something: If your parents try to talk you out of grad school, don't listen to them. It is an incredible experience start to finish.

Mom and Dad: Thank you. I love you! The two of you have been unending fountains of support and kindness and I doubt I will ever be able to return it all back to you, but I will try.

To my wife, Laura: You are my love, my life, my everything. You were front and center through this whole process, listened to every practice presentation (multiple times), read my drafts, accepted that I needed to work through evenings and weekends, and did not complain about any of it. I still cannot believe you agreed to marry me at the end of it all!

Sugar (my dog), I strongly suspect you will never read this, but: Woof woof. You got me up every morning, were happy to see me come home and many of the ideas presented within this dissertation were thought up during our daily walks together.

Table of Contents

List of Tables

List of Figures

List of Acronyms

ADE	Advective-Dispersive Equation
APS	Advanced Photon Source
BTC	Breakthrough curve
CFD	Computational Fluid Dynamics
CFT	Colloid Filtration Theory
CMC90k	Carboxymethyl cellulose 90k
DLVO	Derjaguin-Landau-Verwey-Overbeek
ENP	Engineered nanoparticle
GSECARS	GeoSoilEnviro Center for Advanced Radiation Sources
HSIC	Happel Sphere-in-Cell
IL-PM	Injected Liquid – Porous Media
L-O	Liquid Only
L-PM	Liquid – Porous Media
nAg	Silver nanoparticles
NAPL	Nonaqueous Phase Liquids
NOM	Natural organic matter
nZVI	Nano zero valent iron
PV	Pore volume
qSXCMT	Quantitative Synchrotron X-Ray Computed Microtomography
SXCMT	Synchrotron X-Ray Computed Microtomography
TEM	Transmission Electron Microscopy
XCT	X-Ray Computed Tomography
XMT	X-Ray Microtomography
ZOI	Zone of influence

Chapter 1

1 Introduction

1.1 Background

Engineered nanoparticles are becoming ubiquitous in consumer and industrial technology with applications ranging from UV absorption in sunscreen (TiO_2 and ZnO nanoparticles), reinforcing carbon fiber materials (carbon nanotubes), and anti-microbial bandages and clothing (silver nanoparticles embedded in textiles). The conceptual origins of modern engineered nanoparticle technology are typically attributed to Richard Feynman's now-famous lecture 'There's plenty of room at the bottom' [*Feynman*, 1960], however the historical usage of nanoparticles extends back to the bronze age where they were used to create vibrantly coloured materials such as the stained glass windows of the medieval era [*Colomban*, 2009]. Despite this extended history, only recently have nanoparticles been produced in large enough quantities to pose risks to human and environmental health. Recent estimates of industrial nanoparticle production rates range from 5000 tons/year for TiO_2 nanoparticles, 500 tons/year for silver nanoparticles and 350 tons/year for carbon nanotubes [*Mueller and Nowack*, 2008]; although these estimates are at least 7 years out of date and production rates are now likely higher.

Environmental exposure modelling of diffuse (i.e. non-point source) releases suggests that these production rates are sufficient to yield detectable quantities of engineered nanoparticles in air, soil and water resources, which are potential vectors for human exposure [*Mueller and Nowack*, 2008; *Nowack and Bucheli*, 2007]. In addition, point source releases such as accidental industrial spills and leakages may potentially yield localized regions of highly concentrated engineered nanoparticles in the environment. More recently, it has been suggested that engineered nanoparticles present in water may not be completely removed by drinking water treatment processes [*Tiede et al.*, 2015]. Thus a multi-barrier approach is required to protect drinking water from nanoparticle contamination and to minimize human exposure and potential health effects. The multi-

barrier approach involves minimizing nanoparticle exposure to drinking water source zones (e.g., groundwater and surface water bodies), treatment processes, and distribution systems.

Of particular interest is the risk engineered nanoparticles may pose to groundwater source zones. Groundwater is widely used as a source of drinking water, approximately 25% of Canadians rely on groundwater for drinking water [*Statistics Canada*, 2010] and a third of the public water supply in the U.S.A. is provided from groundwater sources [*Kenny et al.*, 2009]. As such, protecting groundwater resources from contamination by engineered nanoparticles is key to protecting large portions of the population from possible adverse health effects. However, these groundwater resources have historically been susceptible to contamination from industrial pollution; there are an estimated 30,000 sites across Canada which are contaminated with hazardous chemicals [*NRTEE*, 2003].

A key component in protecting groundwater resources from contamination by engineered nanoparticles is understanding the transport, and ultimate fate, of nanoparticles released to the subsurface. Once released to the subsurface environment, nanoparticles will be transported along with the groundwater flow. Understanding the processes which govern their transport, such as attachment onto the soil, is necessary to predict how far the nanoparticles will be transported through the subsurface and, ultimately, the risk nanoparticles pose to groundwater source zones.

1.2   Research Objectives

The overall goal of this study was to develop an improved understanding of how nanoparticles are transported through soils. Specifically, this study develops a new experimental methodology for observing nanoparticle transport within real porous media and subsequently employs that methodology to examine the influence of surface chemistry and grain distribution on the pore-scale processes governing the transport of silver nanoparticles. The first objective was to develop and validate a method for using Synchrotron X-ray Computed Microtomography (SXCMT) to quantify nanoparticle concentrations within real pore spaces. Nanoparticle solutions of varying concentrations were emplaced within glass bead-packed water saturated columns and imaged via

SXCMT. The resulting SXCMT datasets were then examined to develop an understanding of the accuracy and uncertainty of the technique.

The second objective was to link so-called 'anomalous' transport behaviour of nanoparticles with specific pore-scale transport processes and to examine the influence of surface chemistry and pore geometry on these processes. This was conducted by employing SXCMT to examine pore-scale silver nanoparticle distributions during transport through different sand columns.

The third objective was to quantify the distributions of nanoparticle mass flux and flow rates through a soil's pore space and to ascertain how well the conceptual model employed by mechanistic computer models approximated these distributions. This was conducted by coupling the SXCMT datasets of the silver nanoparticle/uniform quartz experiment with computational fluid dynamics modelling of the SXCMT dataset.

1.3   Thesis Outline

The thesis is written in integrated article format. A brief description of each chapter is listed below.

Chapter 1 provides a brief overview of nanoparticles in the environment and outlines the scope of the thesis.

Chapter 2 reviews the current literature on predicting nanoparticle and colloid transport through the subsurface environment.

Chapter 3 presents a new method which employs Synchrotron X-Ray Computed Microtomography to quantify pore-scale nanoparticle concentrations during bench-scale transport experiments.

Chapter 4 employs the method presented in Chapter 3 and examines the impact of 'immobile zones', regions of low or no flow velocity, on nanoparticle transport through soil.

Chapter 5 couples the method presented in Chapter 3 with Computational Fluid Dynamics to examine why Colloid Filtration Theory is unable to accurately predict nanoparticle retention rates during transport through soil.

Chapter 6 summarizes the major conclusions of the thesis, discusses the limitations and identifies areas requiring further research.

1.4 References

Colomban, P. (2009), The use of metal nanoparticles to produce yellow, red and iridescent colour, from bronze age to present times in lustre pottery and glass: solid state chemistry, spectroscopy and nanostructure, paper presented at Journal of Nano Research, Trans Tech Publ.

Feynman, R. P. (1960), There's plenty of room at the bottom, *Engineering and science*, *23*(5), 22-36.

Kenny, J. F., N. L. Barber, S. S. Hutson, K. S. Linsey, J. K. Lovelace, and M. A. Maupin (2009), *Estimated use of water in the United States in 2005*, US Geological Survey.

Mueller, N. C., and B. Nowack (2008), Exposure modeling of engineered nanoparticles in the environment, *Environ. Sci. Technol.*, *42*(12), 4447-4453.

Nowack, B., and T. D. Bucheli (2007), Occurrence, behavior and effects of nanoparticles in the environment, *Environmental Pollution*, *150*(1), 5-22.

NRTEE (2003), Cleaning up the past, building the future: a national brownfield redevelopment strategy for Canada, 9 pp, Government of Canada.

Statistics Canada (2010), *Human Activity and the Environment: Freshwater supply and demand in Canada*, 59 pp., Statistics Canada, Catalogue no. 16-201-X, Ottawa

Tiede, K., S. F. Hanssen, P. Westerhoff, G. J. Fern, S. M. Hankin, R. J. Aitken, Q. Chaudhry, and A. B. A. Boxall (2015), How important is drinking water exposure for the risks of engineered nanoparticles to consumers?, *Nanotoxicology*, 1-9.

<center>Chapter 2</center>

2 Predicting colloid transport through saturated porous media: A critical review

2.1 Introduction

The introduction of Colloid Filtration Theory (CFT) [*Yao et al.*, 1971] sparked four decades of research at the pore, macroscopic, and field scales to develop predictive capabilities for colloid transport and retention in porous media. Significant strides have been made in the development of mechanistic models and their upscaling that link pore scale colloid transport processes to predictions of field scale behavior. This thesis represents an ideal opportunity to review the major contributions in this evolving, highly relevant field. It is also an opportunity to critically reflect on how the accuracy of field-scale predictions may be constrained by the simplifying assumptions built into mechanistic models, correlations equations and their relationship to our growing understanding of actual, pore-scale colloid behavior.

Prediction of colloid transport through the subsurface is important for a wide range of environmental and human-health related risk scenarios. For example, predictive colloid transport models are necessary to assess and minimize the risk of pathogen transport in groundwater. Among numerous examples is the Walkerton Ontario, Canada tragedy [*O'Connor*, 2002] in which the town's drinking water supply well was contaminated by E. coli transported in groundwater flow through the subsurface. Colloid transport from septic systems, agricultural runoff, and other sources through near-shore soils may lead to elevated concentrations of pathogenic colloids in beach sands [e.g. *Lipp et al.*, 2001] and transport across the groundwater/surface water interface may be the cause of frequent beach closures [e.g. *Russell et al.*, 2012]. A wide array of research into pathogen transport has been undertaken including virus transport [*Jin and Flury*, 2002; *Ryan et al.*, 1999; *Schijven et al.*, 1999] and column-scale bacteria transport [e.g. *Albinger et al.*, 1994; *Baygents et al.*, 1998; *Simoni et al.*, 1998; *Torkzaban et al.*, 2008], bacteria

transport in the field [*Bales et al.*, 1989; *Blanford et al.*, 2005; *DeBorde et al.*, 1999; *Harvey et al.*, 1995; *Powelson et al.*, 1993; *Ryan et al.*, 1999; *Ryan et al.*, 2002; *Scheibe et al.*, 2011; *Schijven et al.*, 1999; *Wielen et al.*, 2008; *Zhang et al.*, 2001b] and phage persistence in soils [e.g. *Yates et al.*, 1985] among many others; numerous reviews of pathogen transport in groundwater are available [*Bitton and Harvey*, 1992; *Harvey*, 1997; *Sen*, 2011; *Taylor et al.*, 2004].

Engineered nanoparticles (ENPs), another class of colloids, are of significant interest for their transport in porous media. On one hand, ENPs are an emerging environmental contaminant. Industrial production of engineered nanoparticles, such as carbon nanotubes and nanosilver, has increased significantly in recent years [*Christian et al.*, 2008; *Gao et al.*, 2013; *Majestic et al.*, 2010; *Marambio-Jones and Hoek*, 2010; *Nowack and Bucheli*, 2007; *Petersen et al.*, 2011; *Wiesner et al.*, 2006] and it is expected that their presence in the environment will increase. This can occur through diffuse ENP release [*Mueller and Nowack*, 2008], including ENP dispersal in aerosols, in exhaust emissions, and in land application of wastewater sludge containing nanoparticles originating in consumer products. Point sources of ENPs include leakage from landfills and accidental industrial releases. Prediction of ENP transport in porous media is important for assessing the risk from ENP migration in aquifers and the contamination of wells used for drinking water supply. ENP studies have involved modeling [*Bai and Li*, 2012; *Cullen et al.*, 2010; *Taghavy et al.*, 2013], pore scale experiments [*Dunphy Guzman et al.*, 2006; *May et al.*, 2012; *May and Li*, 2013; *Molnar et al.*, 2014] and column experiments [*Jaisi and Elimelech*, 2009; *Lecoanet et al.*, 2004; *Liang et al.*, 2013; *Lin et al.*, 2011; *Liu et al.*, 2009a; *Neukum et al.*, 2014; *Ren and Smith*, 2013; *Torkzaban et al.*, 2010; *Uyusur et al.*, 2010; *Wang et al.*, 2008; *Zhang et al.*, 2012]. Numerous review papers exist, including Petersen et al. [2011] who present a review of the transport and environmental risks of carbon nanotubes.

ENPs are also being considered as a remediation strategy for sites contaminated with industrial organic liquids. For example, nano-zero-valent iron (nZVI) particles are injected into the subsurface at contaminated sites for the *in-situ* reduction of chlorinated solvents in groundwater [*Johnson et al.*, 2013; *O'Carroll et al.*, 2013; *Tosco et al.*,

A version of this chapter has been published [*Molnar et al.*, 2015b]

2014a]. This novel approach has been evaluated at both the laboratory [e.g. *Berge and Ramsburg*, 2009; *Kocur et al.*, 2013; *Phenrat et al.*, 2009; *Raychoudhury et al.*, 2010] and pilot field scales [*Johnson et al.*, 2013; *Kocur et al.*, 2014]. Recent advances include the tailored design and synthesis of novel ENPs including bimetallic composites and polymer coatings [*Bennett et al.*, 2010; *Gastone et al.*, 2014; *He and Zhao*, 2008; *Sakulchaicharoen et al.*, 2010; *Tosco et al.*, 2014b], which can influence surface charge, fluid viscosity, and other properties atypical of traditional colloid suspensions. The design and optimization of these ENP-based remediation schemes require accurate predictive models of ENP transport in porous media, and users of existing CFT need to understand how and where it is possible to change parameters appropriately for non-traditional suspensions.

Colloids can also enhance the transport of dissolved contaminants in groundwater via their sorption onto colloid surfaces. Colloid-facilitated transport has been studied for a wide range of contaminants including radionuclides [e.g. *Kersting et al.*, 1999; *Novikov et al.*, 2006], hydrocarbons [e.g. *Qi et al.*, 2014] and pesticides [e.g. *de Jonge et al.*, 1998; *Sprague et al.*, 2000]. Research in this area includes modelling the reduction in contaminant retardation [*Corapcioglu and Jiang*, 1993; *Flury and Qiu*, 2008; *Johnson et al.*, 1995b]. Several reviews and special journal sections have provided reviews of colloid-associated contaminant transport [*de Jonge et al.*, 2004; *McCarthy and Zachara*, 1989; *Ouyang et al.*, 1996; *Ryan and Elimelech*, 1996; *Sen and Khilar*, 2006]. Further understanding of colloid transport mechanisms are required to predict the risk posed by colloid-enhanced transport mechanisms.

The predictive tools developed to explore column and field scale colloid transport phenomena are primarily continuum-based numerical models that solve the advection-dispersion equation for solute transport in porous media. Terms employing rate coefficients to drive colloid mass transfer to the stationary (solid) phase and back are used to describe the macroscopically observed transport behavior of colloids as described by breakthrough-elution concentration histories and profiles of retained concentration as a function of distance. Rate constants for colloid transfer to the stationary phase may be independently determined using upscaled predictions from mechanistic models that

A version of this chapter has been published [*Molnar et al.*, 2015b]

employ relevant force and torque balances to determine colloid trajectories in flow fields corresponding to representative pore (collector) geometries. Relevant forces include fluid drag, diffusion, gravity, as well as colloid-surface forces including van der Waals and electric double layer as described by DLVO theory [*Derjaguin and Landau*, 1941; *Verwey and Overbeek*, 1948] and its derivatives. The upscaled mechanistic predictions provide good prediction of colloid transport at the continuum scale for spheroidal colloids in uniform media when colloid-collector repulsion is absent (so-called 'favorable' conditions), as is typically the case for oppositely charged surfaces [e.g. *Elimelech*, 1991].

In the environment, however, the typical condition is that both colloids and collector surfaces carry negative charge. Colloids exhibiting net negatively-charged surfaces under environmental pH conditions include: bacteria [e.g. *Bradford et al.*, 2006a; *Foppen and Schijven*, 2006; *McClaine and Ford*, 2002], protozoa [e.g. *Liu et al.*, 2009b; *Ruohola et al.*], viruses [e.g. *Mondal and Sleep*, 2013; *Ryan et al.*, 1999] and engineered nanoparticles [e.g. *Jiang et al.*, 2012; *Kocur et al.*, 2014; *Liang et al.*, 2013; *Molnar et al.*, 2014; *Torkzaban et al.*, 2010]. Common minerals exhibiting negatively charged surfaces at typical pH include quartz, silica, feldspars, mica and certain clays [*Molnar et al.*, 2011, Table 1]. The combination of both colloids and collectors carrying a negative charge leads to electric double layer repulsion (as well as steric repulsion from surface macromolecules), thereby yielding 'unfavorable' conditions for attachment.

Repulsion between colloids and porous media collectors results in complex transport behavior that is mediated by the topology of the pore domain and the flow field, via such features as low flow (diffusion-limited) zones that may be generated in non-spheroidal or non-uniform media, such as many environmental sediments and soils. In recognition of these complexities, mechanistic models have been adapted to address more complex scenarios [*Long and Hilpert*, 2009; *Long et al.*, 2010; *Ma et al.*, 2009; *Ma and Johnson*, 2010; *Ma et al.*, 2011; *Ma et al.*, 2013; *Pazmino et al.*, 2014a]. However, upscaling of these types of models for implementation into advection-dispersion or other transport equations represents an important ongoing research opportunity.

A version of this chapter has been published [*Molnar et al.*, 2015b]

Whereas mechanistic predictions regarding the above complexities are not yet readily implemented into continuum scale transport models, advances have occurred in descriptive continuum-scale colloid transport models describing these complexities [e.g. *Bradford et al.*, 2009; *Bradford et al.*, 2011; *Katzourakis and Chrysikopoulos*, 2014; *Leij and Bradford*, 2013; *Šimůnek and van Genuchten*, 2008; *Tufenkji and Elimelech*, 2004b; 2005a; b]. These models employ parameters fitted to column-scale breakthrough-elution concentration histories, and provide a method to infer potential pore-scale mechanisms driving complex transport behavior. There is clearly an important ongoing research opportunity associated with obtaining high resolution, pore-scale information on the behavior of colloids and its generalization into continuum-scale models in order to further improve predictive approaches to incorporating colloid interaction with soil and flow heterogeneity.

This chapter provides a critical review of colloid transport literature with a specific focus on linking pore-scale processes to column and field scale observations as well as continuum-scale transport models across a range of relevant subsurface scenarios. This review exclusively discusses colloid transport through water saturated media and aims to help distinguish and clarify the roles of different pore and continuum-scale modeling approaches, focusing on post-1990 colloid transport work. The chapter is structured so as to (i) provide an introduction to the fundamentals and review existing knowledge and knowledge gaps for those who are relatively new to the field, and (ii) provide a more detailed, critical assessment of the state of the art. In Section 2.2, a brief review is provided of mean-field DLVO interactions and experimentally observed colloid transport phenomena, focusing on the contrasting transport behaviors observed under favorable versus unfavorable conditions for attachment. Section 2.3 describes strategies by which kinetic parameters have been used in continuum models to infer mechanisms from experimental observations. Section 2.4 reviews the current and emerging ability of mechanistic approaches to independently predict kinetic parameters used in continuum models (e.g. retention coefficients) in favorable conditions with unfavorable conditions discussed in the Appendix 7.3. In addition, the Appendix 7.4 examines upscaling of mechanistic predictions to rate constants, explores the role of topology in upscaling strategies, and highlights opportunities for future research.

A version of this chapter has been published [*Molnar et al.*, 2015b]

2.2   Mean-field DLVO interactions and experimental observations

2.2.1   Mean-field DLVO forces

As mentioned, the mechanistic models that underpin predictive tools for colloid transport depend upon DLVO interactions. Classic DLVO theory [*Derjaguin and Landau*, 1941; *Verwey and Overbeek*, 1948] attempts to describe the colloid-collector interactions in terms of adhesive and repulsive forces. By summing the adhesive (negative) and repulsive (positive) energies between a colloid and collector over a range of separation distances, an interaction energy profile – the net energy versus separation distance – is constructed. Figure 2.1 presents two typical, classic DLVO interaction energy profiles for favorable (silver colloid – iron oxide) and unfavorable interaction conditions (silver colloid – quartz). The Figure 2.1 illustrates a number of distinct features or regions that are typical of colloid-surface interaction profiles. In unfavorable conditions a repulsive barrier exists that either limits colloid attachment to the surface (experimental observations) or prevents attachment (for energy barriers exceeding several kT in mechanistic simulations).

Outward from this repulsive barrier exists a small region of attraction where colloids may accumulate in a secondary minimum at separation distances tens of nm from the collector surface. In situations where colloids either possesses enough energy to overcome the barrier, or no barrier exists (i.e., favorable conditions), they can enter the primary minimum (Figure 2.1) and physically attach to the surface.

The 'near-surface fluid domain' is defined, for the purposes of this review, as the region between the collector surface and the distance over which van der Waals attraction is significant, i.e., secondary minimum and closer (see Figure 2.1). The 'bulk fluid domain' is defined as the area beyond the near-surface fluid domain beyond which colloid-collector DLVO interactions are insignificant. For typical colloid-collector systems, the interface between the bulk fluid domain and the near-surface domain occurs in the range of several to hundreds of nm [e.g. *Johnson and Hilpert*, 2013].

It is worthwhile mentioning that the energy barrier also influences colloid detachment from the primary minimum. In classic DLVO theory, the primary minimum is an infinitely deep well and the height of the energy barrier is inconsequential to colloids entrapped within the minimum. However, short range forces such as Born repulsion serve to limit the depth of the well to finite values [*Ruckenstein and Prieve*, 1976]. In this finite-depth scenario, the energy barrier now contributes to the effective depth of the energy well and acts as a barrier to both colloid attachment and detachment [*Ryan and Elimelech*, 1996]. Increasing the height of the energy barrier via perturbations in solution chemistry will deepen the energy well holding the colloid on the surface of the collector [*Hahn et al.*, 2004].

The forces acting on the colloids are the derivative of the energies with respect to separation distance, such that both energy and force profiles exhibit the same features: primary minimum, repulsive barrier, and secondary minimum. Using this sign convention, attractive forces are negative and repulsive forces are positive. The separation distances of these features differ slightly between the force and energy profiles, but this is not important to this discussion. This review refers to the features illustrated in Figure 2.1 without distinguishing specifically between force and energy. Traditional mechanistic colloid transport and retention models describe colloid-collector interactions (i.e., repulsion, physical contact and retention in the secondary minimum) by considering the above-described DLVO theory. A shortcoming of this theory (as presented above) is that it considers the surfaces to be monolithic (homogeneous). It is worthwhile emphasizing that this monolithic DLVO approach does not represent a 'mean interaction energy' of colloids, but rather it is an interaction calculated from the bulk surface properties of colloids and collectors. This so-called mean-field DLVO approach is an over-generalization of the surface characteristics of colloids and collectors, since it does not account for micro- to nano-scale heterogeneity that is expected to exist on real surfaces (as discussed in the Appendix 7.3). Hence, while we review below the great utility of mean-field DLVO interactions for interpreting the transport behavior of colloids in porous media, we also discuss in subsequent Sections the emerging opportunities offered by the incorporation of heterogeneity into colloid-surface DLVO interactions.

A version of this chapter has been published [*Molnar et al.*, 2015b]
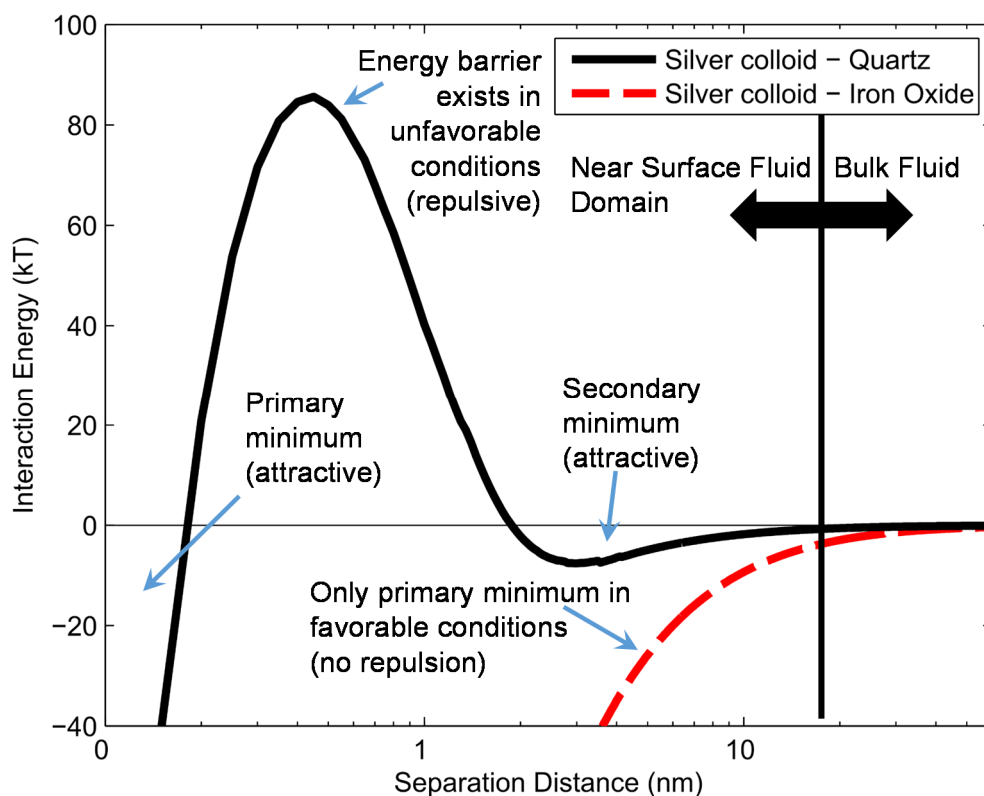
Figure 2.1: Two examples of classic DLVO interaction profiles for favorable conditions (dashed red line) and unfavorable conditions (solid black line) for a 0.3 μm diameter silver colloid interacting with an iron oxide surface and quartz surface respectively in a 300mM ionic strength solution. The calculation was performed using the sphere-plate Surface Element Integration technique [Bhattacharjee et al., 2000] with representative literature values for zeta potentials (silver colloids: -28 mV [*Molnar et al.*, 2015a], quartz: -55mV [Liang et al., 2013], iron oxide: -25 mV [*Molnar et al.*, 2015a]) and Hamaker constants (silver colloids: 15×10^{-20} J [Pinchuk, 2012], quartz: 7.93×10^{-20} J [Ross and Morrison, 1988], iron oxide: 23.2×10^{-20} J [Faure et al., 2011].

2.2.2 Experimental observations: Influence of favorable versus unfavorable conditions

While DLVO forces are significant over small (nanoscale) separation distances (see near surface fluid domain in Figure 2.1), the presence or absence of a repulsive energy barrier controls the transport and retention of colloids at column and field scales. A large number of column-scale transport experiments have demonstrated the implications of these small scale interactions that yield field scale consequences, as described below.

A version of this chapter has been published [*Molnar et al.*, 2015b]

A note on terminology: 'attachment' is herein defined as the immobilization, via physical contact, of the colloid onto the collector surface within the primary energy well. As continuum scale experiments typically cannot distinguish attachment from other retention mechanisms (such as occupancy in the secondary energy minimum), the term 'retention' will be employed to describe colloids that do not exit the system during the term of the experiment. Likewise, continuum scale experiments that observe delayed exit of colloids from the experiment typically cannot distinguish between colloids that detached from a collector surface or colloids that were temporarily retained without attachment. Thus, the term 're-entrainment' will be employed to avoid attributing a particular mechanism to the colloids' delayed exit during these experiments. To be clear, the processes of attachment versus retention, and detachment versus re-entrainment are indeed distinguishable in many pore scale direct observation experiments, as well as in pore scale mechanistic simulations (they must be distinguished in the latter). In those contexts we will refer specifically to attachment and detachment as appropriate.

Column experiments conducted under favorable conditions typically exhibit relatively simple colloid transport behavior: as seen in Figure 2.2 (C), colloid breakthrough during injection reaches a steady-state (i.e., temporally constant) plateau *[Elimelech et al., 2000; Li et al., 2004; Li et al., 2005; Tufenkji and Elimelech, 2004b; 2005b].*

A version of this chapter has been published [*Molnar et al.*, 2015b]
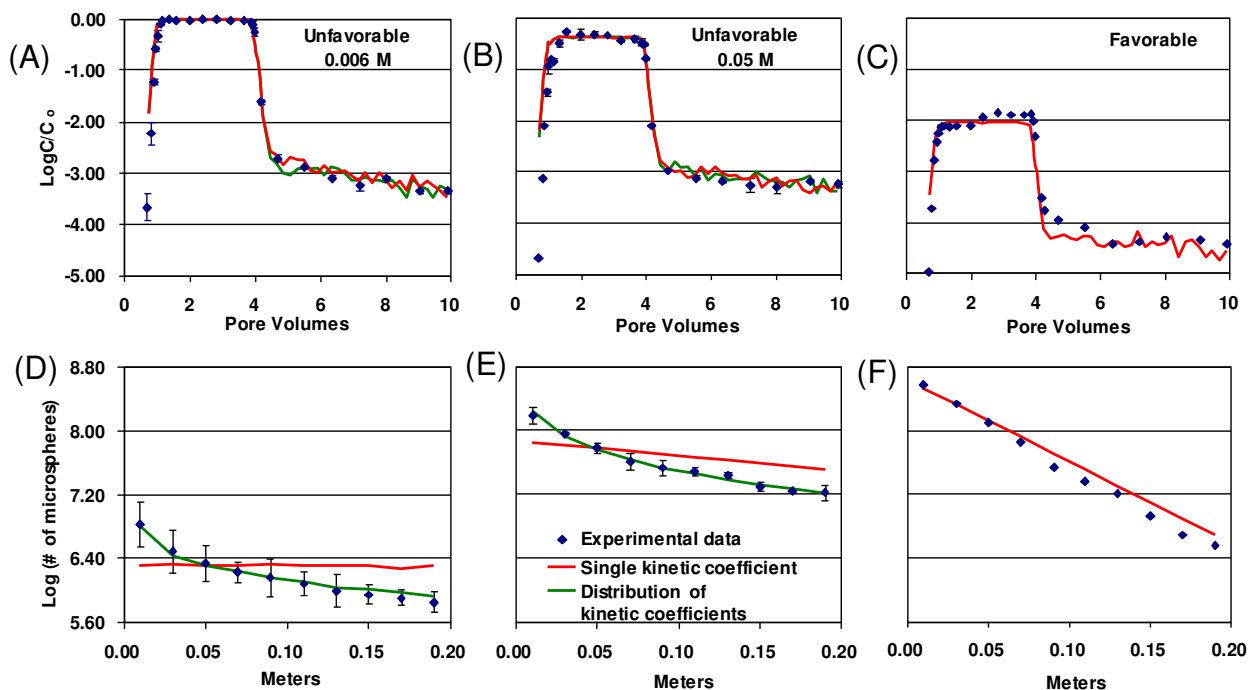
Figure 2.2 Experimental data (symbols) for the breakthrough-elution behavior (A–C) and retained profiles (D–F) of polystyrene latex microspheres in quartz sand in unfavorable and favorable conditions described in [Li and Johnson, 2005] . Lines are continuum model descriptions with a single deposition rate coefficient. The single deposition rate coefficient was used to generate a probabilistic deposition distribution. Adapted from [Li and Johnson, 2005].

During the elution phase in favorable conditions, the concentration of colloids exiting the column decreases sharply with time indicating that there is negligible re-entrainment of previously retained colloids [*Li et al.*, 2004; *Tufenkji and Elimelech*, 2004b; 2005b]. The corresponding profiles of retained colloid concentrations with column length show a classic log-linear decrease under favorable conditions (Figure 2.2, F), as predicted by analytical solutions of the advective-dispersive-colloid transport equation (discussed in Section 2.3) [*Han et al.*, 2014; *Li et al.*, 2004; *Tufenkji and Elimelech*, 2004b; 2005b]. These simple, well defined column-scale behaviors are due to the straightforward colloid-collector interactions at the pore scale under favorable conditions. Colloids that approach the collector experience no repulsion and come into physical contact with the collector surface (immobilize) [*Johnson et al.*, 2010; *Kuznar and Elimelech*, 2007]. These colloids do not typically detach, since the strong attractive forces exceed fluid drag forces [*Bergendahl and Grasso*, 2000].

A version of this chapter has been published [*Molnar et al.*, 2015b]

Column experiments conducted under unfavorable conditions exhibit significantly different behavior from those conducted under favorable conditions (Figure 2.2, A,B,D,E). Depending on the experimental conditions, unfavorable breakthrough behavior may also reach a steady state plateau (Figure 2.2 A,B) [*Elimelech et al.*, 2000; *Jiang et al.*, 2012; *Li et al.*, 2005]. However, non-steady state behavior may also occur. The effluent concentration may gradually increase over time, suggesting that a limited number of sites for colloid retention exist and are progressively filled (i.e., blocking) [*Camesano et al.*, 1999; *Johnson and Elimelech*, 1995; *Liang et al.*, 2013; *Lin et al.*, 2011; *Liu et al.*, 2009a; *Mattison et al.*, 2011; *Wang et al.*, 2012]. Decreasing concentration during breakthrough (called ripening) suggests that favorable colloid-colloid interactions allow already retained colloids (presumably due to inferred 'favorable' heterogeneity as described in the appendix Section 7.3) to serve as additional sites for further colloid retention[*Jiang et al.*, 2012; *Tong et al.*, 2008].

Extended tailing may occur during the elution phase of unfavorable experiments (Figure 2.2 A,B). Tailing is defined by the slow release of colloids from the column (illustrated in Figure 2.2) and is indicative of significant re-entrainment, as observed for microbes in the laboratory [*Fontes et al.*, 1991; *Harter et al.*, 2000; *Hendry et al.*, 1997; 1999; *Hornberger et al.*, 1992; *Johnson et al.*, 1995a; *Li and Johnson*, 2005; *Li et al.*, 2005; *Lindqvist et al.*, 1994; *McCaulou et al.*, 1994; *McCaulou et al.*, 1995], field [*DeBorde et al.*, 1999; *Harvey et al.*, 1995; *Ryan et al.*, 1999; *Schijven et al.*, 1999; *Scholl and Harvey*, 1992] and non-biological colloids [*Johnson et al.*, 2007; *Li et al.*, 2004; *Li et al.*, 2005; *Tong et al.*, 2005; *Tufenkji et al.*, 2004]. The re-entrainment behavior under unfavorable conditions is sensitive to solution chemistry and fluid flow as shown for re-entrainment with perturbations, including: variation in ionic strength [*Jiang et al.*, 2012; *Mattison et al.*, 2011; *Ryan et al.*, 1999; *Shen et al.*, 2007; *Shen et al.*, 2012; *Tufenkji and Elimelech*, 2004b; 2005b], variation in pH [*Ryan et al.*, 1999; *Tufenkji and Elimelech*, 2004b; 2005b] and variation in fluid velocity [*Pazmino et al.*, 2014b; *Shang et al.*, 2008]. Traditionally, such release has been attributed to colloids that were retained in secondary minima, although more recent mechanistic simulations incorporating heterogeneity indicate that detachment from primary minima may contribute as well (as described in the Appendix 7.3).

A version of this chapter has been published [*Molnar et al.*, 2015b]

The resulting retention profiles from unfavorable condition experiments (Figure 2.2, D,E) have shown non-log-linear (e.g. non-monotonic or hyperexponential) decreases in concentration as function of distance [*Li et al.*, 2004; *Liang et al.*, 2013; *Tong and Johnson*, 2007; *Tufenkji and Elimelech*, 2004b; *Tufenkji et al.*, 2004; *Tufenkji and Elimelech*, 2005a; b]. Hyper-exponential and non-monotonic profiles have also recently been described for engineered nanomaterials [*Liang et al.*, 2013; *Wang et al.*, 2014a].

Column-scale experiments have been described using continuum-scale models employing rate constants and other parameters. Trends in these parameters as a function of fluid velocity, solution ionic strength (IS), among others, allow inference of the mechanisms responsible for observed differences in colloid transport and retention in favorable versus unfavorable conditions, as described in the following Section.

2.3   Continuum-scale models: Inferring mechanisms from kinetic coefficients

Continuum scale models of the transport of species in groundwater solve mass balance equations at the macroscopic scale. At this scale, microscopic properties are averaged over a representative elementary volume (REV) and the averaged property (e.g., porosity, fluid pressure, colloid concentration) is treated as a value that represents the property throughout the REV [*Bear and Cheng*, 2010]. Continuum models necessarily blur microscopic details and employ simplifying assumptions in the averaging process. The result is partial differential equations that describe spatial and temporal rate of change of key macroscopic properties (e.g., fluid velocity, colloid concentration) at a practical scale. These equations are typically discretized and solved on a numerical grid that correlates REVs to nodes. The advection-dispersion equation (ADE), which describes the transport of a non-reactive solute tracer in groundwater, is a typical example (see Figure 2.3, tracer equation). Additional continuum scale (averaged) terms are incorporated as additional mechanisms, processes, and reactions and are necessary to describe the behavior of a solute or colloid at this scale (e.g., partitioning to surfaces, filtration, degradation; examples for colloids provided in Figure 2.3 and further discussed below). The values (or functions) assigned to the coefficients of these terms depend on the specific solute/colloid-soil-groundwater conditions being considered and are often

A version of this chapter has been published [*Molnar et al.*, 2015b]

determined through batch studies (e.g., for sorption) or model fitting to experimental column effluent results (e.g., colloid retention).

The treatment of colloid retention in continuum scale models differs significantly from that of solutes due to their interactions with the surface being kinetic (colloids) rather than equilibrium (solutes) [*Schijven and Hassanizadeh*, 2000; *Tufenkji*, 2007]. However, it is worth noting that solute adsorption is not always strictly equilibrium-based as there is evidence that adsorption can, in some circumstances, also be a kinetic process [*Bahr and Rubin*, 1987; *Cvetkovic and Dagan*, 1994; *Dusek et al.*, 2015; *Espinoza and Valocchi*, 1997; *Fujikawa and Fukui*, 1991; *van Kooten*, 1996; *Zhang and Selim*, 2006]. In many scenarios, the high diffusion rates of solutes allows them to reach surfaces (adsorb) and leave (desorb) readily, at rates that are typically high relative to groundwater fluid velocities (i.e., low Peclet numbers). Thus, solute-surface interactions can be represented as a local equilibrium process that can often be represented using a linear proportionality (partition constant). Partition constants are empirical (experimentally measured), independently determined from continuum scale experiments, and the one representing distribution of solute between water and sediment is often referred to as K_d (defined as $C_s = K_d \times C_w$ where C_s is the solid-phase concentration and C_w is the aqueous phase concentration).

In contrast, colloids exhibit relatively low diffusion, which limits their ability to reach surfaces (but also makes the likelihood of colloids reaching surfaces mechanistically predictable as described in Section 2.4). Colloid transfer to surfaces (filtration) is therefore described using kinetic retention coefficients [*Harvey and Garabedian*, 1991; *Schijven and Hassanizadeh*, 2000; *Tufenkji*, 2007]. The resulting breakthrough behaviors of solutes versus colloids are quite distinct (Figure 2.3) in that partitioning (specifically the proportionality between concentrations in water and sediment) retards transient breakthrough of the solute relative to a conservative tracer and yields complete steady-state breakthrough (effluent and influent concentrations equivalent, $C = C_0$). In contrast, filtration (and other predominantly one-way processes such as degradation) yield reduced steady-state breakthrough ($C < C_0$), and transient breakthrough is not generally retarded relative to a conservative tracer (Figure 2.3) [e.g. *Foppen and Schijven*, 2006]. It is noted

A version of this chapter has been published [*Molnar et al.*, 2015b]

that transient breakthrough of colloids may occur earlier than for tracers if Taylor dispersion (intra-pore fluid velocity variation), or size-exclusion of colloids from small pores (inter-pore fluid velocity variation), yields enhanced advection of colloids relative to solutes [e.g. *Bales et al.*, 1989; *Chrysikopoulos and Syngouna*, 2014; *Keller et al.*, 2004; *Powelson et al.*, 1993; *Zhang et al.*, 2001a].

The classic ADE for a non-reactive solute tracer (see Figure 2.3, tracer equation) is commonly modified for solute partitioning behavior (see Figure 2.3, partitioning equation) as well as colloid transport (see Figure 2.3, filtration equation). The modified-ADE commonly employed for colloid transport incorporates a single kinetic retention coefficient for colloid retention. The single-rate description of colloid transport yields continuum-scale behavior that, in the absence of colloid aggregation, generally provides an excellent match to the colloid transport and retention behavior discussed in Section 2.2 for favorable conditions (Figure 2.2)[e.g. *Li et al.*, 2004; *Tufenkji and Elimelech*, 2004b; 2005b].

A version of this chapter has been published [*Molnar et al.*, 2015b]
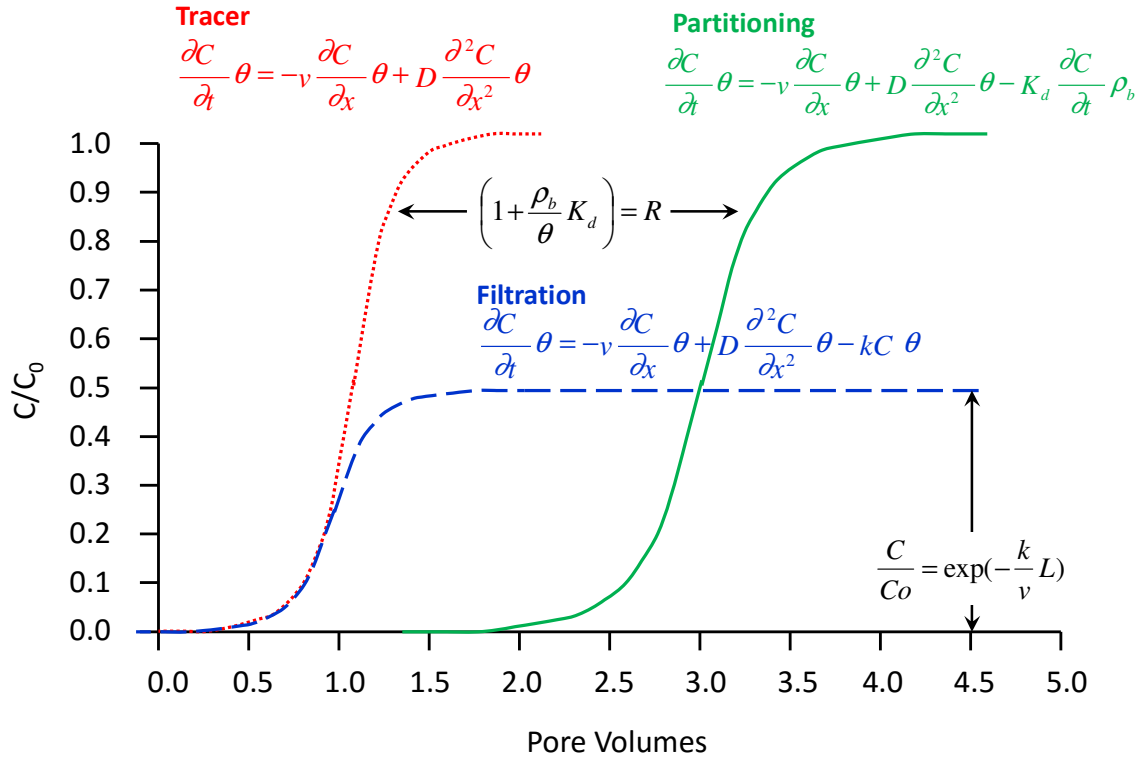
Figure 2.3: Typical breakthrough curve profiles that illustrate how equilibrium partitioning (i.e., retardation) (solid green line) and filtration (i.e., kinetic removal) (dashed blue line) impact breakthrough behavior relative to a conservative tracer (dotted red line). The variables in the equations are defined as: C, effluent concentration; v, advective velocity; t, time; x, position; θ, porosity; D, dispersivity; K_d, partitioning coefficient; ρb, bulk density; R, retardation coefficient; k, kinetic retention coefficient; Co, initial (injection) concentration; L, travel length.

In unfavorable conditions, the single-rate description of colloid transport often fails to capture experimentally observed breakthrough and retention behavior (the non-steady state breakthrough and non-log-linear retention profiles described in Section 2.2; see Figure 2.2). The hyper-exponential retention profiles often observed in unfavorable conditions suggest that there is a high deposition rate near the porous medium inlet followed by a region with low deposition rates. A number of studies have inferred that this depth-dependent retention rate is due to a distribution of retention rates that are present within the experimental system [*Chatterjee et al.*, 2011; *Foppen and Schijven*, 2006; *Foppen et al.*, 2007; *Li et al.*, 2004; *Schijven and Hassanizadeh*, 2000; *Schijven and Šimůnek*, 2002; *Tong and Johnson*, 2007; *Tufenkji et al.*, 2003; *Tufenkji and Elimelech*, 2004b; 2005a; b]. To describe this observation, a second, additional kinetic

A version of this chapter has been published [*Molnar et al.*, 2015b]

retention coefficient is often employed – termed 'dual-deposition' or 'two-site' models – to better fit the experimental retention profiles (discussed in Section 2.2). The two kinetic retention coefficients represent: a) a 'fast' kinetic retention coefficient to describe the early, sharp decrease in retained concentration, and (b) a 'slow' kinetic retention coefficient to describe the later, more gradual decline in retained concentration [*Chatterjee et al.*, 2011; *Mattison et al.*, 2011; *Mondal and Sleep*, 2013; *Schijven and Šimůnek*, 2002; *Tufenkji and Elimelech*, 2004b; 2005a; b]. This results in an improved model fit to experimental hyper-exponential profiles (Figure 2.2).

The hyper-exponential profiles (initially observed for bacteria and protozoa) were attributed to heterogeneity among the bacterial population such that "stickier" individuals were retained upgradient of "less sticky" individuals [*Albinger et al.*, 1994; *Baygents et al.*, 1998; *Bolster et al.*, 1999; *Bolster et al.*, 2000; *Harvey et al.*, 1995; *Hendry et al.*, 1997; *Schijven et al.*, 1999; *Simoni et al.*, 1998]. Distributions in colloid size, surface charge, coatings and hydrophobicity have been inferred to yield heterogeneity among colloid populations, and hyper-exponential retention profiles as illustrated in Figure 2.2 [*Chatterjee et al.*, 2011; *Foppen et al.*, 2007; *Li et al.*, 2004; *Schijven and Hassanizadeh*, 2000; *Schijven and Šimůnek*, 2002; *Simoni et al.*, 1998; *Tong and Johnson*, 2007; *Tufenkji et al.*, 2003].

Other studies have attributed the inferred 'fast' and 'slow' dual-deposition behavior to differences in interactions energies between colloids and collectors emanating partially from localized soil heterogeneities as well as deep secondary energy minima, the latter yielding 'fast' retention, and the former yielding 'slow' retention [*Tufenkji and Elimelech*, 2004b; 2005a; b] on the basis that the former mechanism requires overcoming the repulsive energy barrier prior to retention. Additional studies have also suggested that soil heterogeneities, such as heterogeneities of attractive iron oxyhydroxide situated within bulk repulsive silica, can create "fast" and "slow" deposition rates in the favorable and unfavorable regions [*Schijven and Hassanizadeh*, 2000; *Schijven and Hassanizadeh*, 2002].

A version of this chapter has been published [*Molnar et al.*, 2015b]

Whereas the above studies implicate soil heterogeneity in generating fast versus slow retention rates, they do not articulate how this would generate preferential up-gradient versus down-gradient retention (hyper-exponential profiles) [*Johnson and Li*, 2005]. Assuming that inferred heterogeneity is distributed throughout the column (not predominantly located near the column inlet), then the kinetic retention coefficient across the column would be uniformly increased or decreased across the column by the presence of heterogeneity. Based on similar reasoning, a number of studies have concluded that soil heterogeneity alone is likely not the primary cause of this behavior [*Foppen et al.*, 2007; *Li et al.*, 2004; *Schijven and Šimůnek*, 2002; *Tong and Johnson*, 2007].

The above review demonstrates the utility of continuum scale models for inferring colloid transport, retention, and re-entrainment mechanisms; however, it should be noted that the kinetic parameters used in these models tend to be descriptive rather than predictive. For example, currently only the filtration rate constant under favorable conditions can be independently predicted (for spheroidal uniform colloids and media). No independently-derived mechanistic basis currently exists for predicting 'fast' and 'slow' rate coefficients present in these dual-deposition models; rather, they require fitting to experimental breakthrough and retention profile data. Thus, dual-deposition rate models cannot be used to predict colloid transport without conducting detailed experiments *a priori*. The corollary is that, while this dual-deposition approach successfully produces hyper-exponential profiles, the underlying mechanism(s) can only be inferred, and are not proven by a fit to data. For example, the observed decrease in attachment rate coefficient with increasing transport distance has been attributed to both: (1) straining [*Bradford et al.*, 2002; *Bradford et al.*, 2003; *Bradford et al.*, 2004; *Bradford et al.*, 2006b] and (2) heterogeneity among the colloid population [e.g. *Tong and Johnson*, 2007] which are very different mechanisms for achieving this phenomenon.

Another common example of mechanisms inferred from fitting to continuum-scale data are the dual-region or multiporosity models. The classic ADE for a one-dimensional system employs a single average pore water velocity. This single-velocity approach relies on the assumption that the velocity distribution within the porous medium can be approximated by a single, or volume-averaged, velocity term that predicts, in the absence

A version of this chapter has been published [*Molnar et al.*, 2015b]

of retardation, a classic breakthrough curve with C/C_o = 0.5 at the location of the advective front. It also predicts a symmetrically sharp decrease in concentration during the elution phase of the experiment. As discussed in Section 2.2, this approach provides an excellent description of colloid transport through uniform, homogeneous and simple (i.e., glass bead) porous media in favorable deposition conditions.

However, the anomalous early breakthrough and extended tailing behavior discussed in Section 2.2 suggests that this average-velocity approach may not be appropriate for a wide range of water saturated soils in both favorable and unfavorable conditions. These behaviors have been modeled at the continuum-scale by employing a distribution of permeabilities (e.g., dual-porosity or dual-permeability models). While these models are commonly employed for solute transport behavior in the presence of preferential pathways/low permeability regions and fractures/rock matrix [e.g. *Haggerty and Gorelick*, 1995; *Haggerty et al.*, 2000; *Rotter et al.*, 2008; *Šimůnek et al.*, 2003; *Šimůnek and van Genuchten*, 2008] they have also been adapted for use in colloid transport, although to a relatively limited extent. Specifically, these studies have suggested that early-time colloid breakthrough and bi-modal breakthrough curves may be linked to preferential flow [*Leij and Bradford*, 2013; *Subramanian et al.*, 2013] which may occur in both physically heterogeneous [e.g. *Wang et al.*, 2014b; *Zheng and Gorelick*, 2003] and uniform media [e.g. *Berkowitz et al.*, 2006; *Scheibe et al.*, 2013] and also due to size exclusion effects discussed in Section 2.2.

Continuum-scale solute modeling studies have suggested that extended tailing is linked to the presence of low permeability zones, and is described via dual-porosity (i.e., dual-region) or multiporosity models [e.g. *Haggerty and Gorelick*, 1995; *Haggerty et al.*, 2000]. Colloid transport models typically describe tailing by assuming that a fraction of colloids are temporarily (i.e., reversibly) retained [*Johnson et al.*, 1995a; *Landkamer et al.*, 2013; *Mondal and Sleep*, 2013; *Schijven and Hassanizadeh*, 2002; *Schijven and Šimůnek*, 2002; *Zhang et al.*, 2001b]. Conceptually, this treatment is similar to dual-region models to describe solute tailing as the retention still occurs in regions with below-average velocity, although for colloid transport in uniform media this is typically assumed to be the near-surface zone [*Johnson and Hilpert*, 2013]. Attribution of

A version of this chapter has been published [*Molnar et al.*, 2015b]

temporary colloid retention to residence in the near surface fluid domain (i.e., secondary minima) can be inferred, but is not proven by the match of continuum-scale models to column experiment observations. Notably, recent pore-scale modeling studies have suggested that below-average velocity regions in the bulk pore space may also temporarily retain colloids [*Cardenas*, 2008; *Li et al.*, 2010a; *Li et al.*, 2010b; 2012; *Torkzaban et al.*, 2008] suggesting that the near-surface fluid zone may not be the only contributor to extended tailing.

Mass transfer coefficients used in continuum models are often fitted parameters, determined by inverse modelling of experimental data [*Köhne et al.*, 2009a; b; *Wang et al.*, 2014c]. Results from these continuum models are powerful tools for identifying potential mechanisms and demonstrating the influence of physical heterogeneity (mobile versus immobile zones) and solution chemistry (e.g., favorable versus unfavorable attachment conditions). For example, trends in kinetic parameters describing colloid retention and re-entrainment show qualitative agreement with DLVO predictions (barrier height and secondary minimum depth) as a function of ionic strength [e.g. *Elimelech and Omelia*, 1990a; *Elimelech and Omelia*, 1990b; *Elimelech*, 1991; *Petosa et al.*, 2010]. Although quantification of rate constants through experimentation is useful, *a priori* determination of mechanisms, and independent derivation of rate constants, would enable prediction of colloid transport in a range of scenarios but requires mechanistic modelling as will be discussed in the next Section.

2.4 Mechanistic prediction of retention in favorable and unfavorable conditions

Differences between molecular (e.g., solute) and colloidal transport processes in porous media drive differing modeling approaches to describe their transport. Specifically, solutes exhibit much greater random motion and lack a deterministic trajectory so their likelihood of reaching a surface is determined empirically by laboratory analyses (e.g., batch equilibration tests). By contrast, colloids exhibit relatively limited diffusive (i.e., Brownian) motion and possess largely deterministic trajectories, enabling mechanistically-based prediction of the likelihood of colloids reaching surfaces. Although for nano-sized colloids the distinction between deterministic colloidal

A version of this chapter has been published [*Molnar et al.*, 2015b]

trajectories and random diffusive solute behaviour is blurred as these colloids exhibit a large degree of Brownian motion. The simulation of deterministic trajectories as well as quantification of the likelihood of colloids reaching surfaces is encompassed in CFT.

Most CFT approaches have two major components: (i) a mechanistic force/torque model that describes colloid trajectory and attachment (described in Section 2.4.1), (ii) correlation equations that approximate the results of the mechanistic models (described in Section 2.4.2). A typical predicted model parameter, be it from a mechanistic model or correlation equation, is the 'collector contact efficiency', η, defined as the fraction of colloids entering the mechanistic model geometry that contacts the collector. Both mechanistic models and the resultant correlation equations have largely been successful in predicting η for micron-sized colloids in 'favorable' conditions [e.g. *Rajagopalan and Tien*, 1976; *Tufenkji and Elimelech*, 2004a; *Yao et al.*, 1971]. It is also important to note that these approaches are subject to error arising separately at the mechanistic model and correlation equation level. In the case of mechanistic models, errors may result from employing incorrect physicochemical parameters and numerical approximations. In the case of correlation equations, errors may be due to the extent to which they are able to approximate mechanistic model results. Mechanistic models and correlation equations for unfavorable conditions, the subject of considerable recent research, are discussed in Appendix 7.3. The following Section will discuss model assumptions and their implications for the prediction of colloid and nanoparticle transport. For a conceptual and mathematical summary of the major mechanistic models discussed, including all of the relevant force/torque equations employed by each model, the reader is referred to Tables 7.1 to 7.6 in Appendix 7.1.

2.4.1   Mechanistic simulations: Favorable conditions

There are more than ten different CFT mechanistic models, each employing different environmental conditions, model geometries or force/torque mechanisms [*Burganos et al.*, 1992; *Burganos et al.*, 1994; *Cushing and Lawler*, 1998; *Long and Hilpert*, 2009; *Ma et al.*, 2009; *Nelson and Ginn*, 2011; *Paraskeva et al.*, 1991; *Payatakes et al.*, 1974a; *Payatakes et al.*, 1974b; *Rajagopalan and Tien*, 1976; *Tufenkji and Elimelech*, 2004a; *Yao et al.*, 1971]. Each of these mechanistic models is associated with one or more

A version of this chapter has been published [*Molnar et al.*, 2015b]

approximating correlation equations. Given the large number of mechanistic models and correlation equations, some of which are simple extensions or variations of previous models and correlation equations (discussed below), there may be some confusion related to which mechanistic model or correlation equation is applicable in a given scenario.

2.4.1.1   The Geometry of mechanistic models

The first CFT model proposed by Yao et al. [1971] considered colloids approaching a single, isolated collector that was perfectly spherical and surrounded by an infinite fluid. This approach, as noted by Yao et al. [1971], produced velocity distributions that were likely poor representations of realistic porous media. The isolated-sphere approach was subsequently modified to employ a Happel Sphere-in-Cell geometry [*Happel*, 1958] that included porosity, as well as constricted tube geometry [*Burganos et al.*, 1992; *Burganos et al.*, 1994; *Paraskeva et al.*, 1991; *Payatakes et al.*, 1974a; *Payatakes et al.*, 1974b]. The most popular, the Happel sphere-in-cell approach, considers the collector, otherwise isolated from the influence of other collectors and perfectly spherical, to be surrounded by an envelope of fluid that is associated with the collector. Tables 7.1 and 7.2 in the Appendix illustrate some of the model geometries that are employed in the most popular mechanistic models. This CFT-Happel approach was first employed by Rajagopalan and Tien [1976] and has been employed in more recent CFT models [*Nelson and Ginn*, 2011; *Tufenkji and Elimelech*, 2004a] as it is conceptually straightforward and simple to upscale the results. Figure 2.4, adapted from [*Molnar et al.*, 2015a], illustrates the Happel-sphere in cell geometry along with the boundary conditions that would be employed by Eulerian mechanistic models [e.g. *Tufenkji and Elimelech*, 2004a]. The flow field around the collector is assumed to be equivalent to Stokes (i.e., creeping) flow around a sphere and undisturbed by the presence of nearby collectors (approximate velocity vectors are illustrated in the Figure). v_o and C_o are the fluid velocity and colloid concentration upstream of the collector, respectively, and are considered uniform over the projected area upstream of the collector (A_1 in the Figure).

Because an actual porous medium includes grain-grain contacts, it may yield flow phenomena inconsistent with Stokes flow around a Happel collector, including recirculation/vortex zones [*Cardenas*, 2008; *Li et al.*, 2010b; *Torkzaban et al.*, 2008] and

A version of this chapter has been published [*Molnar et al.*, 2015b]

low-flow zones [*Li et al.*, 2010a; *Li et al.*, 2012]. While Stokes flow incorporates low fluid velocities adjacent to the collector's surface, the low/recirculating flow phenomena induced by grain-grain contacts likely extends this characteristic further outwards. Thus, the flow field illustrated in Figure 2.4 and used in many mechanistic models is simplified relative to the expected actual flow field within a porous medium. It is important to understand the conditions under which this simplification is acceptable and when it may result in poor predictions of the rate at which colloids contact the surface.
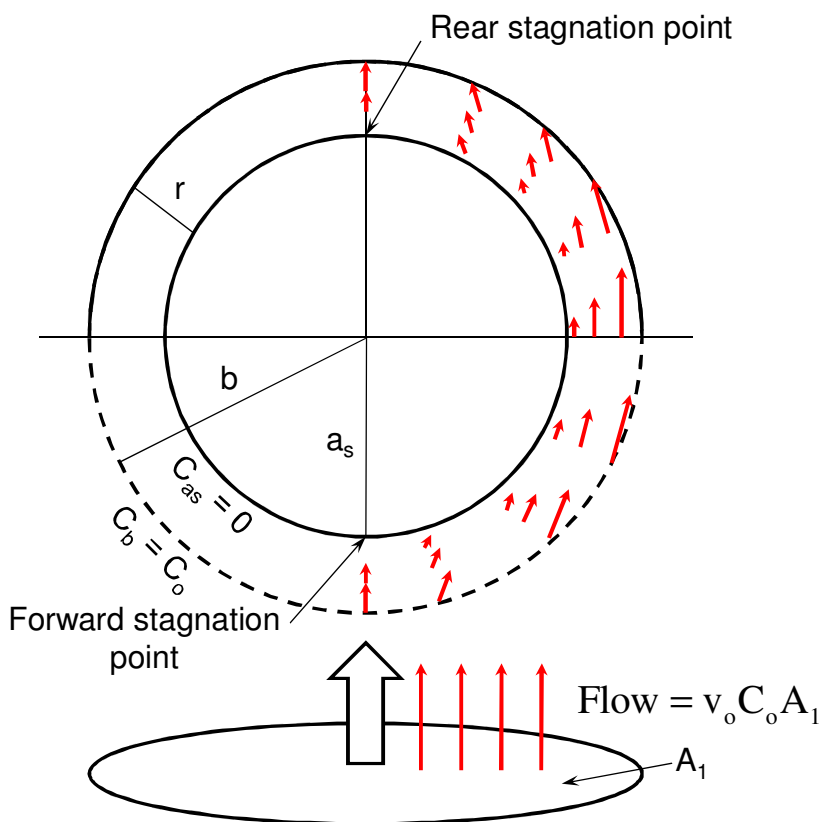
Figure 2.4: Illustration of a typical CFT model employing a Happel sphere-in-cell model with boundary conditions (only applicable to Eulerian models). The geometry of the model is defined by as, the radius of the collector, b, the radius of the Happel cell and r, the thickness of the fluid envelope. The red arrows on the right-hand side of the model represent approximate flow vectors around the sphere. C_b and C_{as} represent the Eulerian constant concentration boundary conditions at the edge of the fluid envelope and collector surface where Co represents the concentration of approaching colloids. Adapted from Molnar et al [2015a].

Predictions from mechanistic models for medium-to-larger sized colloids (e.g., >100 nm) are generally in excellent agreement with experiments performed for favorable conditions [*Nelson and Ginn*, 2011; *Rajagopalan and Tien*, 1976; *Tong and Johnson*, 2006; *Tufenkji*

A version of this chapter has been published [*Molnar et al.*, 2015b]

and Elimelech, 2004a; *Yao et al.*, 1971]. However, there is evidence that smaller colloids (e.g., <100 nm, including viruses and engineered nanoparticles) are potentially impacted by grain-grain contact flow phenomena in even favorable conditions [*Boccardo et al.*, 2014; *Long and Hilpert*, 2009]. Mechanistic single-collector models have been observed to over-predict η for Brownian particle transport experiments in favorable conditions [e.g. *Elimelech and Omelia*, 1990b; *Long and Hilpert*, 2009; *Nelson and Ginn*, 2011; *Tong and Johnson*, 2006]. Hypothesizing that this is due to the simplified geometries employed by single-collector CFT models, Long and Hilpert [2009] and Long et al [2010] explicitly incorporated the impact of grain to grain contacts by performing Lattice Boltzman (LBM) colloid transport and retention simulations in randomly-generated collector packings. The Long and Hilpert [2009] mechanistic model produced η predictions for Brownian particles that were in better agreement with experimental results relative to single collector models [*Nelson and Ginn*, 2011]. This improved prediction may result from including grain to grain contacts and the resulting low flow or recirculation/vortex zones that increase the distance particles must diffuse to reach certain surfaces.

The mechanistic model that incorporates grain to grain contact using a Hemisphere-in-cell approach [*Ma et al.*, 2009; *Ma and Johnson*, 2010] does still somewhat over-predict η [*Nelson and Ginn*, 2011]. This may be due to the orientation of the contacting grains. In the hemisphere-in-cell model the flow direction is always perpendicular to the line connecting adjoining grain centers (see Figure 2.4). In a randomly packed porous medium, the flow direction occurs at many orientations relative to the line connecting adjoining grain centers, which is expected to yield a significantly larger low flow/recirculation zone [*Torkzaban et al.*, 2008].

Nelson and Ginn [2011], employed a Happel sphere mechanistic model to achieve a similarly good match to experiments for Brownian particles. This was likely due to an improved correlation equation (discussed in Section 2.4.2) that better approximated the mechanistic model, notably in the low fluid velocity (i.e., diffusive) regime, as opposed to employing a better mechanistic model. Noting the improved prediction accuracy, Ma et al [2013] subsequently adjusted their correlation equation to extend to the diffusion-dominated velocity regime.

A version of this chapter has been published [*Molnar et al.*, 2015b]

2.4.1.2   Modeling diffusion in mechanistic models

Complexities associated with describing, or predicting, colloid trajectories that exhibit significant Brownian motion are also likely a contributing factor to over prediction of η by mechanistic models. The size of small nanoparticles (e.g., 5 – 50 nm), and the mechanisms governing their transport, fall between that of molecules and larger nanoparticles (e.g., > 50 nm); thus, they exhibit large Brownian motion relative to colloids but possess trajectories that are more deterministic than solutes. While the trajectories of larger, non-Brownian, colloids have been adequately described since the early numerical description by Rajagopalan and Tien [1976], the treatment of Brownian motion has varied considerably. Yao et al [1971] solved for diffusive flux by employing the Levich [1962] solution of the convective-diffusive equation for an isolated sphere in an infinite fluid. The Levich [1962] solution is a simplified description of diffusion as it does not incorporate mechanisms such as anisotropic diffusion. Anisotropic diffusion describes the decrease in colloid diffusivity that occurs within several particle diameters of the surface. As such Brownian motion perpendicular to the surface becomes small relative to the tangential motion [*Eral et al.*, 2010]. Mechanistic models that ignore diffusive mechanisms such as anisotropic diffusion or hydrodynamic retardation (defined as the decrease in colloid velocity near the collector surface due to resistance from the near-surface fluid) could also yield over estimates of η for Brownian particles as the models cannot account for the decrease in particle velocity that occurs near collector surfaces.

Rajagopalan and Tien [1976], despite using a numerical solution to solve for the trajectories of large colloids (i.e., a Lagrangian approach), solved diffusion by employing an analytical method similar to that of Yao et al. [1971] but specific to the Happel Sphere-in-cell geometry [*Cookson*, 1970] which ignores anisotropic diffusion. Tufenkji and Elimelech [2004a] employed the Eulerian numerical model of Elimelech [1994] which solves the advective diffusive equation and included anisotropic diffusion and hydrodynamic retardation. Long and Hilpert [2009] similarly solved diffusion numerically via the ADE but did not include anisotropic diffusion. Nelson and Ginn [2011] added a scaled randomly oriented translation of the colloid to mimic Brownian

A version of this chapter has been published [*Molnar et al.*, 2015b]

motion. Ma et al. [2009] employed a scaled Brownian force so that diffusive movement was subjected to the effects of hydrodynamic retardation equivalent to other governing forces. Tables 7.1 to 7.6 in the Appendix present the equations employed to describe Brownian motion in the most commonly used mechanistic models.

2.4.1.3   Eulerian and Langrangian numerical solution frameworks

Strategies to numerically solve the mechanistic models fall broadly into two categories: Eulerian and Lagrangian frameworks. The exception is the Rajagopalan and Tien [1976] model which employed both approaches, depending on whether the trajectory of the colloid was mostly deterministic (Lagrangian approach) or Brownian (Eulerian approach). Early models tended to be Eulerian [*Elimelech*, 1992; *Tufenkji and Elimelech*, 2004a], and with increased computational power, Lagrangian mechanistic models have been adopted [*Ma et al.*, 2009; *Ma and Johnson*, 2010; *Ma et al.*, 2013; *Nelson and Ginn*, 2011].

While both categories of mechanistic models have successfully described colloid transport and attachment in certain scenarios, Eulerian mechanistic models have limitations, especially within the Happel Sphere geometry. For Happel sphere mechanistic models employing an Eulerian or analytical framework [*Rajagopalan and Tien*, 1976 - diffusion only; *Tufenkji and Elimelech*, 2004a] a constant concentration boundary condition is specified at the outer fluid envelope surrounding the collector. The concentration at this boundary is assumed to be the concentration within the bulk fluid upstream of the collector (i.e., $C_b = C_o$, Figure 2.4). This constant concentration boundary condition represents the distance at which the collector ceases to exert an influence on colloid distribution in the pore space.

For Brownian colloid systems with very high removal rates and low Peclet numbers the constant concentration boundary condition on the downstream half of the Happel fluid envelope may be inappropriate [*Nelson and Ginn*, 2011; *Song and Elimelech*, 1992]. In these circumstances, the colloid concentration at the downstream boundary would be lower than that of the upstream boundary. As a result there would be an implicit

A version of this chapter has been published [*Molnar et al.*, 2015b]

discrepancy between the mechanistic model and what would occur in reality. This would result in overestimates of η for Brownian colloids [*Song and Elimelech*, 1992].

The concentration boundary conditions also implicitly assume a concentration gradient of $\frac{C_b - C_{as}}{r}$ (see Figure 2.4) which describes diffusive flux towards the collector surface. The gradient imposed by these boundary conditions may not be representative of the actual concentration gradient within a realistic porous medium as C_b might not be equivalent to C_o. The pore-scale flow phenomena resulting from grain to grain contacts (discussed earlier) may yield larger low velocity zones than predicted by Stokes flow. This extended low flow zone may yield distances between the collector surface and boundary $C = C_o$ that are larger than the thickness of the Happel sphere fluid envelope. If the distance is larger in reality than in the Happel sphere model, the resulting concentration gradient would be smaller than is predicted. As such the diffusive flux towards the collector surface may be lower than predicted by Eulerian mechanistic models.

With Lagrangian mechanistic models, issues related to boundary conditions are largely avoided by introducing individual particles on the upstream outer fluid envelope boundary. The trajectories of the individual colloids (i.e., attachment or exiting the system) are determined without imposing a concentration at the downstream boundary of the fluid envelope.

2.4.1.4   Stokes flow in mechanistic simulations

As discussed above, mechanistic CFT models assume that the flow regime around a collector can be modeled by assuming Stokes, or creeping, flow [*Nelson and Ginn*, 2011; *Rajagopalan and Tien*, 1976; *Tufenkji and Elimelech*, 2004a; *Yao et al.*, 1971] (Tables 7.1 and 7.2 in the Appendix detail the governing flow equations for the most commonly used models). Stokes flow occurs at very low Reynolds numbers (Re << 1) where inertial forces become insignificant relative to viscous forces. This assumption is likely appropriate at the low flow rates typically associated with filtration and ambient groundwater (i.e., no pumping) in non-fractured systems.

A version of this chapter has been published [*Molnar et al.*, 2015b]

The application of Stokes flow results in streamlines that are mirrored on the forward and rear flow sides of the collector. At low flow rates this results in downstream velocity distributions that are approximately similar to the upstream flow distribution (uniform v_o over area A_1 in Figure 2.4). However, in situations of high flow where Re > 1 [*Potter and Wiggert*, 2002], the flow is no longer strictly within the Stokes regime. Under these conditions, the point at which flow separates from the rear side of the collector will change (i.e., it will produce a wake) and the rear flow stagnation point will widen relative to the forward flow stagnation point [*Potter and Wiggert*, 2002]. This could yield discrepancies between experimental results and mechanistic simulations of colloid transport and retention.

Non-Stokes flow is likely in laboratory experiments conducted at high flow rates. Surveying the literature, and assuming reasonable parameters when values were not available (i.e., viscosity = 1×10^{-3} Pa·s, $T = 293$K), suggests that many experiments were conducted with Re close to or exceeding 1 [e.g. *Elimelech and Omelia*, 1990b; *Elimelech*, 1991; *Lecoanet et al.*, 2004; *Lecoanet and Wiesner*, 2004; *Phenrat et al.*, 2007; *Phenrat et al.*, 2010a; *Yao et al.*, 1971]. Given this finding, conclusions derived from studies where a CFT conceptual model was adopted, but Re was also high, need to be considered with caution.

nZVI experiments typically employ high flow rates with the justification that velocities near the injection well may be very large [*Kocur et al.*, 2013]. Given that non-Stokes flow may occur near the injection well, CFT mechanistic models and correlation equations for prediction of nZVI transport must be used with caution. Overall, this suggests that careful consideration of Reynolds numbers and flow regime is required when designing column-scale transport experiments, interpreting model fits to the data, or modeling field-scale nZVI injection.

2.4.2   Correlation equations derived under favorable conditions

The above discussion focuses on the mechanistic models underlying CFT. However, these models are time consuming to run, and so require approximation via phenomenological expressions to allow easy implementation. To this end mechanistic

A version of this chapter has been published [*Molnar et al.*, 2015b]

models are run under a range of environmental conditions (see Table 2.1). Results from simulations conducted using the mechanistic models are then fit to a phenomenological expression composed of dimensionless groups of relevant physicochemical parameters. This expression serves as a correlation equation thereby serving as a simple predictor for η. Such correlation equations currently exist only for favorable attachment scenarios since the underlying mean-field mechanistic models predict no attachment in unfavorable scenarios; attempts to adapt mechanistic models for unfavorable conditions are discussed in Appendix 7.3.

Table 2.1: Range of parameter values employed to derive recent η correlation equations[a]

	NG 2011	MHJ 2013	MPFJ 2009	Long et al 2010	LH 2009	TE 2004
Particle diameter, d_p (μm)	0.01 – 10	0.01 – 10	0.05 – 10	0.02 – 1	0.1 – 1	0.01 – 10
Collector diameter, d_c (μm)	10 – 1200	510	510	3600	20 – 450	50 – 500
Approach velocity, U (m/s)	$10^{-7} - 2\times10^{-3}$	$1.15\times10^{-7} - 1.7\times10^{-5}$	1.7×10^{-5}	$2.5\times10^{-8} - 10^{-6}$	$10^{-7} - 10^{-5}$	$7\times10^{-6} - 2\times10^{-3}$
Hamaker constant, A (J)	$3\times10^{-21} - 4\times10^{-20}$	3.84×10^{-21}	3.84×10^{-21}	-	10^{-20}	$3\times10^{-21} - 4\times10^{-20}$
Particle density, ρ_p (g/cm^3)	1 – 1.8	1.055, 4	1.055	1.055	1.05	1 – 1.8
Fluid temperature, T (K)	278 – 303	298	298	298	298	298
Porosity, θ	0.26 – 0.48	0.25, 0.37	0.37	0.38	0.3 – 0.42	0.36
Fluid Viscosity, μ (Pa·s)	$0.798\times10^{-3} - 1.518\times10^{-3}$	0.998×10^{-3}	0.998×10^{-3}	-	0.8×10^{-3}	0.8×10^{-3}

[a]η correlation equations: TE 2004, [*Tufenkji and Elimelech*, 2004a]; LH 2009, [*Long and Hilpert*, 2009]; Long et al 2010, [*Long et al.*, 2010]; MPFJ 2009, [*Ma et al.*, 2009]; MHJ 2013, [*Ma et al.*, 2013]; NG 2011, [*Nelson and Ginn*, 2011].

A version of this chapter has been published [*Molnar et al.*, 2015b]

The correlation equations divide colloid transport to the surface into three distinct dimensionless numbers representing inter-related mechanisms: interception via fluid drag interactions alone, diffusion-enhanced interception, and sedimentation-enhanced interception. A separate contribution to the overall η is determined for each dimensionless number (i.e., η_I, η_D and η_G, respectively), such that the overall collector efficiency is described as: $\eta = \eta_I + \eta_D + \eta_G$. In the absence of diffusion or sedimentation, η_I is greater for larger colloids, since the number of streamlines that approach the surface to within 1 colloid radius increases as the colloid size increases. Diffusion enhances interception since it allows colloids to move across streamlines and come into contact with the collector. Because Brownian motion is greater for smaller colloids, η_D is greater for smaller colloids. Because settling allows colloids to move across the streamlines and come into contact with the collector, η_G is greater for larger colloids. The superimposed contributions from these inter-related mechanisms yield a trend of η with colloid size that matches mechanistic simulations and experimental observations wherein a minimum value of η occurs corresponding to colloid diameters of ~ 1 μm, due to smaller colloids undergoing greater diffusion, and larger colloids undergoing greater settling. As an example, the correlation equation of Rajagopalan and Tien [1976] is (corrected version presented in [*Logan et al.*, 1995]):

$$\eta \approx \gamma^2 \left[4 A_s^{1/3} N_{Pe}^{-2/3} + A_s N_{LO}^{1/8} N_R^{15/8} + 0.00338 A_s N_G^{1.2} N_R^{-0.4} \right] \qquad 2.1$$

where the dimensionless parameters (i.e. N_R, N_{PE}, N_{LO}, N_G) are defined in Table 2.2 below, and A_s is a porosity-dependent parameter defined as:

$$A_s = \frac{2(1 - \gamma^5)}{2 - 3\gamma + 3\gamma^5 - 2\gamma^6} \qquad 2.2$$

where $\gamma = (1-\theta)^{1/3}$. A_s accounts for the influence of neighboring collectors on the fluid flow field in the Happel sphere-in-cell geometry and ε represents the porosity of the porous medium. Tables 7.1 and 7.2 in the Appendix list the correlation equations for the six most commonly used models.

A version of this chapter has been published [*Molnar et al.*, 2015b]

Table 2.2: List of dimensionless parameters in predicting colloid filtration

Parameter	Definition	Description
N_R	a_p/a_s	aspect ratio
N_{PE}	Ud_c/D_{BM}	Peclet number
N_{LO}	$H/(9\pi\mu a_p^2 U)$	London number
N_G	$2a_p^2(\rho_p - \rho_f)g/(9\mu U)$	Gravity number

[a] a_p and a_s are the colloid and collector radii; d_c is the collector diameter, U is the approach velocity; D_{BM} is the bulk diffusion coefficient (described by Stokes-Einstein equation); μ is the fluid viscosity, ρ_f and ρ_g are the fluid and colloid densities, respectively; g is the gravitational acceleration constant.

Figure 2.5 illustrates how well the correlation equations listed in Table 2.1 predict the experimental kinetic retention coefficient k. Figure 2.5 compares experimental and predicted values of k (the upscaled η) since the definition of η differs among the different collector geometries (Appendix Tables 7.1 and 7.2 provide the equation for k for each model). As can be seen, the currently existing correlation equations generally provide very good predictions of η for micron-sized colloids in the range of conditions for which the correlations were developed [e.g. *Nelson and Ginn*, 2011; *Tong and Johnson*, 2006]. However, they generally over predict η for Brownian particles (Figure 2.5, the 'nanoparticles' region). While a number of possible causes for this over prediction were identified in the discussion related to mechanistic models, another possible source of error may be the approximating correlation equations themselves. Many of the flow and transport scenarios for Brownian particles involve parameter values that are outside of the limited range of conditions employed to derive the correlations [e.g. *Gastone et al.*, 2014; *Kocur et al.*, 2013; *Kocur et al.*, 2014; *Krol et al.*, 2013; *O'Carroll et al.*, 2013; *Quinn et al.*, 2005; *Tosco et al.*, 2014b].

A version of this chapter has been published [*Molnar et al.*, 2015b]
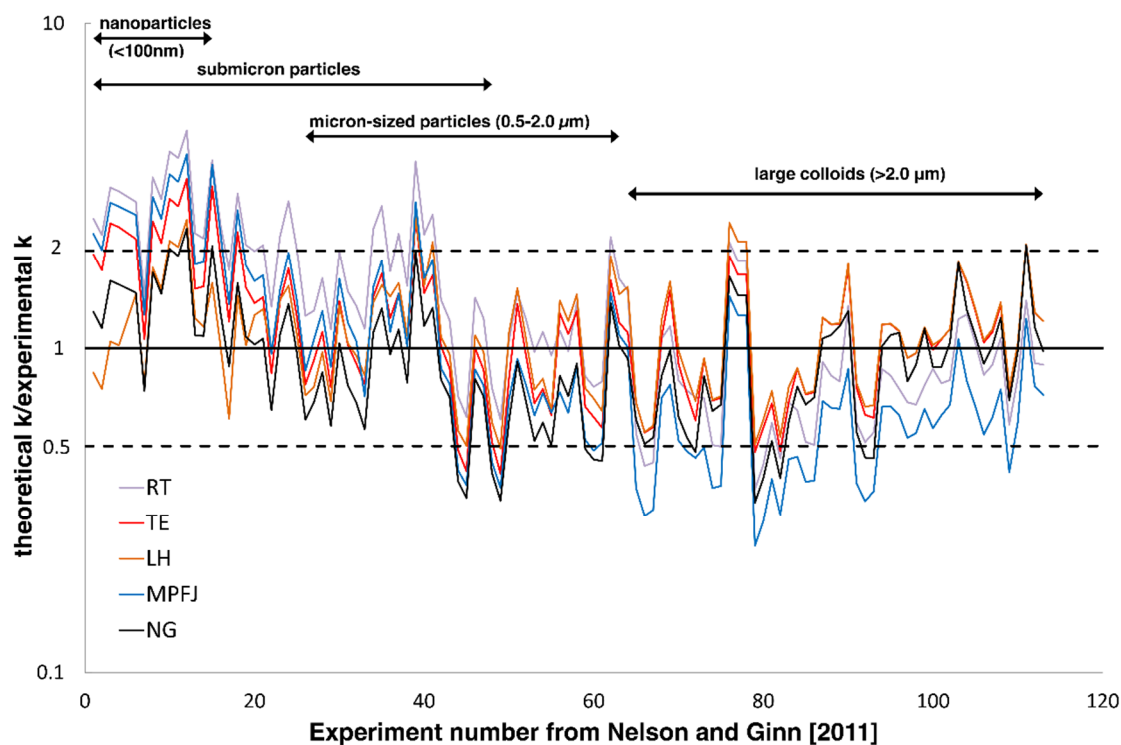
Figure 2.5: A comparison of experimentally determined retention rate coefficients vs. correlation-equation predicted retention rate coefficients (k) for a number of different correlation equations on a semi-log plot. While correlation equations predict η, these values have been converted to k to allow comparisons between different model geometries. The experiment numbers on the x-axis are taken from [*Nelson and Ginn*, 2011]. As indicated on the chart, low experiment numbers correspond to smaller colloids. The solid horizontal line at y = 1 represents an exact match between correlation equation predictions and experimental observations. The dashed horizontal lines at y=0.5 and y=2 represent factor of two differences (i.e., where the correlation equation predication is half as large and twice as large as the experimental observation). RT:[*Rajagopalan and Tien*, 1976], TE: [*Tufenkji and Elimelech*, 2004a], LH: [*Long and Hilpert*, 2009], [*Ma and Johnson*, 2009], NH: [*Nelson and Ginn*, 2011]. Adapted from [*Nelson and Ginn*, 2011].

This is often the case for the prediction of engineered nanoparticle transport. For example a limited range of viscosities, similar to water, have been used in mechanistic model simulations used in the development of correlation equations (Table 2.1). Long and Hilpert [2009] and Tufenkji and Elimelech [2004a] derived their η correlation equation using a single value of water kinematic viscosity at 25°C (0.8×10^{-6} m^2/s) and Nelson and Ginn [2011] employ a range of viscosities, but for a range of water temperatures from 5°C to 30°C. However, ENPs are often stabilized in a polymer solution to prevent aggregation and settling [e.g. *Hotze et al.*, 2010; *Kocur et al.*, 2013; *Phenrat et al.*, 2010b; *Phenrat et al.*, 2010c]. These stabilized ENP solutions tend to be much more

A version of this chapter has been published [*Molnar et al.*, 2015b]

viscous than water: 2×10^{-3}-1.3×10^{-2} Pa·s [*Krol et al.*, 2013], 7×10^{-3} Pa·s [*Kocur et al.,* 2014], 6×10^{-3} Pa·s [*Sakulchaicharoen et al.*, 2010], 1.2×10^{-2}-8.8×10^{-2} Pa·s [*Gastone et al.*, 2014; *Tosco et al.*, 2014b] and upwards of 1.942 Pa·s [*Quinn et al.*, 2005]. Since current η correlation equations were not derived for this range of viscosities, caution should be used in applying existing correlations to engineered nanoparticle subsurface applications. Extending CFT models to include a wider range of viscosities should be considered for future research.

Similarly, η correlation equations, with the exception of Ma et al [2013], were derived for a relatively small range of colloid densities (i.e., 1 - 1.8 g/cm^3) (Table 2.1). While viruses, bacteria and protozoa likely fall within this near-neutrally buoyant range, aggregates of metallic ENPs may have significantly higher densities. No correlation equation has been derived using a mechanistic CFT model that explicitly considers high density colloids such as aggregates of metallic ENPs. Nor have existing correlation equations been experimentally validated for high density colloids.

2.5 Conclusions

In this chapter we have presented the many advances in our understanding of colloid transport in porous media in the past 25 years. There is an increasingly sophisticated understanding of the applications of employing short-range DLVO forces to describe colloid transport through porous media. The favorable and unfavorable deposition conditions that arise from DLVO interactions yield significantly different experimental transport and retention behaviors. However, the experimentally observed behaviors often differ from mean-field DLVO predictions; this is especially true for colloid retention in unfavorable conditions. A large amount of recent research has successfully elucidated a number of causes for these discrepancies such as grain and colloid heterogeneity, secondary minimum interactions, and site blocking. A large portion of our understanding of these mechanisms has arisen from column-scale transport experiments coupled with continuum-scale models that, by fitting various rate parameters, can successfully describe experimental transport behavior.

A version of this chapter has been published [*Molnar et al.*, 2015b]

There have also been significant advances in Colloid Filtration Theory, a two-component method for predicting the colloid attachment rate parameter, k. The first component, a detailed mechanistic model of colloid transport and attachment onto a unit-cell collector by way of a force-torque balance, has become increasingly advanced with modern computational power. Particularly, successes have occurred with describing Brownian motion and moving towards a mechanistic approach to predicting colloid retention (and detachment) in unfavorable conditions, the prevailing condition in the environment. The second component of CFT, correlation equations that summarize the results of the detailed mechanistic models, have also improved significantly and can, for the most part, accurately predict retention of larger colloids in favorable conditions.

Despite the large number of advances and successes, there remain many gaps in our current understanding, limiting our ability to predict colloid transport in a range of porous media systems. Many of the mechanisms invoked to describe discrepancies between DLVO-predicted colloid transport behavior and experimental observations arise from the use of fitted kinetic retention parameters in continuum-scale models. However, fitted parameters can only infer mechanisms, not prove those mechanisms are responsible for the fit. As such, many of the mechanisms attributed to colloid transport and retention behavior remain inferred. There are substantial opportunities available to develop mechanistic approaches to validating, and predicting, the influence of these mechanisms. Relatively new tools, such as XCT, will prove invaluable in this as they are capable of quantitatively extracting pore and grain details (i.e., pore body/throat sizes and distributions, void topologies and grain shapes and mineralogy) as well as directly observing colloid distribution in the pore space and coupling with high-fidelity simulations of the flow fields.

Mechanistic CFT models and their respective correlation equations still struggle to predict nanoparticle transport and retention. It is still unclear if the unit-cell CFT approach is valid for highly diffusive materials. While fitting the α parameter effectively overcomes the discrepancy between theoretical predictions and experimental observations for nanoparticle transport, true prediction of nanoparticle transport and retention will require accurate mechanistic models and correlation equations. Likewise,

A version of this chapter has been published [*Molnar et al.*, 2015b]

existing correlation equations are only derived for a limited range of environmental conditions that are not applicable to many nanoparticle scenarios such as a viscous solution of nano-Zero Valent Iron stabilized with polymer.

Finally, while mechanistic models are now able to quantitatively predict colloid attachment and qualitatively predict detachment under unfavorable conditions, these are limited to idealized systems involving carboxylate modified polystyrene latex microspheres on silica (which reflect the vast majority of existing colloid transport experiments). Even in these simple systems, the need to account for influences such as roughness in addition to charge heterogeneity is well noted and warrants further research. Furthermore, experiments looking at non-silica surfaces and non-ideal colloids, as well as size-distributed porous media present major opportunities to address environmental conditions in a more comprehensive manner.

Together, the above listed challenges represent a significant opportunity for advances that will undoubtedly lead to more informed decisions and design regarding colloids in the environment for the protection of human and ecological health.

A version of this chapter has been published [*Molnar et al.*, 2015b]

2.6 References

Albinger, O., B. K. Biesemeyer, R. G. Arnold, and B. E. Logan (1994), *Effect of bacterial heterogeneity on adhesion to uniform collectors by monoclonal populations*, 321-326 pp.

Bahr, J. M., and J. Rubin (1987), Direct comparison of kinetic and local equilibrium formulations for solute transport affected by surface reactions, *Water Resour. Res.*, *23*(3), 438-452.

Bai, C., and Y. Li (2012), Modeling the transport and retention of nC60 nanoparticles in the subsurface under different release scenarios, *Journal of Contaminant Hydrology*, *136–137*(0), 43-55.

Bales, R. C., C. P. Gerba, G. H. Grondin, and S. L. Jensen (1989), Bacteriophage Transport in Sandy Soil and Fractured Tuff, *Applied and Environmental Microbiology*, *55*(8), 2061-2067.

Baygents, J. C., J. R. Glynn, O. Albinger, B. K. Biesemeyer, K. L. Ogden, and R. G. Arnold (1998), Variation of Surface Charge Density in Monoclonal Bacterial Populations: Implications for Transport through Porous Media, *Environ. Sci. Technol.*, *32*(11), 1596-1603.

Bear, J., and A. H. D. Cheng (2010), *Modeling Groundwater Flow and Contaminant Transport*, Springer, Netherlands.

Bennett, P., F. He, D. Zhao, B. Aiken, and L. Feldman (2010), In situ testing of metallic iron nanoparticle mobility and reactivity in a shallow granular aquifer, *Journal of Contaminant Hydrology*, *116*(1–4), 35-46.

Berge, N. D., and C. A. Ramsburg (2009), Oil-in-Water Emulsions for Encapsulated Delivery of Reactive Iron Particles, *Environ. Sci. Technol.*, *43*(13), 5060-5066.

Bergendahl, J., and D. Grasso (2000), Prediction of colloid detachment in a model porous media: hydrodynamics, *Chemical Engineering Science*, *55*(9), 1523-1532.

Berkowitz, B., A. Cortis, M. Dentz, and H. Scher (2006), Modeling non-Fickian transport in geological formations as a continuous time random walk, *Rev. Geophys.*, *44*(2), 49.

Bhattacharjee, S., J. Y. Chen, and M. Elimelech (2000), DLVO interaction energy between spheroidal particles and a flat surface, *Colloids and Surfaces A: Physicochemical and Engineering Aspects*, *165*(1–3), 143-156.

Bitton, G., and R. W. Harvey (1992), Transport of pathogens through soil, in *Environmental Microbiology*, edited by R. Mitchell, pp. 103-124, Wiley, New York.

Blanford, W. J., M. L. Brusseau, T. C. Jim Yeh, C. P. Gerba, and R. Harvey (2005), Influence of water chemistry and travel distance on bacteriophage PRD-1 transport in a sandy aquifer, *Water Research*, *39*(11), 2345-2357.

Boccardo, G., D. L. Marchisio, and R. Sethi (2014), Microscale simulation of particle deposition in porous media, *Journal of Colloid and Interface Science*, *417*(0), 227-237.

Bolster, C. H., A. L. Mills, G. M. Hornberger, and J. S. Herman (1999), Spatial distribution of deposited bacteria following Miscible Displacement Experiments in intact cores, *Water Resour. Res.*, *35*(6), 1797-1807.

Bolster, C. H., A. L. Mills, G. Hornberger, and J. Herman (2000), Effect of Intra-Population Variability on the Long-Distance Transport of Bacteria, *Ground Water*, *38*(3), 370-375.

Bradford, S. A., S. R. Yates, M. Bettahar, and J. Simunek (2002), Physical factors affecting the transport and fate of colloids in saturated porous media, *Water Resour. Res.*, *38*(12).

Bradford, S. A., J. Simunek, M. Bettahar, M. T. van Genuchten, and S. R. Yates (2003), Modeling Colloid Attachment, Straining, and Exclusion in Saturated Porous Media, *Environ. Sci. Technol.*, *37*(10), 2242-2250.

Bradford, S. A., M. Bettahar, J. Simunek, and M. T. van Genuchten (2004), Straining and attachment of colloids in physically heterogeneous porous media, *Vadose Zone J.*, *3*(2), 384-394.

Bradford, S. A., J. Simunek, and S. L. Walker (2006a), Transport and straining of E. coli O157:H7 in saturated porous media, *Water Resour. Res.*, *42*(12), W12S12.

Bradford, S. A., J. Simunek, M. Bettahar, M. T. van Genuchten, and S. R. Yates (2006b), Significance of straining in colloid deposition: Evidence and implications, *Water Resour. Res.*, *42*(12), W12S15.

Bradford, S. A., S. Torkzaban, F. Leij, im, J. nek, and M. T. van Genuchten (2009), Modeling the coupled effects of pore space geometry and velocity on colloid transport and retention, *Water Resour. Res.*, *45*(2), W02414.

Bradford, S. A., S. Torkzaban, and J. Simunek (2011), Modeling colloid transport and retention in saturated porous media under unfavorable attachment conditions, *Water Resour. Res.*, *47*.

Burganos, V. N., C. A. Paraskeva, and A. C. Payatakes (1992), Three-dimensional trajectory analysis and network simulation of deep bed filtration, *Journal of Colloid and Interface Science*, *148*(1), 167-181.

Burganos, V. N., C. A. Paraskeva, P. D. Christofides, and A. C. Payatakes (1994), Motion and deposition of non-brownian particles in upflow collectors, *Sep. Technol.*, *4*(1), 47-54.

Camesano, T. A., K. M. Unice, and B. E. Logan (1999), Blocking and ripening of colloids in porous media and their implications for bacterial transport, *Colloids and Surfaces A: Physicochemical and Engineering Aspects*, *160*(3), 291-307.

Cardenas, M. B. (2008), Three-dimensional vortices in single pores and their effects on transport, *Geophysical Research Letters*, *35*(18), L18402.

Chatterjee, J., S. Pratap, and S. Abdulkareem (2011), Dual-deposition rates in colloid filtration caused by coupled heterogeneities in a colloidal population, *Journal of Colloid and Interface Science*, *356*(1), 362-368.

Christian, P., F. Von der Kammer, M. Baalousha, and T. Hofmann (2008), Nanoparticles: structure, properties, preparation and behaviour in environmental media, *Ecotoxicology*, *17*(5), 326-343.

Chrysikopoulos, C. V., and V. I. Syngouna (2014), Effect of Gravity on Colloid Transport through Water-Saturated Columns Packed with Glass Beads: Modeling and Experiments, *Environ. Sci. Technol.*, *48*(12), 6805-6813.

Cookson, J. T. (1970), Removal of submicron particles in packed beds, *Environ. Sci. Technol.*, *4*(2), 128-134.

Corapcioglu, M. Y., and S. Jiang (1993), Colloid-facilitated groundwater contaminant transport, *Water Resour. Res.*, *29*(7), 2215-2226.

Cullen, E., D. M. O'Carroll, E. K. Yanful, and B. Sleep (2010), Simulation of the subsurface mobility of carbon nanoparticles at the field scale, *Adv. Water Resour.*, *33*(4), 361-371.

Cushing, R. S., and D. F. Lawler (1998), Depth Filtration: Fundamental Investigation through Three-Dimensional Trajectory Analysis, *Environ. Sci. Technol.*, *32*(23), 3793-3801.

Cvetkovic, V., and G. Dagan (1994), Transport of kinetically sorbing solute by steady random velocity in heterogeneous porous formations, *Journal of Fluid Mechanics*, *265*, 189-215.

de Jonge, H., O. H. Jacobsen, L. W. de Jonge, and P. Moldrup (1998), Particle-Facilitated Transport of Prochloraz in Undisturbed Sandy Loam Soil Columns, *J. Environ. Qual.*, *27*(6), 1495-1503.

de Jonge, L. W., C. Kjaergaard, and P. Moldrup (2004), Colloids and Colloid-Facilitated Transport of Contaminants in Soils, *Vadose Zone J.*, *3*(2), 321-325.

DeBorde, D. C., W. W. Woessner, Q. T. Kiley, and P. Ball (1999), Rapid transport of viruses in a floodplain aquifer, *Water Research*, *33*(10), 2229-2238.

Derjaguin, B., and L. Landau (1941), Theory of the stability of strongly charged lyophobic sols and the adhesion of strongly charged particles in solutions of electrolytes, *Acta Physicochim. USSR*, *14*, 633-662.

Dunphy Guzman, K. A., M. P. Finnegan, and J. F. Banfield (2006), Influence of Surface Potential on Aggregation and Transport of Titania Nanoparticles, *Environ. Sci. Technol.*, *40*(24), 7688-7693.

Dusek, J., M. Dohnal, M. Snehota, M. Sobotkova, C. Ray, and T. Vogel (2015), Transport of bromide and pesticides through an undisturbed soil column: A modeling study with global optimization analysis, *Journal of Contaminant Hydrology*, *175–176*(0), 1-16.

Elimelech, M., and C. R. Omelia (1990a), KINETICS OF DEPOSITION OF COLLOIDAL PARTICLES IN POROUS-MEDIA, *Environ. Sci. Technol.*, *24*(10), 1528-1536.

Elimelech, M., and C. R. Omelia (1990b), EFFECT OF PARTICLE-SIZE ON COLLISION EFFICIENCY IN THE DEPOSITION OF BROWNIAN PARTICLES WITH ELECTROSTATIC ENERGY BARRIERS, *Langmuir*, *6*(6), 1153-1163.

Elimelech, M. (1991), Kinetics of capture of colloidal particles in packed beds under attractive double layer interactions, *Journal of Colloid and Interface Science*, *146*(2), 337-352.

Elimelech, M. (1992), Predicting collision efficiencies of colloidal particles in porous media, *Water Research*, *26*(1), 1-8.

Elimelech, M. (1994), PARTICLE DEPOSITION ON IDEAL COLLECTORS FROM DILUTE FLOWING SUSPENSIONS - MATHEMATICAL FORMULATION, NUMERICAL-SOLUTION, AND SIMULATIONS, *Sep. Technol.*, *4*(4), 186-212.

Elimelech, M., M. Nagai, C.-H. Ko, and J. N. Ryan (2000), Relative Insignificance of Mineral Grain Zeta Potential to Colloid Transport in Geochemically Heterogeneous Porous Media, *Environ. Sci. Technol.*, *34*(11), 2143-2148.

Eral, H. B., J. M. Oh, D. van den Ende, F. Mugele, and M. H. G. Duits (2010), Anisotropic and Hindered Diffusion of Colloidal Particles in a Closed Cylinder, *Langmuir*, *26*(22), 16722-16729.

Espinoza, C., and A. J. Valocchi (1997), Stochastic analysis of one-dimensional transport of kinetically adsorbing solutes in chemically heterogeneous aquifers, *Water Resour. Res.*, *33*(11), 2429-2445.

Faure, B., G. Salazar-Alvarez, and L. Bergström (2011), Hamaker Constants of Iron Oxide Nanoparticles, *Langmuir*, *27*(14), 8659-8664.

Flury, M., and H. Qiu (2008), Modeling Colloid-Facilitated Contaminant Transport in the Vadose Zone, *Vadose Zone J.*, *7*(2), 682-697.

Fontes, D. E., A. L. Mills, G. M. Hornberger, and J. S. Herman (1991), Physical and chemical factors influencing transport of microorganisms through porous media, *Applied and Environmental Microbiology*, *57*(9), 2473-2481.

Foppen, J. W., and J. F. Schijven (2006), Evaluation of data from the literature on the transport and survival of Escherichia coli and thermotolerant coliforms in aquifers under saturated conditions, *Water Research*, *40*(3), 401-426.

Foppen, J. W., M. van Herwerden, and J. Schijven (2007), Transport of Escherichia coli in saturated porous media: Dual mode deposition and intra-population heterogeneity, *Water Research*, *41*(8), 1743-1753.

Fujikawa, Y., and M. Fukui (1991), Analysis of radioactive cesium and cobalt adsorption to rocks using the two-site kinetic model equations, *Journal of Contaminant Hydrology*, *8*(1), 43-69.

Gao, Y., Z. Luo, N. He, and M. Wang (2013), Metallic nanoparticle production and consumption in China between 2000 and 2010 and associative aquatic environmental risk assessment, *J. Nanopart. Res.*, *15*(6), 1-9.

Gastone, F., T. Tosco, and R. Sethi (2014), Guar gum solutions for improved delivery of iron particles in porous media (Part 1): Porous medium rheology and guar gum-induced clogging, *Journal of Contaminant Hydrology*, *166*(0), 23-33.

Haggerty, R., and S. M. Gorelick (1995), Multiple-Rate Mass Transfer for Modeling Diffusion and Surface Reactions in Media with Pore-Scale Heterogeneity, *Water Resour. Res.*, *31*(10), 2383-2400.

Haggerty, R., S. A. McKenna, and L. C. Meigs (2000), On the late-time behavior of tracer test breakthrough curves, *Water Resour. Res.*, *36*(12), 3467-3479.

Hahn, M. W., D. Abadzic, and C. R. O'Melia (2004), Aquasols: On the Role of Secondary Minima†, *Environ. Sci. Technol.*, *38*(22), 5915-5924.

Han, P., X. Wang, L. Cai, M. Tong, and H. Kim (2014), Transport and retention behaviors of titanium dioxide nanoparticles in iron oxide-coated quartz sand: Effects of pH, ionic strength, and humic acid, *Colloids and Surfaces A: Physicochemical and Engineering Aspects*, *454*(0), 119-127.

Happel, J. (1958), VISCOUS FLOW IN MULTIPARTICLE SYSTEMS - SLOW MOTION OF FLUIDS RELATIVE TO BEDS OF SPHERICAL PARTICLES, *Aiche J.*, *4*(2), 197-201.

Harter, T., S. Wagner, and E. R. Atwill (2000), Colloid Transport and Filtration of Cryptosporidium parvum in Sandy Soils and Aquifer Sediments, *Environ. Sci. Technol.*, *34*(1), 62-70.

Harvey, R. W., and S. P. Garabedian (1991), Use of colloid filtration theory in modeling movement of bacteria through a contaminated sandy aquifer, *Environ. Sci. Technol.*, *25*(1), 178-185.

Harvey, R. W., N. E. Kinner, A. Bunn, D. Macdonald, and D. Metge (1995), Transport behavior of groundwater protozoa and protozoan-sized microspheres in sandy aquifer sediments, *Applied and Environmental Microbiology*, *61*(1), 209-217.

Harvey, R. W. (1997), *Microorganisms as tracers in groundwater injection and recovery experiments: a review*, 461-472 pp.

He, F., and D. Zhao (2008), Hydrodechlorination of trichloroethene using stabilized Fe-Pd nanoparticles: Reaction mechanism and effects of stabilizers, catalysts and reaction conditions, *Applied Catalysis B: Environmental*, *84*(3–4), 533-540.

Hendry, M. J., J. R. Lawrence, and P. Maloszewski (1997), The Role of Sorption in the Transport of Klebsiella oxytoca Through Saturated Silica Sand, *Ground Water*, *35*(4), 574-584.

Hendry, M. J., J. R. Lawrence, and P. Maloszewski (1999), Effects of Velocity on the Transport of Two Bacteria Through Saturated Sand, *Ground Water*, *37*(1), 103-112.

Hornberger, G. M., A. L. Mills, and J. S. Herman (1992), Bacterial transport in porous media: Evaluation of a model using laboratory observations, *Water Resour. Res.*, *28*(3), 915-923.

Hotze, E. M., T. Phenrat, and G. V. Lowry (2010), Nanoparticle Aggregation: Challenges to Understanding Transport and Reactivity in the Environment, *Journal of Environmental Quality*, *39*(6), 1909-1924.

Jaisi, D. P., and M. Elimelech (2009), Single-Walled Carbon Nanotubes Exhibit Limited Transport in Soil Columns, *Environ. Sci. Technol.*, *43*(24), 9161-9166.

Jiang, X., M. Tong, R. Lu, and H. Kim (2012), Transport and deposition of ZnO nanoparticles in saturated porous media, *Colloids and Surfaces A: Physicochemical and Engineering Aspects*, *401*(0), 29-37.

Jin, Y., and M. Flury (2002), Fate and Transport of Viruses in Porous Media, *Advances in Agronomy*, *77*, 39-102.

Johnson, P. R., and M. Elimelech (1995), DYNAMICS OF COLLOID DEPOSITION IN POROUS-MEDIA - BLOCKING BASED ON RANDOM SEQUENTIAL ADSORPTION, *Langmuir*, *11*(3), 801-812.

Johnson, R. L., J. T. Nurmi, G. S. O'Brien Johnson, D. Fan, R. L. O'Brien Johnson, Z. Shi, A. J. Salter-Blanc, P. G. Tratnyek, and G. V. Lowry (2013), Field-Scale Transport and Transformation of Carboxymethylcellulose-Stabilized Nano Zero-Valent Iron, *Environ. Sci. Technol.*, *47*(3), 1573-1580.

Johnson, W. P., K. A. Blue, B. E. Logan, and R. G. Arnold (1995a), Modeling Bacterial Detachment During Transport Through Porous Media as a Residence-Time-Dependent Process, *Water Resour. Res.*, *31*(11), 2649-2658.

Johnson, W. P., G. L. Amy, and S. C. Chapra (1995b), Modeling of NOM-Facilitated PAH Transport through Low- f oc Sediment, *Journal of Environmental Engineering*, *121*(6), 438-446.

Johnson, W. P., and X. Li (2005), Comment on Breakdown of Colloid Filtration Theory: Role of the Secondary Energy Minimum and Surface Charge Heterogeneities, *Langmuir*, *21*(23), 10895-10895.

Johnson, W. P., X. Li, and S. Assemi (2007), Deposition and re-entrainment dynamics of microbes and non-biological colloids during non-perturbed transport in porous media in the presence of an energy barrier to deposition, *Adv. Water Resour.*, *30*(6–7), 1432-1454.

Johnson, W. P., E. Pazmino, and H. L. Ma (2010), Direct observations of colloid retention in granular media in the presence of energy barriers, and implications for inferred mechanisms from indirect observations, *Water Research*, *44*(4), 1158-1169.

Johnson, W. P., and M. Hilpert (2013), Upscaling colloid transport and retention under unfavorable conditions: Linking mass transfer to pore and grain topology, *Water Resour. Res.*, *49*(9), 5328-5341.

Katzourakis, V. E., and C. V. Chrysikopoulos (2014), Mathematical modeling of colloid and virus cotransport in porous media: Application to experimental data, *Adv. Water Resour.*, *68*(0), 62-73.

Keller, A. A., S. Sirivithayapakorn, and C. V. Chrysikopoulos (2004), Early breakthrough of colloids and bacteriophage MS2 in a water-saturated sand column, *Water Resour. Res.*, *40*(8), W08304.

Kersting, A. B., D. W. Efurd, D. L. Finnegan, D. J. Rokop, D. K. Smith, and J. L. Thompson (1999), Migration of plutonium in ground water at the Nevada Test Site, *Nature*, *397*(6714), 56-59.

Kocur, C. M., D. M. O'Carroll, and B. E. Sleep (2013), Impact of nZVI stability on mobility in porous media, *Journal of Contaminant Hydrology*, *145*(0), 17-25.

Kocur, C. M., et al. (2014), Characterization of nZVI Mobility in a Field Scale Test, *Environ. Sci. Technol.*, *48*(5), 2862-2869.

Köhne, J. M., S. Köhne, and J. Šimůnek (2009a), A review of model applications for structured soils: b) Pesticide transport, *Journal of Contaminant Hydrology*, *104*(1–4), 36-60.

Köhne, J. M., S. Köhne, and J. Šimůnek (2009b), A review of model applications for structured soils: a) Water flow and tracer transport, *Journal of Contaminant Hydrology*, *104*(1–4), 4-35.

Krol, M. M., A. J. Oleniuk, C. M. Kocur, B. E. Sleep, P. Bennett, Z. Xiong, and D. M. O'Carroll (2013), A Field-Validated Model for In Situ Transport of Polymer-Stabilized nZVI and Implications for Subsurface Injection, *Environ. Sci. Technol.*, *47*(13), 7332-7340.

Kuznar, Z. A., and M. Elimelech (2007), Direct microscopic observation of particle deposition in porous media: Role of the secondary energy minimum, *Colloid Surf. A-Physicochem. Eng. Asp.*, *294*(1-3), 156-162.

Landkamer, L. L., R. W. Harvey, T. D. Scheibe, and J. N. Ryan (2013), Colloid transport in saturated porous media: Elimination of attachment efficiency in a new colloid transport model, *Water Resour. Res.*, *49*(5), 2952-2965.

Lecoanet, H. F., J.-Y. Bottero, and M. R. Wiesner (2004), Laboratory Assessment of the Mobility of Nanomaterials in Porous Media, *Environ. Sci. Technol.*, *38*(19), 5164-5169.

Lecoanet, H. F., and M. R. Wiesner (2004), Velocity effects on fullerene and oxide nanoparticle deposition in porous media, *Environ. Sci. Technol.*, *38*(16), 4377-4382.

Leij, F. J., and S. A. Bradford (2013), Colloid transport in dual-permeability media, *Journal of Contaminant Hydrology*, *150*(0), 65-76.

Levich, V. G. (1962), *Physicochemical hydrodynamics*, Prentice-Hall, Englewood Cliffs, N.J.

Li, X. Q., T. D. Scheibe, and W. P. Johnson (2004), Apparent Decreases in Colloid Deposition Rate Coefficients with Distance of Transport under Unfavorable Deposition Conditions: A General Phenomenon, *Environ. Sci. Technol.*, *38*(21), 5616-5625.

Li, X. Q., and W. P. Johnson (2005), Nonmonotonic Variations in Deposition Rate Coefficients of Microspheres in Porous Media under Unfavorable Deposition Conditions, *Environ. Sci. Technol.*, *39*(6), 1658-1665.

Li, X. Q., P. F. Zhang, C. L. Lin, and W. P. Johnson (2005), Role of hydrodynamic drag on microsphere deposition and re-entrainment in porous media under unfavorable conditions, *Environ. Sci. Technol.*, *39*(11), 4012-4020.

Li, X. Q., Z. L. Li, and D. X. Zhang (2010a), Role of Low Flow and Backward Flow Zones on Colloid Transport in Pore Structures Derived from Real Porous Media, *Environ. Sci. Technol.*, *44*(13), 4936-4942.

Li, Z., D. X. Zhang, and X. Li (2010b), Tracking Colloid Transport in Porous Media Using Discrete Flow Fields and Sensitivity of Simulated Colloid Deposition to Space Discretization, *Environ. Sci. Technol.*, *44*(4), 1274-1280.

Li, Z., D. X. Zhang, and X. Li (2012), Tracking colloid transport in real pore structures: Comparisons with correlation equations and experimental observations, *Water Resour. Res.*, *48*(5), W05533.

Liang, Y., S. A. Bradford, J. Simunek, H. Vereecken, and E. Klumpp (2013), Sensitivity of the transport and retention of stabilized silver nanoparticles to physicochemical factors, *Water Research*, *47*(7), 2572-2582.

Lin, S. H., Y. W. Cheng, Y. Bobcombe, K. L. Jones, J. Liu, and M. R. Wiesner (2011), Deposition of Silver Nanoparticles in Geochemically Heterogeneous Porous Media: Predicting Affinity from Surface Composition Analysis, *Environ. Sci. Technol.*, *45*(12), 5209-5215.

Lindqvist, R., J. S. Cho, and C. G. Enfield (1994), A kinetic model for cell density dependent bacterial transport in porous media, *Water Resour. Res.*, *30*(12), 3291-3299.

Lipp, E. K., S. A. Farrah, and J. B. Rose (2001), Assessment and Impact of Microbial Fecal Pollution and Human Enteric Pathogens in a Coastal Community, *Marine Pollution Bulletin*, *42*(4), 286-293.

Liu, X. Y., D. M. O'Carroll, E. J. Petersen, Q. G. Huang, and C. L. Anderson (2009a), Mobility of Multiwalled Carbon Nanotubes in Porous Media, *Environ. Sci. Technol.*, *43*(21), 8153-8158.

Liu, Y., D. Janjaroen, M. S. Kuhlenschmidt, T. B. Kuhlenschmidt, and T. H. Nguyen (2009b), Deposition of Cryptosporidium parvum Oocysts on Natural Organic Matter Surfaces: Microscopic Evidence for Secondary Minimum Deposition in a Radial Stagnation Point Flow Cell, *Langmuir*, *25*(3), 1594-1605.

A version of this chapter has been published [*Molnar et al.*, 2015b]

Logan, B., D. Jewett, R. Arnold, E. Bouwer, and C. O'Melia (1995), Clarification of Clean-Bed Filtration Models, *Journal of Environmental Engineering*, *121*(12), 869-873.

Long, W., and M. Hilpert (2009), A Correlation for the Collector Efficiency of Brownian Particles in Clean-Bed Filtration in Sphere Packings by a Lattice-Boltzmann Method, *Environ. Sci. Technol.*, *43*(12), 4419-4424.

Long, W., H. Huang, J. Serlemitsos, E. Liu, A. H. Reed, and M. Hilpert (2010), Pore-scale study of the collector efficiency of nanoparticles in packings of nonspherical collectors, *Colloids and Surfaces A: Physicochemical and Engineering Aspects*, *358*(1–3), 163-171.

Ma, H., J. Pedel, P. Fife, and W. P. Johnson (2009), Hemispheres-in-Cell Geometry to Predict Colloid Deposition in Porous Media, *Environ. Sci. Technol.*, *43*(22), 8573-8579.

Ma, H., and W. P. Johnson (2009), Colloid Retention in Porous Media of Various Porosities: Predictions by the Hemispheres-in-Cell Model, *Langmuir*, *26*(3), 1680-1687.

Ma, H., and W. P. Johnson (2010), Colloid Retention in Porous Media of Various Porosities: Predictions by the Hemispheres-in-Cell Model, *Langmuir*, *26*(3), 1680-1687.

Ma, H., E. Pazmino, and W. P. Johnson (2011), Surface Heterogeneity on Hemispheres-in-Cell Model Yields All Experimentally-Observed Non-Straining Colloid Retention Mechanisms in Porous Media in the Presence of Energy Barriers, *Langmuir*, *27*(24), 14982-14994.

Ma, H., M. Hradisky, and W. P. Johnson (2013), Extending Applicability of Correlation Equations to Predict Colloidal Retention in Porous Media at Low Fluid Velocity, *Environ. Sci. Technol.*, *47*(5), 2272-2278.

Majestic, B., G. Erdakos, M. Lewandowski, K. Oliver, R. Willis, T. Kleindienst, and P. Bhave (2010), A Review of Selected Engineered Nanoparticles in the Atmosphere: Sources, Transformations, and Techniques for Sampling and Analysis, *International Journal of Occupational and Environmental Health*, *16*(4), 488-507.

Marambio-Jones, C., and E. M. V. Hoek (2010), A review of the antibacterial effects of silver nanomaterials and potential implications for human health and the environment, *J. Nanopart. Res.*, *12*(5), 1531-1551.

Mattison, N. T., D. M. O'Carroll, R. Kerry Rowe, and E. J. Petersen (2011), Impact of Porous Media Grain Size on the Transport of Multi-walled Carbon Nanotubes, *Environ. Sci. Technol.*, *45*(22), 9765-9775.

May, R., S. Akbariyeh, and Y. Li (2012), Pore-Scale Investigation of Nanoparticle Transport in Saturated Porous Media Using Laser Scanning Cytometry, *Environ. Sci. Technol.*, *46*(18), 9980-9986.

May, R., and Y. S. Li (2013), The effects of particle size on the deposition of fluorescent nanoparticles in porous media: Direct observation using laser scanning cytometry, *Colloid Surf. A-Physicochem. Eng. Asp.*, *418*, 84-91.

McCarthy, J. F., and J. M. Zachara (1989), Subsurface transport of contaminants, *Environ. Sci. Technol.*, *23*(5), 496-502.

A version of this chapter has been published [*Molnar et al.*, 2015b]

McCaulou, D. R., R. C. Bales, and J. F. McCarthy (1994), Use of short-pulse experiments to study bacteria transport through porous media, *Journal of Contaminant Hydrology*, *15*(1–2), 1-14.

McCaulou, D. R., R. C. Bales, and R. G. Arnold (1995), Effect of Temperature-Controlled Motility on Transport of Bacteria and Microspheres Through Saturated Sediment, *Water Resour. Res.*, *31*(2), 271-280.

McClaine, J. W., and R. M. Ford (2002), Reversal of Flagellar Rotation Is Important in Initial Attachment of Escherichia coli to Glass in a Dynamic System with High- and Low-Ionic-Strength Buffers, *Applied and Environmental Microbiology*, *68*(3), 1280-1289.

Molnar, I. L., D. M. O'Carroll, and J. I. Gerhard (2011), Impact of surfactant-induced wettability alterations on DNAPL invasion in quartz and iron oxide-coated sand systems, *Journal of Contaminant Hydrology*, *119*(1-4), 1-12.

Molnar, I. L., C. S. Willson, D. M. O'Carroll, M. L. Rivers, and J. I. Gerhard (2014), Method for Obtaining Silver Nanoparticle Concentrations within a Porous Medium via Synchrotron X-ray Computed Microtomography, *Environ. Sci. Technol.*, *48*(2), 1114-1122.

Molnar, I. L., J. I. Gerhard, C. S. Willson, and D. M. O'Carroll (2015a), The impact of immobile zones on the transport and retention of nanoparticles in porous media, *Water Resour. Res.*

Molnar, I. L., W. P. Johnson, J. I. Gerhard, C. S. Willson, and D. M. O'Carroll (2015b), Predicting colloid transport through saturated porous media: A critical review *Water Resour. Res.*, *51*(50th anniversary special collection), 6804-6845.

Mondal, P. K., and B. E. Sleep (2013), Virus and virus-sized microsphere transport in a dolomite rock fracture, *Water Resour. Res.*, *49*(2), 808-824.

Mueller, N. C., and B. Nowack (2008), Exposure modeling of engineered nanoparticles in the environment, *Environ. Sci. Technol.*, *42*(12), 4447-4453.

Nelson, K. E., and T. R. Ginn (2011), New collector efficiency equation for colloid filtration in both natural and engineered flow conditions, *Water Resour. Res.*, *47*, 17.

Neukum, C., A. Braun, and R. Azzam (2014), Transport of stabilized engineered silver (Ag) nanoparticles through porous sandstones, *Journal of Contaminant Hydrology*, *158*(0), 1-13.

Novikov, A. P., S. N. Kalmykov, S. Utsunomiya, R. C. Ewing, F. Horreard, A. Merkulov, S. B. Clark, V. V. Tkachev, and B. F. Myasoedov (2006), Colloid Transport of Plutonium in the Far-Field of the Mayak Production Association, Russia, *Science*, *314*(5799), 638-641.

Nowack, B., and T. D. Bucheli (2007), Occurrence, behavior and effects of nanoparticles in the environment, *Environmental Pollution*, *150*(1), 5-22.

O'Carroll, D., B. Sleep, M. Krol, H. Boparai, and C. Kocur (2013), Nanoscale zero valent iron and bimetallic particles for contaminated site remediation, *Adv. Water Resour.*, *51*(0), 104-122.

O'Connor, D. R. (2002), Part One Report of the Walkerton Inquiry: The Events of May 2000 and Related Issues, edited by O. M. o. t. A. General, Queen's Printer for Ontario, 2002.

A version of this chapter has been published [*Molnar et al.*, 2015b]

Ouyang, Y., D. Shinde, R. S. Mansell, and W. Harris (1996), Colloid-enhanced transport of chemicals in subsurface environments: A review, *Critical Reviews in Environmental Science and Technology*, *26*(2), 189-204.

Paraskeva, C. A., V. N. Burganos, and A. C. Payatakes (1991), THREE-DIMENSIONAL TRAJECTORY ANALYSIS OF PARTICLE DEPOSITION IN CONSTRICTED TUBES, *Chemical Engineering Communications*, *108*(1), 23-48.

Payatakes, A. C., C. Tien, and R. M. Turian (1974a), Trajectory calculation of particle deposition in deep bed filtration: Part I. Model formulation, *Aiche J.*, *20*(5), 889-900.

Payatakes, A. C., R. Rajagopalan, and C. Tien (1974b), On the use of happel's model for filtration studies, *Journal of Colloid and Interface Science*, *49*(2), 321-325.

Pazmino, E. F., J. Trauscht, B. Dame, and W. P. Johnson (2014a), Power Law Size-Distributed Heterogeneity Explains Colloid Retention on Soda Lime Glass in the Presence of Energy Barriers, *Langmuir*, *30*(19), 5412-5421.

Pazmino, E. F., J. Trauscht, and W. P. Johnson (2014b), Release of Colloids from Primary Minimum Contact under Unfavorable Conditions by Perturbations in Ionic Strength and Flow Rate, *Environ. Sci. Technol.*, *48*(16), 9227-9235.

Petersen, E. J., et al. (2011), Potential Release Pathways, Environmental Fate, And Ecological Risks of Carbon Nanotubes, *Environ. Sci. Technol.*, *45*(23), 9837-9856.

Petosa, A. R., D. P. Jaisi, I. R. Quevedo, M. Elimelech, and N. Tufenkji (2010), Aggregation and Deposition of Engineered Nanomaterials in Aquatic Environments: Role of Physicochemical Interactions, *Environ. Sci. Technol.*, *44*(17), 6532-6549.

Phenrat, T., N. Saleh, K. Sirk, R. D. Tilton, and G. V. Lowry (2007), Aggregation and sedimentation of aqueous nanoscale zerovalent iron dispersions, *Environ. Sci. Technol.*, *41*(1), 284-290.

Phenrat, T., H.-J. Kim, F. Fagerlund, T. Illangasekare, R. D. Tilton, and G. V. Lowry (2009), Particle Size Distribution, Concentration, and Magnetic Attraction Affect Transport of Polymer-Modified Fe0 Nanoparticles in Sand Columns, *Environ. Sci. Technol.*, *43*(13), 5079-5085.

Phenrat, T., J. E. Song, C. M. Cisneros, D. P. Schoenfelder, R. D. Tilton, and G. V. Lowry (2010a), Estimating Attachment of Nano- and Submicrometer-particles Coated with Organic Macromolecules in Porous Media: Development of an Empirical Model, *Environ. Sci. Technol.*, *44*(12), 4531-4538.

Phenrat, T., A. Cihan, H. J. Kim, M. Mital, T. Illangasekare, and G. V. Lowry (2010b), Transport and Deposition of Polymer-Modified Fe-0 Nanoparticles in 2-D Heterogeneous Porous Media: Effects of Particle Concentration, Fe-0 Content, and Coatings, *Environ. Sci. Technol.*, *44*(23), 9086-9093.

Phenrat, T., H. J. Kim, F. Fagerlund, T. Illangasekare, and G. V. Lowry (2010c), Empirical correlations to estimate agglomerate size and deposition during injection of a polyelectrolyte-modified Fe-0 nanoparticle at high particle concentration in saturated sand, *Journal of Contaminant Hydrology*, *118*(3-4), 152-164.

Pinchuk, A. O. (2012), Size-Dependent Hamaker Constant for Silver Nanoparticles, *The Journal of Physical Chemistry C*, *116*(37), 20099-20102.

A version of this chapter has been published [*Molnar et al.*, 2015b]

Potter, M. C., and D. C. Wiggert (2002), *Mechanics of fluids*, Brooks Cole /Thompson Learning, Pacific Grove, CA.

Powelson, D. K., C. P. Gerba, and M. T. Yahya (1993), Virus transport and removal in wastewater during aquifer recharge, *Water Research*, *27*(4), 583-590.

Qi, Z., L. Hou, D. Zhu, R. Ji, and W. Chen (2014), Enhanced Transport of Phenanthrene and 1-Naphthol by Colloidal Graphene Oxide Nanoparticles in Saturated Soil, *Environ. Sci. Technol.*, *48*(17), 10136-10144.

Quinn, J., et al. (2005), Field Demonstration of DNAPL Dehalogenation Using Emulsified Zero-Valent Iron, *Environ. Sci. Technol.*, *39*(5), 1309-1318.

Rajagopalan, R., and C. Tien (1976), TRAJECTORY ANALYSIS OF DEEP-BED FILTRATION WITH SPHERE-IN-CELL POROUS-MEDIA MODEL, *Aiche J.*, *22*(3), 523-533.

Raychoudhury, T., G. Naja, and S. Ghoshal (2010), Assessment of transport of two polyelectrolyte-stabilized zero-valent iron nanoparticles in porous media, *Journal of Contaminant Hydrology*, *118*(3–4), 143-151.

Ren, D., and J. A. Smith (2013), Proteinate-Capped Silver Nanoparticle Transport in Water-Saturated Sand, *Journal of Environmental Engineering*, *139*(6), 781-787.

Ross, S., and I. D. Morrison (1988), *Colloidal systems and interfaces*, Wiley, New York.

Rotter, B. E., D. A. Barry, J. I. Gerhard, and J. S. Small (2008), Modeling U(VI) biomineralization in single- and dual-porosity porous media, *Water Resour. Res.*, *44*(8), W08437.

Ruckenstein, E., and D. C. Prieve (1976), Adsorption and desorption of particles and their chromatographic separation, *Aiche J.*, *22*(2), 276-283.

Ruohola, A.-M. J., R. F. Considine, D. R. Dixon, C. Fong, and C. J. Drummond Mapping the nano-scale interaction between bio-colloidal Giardia lamblia cysts and silica, *Soft Matter*, *8*(22), 6083-6091.

Russell, T. L., K. M. Yamahara, and A. B. Boehm (2012), Mobilization and Transport of Naturally Occurring Enterococci in Beach Sands Subject to Transient Infiltration of Seawater, *Environ. Sci. Technol.*, *46*(11), 5988-5996.

Ryan, J. N., and M. Elimelech (1996), Colloid mobilization and transport in groundwater, *Colloids and Surfaces A: Physicochemical and Engineering Aspects*, *107*(0), 1-56.

Ryan, J. N., M. Elimelech, R. A. Ard, R. W. Harvey, and P. R. Johnson (1999), Bacteriophage PRD1 and Silica Colloid Transport and Recovery in an Iron Oxide-Coated Sand Aquifer, *Environ. Sci. Technol.*, *33*(1), 63-73.

Ryan, J. N., R. W. Harvey, D. Metge, M. Elimelech, T. Navigato, and A. P. Pieper (2002), Field and Laboratory Investigations of Inactivation of Viruses (PRD1 and MS2) Attached to Iron Oxide-Coated Quartz Sand, *Environ. Sci. Technol.*, *36*(11), 2403-2413.

Sakulchaicharoen, N., D. M. O'Carroll, and J. E. Herrera (2010), Enhanced stability and dechlorination activity of pre-synthesis stabilized nanoscale FePd particles, *Journal of Contaminant Hydrology*, *118*(3–4), 117-127.

Scheibe, T. D., S. S. Hubbard, T. C. Onstott, and M. F. DeFlaun (2011), Lessons Learned from Bacterial Transport Research at the South Oyster Site, *Ground Water*, *49*(5), 745-763.

A version of this chapter has been published [*Molnar et al.*, 2015b]

Scheibe, T. D., Z. S. Hou, B. J. Palmer, and A. M. Tartakovsky (2013), Pore-scale simulation of intragranular diffusion: Effects of incomplete mixing on macroscopic manifestations, *Water Resour. Res.*, *49*(7), 4277-4294.

Schijven, J. F., W. Hoogenboezem, M. Hassanizadeh, and J. H. Peters (1999), Modeling removal of bacteriophages MS2 and PRD1 by dune recharge at Castricum, Netherlands, *Water Resour. Res.*, *35*(4), 1101-1111.

Schijven, J. F., and S. M. Hassanizadeh (2000), Removal of Viruses by Soil Passage: Overview of Modeling, Processes, and Parameters, *Critical Reviews in Environmental Science and Technology*, *30*(1), 49-127.

Schijven, J. F., and S. M. Hassanizadeh (2002), Virus removal by soil passage at field scale and groundwater protection of sandy aquifers (vol 46, pg 123, 2002), *Water Sci. Technol.*, *46*(6-7), 411-411.

Schijven, J. F., and J. Šimůnek (2002), Kinetic modeling of virus transport at the field scale, *Journal of Contaminant Hydrology*, *55*(1–2), 113-135.

Scholl, M. A., and R. W. Harvey (1992), Laboratory investigations on the role of sediment surface and groundwater chemistry in transport of bacteria through a contaminated sandy aquifer, *Environ. Sci. Technol.*, *26*(7), 1410-1417.

Sen, T. K., and K. C. Khilar (2006), Review on subsurface colloids and colloid-associated contaminant transport in saturated porous media, *Advances in Colloid and Interface Science*, *119*(2–3), 71-96.

Sen, T. K. (2011), Processes in Pathogenic Biocolloidal Contaminants Transport in Saturated and Unsaturated Porous Media: A Review, *Water Air Soil Pollut*, *216*(1-4), 239-256.

Shang, J., M. Flury, G. Chen, and J. Zhuang (2008), Impact of flow rate, water content, and capillary forces on in situ colloid mobilization during infiltration in unsaturated sediments, *Water Resour. Res.*, *44*(6), W06411.

Shen, C., B. Li, Y. Huang, and Y. Jin (2007), Kinetics of Coupled Primary- and Secondary-Minimum Deposition of Colloids under Unfavorable Chemical Conditions, *Environ. Sci. Technol.*, *41*(20), 6976-6982.

Shen, C., V. Lazouskaya, Y. Jin, B. Li, Z. Ma, W. Zheng, and Y. Huang (2012), Coupled factors influencing detachment of nano- and micro-sized particles from primary minima, *Journal of Contaminant Hydrology*, *134–135*(0), 1-11.

Simoni, S. F., H. Harms, T. N. P. Bosma, and A. J. B. Zehnder (1998), Population Heterogeneity Affects Transport of Bacteria through Sand Columns at Low Flow Rates, *Environ. Sci. Technol.*, *32*(14), 2100-2105.

Šimůnek, J., N. J. Jarvis, M. T. v. Genuchten, and A. Gärdenäs (2003), Review and comparison of models for describing non-equilibrium and preferential flow and transport in the vadose zone, *Journal of Hydrology*, *272*(1), 14-35.

Šimůnek, J., and M. T. van Genuchten (2008), Modeling nonequilibrium flow and transport processes using HYDRUS, *Vadose Zone J.*, *7*(2), 782-797.

Song, L., and M. Elimelech (1992), Deposition of Brownian particles in porous media: Modified boundary conditions for the sphere-in-cell model, *Journal of Colloid and Interface Science*, *153*(1), 294-297.

Sprague, L. A., J. S. Herman, G. M. Hornberger, and A. L. Mills (2000), Atrazine Adsorption and Colloid-Facilitated Transport through the Unsaturated Zone, *J. Environ. Qual.*, *29*(5), 1632-1641.

A version of this chapter has been published [*Molnar et al.*, 2015b]

Subramanian, S. K., Y. Li, and L. M. Cathles (2013), Assessing preferential flow by simultaneously injecting nanoparticle and chemical tracers, *Water Resour. Res.*, *49*(1), 29-42.

Taghavy, A., A. Mittelman, Y. Wang, K. D. Pennell, and L. M. Abriola (2013), Mathematical Modeling of the Transport and Dissolution of Citrate-Stabilized Silver Nanoparticles in Porous Media, *Environ. Sci. Technol.*, *47*(15), 8499-8507.

Taylor, R., A. Cronin, S. Pedley, J. Barker, and T. Atkinson (2004), *The implications of groundwater velocity variations on microbial transport and wellhead protection – review of field evidence*, 17-26 pp.

Tong, M., X. Li, C. N. Brow, and W. P. Johnson (2005), Detachment-Influenced Transport of an Adhesion-Deficient Bacterial Strain within Water-Reactive Porous Media, *Environ. Sci. Technol.*, *39*(8), 2500-2508.

Tong, M., and W. P. Johnson (2006), Excess Colloid Retention in Porous Media as a Function of Colloid Size, Fluid Velocity, and Grain Angularity, *Environ. Sci. Technol.*, *40*(24), 7725-7731.

Tong, M., and W. P. Johnson (2007), Colloid Population Heterogeneity Drives Hyperexponential Deviation from Classic Filtration Theory, *Environ. Sci. Technol.*, *41*(2), 493-499.

Tong, M., H. Ma, and W. P. Johnson (2008), Funneling of Flow into Grain-to-grain Contacts Drives Colloid−Colloid Aggregation in the Presence of an Energy Barrier, *Environ. Sci. Technol.*, *42*(8), 2826-2832.

Torkzaban, S., S. S. Tazehkand, S. L. Walker, and S. A. Bradford (2008), Transport and fate of bacteria in porous media: Coupled effects of chemical conditions and pore space geometry, *Water Resour. Res.*, *44*(4).

Torkzaban, S., Y. Kim, M. Mulvihill, J. M. Wan, and T. K. Tokunaga (2010), Transport and deposition of functionalized CdTe nanoparticles in saturated porous media, *Journal of Contaminant Hydrology*, *118*(3-4), 208-217.

Tosco, T., M. Petrangeli Papini, C. Cruz Viggi, and R. Sethi (2014a), Nanoscale zerovalent iron particles for groundwater remediation: a review, *Journal of Cleaner Production*, *77*(0), 10-21.

Tosco, T., F. Gastone, and R. Sethi (2014b), Guar gum solutions for improved delivery of iron particles in porous media (Part 2): Iron transport tests and modeling in radial geometry, *Journal of Contaminant Hydrology*, *166*(0), 34-51.

Tufenkji, N., J. A. Redman, and M. Elimelech (2003), Interpreting Deposition Patterns of Microbial Particles in Laboratory-Scale Column Experiments, *Environ. Sci. Technol.*, *37*(3), 616-623.

Tufenkji, N., and M. Elimelech (2004a), Correlation equation for predicting single-collector efficiency in physicochemical filtration in saturated porous media, *Environ. Sci. Technol.*, *38*(2), 529-536.

Tufenkji, N., and M. Elimelech (2004b), Deviation from the classical colloid filtration theory in the presence of repulsive DLVO interactions, *Langmuir*, *20*(25), 10818-10828.

Tufenkji, N., G. F. Miller, J. N. Ryan, R. W. Harvey, and M. Elimelech (2004), Transport of Cryptosporidium Oocysts in Porous Media: Role of Straining and Physicochemical Filtration†, *Environ. Sci. Technol.*, *38*(22), 5932-5938.

Tufenkji, N., and M. Elimelech (2005a), Breakdown of colloid filtration theory: Role of the secondary energy minimum and surface charge heterogeneities, *Langmuir*, *21*(3), 841-852.

Tufenkji, N., and M. Elimelech (2005b), Spatial Distributions of Cryptosporidium Oocysts in Porous Media: Evidence for Dual Mode Deposition, *Environ. Sci. Technol.*, *39*(10), 3620-3629.

Tufenkji, N. (2007), Modeling microbial transport in porous media: Traditional approaches and recent developments, *Adv. Water Resour.*, *30*(6–7), 1455-1469.

Uyusur, B., C. J. G. Darnault, P. T. Snee, E. Koken, A. R. Jacobson, and R. R. Wells (2010), Coupled effects of solution chemistry and hydrodynamics on the mobility and transport of quantum dot nanomaterials in the vadose zone, *Journal of Contaminant Hydrology*, *118*(3-4), 184-198.

van Kooten, J. J. A. (1996), A method to solve the advection-dispersion equation with a kinetic adsorption isotherm, *Adv. Water Resour.*, *19*(4), 193-206.

Verwey, E. J. W., and J. T. G. Overbeek (1948), Theory of the Stability of Lyophobic Colloids, edited, Elsevier, Amsterdam.

Wang, C., A. D. Bobba, R. Attinti, C. Shen, V. Lazouskaya, L.-P. Wang, and Y. Jin (2012), Retention and Transport of Silica Nanoparticles in Saturated Porous Media: Effect of Concentration and Particle Size, *Environ. Sci. Technol.*, *46*(13), 7151-7158.

Wang, D., L. Ge, J. He, W. Zhang, D. P. Jaisi, and D. Zhou (2014a), Hyperexponential and nonmonotonic retention of polyvinylpyrrolidone-coated silver nanoparticles in an Ultisol, *Journal of Contaminant Hydrology*, *164*(0), 35-48.

Wang, Y., Y. Li, J. D. Fortner, J. B. Hughes, L. M. Abriola, and K. D. Pennell (2008), Transport and Retention of Nanoscale C60 Aggregates in Water-Saturated Porous Media, *Environ. Sci. Technol.*, *42*(10), 3588-3594.

Wang, Y., S. A. Bradford, and J. Šimůnek (2014b), Physicochemical Factors Influencing the Preferential Transport of Escherichia coli in Soils, *Vadose Zone J.*, *13*(1).

Wang, Y., S. A. Bradford, and J. Šimůnek (2014c), Estimation and upscaling of dual-permeability model parameters for the transport of E. coli D21g in soils with preferential flow, *Journal of Contaminant Hydrology*, *159*(0), 57-66.

Wielen, P. W. J. J. v. d., W. J. M. K. Senden, and G. Medema (2008), Removal of Bacteriophages MS2 and ΦX174 during Transport in a Sandy Anoxic Aquifer, *Environ. Sci. Technol.*, *42*(12), 4589-4594.

Wiesner, M. R., G. V. Lowry, P. Alvarez, D. Dionysiou, and P. Biswas (2006), Assessing the risks of manufactured nanomaterials, *Environ. Sci. Technol.*, *40*(14), 4336-4345.

Yao, K.-M., M. T. Habibian, and C. R. O'Melia (1971), Water and waste water filtration. Concepts and applications, *Environ. Sci. Technol.*, *5*(11), 1105-1112.

Yates, M. V., C. P. Gerba, and L. M. Kelley (1985), Virus persistence in groundwater, *Applied and Environmental Microbiology*, *49*(4), 778-781.

Zhang, H., and H. M. Selim (2006), Modeling the Transport and Retention of Arsenic (V) in Soils, *Soil Science Society of America Journal*, *70*(5), 1677-1687.

Zhang, L., L. Hou, L. Wang, A. T. Kan, W. Chen, and M. B. Tomson (2012), Transport of Fullerene Nanoparticles (nC60) in Saturated Sand and Sandy Soil: Controlling Factors and Modeling, *Environ. Sci. Technol.*

Zhang, P., W. P. Johnson, M. J. Piana, C. C. Fuller, and D. L. Naftz (2001a), Potential Artifacts in Interpretation of Differential Breakthrough of Colloids and Dissolved Tracers in the Context of Transport in a Zero-Valent Iron Permeable Reactive Barrier, *Ground Water*, *39*(6), 831-840.

Zhang, P., W. P. Johnson, T. D. Scheibe, K.-H. Choi, F. C. Dobbs, and B. J. Mailloux (2001b), Extended tailing of bacteria following breakthrough at the Narrow Channel Focus Area, Oyster, Virginia, *Water Resour. Res.*, *37*(11), 2687-2698.

Zheng, C., and S. M. Gorelick (2003), Analysis of solute transport in flow fields influenced by preferential flowpaths at the decimeter scale, *Ground Water*, *41*(2), 142-155.

Chapter 3

3 A Method for Obtaining Silver Nanoparticle Concentrations Within a Porous Medium via Synchrotron X-Ray Computed Microtomography

3.1 Introduction

Nanoparticles are playing an increasingly important role in manufacturing and consumer technology. Worldwide investment in nanotechnology has increased by approximately an order of magnitude between 1997 and 2005, from $432 million to $4.1 billion [*Baalousha and Lead*, 2009] and this number is expected to increase rapidly in the coming years. Up to $1 trillion worth of engineered nanoparticle products are expected to be in use globally by 2015 [*Baalousha and Lead*, 2009], with many of these products exhibiting toxicological properties [*Borm et al.*, 2006; *Niazi et al.*, 2011; *Song et al.*, 2011; *Stone et al.*, 2009; *Sycheva et al.*, 2011]. This proliferation of nanotechnology has led to significant interest in understanding the fate of engineered nanoparticles if released to the subsurface environment. Nanoparticles might either be a) injected deliberately into the subsurface for contaminant remediation [*O'Carroll et al.*, 2013] b) accidentally released to the subsurface environment or c) already present in the subsurface environment as naturally occurring colloids. In the case of an accidental release, engineered nanoparticles might remain mobile long enough to enter and contaminate aquifers used for municipal drinking water. When used for remediation of contaminants, the behaviour of nanoparticles in the subsurface will dictate design of a site-specific remediation strategy.

Despite the need to better understand the behaviour of engineered nanoparticles in the subsurface, few tools exist that are capable of quantitatively assessing their behaviour in soil. Currently, the most common approach is to inject a nanoparticle solution into a soil column and compare the influent/effluent concentrations as a function of the amount injected [See *Petosa et al.*, 2010, Table 3]. While this method offers insights into

A version of this chapter has been published [*Molnar et al.*, 2014]

nanoparticle mobility and deposition, it is unable to provide direct information about how the nanoparticles are interacting with the soil grains and what role pore-geometry might play. Variations of this method have been used to conduct 2-dimensional experiments [*Phenrat et al.*, 2010] but suffer similar shortcomings due to an inability to quantify in-situ nanoparticle concentrations without destructive sampling. Other studies investigate nanoparticle fate and transport by studying individual characteristics related to mobility (ie. aggregation, sedimentation, dissolution) in realistic aqueous solutions without relying on column experiments [*Ma et al.*, 2012; *Piccapietra et al.*, 2012; *Thio et al.*, 2012]. However, a number of studies have proposed novel methods for quantitatively studying nanoparticle transport in-situ and non-destructively: Ramanan et al. [2012] demonstrated the viability of using Magnetic Resonance Imaging to track the transport of superparamagnetic nanoparticles through coarse soil. Other methods employ fluorescent optical-probes [*Shang et al.*, 2010] and time-lapse fluorescent imaging [*Bridge et al.*, 2006] to track colloids in a porous medium.

Synchrotron x-ray computed microtomography (SXCMT) is a non-destructive, three-dimensional imaging method commonly used in the field of water resources, environmental and petroleum engineering. It is typically used to extract and model realistic pore-network structures [ie. *Al-Raoush and Willson*, 2005a; *Bhattad et al.*, 2011; *Thompson et al.*, 2008] and non-aqueous phase liquid (NAPL) distributions [ie. *Al-Raoush and Willson*, 2005b; *Russo et al.*, 2009; *Schnaar and Brusseau*, 2006]. Colloid transport studies have used x-ray computed microtomography datasets to characterize the structure of porous media used in transport experiments [*Pazmino et al.*, 2011; *Sagee et al.*, 2012], and as inputs for Lattice-Boltzmann modelling [*Li et al.*, 2012; *Long et al.*, 2010; *Pazmino et al.*, 2011].

SXCMT has been used to successfully track the transport of micron-sized colloids through porous media [*Chen et al.*, 2008; *Chen et al.*, 2001; *Gaillard et al.*, 2007; *Li et al.*, 2006] and to map the distribution of biofilm in porous media using silver microspheres [*Iltis et al.*, 2011]. Previous studies have coupled SXCMT with nanoparticle solutions to monitor nanoparticle accumulation within biological tissues [*Giuliani et al.*, 2011; *Lee et al.*, 2013; *Marinescu et al.*, 2013; *Shilo et al.*, 2012;

A version of this chapter has been published [*Molnar et al.*, 2014]

Torrente et al., 2006] and agglomeration within fluidized beds [*Jenneson and Gundogdu*, 2006]. X-ray computed microtomography techniques have also been used to quantify heavy metal concentrations in plants [*McNear et al.*, 2005] and salt tracers in dolostone samples [*Agbogun et al.*, 2013]. While the aforementioned studies have successfully extended the applicability of XCMT techniques, SXCMT's potential to create high-resolution, three-dimensional maps of nanoparticle or chemical concentrations within a porous medium have been relatively unexplored.

While the resolution of typical SXCMT datasets currently available (*ca.* 2 to 12 μm) is too coarse to detect individual nanoparticles, it is hypothesized that the concentration of nanoparticle solutions can be determined within a porous medium. Silver nanoparticles (nAg), due to their x-ray absorption characteristics, are especially suited to imaging with SXCMT and are of interest due to the increasing concern regarding their transport and mobility in the subsurface environment. To the best of the authors' knowledge there have been no studies published to-date that use SXCMT to examine nanoparticle behaviour in a porous medium.

This study outlines a method for imaging and quantifying aqueous silver nanoparticle solutions in a glass bead porous media using absorption-edge SXCMT. While this study focuses specifically on employing SXCMT to determine concentrations of silver nanoparticles, it is hypothesized that this method can be applied more generally to quantify elemental constituents (either colloidal or dissolved) in a porous medium. Similarly, it is hypothesized that the method can be applied equally well to quartz grains and mineral oxide-coated quartz grains. The process used to extract dissolved phase concentrations is the same as the method presented herein. It should be noted that this proposed method is unable to distinguish between the dissolved and colloidal phases for the element of interest. Given the inability to distinguish between phases, this method is intended to be used in experimental conditions under which the presence of the dissolved phase is minimized [e.g. *El Badawy et al.*, 2013; *Liang et al.*, 2013; *Torkzaban et al.*, 2012] and thus would not interfere with attempts at quantifying the colloidal phase (or vice versa). This method is, to the best of the authors' knowledge, the first study that uses only absorption-edge SXCMT to quantify the spatial distribution of elemental

A version of this chapter has been published [*Molnar et al.*, 2014]

constituents (dissolved or nano) either within an aqueous phase or a water-saturated porous medium.

This method can extract nanoparticle concentrations from a porous media column during nanoparticle injection and elution via SXCMT imaging. The nanoparticle concentrations determined from the reconstructed 3-dimensional datasets represent the physical distribution of nanoparticles within that column at the pore-scale, and even within individual pores. Experimental data on the pore-scale distribution of nanoparticles has been typically obtained via micromodels or open-faced visualization flow cells with a mono-layer of grains [*Ochiai et al.*, 2006]. However these techniques are limited to 2-dimensional or quasi-2-dimensional systems, limiting their applicability when studying complex natural soils. The presented SXCMT method overcomes this limitation with its ability to determine nanoparticle concentrations throughout real 3-dimensional pore-networks.

The first part of the study examines the accuracy of the method by studying static, known concentrations of silver nanoparticles in a simple liquid-only sample (L-O) as well as within the pore space of a liquid-porous media sample (L-PM). These static L-O and L-PM samples were also used to investigate: sources of uncertainty in the method, methods for reducing uncertainty, optimizing the imaging process and understanding the sources of error in the images. The second part of this study analyzes a series of datasets of nAg invading a water saturated glass-bead column (hereafter referred to as IL-PM, injected liquid-porous media). A nanoparticle solution was injected into the 0g/L L-PM column and the column was imaged after every 7.6 minutes of injection time. After 45 minutes of injection, the source was switched to a non-nAg aqueous solution which was used to flush nanoparticles out of the column. These datasets were used to investigate the ability of the method to quantify nAg within a porous medium when the concentration and distribution is unknown. Both parts of the presented study demonstrate the usefulness and potential of SXCMT when attempting to elucidate the role of pore-network geometry in nanoparticle transport.

A version of this chapter has been published [*Molnar et al.*, 2014]

3.2   Materials and Methods

3.2.1   Silver Nanoparticle Synthesis

The nAg solutions used in this study were synthesized at the Argonne National Lab's Advanced Photon Source (APS) in the GeoSoilEnviro Center for Advanced Radiation Sources (GSECARS) wet lab the day before the allotted synchrotron x-ray beam time. The nAg solution was synthesized via chemical reduction using a method similar to Wang et al. [1998] and was stabilized in a 1% solution of Sodium carboxymethyl cellulose (CMC90k) (Aldrich Chemistry). Prior to synthesis all aqueous solutions were de-oxygenated by bubbling nitrogen through the solutions for at least 2 hours. This deoxygenation procedure was conducted to minimize the dissolution of silver nanoparticles occurring during the experimental procedures. A 70mL 0.1N Silver Nitrate ($AgNO_3$) solution (Alfa Aesar) was mixed with 70mL of the CMC90k solution and titrated with nitric acid (Environmental Grade, Alfa Aesar) to dissolve a gel-like substance that had formed. The CMC90k/$AgNO_3$ solution was stirred continuously while 70mL of a 0.4M solution of Sodium Borohydride ($NaBH_4$) (Granulated, 97+%, Alfa Aesar) was added dropwise to reduce the Ag^+_{aq} to silver nanoparticles. A jet black solution formed immediately following the addition of $NaBH_4$ indicating that silver nanoparticles had indeed formed at a very high concentration (target concentration = 3.6 g/L). The target concentration of 3.6 g/L was chosen as it was believed to be the highest concentration at which stable nanoparticles could be synthesized at the GSECARS wetlab. At the target concentration of 3.6 g/L there are approximately 3.6×10^4 silver nanoparticles within each voxel in the reconstructed datasets.

After synthesis, the pH of the nanoparticle solution was determined to be 8.7. A CMC90k solution containing no nanoparticles was titrated with NaOH (10N, Fisher Scientific) to the same pH and used for both dilution and in the transport experiment. Ionic strength was controlled to 0.12M with Sodium Nitrate (Certified A.C.S, Fisher Scientific) for both silver nanoparticle and CMC90k solutions.

The yield of the nanoparticle synthesis procedure was determined by passing a synthesized sample through an Amicon 8400 ultrafiltration unit and it was found that

A version of this chapter has been published [*Molnar et al.*, 2014]

98% of all silver had been reduced to silver nanoparticles (see Appendix 8 for details). The target silver nanoparticle concentration (3.6 g/L, 0.36%) is high relative to typical nanoparticle transport studies [See *Petosa et al.*, 2010, Table 3]. However the target concentration is much lower than the concentration of dopants typically used in absorption-edge imaging (~10%) [*Al-Raoush and Willson*, 2005b]. The resulting nAg solution was very stable and no settling was observed between the time of synthesis and the end of the allotted beam time. Silver nanoparticle samples were shipped back to the University of Western Ontario, Canada for analysis.

Due to the complication of shipping nanomaterials across the US-Canada border, 3 weeks elapsed between synthesis and analysis; however, the solutions had not visibly changed during that time nor had any major settling occurred. The measured d_{50} was 27.5 nm (ZetaPlus Zeta Potential Analyzer, Brookhaven). This parameter was monitored over several months and was found to stay relatively constant. The measured zeta potential of the silver nanoparticles was -17.9 mV (ZetaPlus Zeta Potential Analyzer, Brookhaven).

3.2.2   L-O/L-PM Experimental Procedure

The L-O and L-PM samples were prepared by creating several dilutions of the nAg solution. The samples were diluted in a 1% CMC90k mixture with the same pH and ionic strength. The following nAg concentrations were used: 0g/L (no nAg), 1/3rd dilution, 2/3rd dilution, and undiluted nAg. For the L-O samples, the solutions were injected into a bundle of glass capillary tubes (ID: 1.1 - 1.2 mm). For the L-PM samples, glass beads were chosen as a standard first step due to their simplified geometry. The L-PM samples were housed in small aluminum columns (ID: 5.6 mm, length: 5cm, see Figure 8.2). The soda-lime glass beads (class V; diameter, 425-500 μm; MO-SCI Corporation) were acid-washed prior to packing. The columns were wet-packed, using the aforementioned solutions, by maintaining a meniscus of solution on top of the column and slowly adding glass beads to the column.

The silver concentrations of the L-O/L-PM samples were determined via inductively coupled plasma optical emission spectrometry (ICP-OES), a technique used to determine elemental concentrations. The ICP-OES was calibrated with an elemental silver standard

A version of this chapter has been published [*Molnar et al.*, 2014]

stabilized in nitric acid. The L-O/L-PM samples were digested in concentrated nitric acid to dissolve the nanoparticles because ICP-OES cannot quantify solid-phase particulates. The concentrated nitric acid/Ag solution was diluted to 2% nitric acid in Milli-Q water and passed through the ICP-OES to quantify the amount of Ag present in each sample; hereafter referred to as "ICP-determined [nAg]".

3.2.3   Imaging

Imaging for this study was conducted at the APS 13-BM-D beamline with the GSECARS research group. The L-O and L-PM samples were imaged approximately 2.5 cm above the base of the columns. A double Si(111) crystal monochromator was used to select X-ray energies with a resolution of $\Delta E/E= 10^{-4}$, meaning the monochromator selected the X-ray energy to within 0.01%. The x-rays were converted to visible light via a 100 μm thick lutetium aluminum garnet (LAG) scintillator crystal and the resulting projections were captured on a Princeton Instruments CoolSnap HQ-2 CCD camera. Imaging was performed above and below the silver (Ag) K-edge of 25.5 keV [*M.J. Berger et al.*, 2010]. The L-O samples were imaged at 4 different energies and the L-PM samples were imaged with 3 energies: 25.414, 25.614, 25.814 keV and 25.914 keV (L-O only). The sample was rotated through 180° while 1440 projections were captured. The exposure time for each projection was 0.26 seconds. Pixels were binned together (2x2) to increase imaging speed and preliminary imaging suggested that binning pixels also reduced noise in simple, homogeneous samples. The number of pixels in each projection was 696 x 520 (horizontal x vertical). The pixel resolution of the projections was measured to be 10.47 x 10.47 μm. The resolution (10.47 μm) was selected to optimize practical considerations (e.g. larger column size, ease of column packing, accurate effluent sampling) with image capture time (limiting nAg diffusion).

3.2.4   Reconstruction

After imaging, the projections were reconstructed with GSECARS-specific reconstruction software [*Rivers et al.*, 2010] in IDL 8.1 (ITT Visual Information Solutions). The reconstruction software transforms the series of two-dimensional projections into a three-dimensional map of x-ray mass linear attenuation values. Each

A version of this chapter has been published [*Molnar et al.*, 2014]

10.47 × 10.47 × 10.47 μm voxel within the image represents 1 x-ray mass linear attenuation value. The software used filtered back projection with a Radon transform and linear interpolation enabled. A general Hamming filter was selected and was set to be the width of the image. Images were not normalized to match the sinogram. The dark current correction was set to its default value of 100.

Following reconstruction, subvolumes were extracted from the L-O and L-PM datasets for analysis. The extracted L-PM and L-O subvolumes were, respectively, 350 × 350 × 450 volume elements (ie. voxels) and 20 × 20 × 520 volume elements in size.

3.2.5   Segmentation and Pore-Network Extraction

The reconstructed L-PM datasets were segmented into grain and water phases via an indicator kriging method to separate the phases [*Bhattad et al.*, 2010; *Oh and Lindquist*, 1999]. Custom software [*Thompson et al.*, 2006; *Thompson et al.*, 2008] was used for the grain characterization and pore-network extraction processes. The grain identification and pore-network extraction algorithms (fully described in [*Bhattad et al.*, 2010; *Thompson et al.*, 2008]) identified each unique pore and grain within the reconstructed volume and then associated every voxel with either an identified pore or grain. These pore identifiers were employed to capture pore-average nAg concentrations.

Care was taken to ensure all L-PM and IL-PM datasets had consistent grain and pore size distributions as it is possible to overestimate or underestimate grain sizes during the solid/void segmentation process. Misestimating the grain sizes in various datasets could then interfere with attempts to compare SXCMT-determined silver concentrations between datasets. Consistency was ensured by iterating the segmentation/pore-network process until the average grain inscribed radii for each dataset was within 1 voxel (10.47 μm) of all other datasets. Table 8.1 in the supplementary information demonstrates the consistency of the grain and pore-network statistics for each of the imaged subvolumes.

3.2.6   Analysis

Upon completion of the reconstruction and segmentation/pore-network extraction process, Beer's law was modified (eq. 3.1) and applied to the L-O and L-PM datasets to

A version of this chapter has been published [*Molnar et al.*, 2014]

convert the x-ray mass linear attenuation value in each water voxel to silver (Ag) concentrations. A derivation of eq. 3.1 can be found in Appendix 8.

$$c_{silver} = \frac{\frac{\Delta A}{l} - [(\alpha_a - \alpha_b)\rho]_{water}}{(\alpha_a - \alpha_b)_{silver}} \qquad 3.1$$

This process provided a silver concentration at each voxel in the pore space; it is assumed that the silver concentration is equal to the nAg concentration due to the redox conditions of the synthesized silver solutions. The nAg concentration at one or more voxels is then averaged, excluding those immediately adjacent to grains (details on averaging and the exclusion process provided in the Results and Discussion: Accuracy section). Each average value is hereafter referred to as the "SXCMT-determined [nAg]" for the voxels in the pore space over which the averaging occurred. It should be noted that, due to the resolution of the images, this method cannot detect individual nanoparticles, but rather quantifies the concentration of the nanomaterial solution at each voxel in the reconstructed volume.

Figure 3.1 illustrates and describes the major steps of the analysis procedure listed above.

A version of this chapter has been published [*Molnar et al.*, 2014]
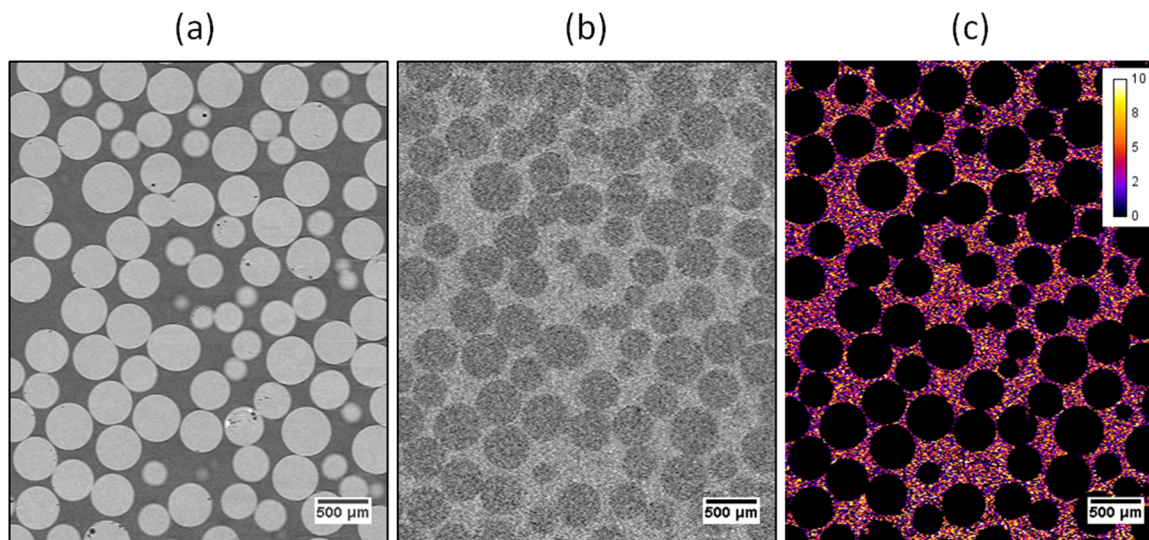
Figure 3.1: A pictorial representation of the quantification process for one slice of the 3.6g/L L-PM sample. (a) The column is scanned at 1 energy below the silver k-edge and at 2 energies above the silver k-edge. These images are then reconstructed to create a 3-dimensional map of the x-ray mass attenuation values. (b) The above and below edge datasets are subtracted to create 2 difference datasets. (c) eq. 3.1 is applied to each pore space voxel within the 2 difference datasets. The 2 datasets are then averaged to obtain the SXCMT-determined [nAg] map for the pore space (legend given in g/L).

3.2.7   IL-PM Experimental Procedure

The nanoparticle injection (IL-PM) experiment was identical to the L-PM experiments except for the following details. 3.25 g/L nAg was injected into the column (ID 5.6 mm, length=5cm, see Figure 8.2), initially at 0g/L nAg, using a syringe pump at 1.2 cm/min (i.e., 16.9 m/day) for 45 min (total active pump time). The column was then flushed for an additional 30 min (total active pump time) with an identical solution (CMC90k concentration, ionic strength) but containing 0g/L nAg. Imaging occurred at t=0 and then after every 7.6 min of active pump time for the entire experiment, resulting in eleven three-dimensional images. Note that the injection pump was stopped during the acquisition of each image, which lasted approximately 40 min. There was an approximate 1-2 minute delay between injection and imaging due to the safety procedures required to secure the imaging hutch. A conservative tracer test was not performed due to concerns that Br^- and Cl^- may form insoluble complexes with Ag^+.

A version of this chapter has been published [*Molnar et al.*, 2014]

Effluent samples were collected every 7.6 minutes for analysis. Inlet samples were collected at the beginning and end of the experiment to assess whether the influent nAg concentration was steady. The silver concentrations of the collected IL-PM samples were analyzed via ICP-OES in the same manner as the L-O/L-PM samples.

3.3 Results and Discussion

To aid the discussion in the following sections, the terms 'accuracy' and 'uncertainty' are defined as follows: since averaging is involved in each SXCMT-determined [nAg] value, 'uncertainty' quantifies the 99% confidence interval on the average value; in other words, the true average of the underlying population of voxel-specific nAg values is expected to lie within this interval with 99% certainty. 'Accuracy' considers how closely the SXCMT-determined [nAg] matches the ICP-determined [nAg]; this is quantified as 'error'. Considering uncertainty and accuracy necessarily requires discussions of precision (i.e., repeatability), noise (random fluctuations in the underlying dataset), and signal discrepancy (apparent absorption, the difference between the actual amount of x-ray attenuation and what is observed via the CCD).

3.3.1 Accuracy

The global accuracy of the technique for the L-O and L-PM samples is presented in Figure 3.2. The SXCMT-determined [nAg] values were obtained by averaging every water voxel within each dataset (approximately 200,000 water voxels in each L-O dataset and 20,000,000 water voxels in each L-PM dataset). As shown, the accuracy for the L-O columns is good, with a linear relationship (R^2=0.9986). The presented slope deviates from unity by 8%, and the y-intercept error is 0.06 g/L. It is noted that the SXCMT-determined [nAg] for the L-PM samples are less accurate, with a slope 22% below unity and a y-intercept error of 0.4 g/L. However, the SXCMT-determined [nAg] is still linearly related to the ICP-determined [nAg] (R^2=0.9983). The linearity in both the L-PM and L-O data indicate that this method detects differences in aqueous silver concentration and that these relationships can be employed as calibration curves. In other words, the presented linear functions can be used to transform the SXCMT-determined

A version of this chapter has been published [*Molnar et al.*, 2014]

concentration into the actual (i.e., ICP-determined) nAg concentration within the range of concentrations presented here.
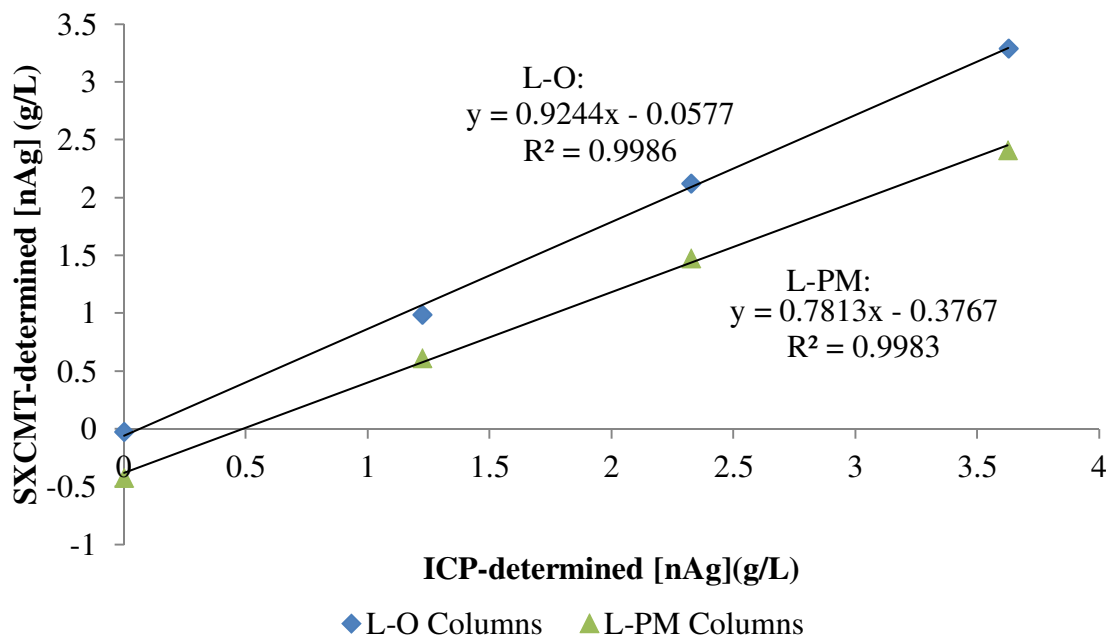
Figure 3.2: The average SXCMT-determined [nAg] for all water voxels in both L-O columns and L-PM columns vs. the concentration of silver determined via ICP analysis. The SXCMT-determined [nAg] values were calculated from datasets captured at 25.414, 25.614 and 25.814 keV. The size of the 99% confidence interval (L-O: +/- 0.01g/L   L-PM: +/- 0.002g/L) is smaller than the data point icons.

The standard deviation associated with the SXCMT-determined [nAg] for each dataset is large (L-O: 1.9g/L, L-PM: 3.5- 4.2 g/L); this reflects the wide distribution of values in the underlying, voxel-specific population (e.g., Figure 3.1c). However, due to the large number of water voxels averaged to generate the single SXCMT-determined concentration for each sample, the 99% confidence intervals on the SXCMT-determined concentrations shown in Figure 3.2 are small (L-O: 10^{-2} g/L, L-PM: 10^{-3} g/L). Thus, a high degree of confidence in the SXCMT-determined [nAg] is obtained by averaging the voxel-specific values. The large number of water voxels in each image and within each pore is one of the major strengths of this technique.

As mentioned above, the SXCMT-determined concentrations were calculated using energies of 25.4, 25.6, 25.8 keV and 25.9 keV (L-O only). Increasing the number of

A version of this chapter has been published [*Molnar et al.*, 2014]

energy-pairs from 1 to 3 decreased the standard deviation in the SXCMT-determined nAg concentration in the L-O samples by 19% (2.3 to 1.9g/L). Over-determination with the L-PM samples led to a similar reduction in standard deviation. Previous studies have successfully employed a similar method of over-determining Beer's law with x-ray microtomography to quantify fire retardants dispersed throughout various materials [*Barnett et al.*, 2010; *Ham et al.*, 2004].

There are a number of reasons why the calibration curves for the L-PM and L-O columns are different. These reasons are discussed in turn below, but mostly relate to two main factors: (a) x-ray refraction increases in the presence of a porous medium (causing increased noise) and (b) apparent absorption decreases in the presence of a porous medium (causing decreased signal:noise ratio).

The accuracy of the SXCMT-determined concentrations is limited by two assumptions that are fundamental to the application of Beer's law. The first assumption is that the compound of interest is infinitely dilute. While the solution is not infinitely dilute, the linear relationships in Figure 3.2 suggests that it remains a reasonable approximation. The second assumption is that the compound of interest is the only absorbing compound within the sample. As indicated by eq 3.1, both silver and water absorb x-rays within the L-O and L-PM samples. However, by incorporating the terms for water in eq. 3.1 it is possible to minimize the impact of this assumption on the accuracy of the technique.

Figure 3.3, a plot of SXCMT-determined [nAg] as a function of distance from a grain surface, illustrates one of the major sources of error in the SXCMT datasets. The figure reveals that water voxels close to a grain surface (<18.1 μm distant) have relatively lower SXCMT-determined [nAg] values than the more distant voxels with a relatively constant concentration. The distance between each pore space voxel in the L-PM datasets and the nearest voxel in the outer surface of a grain was calculated by measuring the actual distance between the centers of these two voxels. For example, a water voxel with 1 face contacting that of a grain voxel has a "distance to grain" of 10.47 μm (1 voxel). The algorithm used to find the closest glass bead surface for each pore space voxel, and measure the distance between them, is detailed in Appendix 10.1. Each point in Figure

A version of this chapter has been published [*Molnar et al.*, 2014]

3.3 represents the average of all water voxels within a narrow range of distances to grains (i.e., 10.47-18.11 μm, 18.11-26.17μm, etc.).

The lowered concentrations observed near grain surfaces are likely artifacts from the tomography process and not real concentration gradients. The L-PM samples involve a porous medium emplaced within a stable, static, homogeneous nanoparticle solution (i.e., no transport processes) so no bulk concentration gradients throughout the pore space were expected. The same effect is observed at 0g/L, so it cannot be a real concentration gradient. Indeed, Figure 3.3 confirms that the nAg concentration is, on average, invariant throughout pore space. In fact, the SXCMT-determined concentration remains relatively uniform until at least 160 μm average distance from the nearest grain (data not shown); larger distances cannot be evaluated since the number of voxels within the L-PM subvolumes available for averaging falls below 100.
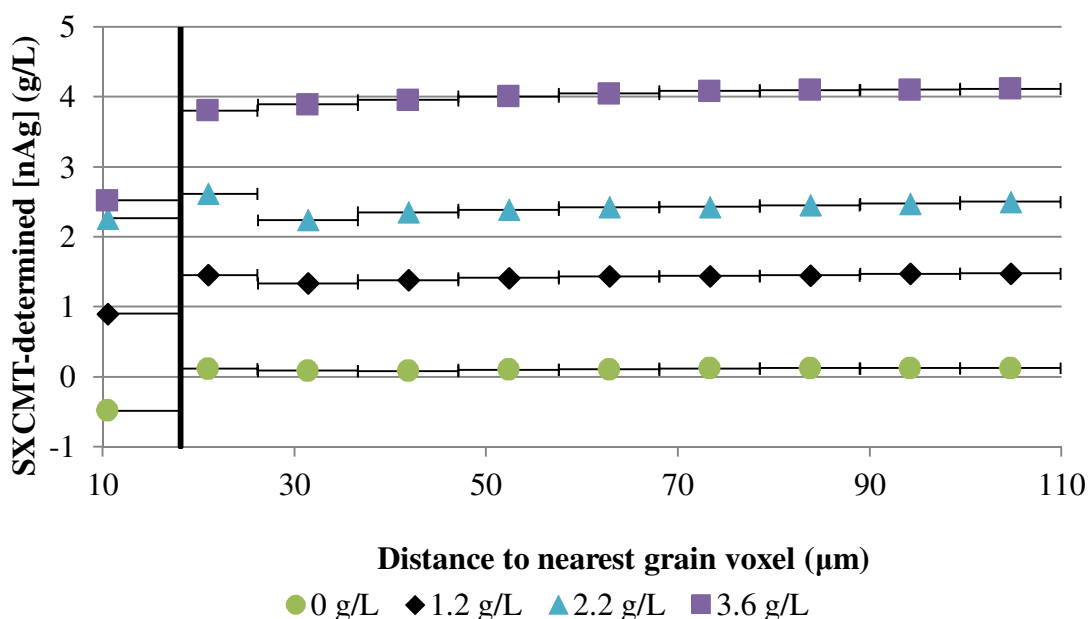
Figure 3.3: SXCMT-determined [nAg] as a function of distance to closest glass bead illustrates the interference a glass bead may have on neighboring water voxels due to x-ray refraction. The concentrations have been calibrated via the curve in Figure 3.2. The distances were rounded to the nearest integer and the calculated concentrations were averaged. The vertical black line represents the threshold distance for the 'shadow zone' effect, 18.11 μm (ie. 1.73 voxels) away from the nearest grain surface. The horizontal bars represent the range of voxels (by distance) that were binned to create an average SXCMT-determined concentration value at each data point. The size of the 99% confidence interval is smaller than the thickness of the data points and has thus been excluded.

A version of this chapter has been published [*Molnar et al.*, 2014]

The source of error leading to the lowered SXCMT-determined concentrations, and also partially accounting for the differences between the L-O and L-PM calibration curves in Figure 3.2, is the refraction of x-rays passing through the porous medium in the L-PM samples. At grain-water interfaces, x-rays refract slightly. This refraction is used advantageously when imaging systems with low-absorption contrast as this refraction will enhance visibility of the material interface, with the level of contrast enhancement dependent on the distance between the point of refraction and the scintillator [*Cloetens et al.*, 1996]. This is referred to in the literature as "propagation phase contrast". However, in this application, the contrast enhancement decreases the reconstructed x-ray absorption values of voxels close to grain surfaces because x-rays are bent away from the grain into the liquid, leading to an excess intensity in the liquid immediately adjacent to the grain.

As a result, it was hypothesized that the water voxels in these "refraction zones" belong to a separate population of absorbance values than the rest, and excluding them would decrease the error in the SXCMT-determined [nAg]. The refraction zone was determined to extend 18.11 μm (1.73 voxels) outwards from a grain surface. This refraction zone thickness is based on the data presented in Figure 3.3; voxels that were 18.11 μm distant from a grain surface did not appreciably lower the average SXCMT-determined silver concentration in the 18.11 to 26.17 μm bin and were hence determined to not be within the refraction zone. Discarding all the water voxels within the refraction zone resulted in an improved L-PM calibration curve; the slope increased from 0.78 to 0.81 and the y-intercept error reduced from -0.4g/L to -0.3g/L. It should be noted that the thickness of this refraction zone (18.11 μm) is specific to this experimental setup and is present in both L-PM and IL-PM experiments as it depends on the distance from the sample to the scintillator.

Another source of error is the non-uniform distribution of x-ray intensity throughout the sample coupled with x-ray scattering. A non-uniform vertical distribution of SXCMT-determined nAg concentrations is observed in the L-PM columns (Figure 8.4). This is because the x-ray intensity is highest in the center of the beam and lower near the top and bottom. Note how all four L-PM columns in Figure 8.4 exhibit the same pattern of deviation with height regardless of concentration, underscoring the common source of

A version of this chapter has been published [*Molnar et al.*, 2014]

error in the energy distribution. The higher intensity center x-rays are likely to scatter and interfere with the observed x-ray attenuation nearer the top and bottom of the datasets. The L-O columns exhibit little to no influence of the x-ray intensity variability even though it is constant for all experiments. This is because the L-PM samples are more absorbing due to thicker column walls and the presence of porous media; the higher absorption decreases the total signal received by the CCD, and thus the vertically scattered x-rays exert a larger impact on the SXCMT-determined nAg concentration. Scattering of light within the scintillator can further increase the error. The vertical profile of x-ray intensity also creates a vertical profile in the standard deviation of SXCMT-determined [nAg] (Figure 8.3), with the highest standard deviations near the top and bottom of the dataset where the x-ray intensity is the lowest.

The error associated with intensity distribution and scattering can be, in part, corrected in the pre-processing step of the dataset reconstruction. Increasing the level of the dark current correction for each dataset will increase the average SXCMT-determined [nAg] and will change its vertical distribution, potentially smoothing out the curve observed in Figure 8.4, it will also increase the standard deviation of the dataset's SXCMT-determined [nAg]. However, due to the laborious nature of the trial-and-error approach required for finding the proper level of dark current correction for each dataset, the calibration curve in Figure 3.2 was used instead.

3.3.2   Sources of Uncertainty

All of the sources of refraction/noise discussed above result in significant variation in the SXCMT-determined [nAg] values at the voxel level. Thus, it is essential to treat the voxel-specific values statistically, averaging to attain a reasonable level of confidence in a determined mean concentration that applies to a specific subvolume of the pore space. The number of voxels averaged is directly related to the magnitude of uncertainty, an important consideration for distinguishing between real and artificial nAg distributions. The magnitude of uncertainty for SXCMT-determined [nAg] in the L-PM datasets was investigated for voxels that are averaged spatially (referred to as box sampling) as well as voxels that are randomly distributed throughout the dataset (referred to as random

A version of this chapter has been published [*Molnar et al.*, 2014]

sampling). Box sampling is analogous to considering a range of representative elementary volumes, such as a mean [nAg] for a single pore as well as for different subvolume sizes within a pore.

The above error analysis provided two additional steps in the methodology employed for these subsequent investigations. First, only data between the two horizontal black lines in Figure 8.4 were considered since this corresponded to where the SXCMT-determined [nAg] was considered approximately constant as a function of height. In addition, all voxels to the left of the vertical black line in Figure 3.3 (i.e., within 18.1 μm of the outer surface of a grain voxel) were excluded due to the refraction effect around grains.

Box sampling was conducted by considering a randomly chosen three-dimensional subvolume (dimensions of 3 voxels on all sides) within a pore and averaging the voxel-specific SXCMT-determined [nAg] values within; then the box was expanded (by 1 voxel on all sides) and the average recalculated. This process was continued until the box filled the pore (i.e., until all voxels within the pore were included in the box, excluding the voxels in the refraction zone). This process was repeated for every pore within the subvolume. The results of this box sampling procedure for the 3.6g/L L-PM column is shown in Figure 8.5a. The 99% confidence interval (CI) on the mean $\bar{x}$ as a function of the number of voxels averaged (n), shown by the thick black lines in Figure 8.5a, is given by:

$$\bar{x} \pm 3.0 \left(\frac{\sigma_p}{\sqrt{n}} \right)$$
<div align="right">3.2</div>

where σ_p represents the standard deviation of the population, initially assumed to be equivalent to the standard deviation of all of the pore space voxels in the subvolume and is independent of sample size and type. Under that hypothesis, the standard deviation of each sample (σ_s) is related to σ_p by:

A version of this chapter has been published [*Molnar et al.*, 2014]

$$\sigma_s = \frac{\sigma_p}{\sqrt{n}} \qquad\qquad 3.3$$

However, the σ_p assumption caused Equations 3.2 and 3.3 to significantly underestimate the spread of boxed sample means shown in Figure 8.5a. This discrepancy is due to the fact that σ_p for the boxed samples was not equivalent to the standard deviation of the pore space voxels (3.29g/L); likely due to spatial artifacts introduced by imperfections in the imaging equipment (e.g. scintillator crystal defects) and has already been discussed elsewhere for the APS 13-BM-D beamline [*Rivers et al.*, 2010]. Equation 3.3 was applied to the data shown in Figure 8.5a to back-calculate σ_p over a range of boxed sample sizes using n and σ_s from the data in Figure 8.5a; σ_p was found to be inversely related to n, increasing from 8g/L at n=40,000 voxels up to 20g/L for n=100 voxels.

This process was repeated for random sampling, with voxels being chosen randomly within the pore space with the sample size ranging from 30 to 1,000,000 voxels. The 99% confidence interval for the random sampling data set in Figure 8.5b was back-calculated using the above method and compared to the confidence interval calculated using equations 3.2 and 3.3. It was found that the confidence intervals for the random samples can be approximated using σ_p=3.29g/L regardless of sample size. The smaller σ_p, and confidence interval size, observed for random sampling is attributed to the random distribution of voxels mitigating the influence of the spatial artifacts mentioned earlier.

The size of the back-calculated confidence intervals (i.e., margin of error), presented in Figure 8.6 for box and random sampling, provides a quantitative measure of the uncertainty for the presented SXCMT method, depending on whether random or co-located voxels are employed in the averaging. For example, the values in Figure 3.3, which presented SXCMT-determined [nAg] as a function of distance from the nearest grain, which is equivalent to averaging random voxels, exhibited an uncertainty of $\pm$ 0.03g/L at a distance-to-grain of 104.7 μm (number of voxels averaged = 150,000) and an uncertainty of $\pm$ 0.003g/L at a distance-to-grain of 20.94 μm (number of voxels averaged = 4×10^6). Thus, any concentration differences that exceed these confidence intervals can

A version of this chapter has been published [*Molnar et al.*, 2014]

be attributed to real differences in [nAg] due to physical phenomena and not a result of the method.

The authors are confident that, having accounted for the sources of error and uncertainty within the datasets, it is possible to distinguish between physical phenomenon occurring within the sample of interest and any artifacts introduced by the aforementioned sources of noise and uncertainty.

3.3.3   Silver nanoparticle injection experiment

The effluent breakthrough curve for the IL-PM experiment is presented in Figure 3.4, illustrating how the normalized effluent concentration (C/C_o) changed as a function of injection time. Where C refers to the effluent or SXCMT-determined concentration and C_o refers to the influent concentration or SXCMT-determined concentration from Figure 3.2. After 45 minutes of nAg injection, the source was switched to a non-silver solution and another 30 minutes of water was injected. The average SXCMT-determined [nAg] from each of the collected datasets has been plotted also as a function injection time. The 'improved' L-PM calibration curve has been applied to the determined concentrations in Figure 3.4.

The breakthrough curve generated using the effluent data and the SXCMT-determined data are similar indicating that this method is an acceptable way of tracking quasi-dynamic concentrations of nanoparticles in a porous medium. The difference between the SXCMT-determined and effluent concentrations at the early injection time point (7 minutes) is due to the spatial separation of the two sampling points. The SXCMT imaging window was at the approximate mid-point of the column while the effluent samples were collected at the column's end. The figure reveals, as expected, the nanoparticle solution reached the mid-point of the column prior to reaching the end of the column.

A potential source of uncertainty in IL-PM experiments is diffusion occurring within the sample during imaging. Note that this does not apply to the L-O or L-PM samples because they have an equal concentration everywhere. This is a potential issue for

A version of this chapter has been published [*Molnar et al.*, 2014]

experiments involving transient nAg concentrations. The optimized imaging process required flow in the column to be turned off for at least 40 minutes while the four three-dimensional datasets were obtained (every 7.6 minutes). However, the impact of diffusion on the distribution of SXCMT-determined [nAg] can be minimized by imaging above the silver K-edge prior to below K-edge imaging. The imaging order of energies will determine whether the SXCMT-determined [nAg] distribution will more closely match the pre-diffusion or post-diffusion pore space distribution of nAg.
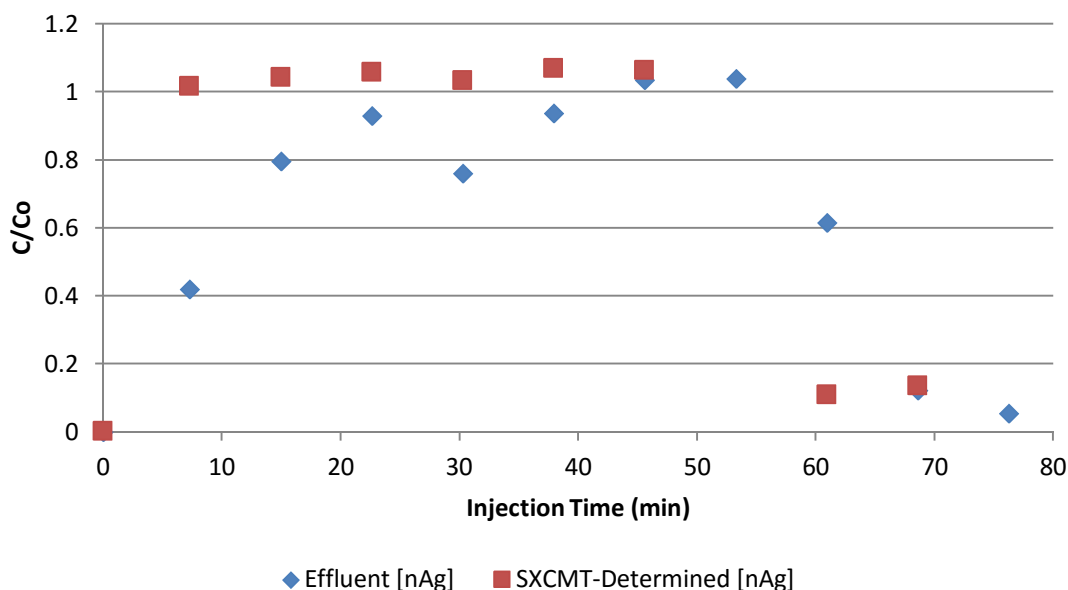
Figure 3.4: Concentration curve for silver nanoparticles exiting the column and for silver nanoparticles within the SXCMT imaging window. The two curves have been plotted so that each point represents the concentration of silver (either from effluent or SXCMT) after a certain amount of time spent injecting liquid into the column. C_o for the effluent curve was determined to be 3.25g/L. For the SXCMT-Determined silver nanoparticle curve, C_o was assumed to be 3.25 g/L and C was determined using the 'improved' L-PM calibration curve.

3.3.4   Range of Suitable Nanomaterials

The range of nanomaterials suitable for quantification with the proposed imaging method is limited by 1) x-ray attenuation of the porous media and column material and 2) the monochromator. Below energies of approximately 22 keV, the L-PM samples attenuate too many x-rays for the high quality reconstruction necessary for the proposed method; this corresponds to the K-edge of Ruthenium [*M.J. Berger et al.*, 2010]. The upper limit

A version of this chapter has been published [*Molnar et al.*, 2014]

of energy possible at the APS 13-BM-D beamline is set by the monochromator which has a limit of 70 keV (Tungsten K-edge [*M.J. Berger et al.*, 2010]). While the upper limit is 70 keV, the scintillator efficiency decreases at higher energies [*Koch et al.*, 1999] and this is expected to increase both the uncertainty and error in the SXCMT-determined concentration values at energies approaching the monochromator limit. It should be noted that this range is specific to the APS 13-BM-D beamline and may be different at different SXCMT stations depending on the imaging equipment. The usable energy range 22 keV to 70keV suggests that the presented method is suitable for imaging a range of nanomaterials such as quantum dots, cesium and palladium nanoparticles.

A version of this chapter has been published [*Molnar et al.*, 2014]

3.4   References

Agbogun, H. M. D., T. A. Al, and E. M. A. Hussein (2013), Three dimensional imaging of porosity and tracer concentration distributions in a dolostone sample during diffusion experiments using X-ray micro-CT, *Journal of Contaminant Hydrology*, *145*(0), 44-53.

Al-Raoush, R. I., and C. S. Willson (2005a), Extraction of physically realistic pore network properties from three-dimensional synchrotron X-ray microtomography images of unconsolidated porous media systems, *Journal of Hydrology*, *300*(1-4), 44-64.

Al-Raoush, R. I., and C. S. Willson (2005b), A pore-scale investigation of a multiphase porous media system, *Journal of Contaminant Hydrology*, *77*(1-2), 67-89.

Baalousha, M., and J. R. Lead (2009), *Overview of Nanoscience in the Environment*, 1-29 pp., John Wiley & Sons, Ltd.

Barnett, H. A., K. Ham, J. T. Scorsone, and L. G. Butler (2010), Synchrotron X-ray Tomography for 3D Chemical Distribution Measurement of a Flame Retardant and Synergist in a Fiberglass-Reinforced Polymer Blend, *Journal of Physical Chemistry B*, *114*(1), 2-9.

Bhattad, P., C. S. Willson, and K. E. Thompson (2010), Segmentation of low-contrast three-phase X-Ray Computed Tomography images of porous media, paper presented at Proceedings of the GeoX 2010: 3rd International Workshop on X-ray CT for Geomaterials, New Orleans, LA.

Bhattad, P., C. S. Willson, and K. E. Thompson (2011), Effect of Network Structure on Characterization and Flow Modeling Using X-ray Micro-Tomography Images of Granular and Fibrous Porous Media, *Transp Porous Med*, *90*(2), 363-391.

Borm, P. J. A., et al. (2006), The potential risks of nanomaterials: a review carried out for ECETOC, *Particle and fibre toxicology*, *3*(1).

Bridge, J. W., S. A. Banwart, and A. L. Heathwaite (2006), Noninvasive quantitative measurement of colloid transport in mesoscale porous media using time lapse fluorescence imaging, *Environ. Sci. Technol.*, *40*(19), 5930-5936.

Chen, C., A. I. Packman, and J.-F. Gaillard (2008), Pore-scale analysis of permeability reduction resulting from colloid deposition, *Geophys. Res. Lett.*, *35*(7), L07404.

Chen, J. Y., C. H. Ko, S. Bhattacharjee, and M. Elimelech (2001), Role of spatial distribution of porous medium surface charge heterogeneity in colloid transport, *Colloid Surf. A-Physicochem. Eng. Asp.*, *191*(1-2), 3-15.

Cloetens, P., R. Barrett, J. Baruchel, J. P. Guigay, and M. Schlenker (1996), Phase objects in synchrotron radiation hard x-ray imaging, *Journal of Physics D-Applied Physics*, *29*(1), 133-146.

El Badawy, A. M., A. Aly Hassan, K. G. Scheckel, M. T. Suidan, and T. M. Tolaymat (2013), Key Factors Controlling the Transport of Silver Nanoparticles in Porous Media, *Environ. Sci. Technol.*

Gaillard, J.-F., C. Chen, S. H. Stonedahl, B. L. T. Lau, D. T. Keane, and A. I. Packman (2007), Imaging of colloidal deposits in granular porous media by X-ray difference micro-tomography, *Geophys. Res. Lett.*, *34*(18), L18404.

A version of this chapter has been published [*Molnar et al.*, 2014]

Giuliani, A., et al. (2011), High-resolution X-ray microtomography for three-dimensional imaging of cardiac progenitor cell homing in infarcted rat hearts, *Journal of Tissue Engineering and Regenerative Medicine*, *5*(8), E168-E178.

Ham, K., H. Jin, R. Al-Raoush, X. G. Xie, C. S. Willson, G. R. Byerly, L. S. Simeral, M. L. Rivers, R. L. Kurtz, and L. G. Butler (2004), Three-dimensional chemical analysis with synchrotron tomography at multiple x-ray energies: Brominated aromatic flame retardant and antimony oxide in polystyrene, *Chemistry of Materials*, *16*(21), 4032-4042.

Iltis, G. C., R. T. Armstrong, D. P. Jansik, B. D. Wood, and D. Wildenschild (2011), Imaging biofilm architecture within porous media using synchrotron-based X-ray computed microtomography, *Water Resour. Res.*, *47*(2).

Jenneson, P. M., and O. Gundogdu (2006), In situ x-ray imaging of nanoparticle agglomeration in fluidized beds, *Applied Physics Letters*, *88*(3), -.

Koch, A., F. Peyrin, P. Heurtier, B. Ferrand, B. Chambaz, W. Ludwig, and M. Couchaud (1999), X-ray camera for computed microtomography of biological samples with micrometer resolution using Lu3Al5O12 and Y3Al5O12 scintillations, in *Medical Imaging 1999: Physics of Medical Imaging, Pts 1 and 2*, edited by J. M. Boone and J. T. Dobbins, pp. 170-179, Spie-Int Soc Optical Engineering, Bellingham.

Lee, N., S. H. Choi, and T. Hyeon (2013), Nano-Sized CT Contrast Agents, *Advanced Materials*, *25*(19), 2641-2660.

Li, X. Q., C. L. Lin, J. D. Miller, and W. P. Johnson (2006), Pore-scale observation of microsphere deposition at grain-to-grain contacts over assemblage-scale porous media domains using X-ray microtomography, *Environ. Sci. Technol.*, *40*(12), 3762-3768.

Li, Z., D. X. Zhang, and X. Li (2012), Tracking colloid transport in real pore structures: Comparisons with correlation equations and experimental observations, *Water Resour. Res.*, *48*(5), W05533.

Liang, Y., S. A. Bradford, J. Simunek, H. Vereecken, and E. Klumpp (2013), Sensitivity of the transport and retention of stabilized silver nanoparticles to physicochemical factors, *Water Research*, *47*(7), 2572-2582.

Long, W., H. Huang, J. Serlemitsos, E. Liu, A. H. Reed, and M. Hilpert (2010), Pore-scale study of the collector efficiency of nanoparticles in packings of nonspherical collectors, *Colloids and Surfaces A: Physicochemical and Engineering Aspects*, *358*(1–3), 163-171.

M.J. Berger, J.H. Hubbell, S.M. Seltzer, J. Chang, J.S. Coursey, R. Sukumar, D.S. Zucker, and K. Olsen (2010), NIST XCOM: Photon Cross Sections Database, edited.

Ma, R., C. m. Levard, S. Marinakos, Y. Cheng, J. Liu, F. M. Michel, G. E. Brown, and G. V. Lowry (2012), Size-Controlled Dissolution of Organic-Coated Silver Nanoparticles, *Environ. Sci. Technol.*, *46*(2).

Marinescu, M., et al. (2013), Synchrotron Radiation X-Ray Phase Micro-computed Tomography as a New Method to Detect Iron Oxide Nanoparticles in the Brain, *Molecular Imaging and Biology*, *15*(5), 552-559.

McNear, D. H., E. Peltier, J. Everhart, R. L. Chaney, S. Sutton, M. Newville, M. Rivers, and D. L. Sparks (2005), Application of Quantitative Fluorescence and Absorption-Edge Computed Microtomography to Image Metal

Compartmentalization in Alyssum murale, *Environ. Sci. Technol.*, *39*(7), 2210-2218.

Molnar, I. L., C. S. Willson, D. M. O'Carroll, M. L. Rivers, and J. I. Gerhard (2014), Method for Obtaining Silver Nanoparticle Concentrations within a Porous Medium via Synchrotron X-ray Computed Microtomography, *Environ. Sci. Technol.*, *48*(2), 1114-1122.

Niazi, J. H., B. I. Sang, Y. S. Kim, and M. B. Gu (2011), Global Gene Response in Saccharomyces cerevisiae Exposed to Silver Nanoparticles, *Applied Biochemistry and Biotechnology*, *164*(8), 1278-1291.

O'Carroll, D., B. Sleep, M. Krol, H. Boparai, and C. Kocur (2013), Nanoscale zero valent iron and bimetallic particles for contaminated site remediation, *Adv. Water Resour.*, *51*(0), 104-122.

Ochiai, N., E. L. Kraft, and J. S. Selker (2006), Methods for colloid transport visualization in pore networks, *Water Resour. Res.*, *42*(12), W12S06.

Oh, W., and W. B. Lindquist (1999), Image thresholding by indicator kriging, *Ieee Transactions on Pattern Analysis and Machine Intelligence*, *21*(7), 590-602.

Pazmino, E. F., H. L. Ma, and W. P. Johnson (2011), Applicability of Colloid Filtration Theory in Size-Distributed, Reduced Porosity, Granular Media in the Absence of Energy Barriers, *Environ. Sci. Technol.*, *45*(24), 10401-10407.

Petosa, A. R., D. P. Jaisi, I. R. Quevedo, M. Elimelech, and N. Tufenkji (2010), Aggregation and Deposition of Engineered Nanomaterials in Aquatic Environments: Role of Physicochemical Interactions, *Environ. Sci. Technol.*, *44*(17), 6532-6549.

Phenrat, T., A. Cihan, H. J. Kim, M. Mital, T. Illangasekare, and G. V. Lowry (2010), Transport and Deposition of Polymer-Modified Fe-0 Nanoparticles in 2-D Heterogeneous Porous Media: Effects of Particle Concentration, Fe-0 Content, and Coatings, *Environ. Sci. Technol.*, *44*(23), 9086-9093.

Piccapietra, F., L. Sigg, and R. Behra (2012), Colloidal Stability of Carbonate-Coated Silver Nanoparticles in Synthetic and Natural Freshwater, *Environ. Sci. Technol.*, *46*(2).

Ramanan, B., W. M. Holmes, W. T. Sloan, and V. R. Phoenix (2012), Investigation of Nanoparticle Transport Inside Coarse-Grained Geological Media Using Magnetic Resonance Imaging, *Environ. Sci. Technol.*, *46*(1).

Rivers, M. L., D. T. Citron, and Y. B. Wang (2010), Recent developments in computed tomography at GSECARS, in *Developments in X-Ray Tomography Vii*, edited by S. R. Stock, Spie-Int Soc Optical Engineering, Bellingham.

Russo, A. E., M. Narter, and M. L. Brusseau (2009), Characterizing Pore-Scale Dissolution of Organic Immiscible Liquid in a Poorly-Sorted Natural Porous Medium, *Environ. Sci. Technol.*, *43*(15), 5671-5678.

Sagee, O., I. Dror, and B. Berkowitz (2012), Transport of silver nanoparticles (AgNPs) in soil, *Chemosphere*, *88*(5), 670-675.

Schnaar, G., and M. L. Brusseau (2006), Characterizing pore-scale configuration of organic immiscible liquid in multiphase systems with synchrotron X-ray microtomography, *Vadose Zone J.*, *5*(2), 641-648.

Shang, J. Y., C. X. Liu, Z. M. Wang, H. Wu, K. K. Zhu, J. A. Li, and J. Liu (2010), In-Situ Measurements of Engineered Nanoporous Particle Transport in Saturated Porous Media, *Environ. Sci. Technol.*, *44*(21), 8190-8195.

Shilo, M., T. Reuveni, M. Motiei, and R. Popovtzer (2012), Nanoparticles as computed tomography contrast agents: current status and future perspectives, *Nanomedicine*, *7*(2), 257-269.

Song, Y. G., X. Li, L. Y. Wang, Y. Rojanasakul, V. Castranova, H. L. Li, and J. Ma (2011), Nanomaterials in Humans: Identification, Characteristics, and Potential Damage, *Toxicologic Pathology*, *39*(5), 841-849.

Stone, V., M. J. D. Clift, and H. Johnston (2009), *Human Toxicology and Effects of Nanoparticles*, 357-388 pp., John Wiley & Sons, Ltd.

Sycheva, L. P., V. S. Zhurkov, V. V. Iurchenko, N. O. Daugel-Dauge, M. A. Kovalenko, E. K. Krivtsova, and A. D. Durnev (2011), Investigation of genotoxic and cytotoxic effects of micro- and nanosized titanium dioxide in six organs of mice in vivo, *Mutation Research-Genetic Toxicology and Environmental Mutagenesis*, *726*(1), 8-14.

Thio, B. J. R., M. Montes, M. A. E. m. Mahmoud, D.-W. Lee, D. Zhou, and A. A. Keller (2012), Mobility of Capped Silver Nanoparticles under Environmentally Relevant Conditions, *Environ. Sci. Technol.*, *46*(13).

Thompson, K. E., C. S. Willson, and W. L. Zhang (2006), Quantitative computer reconstruction of particulate materials from microtomography images, *Powder Technology*, *163*(3), 169-182.

Thompson, K. E., C. S. Willson, C. D. White, S. L. Nyman, J. P. Bhattacharya, and A. H. Reed (2008), Application of a new grain-based reconstruction algorithm to microtomography images for quantitative characterization and flow modeling, *Spe Journal*, *13*(2), 164-176.

Torkzaban, S., J. M. Wan, T. K. Tokunaga, and S. A. Bradford (2012), Impacts of bridging complexation on the transport of surface-modified nanoparticles in saturated sand, *Journal of Contaminant Hydrology*, *136*, 86-95.

Torrente, Y., A. Gavina, A. Belicchi, F. Fiori, V. Komlev, N. Bresolin, and F. Rustichelli (2006), High-resolution X-ray microtomography for three-dimensional visualization of human stem cell muscle homing, *Febs Letters*, *580*(24), 5759-5764.

Wang, W., S. Efrima, and O. Regev (1998), Directing oleate stabilized nanosized silver colloids into organic phases, *Langmuir*, *14*(3), 602-610.

A version of this chapter has been published [*Molnar et al.*, 2014]

Chapter 4

4   The impact of immobile zones on the transport and retention of nanoparticles in porous media

4.1   Introduction

With nanotechnology becoming a $1 trillion industry [*Baalousha and Lead*, 2009], risk assessments associated with transport to groundwater wells are needed when nanoparticles are accidentally released into the environment. Also, engineered nanoparticles, such as nano-Zero Valent Iron (nZVI), are being deliberately injected at contaminated sites to remediate chlorinated solvent source zones [*Bennett et al.*, 2010; *Kocur et al.*, 2014; *O'Carroll et al.*, 2013]. Whether for assessing a health risk or designing an optimal remediation strategy, accurate tools for predicting subsurface nanoparticle transport are required.

Colloid Filtration Theory (CFT), commonly used to predict nanoparticle transport through a porous medium *[El Badawy et al., 2013; Jaisi and Elimelech, 2009; Krol et al., 2013; Lecoanet et al., 2004; Lin et al., 2011; Liu et al., 2009a; Mattison et al., 2011; Phenrat et al., 2010a; Phenrat et al., 2010b; Ryan et al., 2002; Taghavy et al., 2013; Tong and Johnson, 2006]*, often over predicts nanoparticle retention rates in favorable deposition conditions [*Long and Hilpert*, 2009; *Nelson and Ginn*, 2011; *Tong and Johnson*, 2006] despite accurately predicting retention rates for micron-sized colloids in similar conditions [*Nelson and Ginn*, 2011; *Tong and Johnson*, 2006]. Favorable deposition conditions refer to scenarios where adhesive forces dominate colloid-collector interactions and there is no repulsive energy barrier hindering deposition. Favourable conditions apply to some environmental scenarios, such as silver nanoparticles and iron-oxide soils [*Lin et al.*, 2011], where the nanoparticles and soil surfaces have oppositely charged surfaces. Over-predicting retention rates – i.e., predicting more colloids retained than occurs in a given time or distance from the injection point - in favorable conditions

A version of this chapter has been published [*Molnar et al.*, 2015]

can lead to under-predicting risk due to accidental nanoparticle release and ineffective remediation scheme design.

While the over-predicted retention rates were observed for favorable conditions, it is difficult to ascertain whether the causes of over-prediction in favorable conditions would also influence retention rates in unfavorable conditions. Unfavorable deposition conditions refer to scenarios where electrostatic forces create a repulsive energy barrier that hinders colloid deposition. Unfavorable conditions apply in many environmental scenarios: for example, between silver nanoparticles and quartz sands, where nanoparticles and collectors both possess negatively charged surfaces [*El Badawy et al.*, 2013]. Nanoparticle attachment will still occur in unfavorable deposition conditions, although fewer nanoparticles will attach than in favorable conditions [*Petosa et al.*, 2010].

CFT predicts retention in favorable conditions using 'contact efficiency' (η), the fraction of colloids approaching a collector that will contact and subsequently attach to the collector by assuming that every contact event results in attachment. However, CFT requires a fitted parameter, termed 'attachment efficiency' (α), to adjust the prediction for unfavorable conditions. Attachment efficiency is defined as the fraction of colloid-collector contact events that result in attachment and is typically determined by fitting a CFT-based model to experimental results. Fitting attachment efficiency to experimental results effectively masks any over-prediction of η for unfavorable systems. However it is hypothesized that the sources of η over-prediction in favorable conditions would also impact η in unfavorable conditions and would interfere with attempts at developing predictive transport and retention models for unfavorable conditions.

Over-predicted nanoparticle retention rates have been hypothesized to be due to CFT's reliance on oversimplified grain and pore geometry, with these geometries unable to account for complex nanoparticle/fluid/collector interactions in a realistic three-dimensional pore space [*Boccardo et al.*, 2014; *Long and Hilpert*, 2009; *Long et al.*, 2010]. The original CFT formulation considered colloids approaching a single, isolated sphere surrounded by an infinite fluid [*Yao et al.*, 1971]. This collector is considered to

A version of this chapter has been published [*Molnar et al.*, 2015]

be independent of any neighboring collectors; i.e., there are no collector-collector contact points and the velocity and concentration of colloids approaching the collector is assumed to be unaffected by the presence of other collectors. More recent CFT models [*Nelson and Ginn*, 2011; *Rajagopalan and Tien*, 1976; *Tufenkji and Elimelech*, 2004a] have replaced the isolated sphere geometry with a Happel Sphere-in-cell geometry [*Happel*, 1958] where the thickness of the fluid envelope is not infinite but is defined by the porosity of the porous medium. This finite fluid envelope thickness allows Happel-based models to account for the effects of flow constriction from nearby collectors. However the Happel Sphere-in-cell geometry does not consider the influence of grain-grain contacts.

A number of studies have employed Happel and isolated-sphere geometries to create η correlation equations for a wide range of colloid sizes and flow conditions [*Nelson and Ginn*, 2011; *Rajagopalan and Tien*, 1976; *Tufenkji and Elimelech*, 2004a; *Yao et al.*, 1971]. Despite being derived from simple single-collector geometries, the correlation equation-predicted retention rates are generally in excellent agreement with experimentally observed retention rates for micron-sized colloids in favorable deposition conditions. However, as mentioned above, these η correlation equations over predict nanoparticle retention rates relative to experimental observations [*Nelson and Ginn*, 2011; *Tong and Johnson*, 2006]. Recently, other CFT models have been proposed that employ non-standard geometries such as hemisphere-in-cell [*Ma et al.*, 2009] and random packings of spherical [*Long and Hilpert*, 2009]and non-spherical [*Long et al.*, 2010] collectors. These non-standard CFT models, while maintaining good agreement with experimentally observed retention rates for micron-sized colloids, still generally over predict η for nanoparticle transport [*Nelson and Ginn*, 2011].

Nanoparticles differ from micron-sized colloids in that their particle diameters are orders of magnitude smaller and possess higher surface areas per unit mass. Few studies have attempted to understand why these differences between nanoparticles and micron-sized colloids lead to CFT's over-predicted nanoparticle retention rates. In addition, there have also been few studies attempting to understand how the pore-space near collector-collector contact points contributes to predicted retention rates. This study will test the

A version of this chapter has been published [*Molnar et al.*, 2015]

hypothesis that one important component of over predicted CFT-based nanoparticle retention rates are flow regimes that are much more complicated than that represented by a simple isolated sphere or Happel sphere approach. Specifically, immobile zones (areas of low flow) may be dominating the rate of diffusive flux towards the collectors' surfaces and these zones may play a much more significant role for nanoparticles than larger colloids. The hypothesis will be tested by examining nanoparticle elution at the column-scale and nanoparticle concentration distributions and gradients at the pore-scale; relevant literature is reviewed below.

4.1.1 Favorable vs. unfavorable deposition: column scale elution behaviour

A general CFT model using a Happel Sphere-in-cell geometry is illustrated in Figure 4.1a. The model in Figure 4.1a is only valid for favorable deposition scenarios as CFT models are currently not able to predict retention in unfavorable deposition scenarios without the fitting parameter 'α' [*Nelson and Ginn*, 2011]. The CFT model in Figure 4.1a has been upscaled to consider two collectors to illustrate how traditional CFT considers each collector isolated from other collectors by not incorporating grain-grain contacts (but including flow constriction). The velocity fields, based on Stokes flow around the Happel spheres in Figure 4.1a, are shown by the red velocity vectors. Due to the assumption of isolated collectors, the flow regime around each collector in Figure 4.1a is not affected by the presence of the other collector.

CFT models consider colloid-collector contact events arising from interception (η_I), gravitation (η_G) and diffusion (η_D). While diffusion is relatively minor for micron-sized colloids [*Yao et al.*, 1971], the dominant mechanism for nanoparticle-collector contact is diffusion arising from Brownian motion (i.e., $\eta_D \gg \eta_I, \eta_G$)[*Yao et al.*, 1971]. The rate of diffusion towards the collector is a function of the concentration gradient, arising from the boundary conditions defined in Figure 4.1a ($C_b = C_1$, $C_{as} = 0$), and the flow regime around the collector.

A more realistic porous medium may have a substantially different flow regime than the CFT model presented in Figure 4.1A due to the presence of collector-collector contact

A version of this chapter has been published [*Molnar et al.*, 2015]

points. Figure 4.1B presents a more realistic conceptual model of two collectors that are contacting each other (i.e., no assumption of isolation). A comparison of the conceptual models in Figures 4.1A and 4.1B illustrates potential reasons for discrepancies between experimental observations and CFT predictions. The traditional CFT model in Figure 4.1A does not account for the presence of the grain-grain contact point, whereas Figure 4.1B illustrates how these contact points may yield zones of circulating flow [*Torkzaban et al.*, 2008] or immobile zones with low or no flow [*Li et al.*, 2010a; *Li et al.*, 2010b; 2012]. Immobile zones may be particularly important for Brownian particles (i.e., nanoparticles) with implications for both retention and elution (i.e., flushing particles out of a porous medium).

In favorable deposition scenarios, CFT-based advective-dispersive transport models predict elution as a sharp decrease in concentration with time. This is typically ascribed to CFT's assumption of irreversible attachment as colloids are attached in the primary energy well and will not be released under typical groundwater pore water velocities [*Bergendahl and Grasso*, 2000].

A version of this chapter has been published [*Molnar et al.*, 2015]

(A) <u>CFT Model without Grain-Grain Contact</u> (B) <u>CFT Model with Grain-Grain Contact</u>

Potential immobile zone

r

b

a_s

$C_{as} = 0$

$C_b = C_2$

Flow = $v_o C_2 A_1$

A_1

r

b

a_s

$C_{as} = 0$

$C_b = C_1$

Flow = $v_o C_1 A_1$

A_1

a_s

$C_{as} = 0$

a_s

$C_{as} = 0$

Flow = $v_o C_1 A_1$

A_1
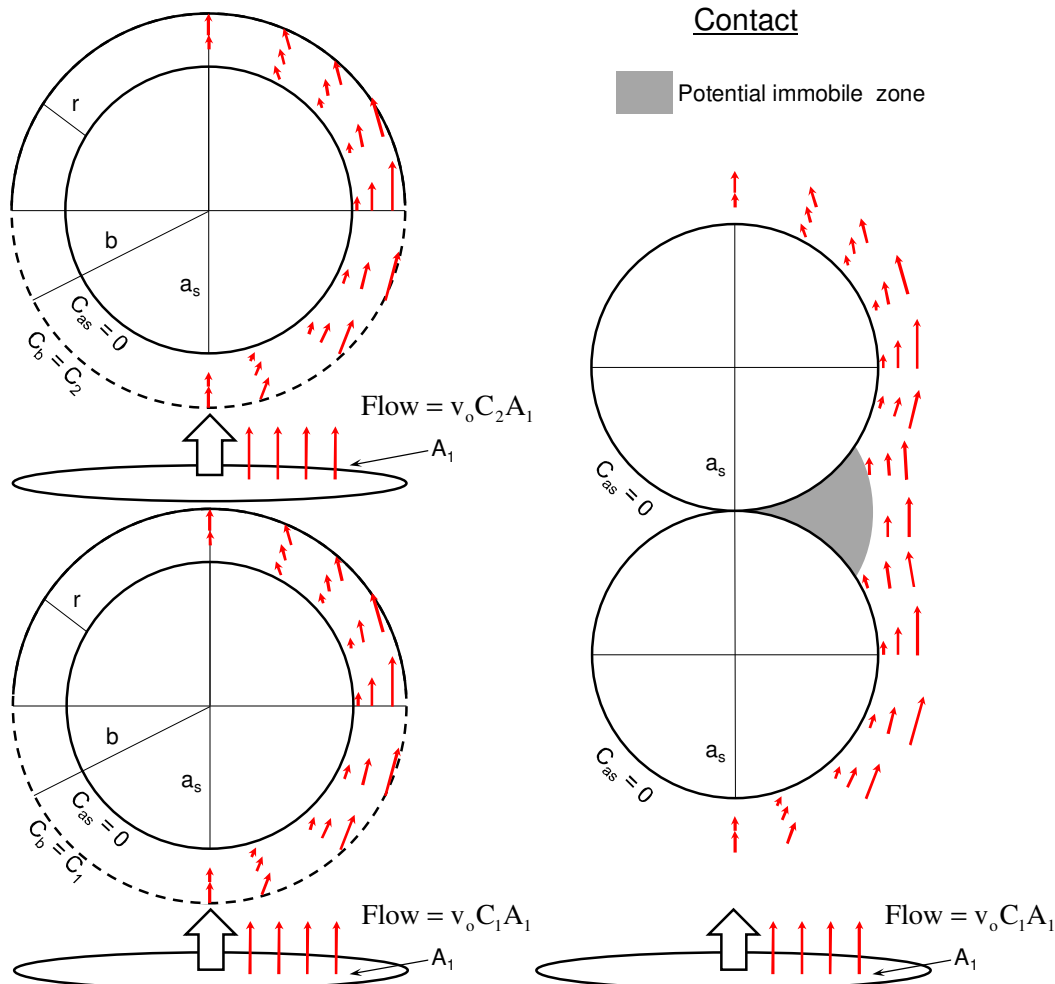
Figure 4.1A: Visualization of a traditional single-collector colloid filtration theory model upscaled to consider two collectors. The traditional upscaled CFT model considers each collector to not have any grain-grain contacts, such that is the flow field around a collector is not influenced by other contacting collectors. An approximate visualization of Stokes flow around the two isolated collectors is depicted by red arrows on the right side of the model. The red arrows represent a velocity field with length of the arrows illustrating velocity magnitude. The CFT model is utilizing the Happel sphere-in-cell geometry and there is no energy barrier to deposition (i.e., favorable conditions). The radius of the fluid envelope is given by b, as is the radius of the collector, r is the thickness of the fluid envelope and C_b and C_{as} are boundary conditions applied by CFT models. The thickness of the fluid envelope (r) has been exaggerated for ease of interpretation. The velocity of the approaching fluid is given by vo, C_1 and C_2 are the concentrations of colloids approaching the first and second collectors and A1 is the projected area of the collector + fluid envelope.

Figure 4.1B: Visualization of two collectors identical to the traditional CFT model in Figure 4.1A but with collector-collector contacts. In this scenario, the flow field is influenced by the presence of the extra collector which may yield flow phenomena such as immobile zones near grain-grain contacts (gray shaded region). An approximate visualization of flow around the two collectors is depicted by red arrows on the right side of the model.

A version of this chapter has been published [*Molnar et al.*, 2015]

In the case of micron-sized colloids there is both experimental and modeling evidence that extended tailing (i.e., release of colloids leading to a gradual decline in eluted concentrations) can occur in unfavorable deposition scenarios [*Cortis et al.*, 2006; *Johnson and Hilpert*, 2013; *Landkamer et al.*, 2013; *Li et al.*, 2004; *Li et al.*, 2005] but not favorable conditions[*Li et al.*, 2004; *Li et al.*, 2005]. Extended tailing behaviour has been attributed to colloids re-entraining into the bulk pore space from the secondary minimum (i.e., reversible retention) [*Johnson and Hilpert*, 2013; *Landkamer et al.*, 2013; *Li et al.*, 2005] due to hydrodynamic forces (e.g., torque) acting on the colloids that can cause rolling or skimming of the colloids across the secondary minimum [*Bradford et al.*, 2011; *Li et al.*, 2005; *Torkzaban et al.*, 2007; *Torkzaban et al.*, 2008]. It has also recently been shown that perturbations in ionic strength and flow rate may release colloids from the primary minimum [*Pazmino et al.*, 2014a]. A study by Cortis et al. [2006] examined extended tailing of C. Parvum oocysts out of a uniform, homogeneous sand over several thousand pore volumes and, by fitting the results to a continuous time random walk (CTRW) model, identified that both complex pore geometries and physicochemical heterogeneities (i.e., reversible and irreversible retention sites) contributed to tailing. Cortis et al. [2006] concluded that the physicochemical heterogeneities (i.e., reversible/irreversible retention) contributed more to oocyst tailing than pore geometry.

Additionally, pore-scale modeling studies have shown that immobile zones and recirculating flow zones can act as temporary hydraulic retention mechanisms in unfavorable scenarios, contributing significantly to overall retention [*Li et al.*, 2012; *Petosa et al.*, 2010; *Torkzaban et al.*, 2008] and lead to tailing [*Li et al.*, 2010a; *Li et al.*, 2010b; 2012; *Torkzaban et al.*, 2008]. The micron-sized colloids in the pore-scale modeling studies predominantly entered the immobile zones via translation along the secondary energy minimum[*Li et al.*, 2010a; *Li et al.*, 2012]. In favorable conditions (no secondary energy minimum) temporary hydraulic retention and tailing was minimal [*Li et al.*, 2010a; *Li et al.*, 2012]. The studies noted that direct mass transfer between the mobile/immobile porosities, which would theoretically yield tailing regardless of favorable/unfavorable conditions, was relatively minor and unlikely to lead to tailing in favorable scenarios [*Li et al.*, 2010a; *Li et al.*, 2012].

A version of this chapter has been published [*Molnar et al.*, 2015]

The finding that tailing is unlikely to occur in favorable conditions likely arises due to almost exclusive consideration of micron-sized colloids which, as discussed above, require a secondary minimum to enter immobile zones in significant quantities. Diffusive mass transfer between mobile and immobile zones, a mechanism that exists in both favorable and unfavorable conditions relies on Brownian motion to transport colloids into the immobile zone. The limited Brownian motion of micron-sized colloids suggests that they are unlikely to diffuse into immobile zones in sufficient quantity to yield tailing. The pore-scale modeling studies mentioned previously [*Li et al.*, 2010a; *Li et al.*, 2012] noted that diffusive mass transfer between mobile/immobile porosities was not a significant contributor for hydraulic retention of larger colloids. However, nanoparticles, with greater Brownian motion, are more likely to have significant diffusive mass transfer between mobile and immobile porosity. If a sufficient quantity of nanoparticles diffused into immobile zones, the differences in tailing behaviour between favorable and unfavorable conditions would not be significant.

In the case of solutes, pore-scale transport modeling studies have noted that extended tailing can arise from diffusive mass transfer between mobile and immobile zones [*Scheibe et al.*, 2013] and from vortices near grain-grain contacts [*Cardenas*, 2008]. While nanoparticle diffusive flux is less than solute molecules, the results of Scheibe et al. [2013] suggest that diffusive transfer between mobile/immobile zones could be significant for nanoparticles.

Extended solute tailing has been observed experimentally from homogenous media such as glass beads and uniform sand packs [*Cortis et al.*, 2004; *Cortis et al.*, 2006] and have been attributed to heterogeneities present in the pore-scale geometry which yield immobile and mobile regions. Other pore-scale solute transport studies, both modeling and experimental, have examined the relationships between heterogeneous pore space geometry, velocity distributions and anomalous transport behaviour (i.e., behaviour not describable by the classic advective-dispersive equation) [*Bijeljic et al.*, 2011; *Bijeljic et al.*, 2013a; *Bijeljic et al.*, 2013b; *Scheven et al.*, 2005]. These studies have observed that the complexity of the pore space – with glass beads and uniform sand packs being less complex, and media such as sandstones and carbonates being more complex – is directly

A version of this chapter has been published [*Molnar et al.*, 2015]

linked to increasingly anomalous transport behaviour, large stagnant concentrations and extended tailing. Other studies have also examined how the aforementioned heterogeneities in the pore geometry can influence reactive transport [*Edery et al.*, 2013].

Solute transport studies often employ a continuous time random walk (CTRW) approach to modeling the discussed anomalous behaviour such as early breakthrough and extended tailing [*Berkowitz et al.*, 2006; *Edery et al.*, 2014]. While the CTRW approach has also been extended to colloid transport [*Cortis et al.*, 2006], CFT combined with variations of the advective-dispersive equation remain the most common approach to modeling colloid transport[*Bradford et al.*, 2009; *El Badawy et al.*, 2013; *Jaisi and Elimelech*, 2009; *Krol et al.*, 2013; *Lecoanet et al.*, 2004; *Lin et al.*, 2011; *Liu et al.*, 2009a; *Mattison et al.*, 2011; *Phenrat et al.*, 2010a; *Phenrat et al.*, 2010b; *Ryan et al.*, 2002; *Taghavy et al.*, 2013; *Tong and Johnson*, 2006; *Tufenkji and Elimelech*, 2004b; *Tufenkji*, 2007]. This is likely due to CFT's use of physically-based force/torque balances to describe colloid attachment onto the collector surface. The force/torque balance approach is powerful as the generalized correlation equations derived from these balances can accurately predict retention rates. However, quantitatively describing elution and tailing from the force/torque balances remains a challenge for even the well-studied micron-sized colloids discussed earlier.

The mechanisms governing the elution of nano-sized colloids are poorly understood and have received little attention in the colloid transport literature. It is common for nanoparticle transport studies to only present breakthrough and to not discuss elution behaviour [*El Badawy et al.*, 2013; *Ko and Chen*, 2000; *Kocur et al.*, 2013; *Lecoanet and Wiesner*, 2004; *Lin et al.*, 2011]. One study does present evidence of extended tailing during nanoparticle elution [*Uyusur et al.*, 2010], with tailing observed in both saturated and unsaturated porous media and in both favorable and unfavorable deposition conditions, but did not discuss the tailing in depth. As such, more work is needed to assess the impact of more realistic flow regimes on nanoparticle retention and elution.

A version of this chapter has been published [*Molnar et al.*, 2015]

4.1.2 Favorable vs. unfavorable deposition: pore-scale concentration gradients

An improved understanding of pore scale nanoparticle transport and retention phenomena will ultimately improve the ability to predict larger scale nanoparticle transport. As discussed, Figure 4.1a is commonly used as a conceptual model for the derivation of theoretical and pore scale modeling studies. Under both favorable and unfavorable conditions, the dominant mechanism transporting nanoparticles to the collector surface is diffusion arising from Brownian motion (i.e., η_D (diffusion) >> η_I (interception), η_G(gravitation))[*Yao et al.*, 1971]. As such, this discussion will focus on diffusion. The boundary at the edge of the fluid envelope in Figure 4.1a is assumed to have concentration C_1 (i.e., $C_b = C_1$), the concentration in an upstream area where the flow is unaffected by the collector [*Yao et al.*, 1971]. For favorable conditions it is assumed that the surface at the collector boundary is a perfect sink. The rate of diffusion towards the collector is a function of the concentration gradient between the fluid envelope boundary ($C_b = C_1$) and collector surface ($C_{as} = 0$) and the flow regime around the collector.

As discussed previously, the model in Figure 4.1a is only valid for favorable deposition scenarios as CFT models are not currently able to predict retention in unfavorable deposition scenarios [*Nelson and Ginn*, 2011]. A considerable volume of literature has attempted to understand the mechanisms of colloid retention in unfavorable conditions. These mechanisms include: deposition into a secondary energy minimum [*Hahn and O'Melia*, 2004; *Kuznar and Elimelech*, 2007; *Qiu et al.*, 2012; *Shen et al.*, 2007; *Tufenkji and Elimelech*, 2005], surface roughness [*Saiers and Ryan*, 2005], geochemical heterogeneities that create localized zones of unfavorable/favorable deposition conditions [*Johnson et al.*, 1996; *Johnson et al.*, 2010; *Lin et al.*, 2011; *Liu et al.*, 2009b; *Pazmino et al.*, 2014b; *Tufenkji and Elimelech*, 2005], straining at pore-throats [*Bradford et al.*, 2004; *Bradford et al.*, 2006], and adsorption site-blocking [*Cullen et al.*, 2010; *Johnson and Elimelech*, 1995; *Li et al.*, 2008; *Liu et al.*, 2009a]. These mechanisms likely yield a C_{as} boundary condition greater than 0 (i.e., $C_1 > C_{as} > 0$). Because $C_{as} > 0$ in unfavorable scenarios, the concentration gradient driving diffusive flux towards the surface should be smaller than the gradient in a favorable deposition scenario.

A version of this chapter has been published [*Molnar et al.*, 2015]

The concentration gradient in the CFT Happel sphere model is given as $(C_b - C_{as})/r$ where r is the thickness of the fluid envelope. With immobile zones, r depends on the distance from the edge of the immobile porosity ($C_b = C_1$) to the collector surface ($C_{as} = 0$ in favorable conditions). If the immobile zone is wider than the Happel fluid envelope (i.e., $r_{immobile} > r_{Happel}$) then concentration gradients may be significantly lower than predicted by the Happel sphere model. These smaller gradients in the immobile porosity may dominate the overall diffusive flux towards the collectors' surfaces and result in unexpectedly low values of nanoparticle retention on the collectors. In this scenario, where immobile zones are controlling the diffusive flux, the concentration gradients would depend only upon the geometry of the immobile zones and would be independent of favorable/unfavorable conditions.

In this study, nanoparticle behaviour at the column- and pore-scale will be examined to investigate nanoparticle retention mechanisms. Specifically, the relative importance of immobile zones on nanoparticle retention and elution are explored with a variety of complementary datasets. At the column scale, elution behaviour for both favorable (irreversible attachment, iron oxide-coated sand and nanosilver) and unfavorable conditions (reversible retention, quartz sand with nanosilver) is examined in transport experiments. Different elution behaviour in the favorable/irreversible and unfavorable/reversible retention systems would suggest that nanoparticle interaction with the collector surfaces dominates elution behaviour; however similar tailing behaviours in both systems would suggest that temporary hydraulic retention in immobile zones (i.e., retention purely due to hydraulics with no nanoparticle-surface interaction) controls the elution behaviour instead. At the pore scale, nanoparticle concentration distributions in the pore space are determined from reconstructed synchrotron x-ray computed microtomography (SXCMT) datasets of the same column experiments. Using the pore space reconstructions, the potential occurrence of immobile zones is mapped using computational fluid dynamics modelling. Furthermore, the nanoparticle concentration in the pore space is mapped as a function of distance to grain-grain contact points. Also quantified is the evolving mean concentration gradient from the pore centers towards the grain. Finally, results in uniform sand are compared to well-graded sand in order to

A version of this chapter has been published [*Molnar et al.*, 2015]

consider the influence of pore size distribution on these metrics. Overall, this represents a unique exploration of the dominant mechanisms affecting nanoparticle retention in real porous media systems, revealing where CFT requires further development in this context.

4.2   Materials and Methods

4.2.1   Silver Nanoparticle Synthesis

Silver nanoparticles were synthesized at the GeoSoilEnviro Center of Advanced Radiation Sources (GSECARS) wet lab the day before the allotted 24-hour SXCMT beamtime. The details of the synthesis procedure are presented elsewhere [*Molnar et al.*, 2014; *Wang et al.*, 1998]. Briefly, silver nitrate (0.1N, Alfa Aesar) was reduced by chemical reduction with sodium borohydride (Granulated, 97+%, Alfa Aesar) and electrosterically stabilized with a 1% solution of sodium carboxymethyl cellulose (CMC90k, Aldrich Chemistry). It was demonstrated that, using this method, more than 97% of the silver is in nanoparticle form [*Molnar et al.*, 2014]. The nanoparticles were synthesized in a single batch that was continuously stirred. A subsample of nanoparticle solution was extracted from the batch at the start of each experiment and remained in an air-tight plastic syringe for the duration of the experiment (approximately 6 hours per experiment). The pH and ionic strength of the solution were 8.4 and 120 mM, respectively. The resulting nanoparticles were spherical (Figure 9.1, supplementary information), with a hydrodynamic diameter of 29.8 nm and zeta potential of -27.97 mV (ZetaPlus Zeta Potential Analyzer, Brookhaven). The solution was very stable and no aggregation or settling was observed between synthesis, beamtime and shipment back to the parent lab for analysis.

4.2.2   Column Experiments

The quartz sand (Unimin Accusand) used in all experiments was rinsed with concentrated nitric acid (Environmental grade, Alfa Aesar) to remove impurities, then rinsed with deionised water and dried overnight. Following sieving to achieve the desired grain size distribution, uniform or well graded, approximately half of the uniform quartz sand was treated to achieve an iron oxide coating consisting mostly of hematite and goethite [*Molnar et al.*, 2011]. Three columns were prepared by wet-packing the sands into small

A version of this chapter has been published [*Molnar et al.*, 2015]

aluminum columns (ID: 5.6 mm, length: 5 cm). The sand was packed into a 1% CMC90k aqueous suspension (no nAg present) controlled to the same pH and ionic strength as the synthesized nAg solution with NaOH (10N, Fisher Scientific) and $NaNO_3$ (Certified A.C.S, Fisher Scientific). Characteristics of the packed columns are listed in Table 4.1. Porosity of the columns was experimentally determined by measuring the volume of each column, weighing the mass of the sand added to each column and measuring the specific gravity of the sands (2.65 g/cm^3).

The setup for the column experiments is shown in Figure 9.2 in the Appendices. After securely mounting the column in the imaging hutch, a pre-injection image was recorded (i.e., 0 pore volume image). The volume of column imaged, referred to as the SXCMT imaging window, was at the approximate mid-point of the column. This SXCMT imaging window height was consistent across all 3 experiments and did not change during the injection/elution process for each column. Following the pre-injection image, the synthesized nAg solution was injected into the columns at a rate of 0.11 mL/min with a syringe pump. The columns were imaged after injecting 0.25, 0.5, 0.75, 1 and 2 pore volumes (PV) of nAg solution (except the iron oxide column was not imaged at 0.25 PV). A total of 3 PV of nAg solution was injected into each column, after which the injection was switched to a 1% CMC90k solution containing no silver nanoparticles but the same pH and ionic strength to examine the elution behaviour of nAg from the columns. The columns were imaged again after 1 PV of nAg elution. The uniform quartz sand was imaged an additional time following a 2nd PV of elution. The columns were then removed from the imaging hutch and elution continued for another 5 to 7 PV's.

A version of this chapter has been published [*Molnar et al.*, 2015]

Table 4.1: Overview of soil and hydraulic properties of the column experiments

	Uniform Quartz	Uniform Iron Oxide	Well Graded Quartz
Experiment #	1	3	2
Grain size (μm)	420 - 600	420 - 600	215 - 853
Porosity	33%	31%	29%
Pore volume	0.40 mL	0.38 mL	0.35 mL
Pore water velocity	1.38 cm/min	1.47 cm/min	1.55 cm/min
C_o average	2.6 g/L	2.4 g/L	2.0 g/L
nAg volume injected	3 PV	3 PV	3 PV
nAg mass injected	2.8 mg	2.7 mg	2.1 mg
nAg retained (mg Ag/g sand)	0.01 mg/g	0.2 mg/g	0.0073 mg/g

After each injection interval was completed (e.g., 0 - 0.25 PV, 0.25 - 0.5 PV etc.) the syringe pump was stopped and all valves were closed to prepare for imaging. Each SXCMT image required approximately 40 minutes of imaging time along with an additional 3 – 4 minutes for imaging hutch safety procedures. As shown in Table 4.1, an equal volume of nAg solution was injected into each of the 3 columns, although the injected nAg concentration, and therefore injected Ag mass, differed slightly. The discrepancy was most likely due to minor settling/re-suspension behavior in the stock nAg solution over the 24 hour experiment. The influent nAg was sampled pre- and post-injection to quantify any temporal changes in influent concentration and all of the effluent was collected in 0.5 PV intervals. The influent concentration in the pre- and post-injection samples differed by less than 7%, indicating excellent nAg stability. The collected samples were sent back to the parent laboratory for analysis.

A number of tracer experiments were also conducted through SXCMT-columns for each of the sands employed in this study including replicates: 3 for the uniform quartz, 2 for the uniform iron oxide and 2 for the well graded quartz. The columns were emptied, cleaned and re-packed between each repetition for each sand type. A pulse of

A version of this chapter has been published [*Molnar et al.*, 2015]

approximately 3 pore volumes of 1mM sodium fluorescein was injected into the SXCMT columns and eluted with a non-tracer solution for an additional number of pore volumes. The sodium fluorescein was quantified by UV/Vis spectroscopy with a peak absorbance at 488nm. Mass recovery from the tracer tests was excellent (96% - 100%) considering the very small volumes sampled from the effluent (0.08 – 0.3mL). The experiments were conducted under conditions identical to the nAg transport tests, but were not imaged by SXCMT. The experimental conditions identical to the nAg transport tests included: stagnant periods representing SXCMT imaging time, 1% CMC90k solution in the tracer and non-tracer fluids and identical mass flow rates (0.11 mL/min). The porosities and pore volumes of the tracer columns were also very similar to their corresponding nAg columns. The results of the tracer test breakthrough curves are presented in Figure 9.3 in the supplementary information. Simple batch experiments were also performed, in which fluorescein dye solution was mixed with quartz and iron oxide sands for a period of time equivalent to an SXCMT experiment; the excellent mass recovery (>99%) underscored that sorption of the dye was insignificant.

4.2.3   ICP-determination of Ag concentration

A mass balance on Ag was determined for each experiment. The liquid samples were digested in 68-70% nitric acid, rested for at least 12 hours, diluted to 2% nitric acid and analyzed for silver concentration via ICP-OES [*Molnar et al.*, 2014]. The sand from each experiment was digested with nitric acid and tested for silver concentration in a manner similar to the influent and effluent samples. The influent nAg mass was calculated by multiplying the ICP-determined C_o (Table 4.1) with the injected volume programmed into the syringe pump. The effluent mass was calculated by multiplying the ICP-determined Ag concentration of each effluent sample with the volume of effluent in the sample.

The concentration of Ag retained by the sand was determined directly from the acid-digested sand. Acid digestion and ICP-analysis of the nAg retained in the iron oxide sand was complicated due to an incomplete mass balance of Ag in the iron oxide experiment. This incomplete Ag mass balance is hypothesized to be due to unknown iron oxide/Ag

A version of this chapter has been published [*Molnar et al.*, 2015]

interactions that rendered part of the retained nAg non-digestible. Simple batch experiments with nAg in iron oxide sand proved that the incomplete mass balance was repeatable and thus not due to experimental error reinforcing the hypothesis that iron oxide/Ag interactions were responsible. Given the consistency of the batch experiments, the concentration of deposited nAg on the iron oxide sand reported in this study is the ICP-determined concentration from the acid-digestion solution + residual where residual is the amount of Ag required to complete the mass balance. More details regarding the nAg/iron oxide interactions and the batch experiments are discussed in Appendix 9.1.

4.2.4   DLVO Calculations

Standard DLVO (Derjaguin and Landau, Verwey and Overbeek) theory was used to confirm that iron oxide sand/nAg interactions were favorable and that the quartz sand had a primary energy barrier as well as a secondary energy minimum. The calculation was performed using the sphere-plate Surface Element Integration technique detailed in [*Bhattacharjee et al.*, 2000] with an existing code [*Liu*, 2008]. The zeta potential of the Iron Oxide sand at pH 8.4 and ionic strength of 0.12M was determined to be -25 mV via a streaming potential measurement (Anton Paar SurPASS system, Saint Laurent, Canada). The zeta potential value for quartz was taken from the literature as -55 mV [*Liang et al.*, 2013] as it was found to have relatively little impact on the DLVO profile. Hamaker constants were taken from the literature for quartz (7.93×10^{-20} J)[*Ross and Morrison*, 1988], water (5.5×10^{-20} J)[*Fernández-Varea and Garcia-Molina*, 2000], silver nanoparticles (17×10^{-20} J) [*Pinchuk*, 2012] and iron oxide (23.2×10^{-20} J)[*Faure et al.*, 2011]. Figure 9.4 in the Appendix shows the calculated DLVO curves.

All of the surfaces employed by this study (i.e., silver, quartz, iron oxide) possess negative zeta potentials indicating that the electrostatic forces between all surfaces are repulsive. However, the overall interaction energy is a combination of the repulsive electrostatic and attractive van der Waals forces. In the silver-quartz sands systems this leads to regions of repulsive forces (the repulsive energy barrier) and attractive forces (primary energy minimum) creating unfavorable deposition conditions (illustrated in Figure 9.4). In the silver-iron oxide sand system the attractive van der Waals forces

A version of this chapter has been published [*Molnar et al.*, 2015]

dominate at all separation distances, yielding no repulsive energy barrier and favorable deposition conditions (illustrated in Figure 9.4).

4.2.5   Imaging and Reconstruction

Imaging was completed at the Argonne National Lab, Advanced Photon Source Synchrotron, 13-BM-D beamline with the GSECARS research group. The imaging procedure and equipment is detailed in Molnar et al [2014]. Imaging was performed above and below the Ag K-edge at 25.414, 25.614, 25.714 and 25.814 keV. The column was imaged at the 4 energies each time (i.e., 0, 0.25, 0.5 PV, etc.). During imaging the column was rotated 180º while collecting 1440 projections. The pixels in the projection were binned together (2x2) to reduce imaging time and noise. The resolution of each projection was 9.87µm/pixel. The bottom of the SXCMT imaging window was 2.55 cm above the base of the column and extended upwards approximately 0.51 cm.

4.2.6   Reconstruction, Segmentation and Pore-Network Extraction

The collected projections were reconstructed into 3-dimensional datasets using GSECARS-specific reconstruction software [*Rivers et al.*, 2010] in IDL 8.1 (ITT Visual Information Solutions). The reconstruction software used filtered back projection with a radon transform and a general hamming filter to convert each set of 1440 projections into a 3-dimensional map of x-ray linear mass attenuation values. Each value in the reconstructed dataset is the x-ray linear mass attenuation averaged over a $9.87 \times 9.87 \times 9.87 \, \mu m$ voxel. Following reconstruction, a consistent subvolume ($350 \times 350 \times 450$ voxels) was extracted from all of the datasets captured at each time, providing 4-subvolumes per time-step for each of the 6-8 time-steps. An established segmentation and pore-network extraction procedure[*Molnar et al.*, 2014] was applied to one subvolume; it was not repeated on the other images for a given experiment because the grain/pore structure in the four images were identical. The images were checked to ensure that the segmentation properly identified the grain/water boundaries. In addition, distances between every pore space voxel and the closest, and second closest, grain surfaces were determined via the algorithm outlined in Appendix 10.1.

A version of this chapter has been published [*Molnar et al.*, 2015]

4.2.7　Dataset Analysis

The x-ray linear mass attenuation values for each voxel in the extracted subvolumes were converted to SXCMT-determined silver nanoparticle concentrations (hereafter referred to as [nAg]) using the method outlined in Molnar et al [2014] and summarized in the supplementary information. The method of Molnar et al. [2014] was verified at the beginning of the SXCMT beam time by imaging a bundle of capillary tubes filled with known concentrations of silver nanoparticles (determined via ICP-OES). This verification determined that the relationship between SXCMT-determined [nAg] and ICP-determined [nAg] was linear and that the method of Molnar et al. [2014] could be applied. See Molnar et al. [2014] for a full discussion of the method's verification, accuracy and uncertainty. During analysis of the collected datasets, it was discovered that the 'shadow zone' thickness was energy dependent. The thickness of the 'shadow zone' increased with increasing distance from the Ag K-edge. Due to this energy-dependent behavior, the SXCMT-determined [nAg] values for voxels 17-25 μm away from a grain surface were calculated using only the 25.614/25.414 keV difference dataset. Voxels > 25μm away from the grain surface used all datasets for [nAg] determination. It is important to note that due to the voxel resolution of the SXCMT datasets being orders of magnitude larger than the size of the nanoparticles, this method is unable to resolve individual nanoparticles, but instead provides an SXCMT-determined silver concentration within each voxel of the three-dimensional datasets. There are approximately 10^4 nanoparticles for every 1g/L of SXCMT-determined [nAg] within each voxel [*Molnar et al.*, 2014].

4.2.8　Computational Fluid Dynamic Analysis of Pore Water Flow

The ANSYS FLUENT 13.0 commercial software was employed to model the fluid flow through a subvolume of the uniform quartz dataset. FLUENT employs a finite volume method to solve momentum and continuity equations across a mesh. Modelling of the flow through the imaged subvolume essentially followed standard CFD methods[*Boccardo et al.*, 2014; *Cardenas*, 2008]. The subvolume ($150 \times 150 \times 350$ voxels) was meshed in ANSYS ICEM CFD 13.0 with 24 million elements, corresponding to approximately 10 elements for each pore space voxel. The inlet and outlet boundaries were set as constant pressure. The magnitude of the pressure drop from the inlet to outlet

A version of this chapter has been published [*Molnar et al.*, 2015]

boundary was adjusted until the average simulated pore water velocity approximated the bulk pore water velocity in the uniform quartz experiment (Table 4.1). Grain surface boundaries were set as no flow. The sides of the sub-volume were set to allow flow parallel to the boundary, but not across it. The viscosity of the simulated fluid matched the viscosity of the fluids used in the experiments, 14 cP.

4.3 Results and Discussion

The results and discussion section is divided into three subsections. The first discusses the column-scale results of the three experiments including overall nAg retention and the effluent breakthrough curves (BTC). The second examines the pore-scale distribution of nAg with respect to distance from grain-grain contacts for the three experiments. The third subsection compares the pore-scale concentration gradients in the favorable (iron oxide) and unfavorable (quartz) experiments. In all of the subsections, the results speak to whether immobile zones or surface chemistry controls the rate of diffusive flux to the grain surface and, thus, nanoparticle retention.

4.3.1   Column-Scale Results

The amounts of silver nanoparticles retained on the basis of acid-digestion and ICP-determination in the different experiments are listed in Table 4.1 and are, in descending order: iron oxide (0.2 mg nAg/g soil) > uniform quartz (0.01mg/g) > well graded quartz (0.0073 mg/g). There was some concern that the nAg stabilizing agent CMC90k could interfere with nAg retention in this study as it has been shown that a) nanoparticle stabilizing agents can alter retention behaviour by competing for deposition sites [*El Badawy et al.*, 2013] and b) CMC90k has demonstrated an affinity for iron oxide surfaces [*Pensini et al.*, 2013]. However, the concentration of nAg retained on the quartz sand agrees well with previously published nAg/quartz isotherm data [*Abraham et al.*, 2013] providing confidence that CMC90k was not interfering with nAg retention on the quartz sands. In addition, the retention data presented above agrees with previous studies that have demonstrated – in absence of a stabilizer - greater retention on iron oxide sands compared to quartz [*El Badawy et al.*, 2013; *Lin et al.*, 2011] which suggests that site competition with CMC90k was not a significant factor here.

A version of this chapter has been published [*Molnar et al.*, 2015]

Retention is often conceptualized as a two-step system: 1) nanoparticle transport towards the collector and 2) nanoparticle retention by the collector. As expected, the retention data (Table 4.1) shows that surface chemistry (i.e., favorable/unfavorable) controls the second step, retention at the collector surface. This finding matches the favorable/unfavorable conditions predicted by the DLVO curves in Figure 4.4 in the supplementary information indicating the presence of an electrostatic energy barrier on the quartz sands but not on the iron oxide sand and confirms that the iron oxide and quartz sands employed by this study represent favorable and unfavorable conditions, respectively. This highlights that, while immobile zones are hypothesized to contribute to temporary hydraulic retention of nanoparticles, attachment on the collector surface dominates the overall retention in favorable conditions.

Figure 4.2 examines the nAg breakthrough in the column effluent for the three experiments as a function of pore volumes injected. The nAg concentration values were obtained via ICP-determination of each collected effluent sample normalized to the ICP-determined influent concentration (C_o). The effluent BTCs were compared to CFT predictions via the upscaled CFT equation: $C/C_o = (1-\eta)^{Nc}$ where C is the concentration after passing by a number of linearly aligned collectors (Nc)[*Johnson and Hilpert*, 2013]. Assuming the average diameter of a grain is 500 μm, Nc can be calculated by representing the column as a long string of grains (Nc~100). The upscaled CFT equation was used to calculate the collector contact efficiencies for each experiment (η_{expt}). To minimize the influence of dispersion, η_{expt} was determined only for the peak C/C_o values at 3 PV. These η_{expt} values were compared to those obtained from the Nelson and Ginn [*Nelson and Ginn*, 2011] η_{CFT} correlation equation and are presented in Table 4.2. The Nelson and Ginn [*Nelson and Ginn*, 2011] η_{CFT} value (0.003) over predicts the column-scale iron oxide η_{expt} value (0.002) by 50%. This over prediction is consistent with previous findings that CFT-predicted η values are generally larger than experimentally-determined η values for nanoparticles in favourable conditions [*Long and Hilpert*, 2009; *Long et al.*, 2010; *Nelson and Ginn*, 2011]. This suggests that the single-collector CFT model presented in Figure 4.1a does not adequately account for all the relevant mechanisms.

A version of this chapter has been published [*Molnar et al.*, 2015]

A comparison of the quartz sands' η_{CFT} and η_{expt} values is complicated by the presence of the electrostatic energy barrier. CFT cannot predict η_{CFT} in unfavorable conditions and requires the 'attachment efficiency' (α) fitting parameter to compensate for the presence of an electrostatic energy barrier. Attachment efficiency is typically fit from experimental data and is calculated as: $\eta_{expt} = \alpha \times \eta_{CFT}$. Table 4.2 presents the calculated α for each experiment. While attachment efficiency is used for unfavorable conditions, the overprediction of η_{CFT}, due to mechanisms such as immobile zones, yields α values < 1 in favorable conditions as exhibited by the iron oxide column experiment ($\alpha = 0.67$). As expected, the quartz sands' α values are significantly smaller than the iron oxide α, 0.17 for uniform quartz and 0.03 for well graded quartz. Both quartz sands have identical surface chemistries and a similar grain d_{50} which, according to CFT, should yield identical retention rates and η_{CFT} values. The η_{expt} and α values are close to an order of magnitude larger for the uniform quartz than the well graded quartz despite the identical surface chemistries. This suggests that some physical mechanism related to the distribution of grain and pore sizes can inhibit nAg retention rates and influence both η_{expt} and the accuracy of single-collector CFT models.

Table 4.2: Comparison of Experimental and Predicted Contact Efficiency (η) at Maximum C/Co

	Uniform Iron Oxide	Uniform Quartz	Well Graded Quartz
Experimental (η_{expt})	0.002	0.0005	0.00009
Nelson-Ginn [*Nelson and Ginn*, 2011] (η_{CFT})	0.003	0.003	0.003
Attachment efficiency (α)	0.67	0.17	0.03

A version of this chapter has been published [*Molnar et al.*, 2015]
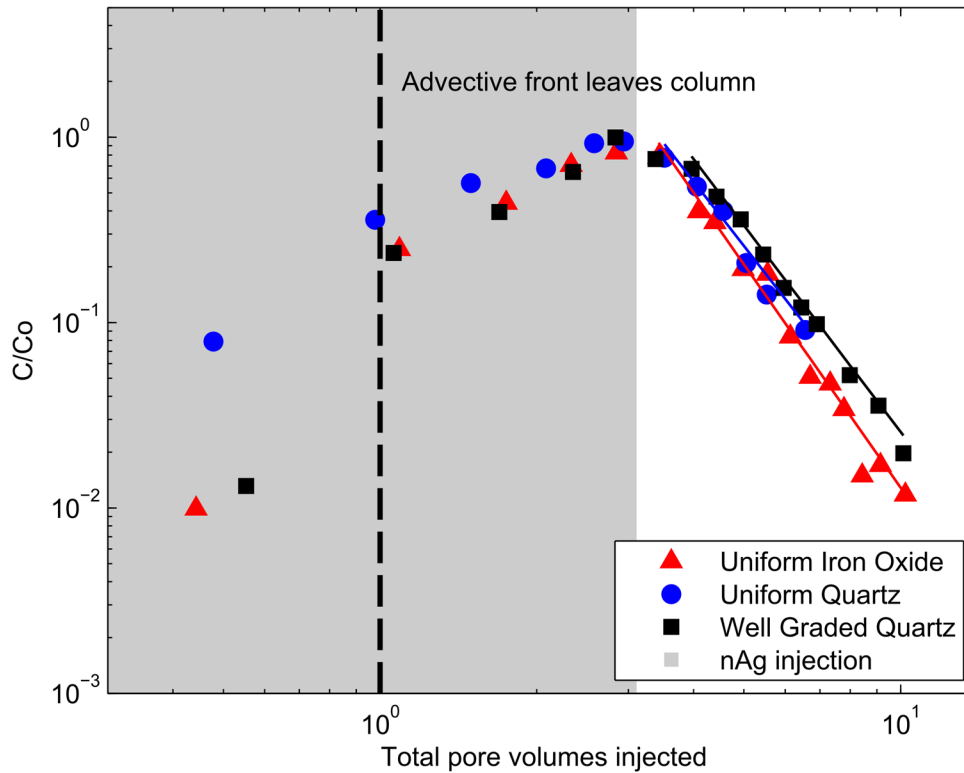
Figure 4.2: Effluent sample C/C$_o$ breakthrough on a log-log scale to emphasize extended tailing in the samples. The grey box represents the nAg injection period and the white background represents the elution. The vertical dotted line indicates when the advective front reached the top of the column. The red, blue and black lines are the results of Equation 4.1 fitted to the elution portion of the uniform iron oxide, uniform quartz, and well graded quartz breakthrough curves respectively. C$_o$ was measured at the start and end of the 3 PV injection period. Error bars representing C/C$_o$ for the maximum and minimum measured values of C$_o$ are plotted but are smaller than the marker size for each data point and are not visible.

The elution behaviour in Figure 4.2 was examined for evidence of extended tailing, specifically for evidence of power law tailing. Power law tailing appears as a linear decrease in C/C$_o$ on a log-log plot [*Haggerty et al.*, 2000] and is usually described by:

$$C = b \times t^{-k} \qquad\qquad 4.1$$

Where C is concentration, t is time or pore volumes injected, and k and b are fitted coefficients. As mentioned previously, tailing in colloid experiments is typically only associated with unfavorable conditions when colloids re-entrain into the bulk pore space from the secondary minimum [*Johnson and Hilpert*, 2013; *Landkamer et al.*, 2013; *Li et al.*, 2005]. If re-entrainment from the secondary minimum was the dominant source of

A version of this chapter has been published [*Molnar et al.*, 2015]

extended tailing, the tailing should only occur in the quartz sand experiments and not the iron oxide, as both the DLVO profile in Figure 4.4 and the column-scale retention data indicates that nanoparticles are irreversibly attached onto the iron oxide sand**.** However, all three experiments in Figure 4.2 exhibit the linear decrease in concentration indicative of power-law tailing. This suggests that extended tailing of nanoparticles can occur in both favorable and unfavorable deposition scenarios and, in these systems, is not linked to reversible/irreversible retention behaviour on the collector surface.

To compare the magnitude of tailing for the unfavorable (quartz) and the favorable (iron oxide) experiments, eq 4.1 was fit to the elution portion of each BTC. The fitted equation is represented by a line overlain on the tailing portion of each BTC in Figure 4.2. The parameter k from eq 4.1 represents the slope of the elution phase in log-log space. The unitless fitted k values, with +/- 95% confidence intervals, are: uniform iron oxide = 4.0+/- 0.4, uniform quartz = 3.6 +/- 0.8, well graded quartz = 3.7 +/- 0.2. Thus, the tailing behaviour observed in Figure 4.2 for the iron oxide and quartz experiments are statistically similar. This similar behaviour indicates that elution from the iron oxide and quartz sands are governed by a mechanism that is independent of surface chemistry, implying that nanoparticle re-entrainment from the secondary minimum is not an important mechanism in the two quartz experiments. As the tailing behaviour is independent of surface chemistry, a physical mechanism is likely responsible.

The conducted tracer tests (presented in Figure 9.3) reinforce the observation that physical mechanisms are likely responsible for nAg tailing. The tracer tests all exhibited extended tailing during elution and linearly decreasing concentration in log-log space. The linear decrease occurred over approximately 3 orders of magnitude of concentration. The high repeatability of the tracer experiments indicate that this observed tailing, for both the tracer and the nAg, are real and consistent for the experimental systems employed. The unitless k values from eq. 4.1 were fitted to each of the tracer test elution curves and were relatively consistent across all tracer experiments (uniform quartz: 7.6 +/- 1.2, 6.3 +/- 0.8, 7.9 +/- 0.6; well graded quartz: 7.3 +/- 0.6, 7.0 +/- 0.7; uniform iron oxide: 7.1 +/- 0.8, 6.4 +/- 0.6). The tracer k-values are higher than the nAg values, indicating a higher slope of eluted concentration and therefore less extended tailing

A version of this chapter has been published [*Molnar et al.*, 2015]

relative to the nAg. This is hypothesized to be due to the fact that the higher diffusivity of solutes yields higher diffusive mass fluxes relative to nanoparticle diffusion.

Traditional CFT models (i.e., Figure 4.1a) do not include physical mechanisms that could yield the extended tailing behaviour in Figure 4.2. The immobile areas that were hypothesized to be the source of the CFT discrepancies in Table 4.2 are likely the source of the tailing behaviour in Figure 4.2. Specifically, diffusive mass transfer into and out of the immobile areas is the hypothesized source of temporary hydraulic retention. The quantities of nanoparticles interacting with the hypothesized immobile zones are significant enough to yield both extended tailing and reduced attachment rates onto the collectors' surfaces at the column-scale. This suggests that the pore-scale concentration gradients, responsible for driving diffusive flux towards the collector surface, may be independent of surface chemistry and dominated by immobile zones. The next section will test the hypothesis that immobile zones are present in the three experiments by examining pore-scale concentrations and pore water fluid velocities near grain-grain contacts using pore-scale SXCMT data.

4.3.2   Pore-Scale Concentrations near Grain-Grain Contacts

Pore-scale modeling studies have suggested that hydraulic retention in the pore space, the hypothesized source of the tailing behaviour observed in Figure 4.2, will typically occur near grain-grain contact points [*Cardenas*, 2008; *Li et al.*, 2010b; 2012; *Torkzaban et al.*, 2008]. However, there are contradictory results in the literature regarding the governing mechanism that causes temporary retention in immobile zones. Pore-scale models of colloid transport [*Li et al.*, 2010a; *Li et al.*, 2012] have suggested that colloids primarily enter the immobile zones via translation along a secondary minimum, and suggested that these zones are not significant sources of retention in favorable deposition conditions. Solute transport studies have suggested that variations in pore-scale fluid velocity (i.e., mobile and immobile regions) and diffusive mass transfer between mobile/immobile regions are important contributors to temporary retention and extended tailing [*Bijeljic et al.*, 2011; *Bijeljic et al.*, 2013a; *Bijeljic et al.*, 2013b; *Cortis et al.*, 2004; *Scheibe et al.*,

A version of this chapter has been published [*Molnar et al.*, 2015]

2013]. In addition, another study determined that solutes would always exhibit temporary retention and extended tailing if vortices are present in the pore space [*Cardenas*, 2008].

Direct comparisons of the above studies to the nanoparticle transport experiments presented here is difficult due to the scale of the particles or molecules in the literature studies. The solute transport [*Cardenas*, 2008; *Scheibe et al.*, 2013] studies consider the transport of aqueous molecules. The colloid modeling studies [*Li et al.*, 2010a; *Li et al.*, 2012] present hydraulic retention data only for larger colloids (i.e., diameter = 1.1 μm) where Brownian motion is limited compared to the solute molecules. The silver nanoparticles employed in this study (i.e., diameter = 29.8 nm) are between the two sizes considered above and as such it is unknown whether immobile zones are important contributors to nanoparticle tailing in both favorable and unfavorable conditions.

A computational fluid dynamics (CFD) analysis, described in section 4.2.8, was undertaken on a subvolume of the uniform quartz SXCMT dataset to consider whether regions of low- and no-flow (i.e., immobile zones) are expected. Figure 4.3 presents a representative sampling of vertical cross-sectional contour plots of predicted velocity magnitude; it reveals that there are substantial regions of pore space that have pore water velocities more than an order-of-magnitude lower than the average pore water velocity (1.38 cm/min). These observations are in qualitative agreement with solute transport studies that have noted that pores in even homogenous media will possess pore-scale variations in velocity and immobile regions [*Cortis et al.*, 2004; *Cortis et al.*, 2006]. Also, these immobile regions appear to occur predominantly near grain-grain contacts, consistent with the conceptual model in Figure 4.1b. It should be noted that many of the low-flow locations in Figure 4.3 that appear to occur within pore throats (i.e., a narrow gap between neighbouring grains) are actually regions directly adjacent to grain-grain contacts; these contact points do not appear in the image because they are slightly offset from the examined cross-sections.

A version of this chapter has been published [*Molnar et al.*, 2015]
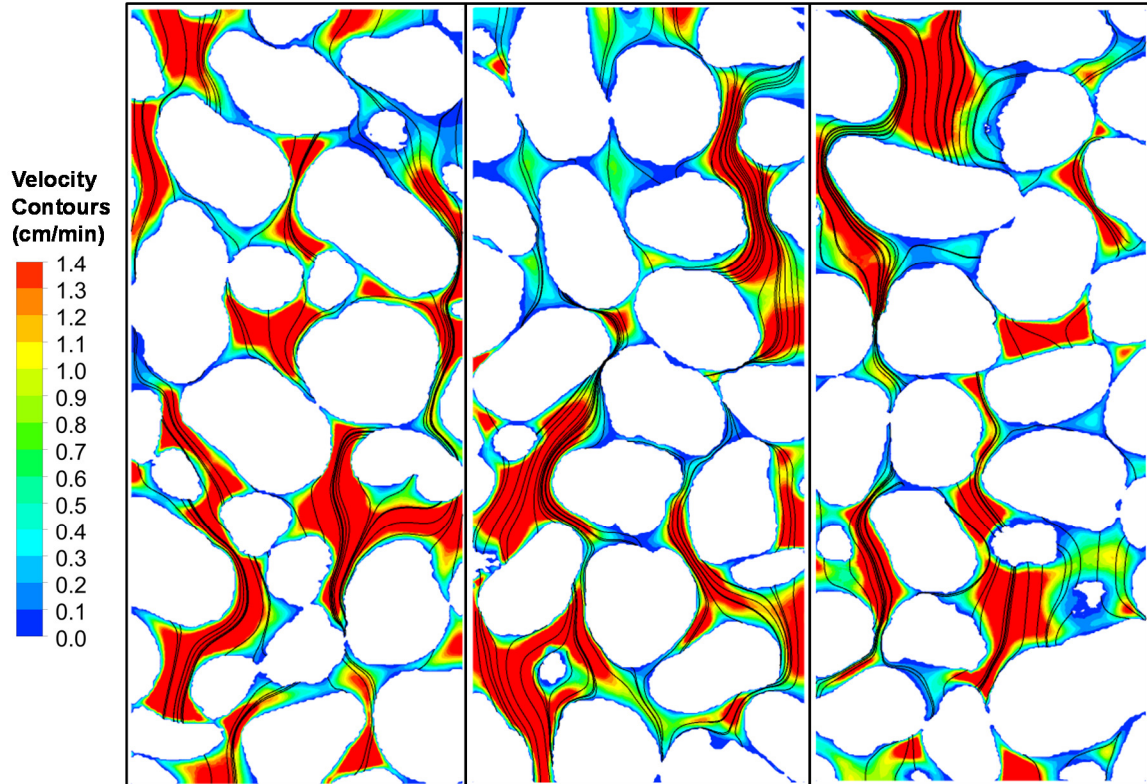
Figure 4.3: Contour plots of CFD-predicted velocity magnitude for three vertical cross-sections of the uniform quartz sub-volume. The velocity profiles in the three cross-sections are representative of the entire uniform quartz sub-volume. The colour map was cropped at 1.4 cm/min (average pore water velocity) to emphasize regions of low velocity. As a result, the red regions represent areas where pore water velocity is greater than the average pore water velocity (i.e., ≥1.4 cm/min). A random selection of streamlines were visualized near each selected cross-section and have been overlain in black on the images. Due to the 3-dimensional nature of the sub-volume, streamlines will appear and disappear from the image as they approach and leave the plane of the cross-section.

The velocity distribution observed in Figure 4.3 was examined for quantitative evidence that the pore space near grain-grain contacts had lower pore water velocities. This was examined by plotting the CFD-simulated pore water velocity as a function of distance from the nearest grain and as a function of distance from the second closest grain. The CFD-simulated velocity for each of the mesh's cells was converted to voxel-averaged velocity by importing the mesh into the SXCMT sub-volume and averaging all of the mesh's cells that were contained within each voxel in the sub-volume. The distance to the nearest grain and second nearest grain was measured for every pore space voxel in the dataset. The pore space voxels >17 µm distant from a grain surface were then sorted into 9.87×9.87 µm blocks and pore space voxels <17µm distant from a grain surface were

A version of this chapter has been published [*Molnar et al.*, 2015]

sorted into 9.87×17µm blocks. An average CFD-simulated pore water velocity for each block was calculated and plotted as a two-dimensional surface plot. The average CFD-simulated pore water velocity in each block represents the average pore water velocity at a certain distance considering every pore in the CFD sub-volume.

Figure 4.4 shows the CFD-simulated pore water velocity contour plot for the uniform quartz sub-volume. The bottom left corner of the plot represents the voxels closest to the grain-grain contact points, the top left corner represents voxels close to one grain surface but far from the next closest grain surface, and the top-right represents voxels in the centers of the pores. The dataset extends out to approximately 180 µm in the x-axis and to approximately 300 µm on the y-axis but has been cropped in the figure to highlight the area of interest.

The block-averaged velocity values in Figure 4.4 are a strong function of distance from the nearest grain: velocities were lower near the grains' surfaces than the centers of pores regardless of distance from the second closest grain. This trend was expected due to the no-slip boundary condition employed at the grains' surfaces and also matches the predicted velocity distribution from the Stokes flow around a single sphere (visualized in the right half of Figure 4.1a). However, the simulated velocities in Figure 4.4 are also, on average, lower near grain-grain contacts than other points near the grains' surfaces (i.e., velocity decreases with decreasing distance to second closest gain); this simulated velocity distribution closely matches the distribution visualized by the conceptual model in Figure 4.1b. The lower velocities observed near the grain-grain contact points in Figure 4.4 strongly suggests the presence of low flow/immobile zones near grain-grain contacts. The maximum pore velocities do not occur at the maximum distance from the grains; this likely occurs because the plotted values are the average values from all pores in the system. Given the wide range of pore sizes (with radii ranging from 10-200 µm), pore centers with their corresponding peak velocities will be found at a range of distances from the nearest grain surface (e.g., some pore centers will be 40, 50, 60, 100 µm distant from a grain surface). As a result, Figure 4.4 presents a generalized map of how pore water velocities vary with distance from two grain surfaces.

A version of this chapter has been published [*Molnar et al.*, 2015]
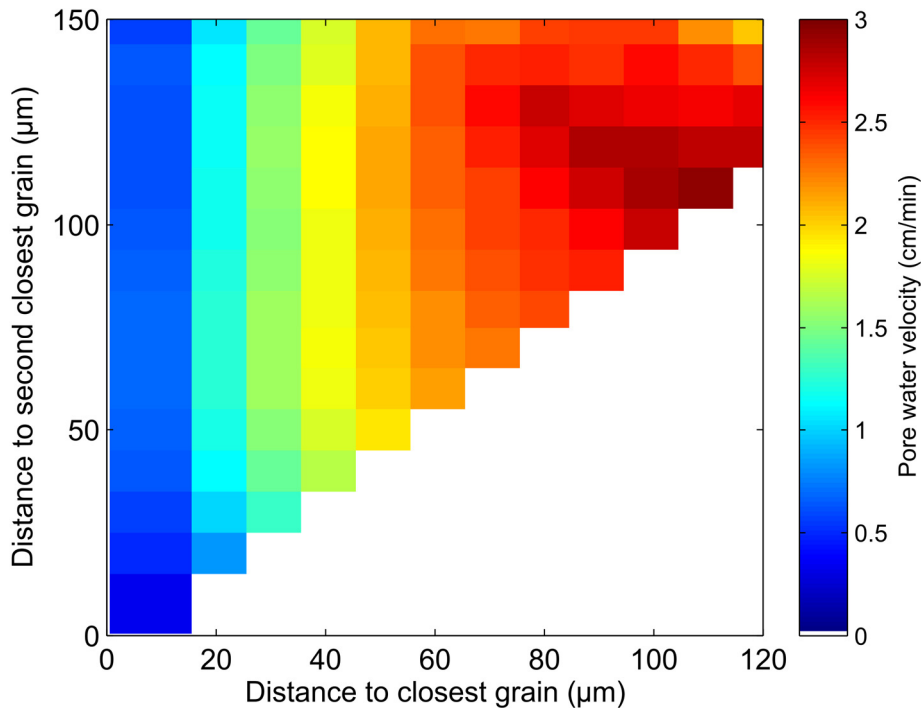
Figure 4.4: A contour plot of average CFD-simulated pore water velocity as a function of distance to the nearest grain surface (x-axis) and distance to the second closest grain (y-axis) for the uniform quartz experiment. It should be noted that while the voxels within the 'shadow zone' are not suitable for SXCMT-determined concentrations, they are suitable for CFD simulations of pore water velocity and are presented here. Each block represents an average velocity of many pore space voxels (>1000). The plot is triangular in shape with white space because the distance to the second closest grain can never be smaller than the distance to the closest grain.

The SXCMT-datasets were examined for evidence that the immobile zones in Figure 4.3 and 4.4 were impacting the pore space distribution of nanoparticle concentration, specifically if the immobile zones possessed lower nanoparticle concentrations. The average SXCMT-determined concentration was plotted as a function of distance from the nearest grain and as a function of distance from the second closest grain, similar to Figure 4.4. The SXCMT-determined concentration plots were created in a similar manner to Figure 4.4 but employed the SXCMT-determined [nAg] datasets, not the cropped sub-volume used for CFD simulations. The distance to the nearest grain and second nearest grain was measured for every pore space voxel in the dataset, the pore space voxels >17 µm distant from a grain surface were then sorted into 9.87×9.87 µm blocks. An average SXCMT-determined concentration for each block was calculated and plotted as a two-

A version of this chapter has been published [*Molnar et al.*, 2015]

dimensional surface plot. The average SXCMT-determined concentration in each block represents the average concentration at a certain distance considering every pore in the dataset.

Figure 4.5a shows the distance-distance concentration plot for all three experiments at 1.3 SXCMT pore volumes. The datasets extend out to approximately 180 μm in the x-axis and to approximately 300 μm on the y-axis but have been cropped in the figure to highlight the area of interest.

The block-averaged SXCMT-determined [nAg] values in Figure 4.5a decrease near the grain-grain contact points (lower left corner) and increase towards the centers of the pores (top right corner). Figure 4.5b plots the same data but with concentrations binned into 3 categories via 95% confidence intervals: significantly below average [nAg] (blue), average [nAg] (light green), and significantly above average [nAg] (red). Figure 4.5b clearly illustrates that the pore space voxels close to grain-grain contact points possess significantly below average nAg concentrations. While the blue region identified in Figure 4.5b appears to be relatively small, the pore space is not evenly distributed across the contour plots (i.e., some data points in Figure 4.5 represent a greater number of pore space voxels than others). Approximately 40% of all pore space voxels in each dataset are contained within the blue region in Figure 4.5b.

Uniform Quartz	Well Graded Quartz	Uniform Iron Oxide

1.3 SXCMT pore volumes

(A)

(B)
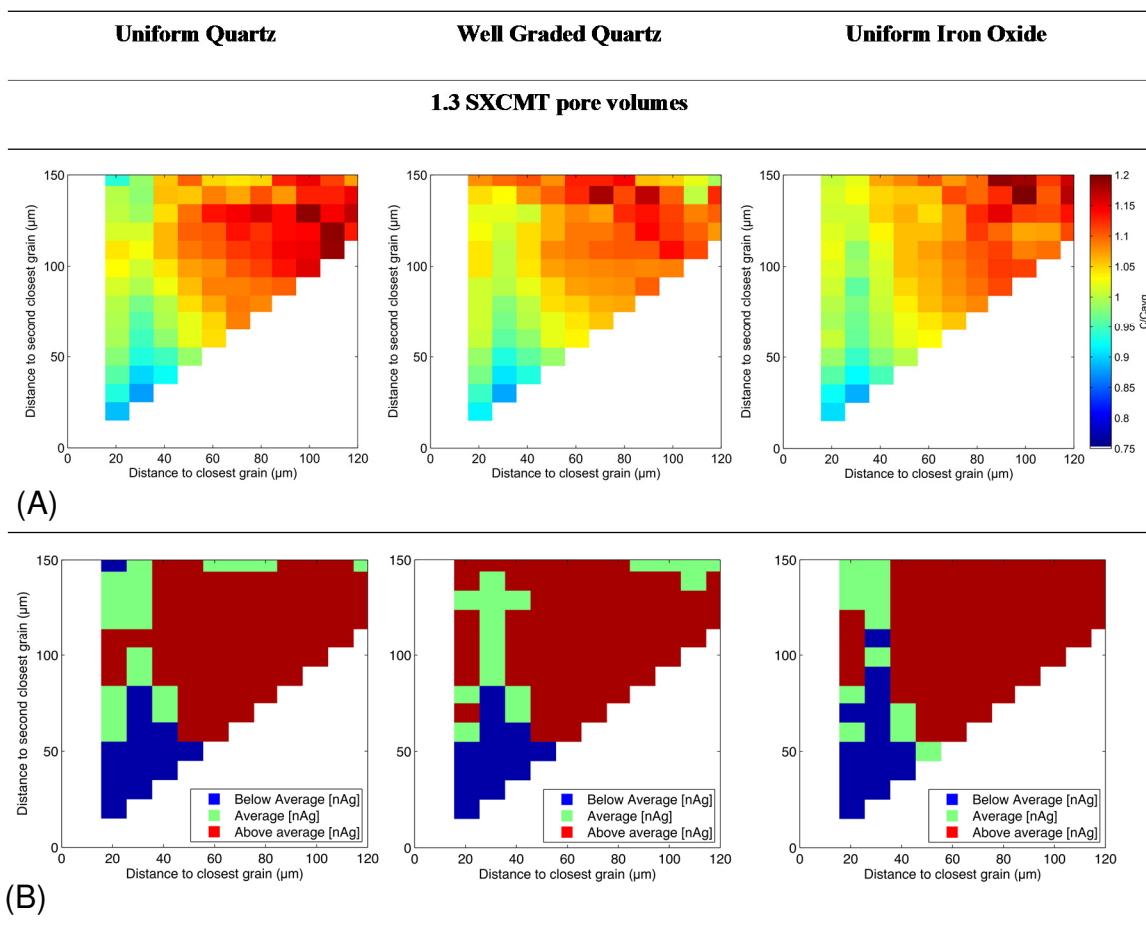
Figure 4.5A: A contour plot of SXCMT-determined [nAg] as a function of distance to the nearest grain surface (x-axis) and distance to the second closest grain (y-axis) for all three experiments at 1.3 SXCMT pore volumes. Each block represents an average concentration of many pore space voxels (>1000). The plotted 'block averaged' nAg concentrations are normalized to the average SXCMT-detemined concentration (C_{avg}) in each sand at 1.3 SXCMT-PV's. The average concentration for each dataset (uniform quartz, uniform iron oxide and well graded quartz at 1.3 SXCMT PV's) was calculated by summing the SXCMT-determined concentration value in all usable pore space voxels and dividing by the number of voxels summed. Normalizing the plotted concentration to C_{avg} instead of input concentration (C_o) enables comparisons of silver nanoparticle distribution between the datasets even though they have different input concentrations (C_o) and different C/C_o values at 1.3 SXCMT PV's. The plot is triangular in shape with white space because the distance to the second closest grain can never be smaller than the distance to the closest grain. Due to the shadow zone extending outwards to 17μm, all data points within 17μm of a grain surface have been cropped from the plots.

Figure 4.5B: A two-dimensional plot identifying each block in Figure 4.5a as being either significantly above the average pore space concentration (red), below the average pore space concentration (blue) or not significantly different from the pore space average concentration (light green). 95% confidence intervals were used to determine significance.

A version of this chapter has been published [*Molnar et al.*, 2015]

The decrease in concentration near the grain-grain contact points in Figure 4.5 coincides with the results in Figures 4.3 and 4.4, and suggests that the pore space near grain-grain contacts is relatively immobile and therefore nanoparticle access is limited by diffusion. The reduced concentrations relative to the centers of the pores are evidence that advective transport near grain-grain contacts is limited. Nanoparticles that diffuse into these immobile pore spaces, do not attach to the grains' surfaces, and diffuse back into the mobile porosity during elution could lead to extended tailing observed in Figure 4.2. The C/C_{avg} trends in Figure 4.5A as well as the below-average concentration zones (blue, Figure 4.5B) are consistent between favorable and unfavorable sands. These similarly sized below-average concentration zones suggest that nanoparticle diffusive flux into the immobile zones are relatively consistent regardless of favorable or unfavorable deposition conditions or the grain size distributions employed in this study. Consistent nanoparticle diffusive flux into the immobile zones in each of the three sands coincides with the similar tailing behaviours identified in Figure 4.2. This supports the hypothesis that diffusion, not colloid/surface interactions, is driving the temporary retention that led to the observed tailing. The nanoparticle interactions with immobile pore spaces appear to be more similar to the solute transport simulations discussed previously [*Bijeljic et al.*, 2011; *Bijeljic et al.*, 2013a; *Bijeljic et al.*, 2013b; *Cardenas*, 2008; *Cortis et al.*, 2004; *Cortis et al.*, 2006; *Scheibe et al.*, 2013] than the micron-sized colloids simulations [*Li et al.*, 2010a; *Li et al.*, 2012].

4.3.3   Pore-Scale Concentration Gradients

To further explore the hypothesis that immobile zones controlled the rate of diffusive flux towards the grain surface, pore-space concentration gradients in the quartz (unfavorable) and iron oxide (favorable) experiments were compared. If surface chemistry controlled the flux then the concentration gradients in the iron oxide/favorable experiment would be greater than in the quartz/unfavorable experiment. However, if the immobile zones and diffusion were controlling the rate of flux towards the grain then the concentration gradients should be similar between the three experiments.

A version of this chapter has been published [*Molnar et al.*, 2015]

To simplify the analysis, one-dimensional pore-scale concentration gradients (dC/dr) away from the grain surface were considered. These concentration gradients were obtained by plotting the average SXCMT-determined concentration as a function of distance from the nearest grain surface (Figure 4.6). The distance to the nearest grain surface was measured for every pore space voxel in the dataset and then the pore space voxels were binned into 9.87 µm distance bins, a distance of 1 voxel. An average SXCMT-determined concentration for each bin was calculated and plotted as a function of the average distance from the grain surface. The average SXCMT-determined concentration in each bin represents the average concentration at a certain distance for every pore in the dataset, not individual pores; by this method, the one-dimensional dC/dr is not for a specific direction or angle but an average over the entire pore space considering all angles around all grains. Lines of best fit for each time step are also shown in Figure 4.6; the slope of these lines represent average dC/dr for the imaged volume as a function of time.

Figure 4.6 reveals that nanoparticle concentration is an approximately linear function of distance from the grain surface in all experiments. The small positive slopes at 0PV are the result of x-ray refraction away from the grain surface. While this x-ray refraction predominantly affects the SXCMT-determined [nAg] values close to the grain surface (< 17 µm distant, and thus this data is excluded from this analysis), it does exert some minor influence throughout the rest of the pore space. This small slope at 0PV is consistent with the results of Molnar et al. [2014].

A version of this chapter has been published [*Molnar et al.*, 2015]

A version of this chapter has been published [*Molnar et al.*, 2015]
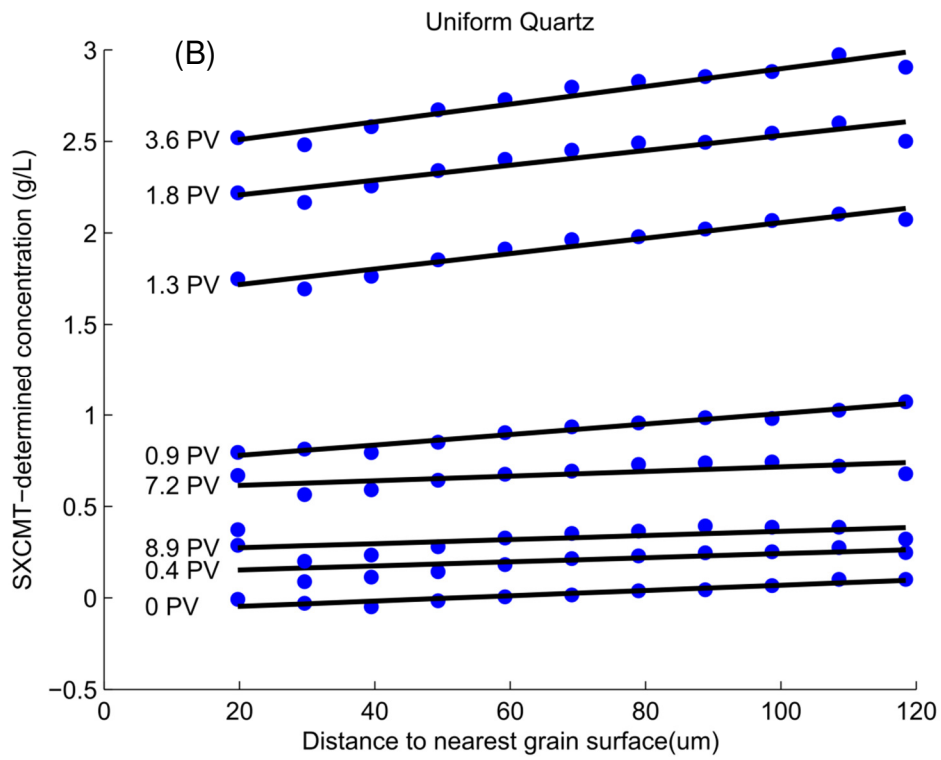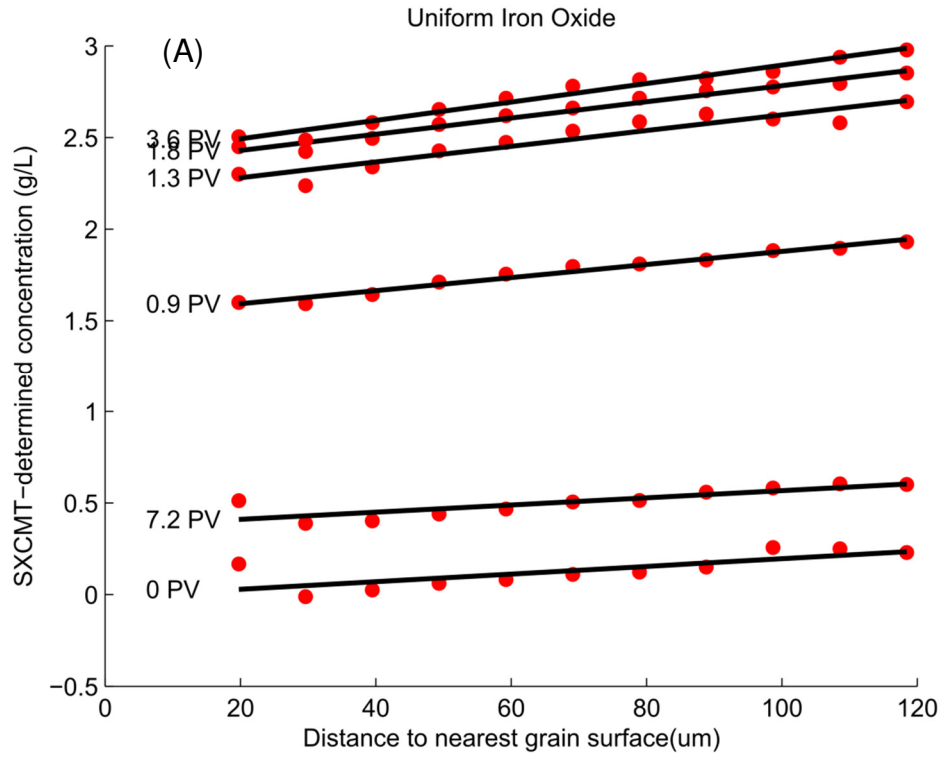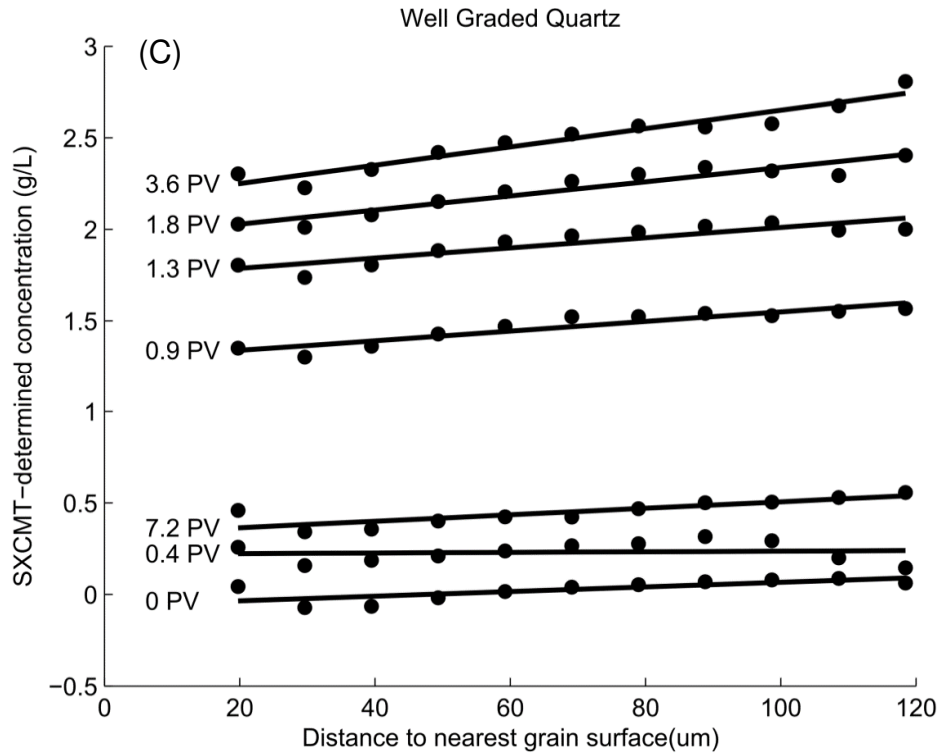
Figure 4.6: SXCMT-determined [nAg] as a function of distance to the nearest grain surface for every time-step in each of the 3 injection experiments (A: uniform iron oxide, B: uniform quartz, C: well graded quartz). The labeled the pore volume numbers represent SXCMT pore volumes but were labeled as simply 'PV' for convenience. The colored circles represent the average SXCMT-determined [nAg] for each bin (blue: uniform quartz, red: uniform iron oxide, black: well graded quartz) and the thick black lines are fitted linear trends. All voxels were binned and averaged in 9.87μm increments with the exception of the first datapoint at x = 20. Due to the shadow zone extending outwards to 17μm, the first datapoint only bins 17-25μm distance from a grain surface.

Figure 4.7 plots dC/dr over time for each of the experiments normalized to the dC/dr in the SXCMT 0 PV datasets. In all three experiments the value of dC/dr increases during nAg injection and decreases during elution to background levels. It was expected that dC/dr would decrease to a negative value during elution, indicating nanoparticle re-entrainment in the mobile porosity, either due to detachment from the grains or diffusive mass transfer out of the immobile zones, however this was not observed. A dC/dr value of 0 does not mean that nanoparticle re-entrainment in the mobile porosity did not occur (as it clearly did), but that this method of analysis was unable to distinguish between nanoparticles re-entrained within the SXCMT-imaging window and nanoparticles re-entrained from immobile zones/grains upstream from the SXCMT-imaging window.

A version of this chapter has been published [*Molnar et al.*, 2015]

The general trend and magnitude of dC/dr in Figure 4.7 is similar for all three experiments. This shows that immobile zones, not surface chemistry, are controlling nAg concentration gradients and diffusive flux rates towards grain surfaces. As previously discussed, retention is conceptualized as a two-step system: 1) nanoparticle transport towards the collector and 2) nanoparticle retention by the collector. Section 4.3.1 showed that surface chemistry (i.e., favorable/unfavorable) controlled attachment at the collector surface (i.e., step 2). Figure 4.6 provides further evidence for this two-step attachment process by illustrating that immobile zones are limiting the first step, the rate of nanoparticle transport towards the collector, while also acting as a temporary retention mechanism in both favorable and unfavorable conditions.
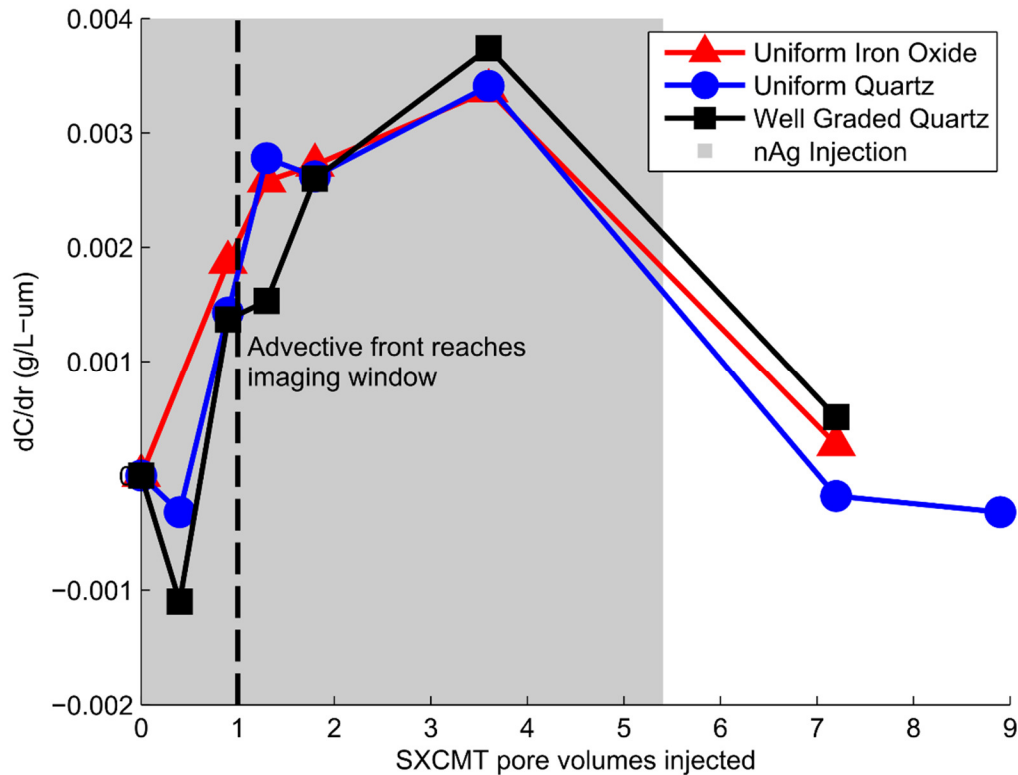
Figure 4.7: dC/dr plotted as a function of SXCMT pore volumes injected. The plotted values of dC/dr are the slope of the fitted lines in Figure 4.6 normalized to the 0 SXCMT PV dC/dr so that dC/dr = 0 at SXCMT PV = 0. The grey box represents the time during which nAg was injected into the solution

The similarity in concentration gradients between the uniform quartz and well graded quartz in Figure 4.7 suggests that grain and pore size distribution does not significantly

A version of this chapter has been published [*Molnar et al.*, 2015]

influence pore-scale concentration gradients. Given the identical DLVO profiles of the well graded and uniform quartz sands, similar concentration gradients should yield similar retention rates. The retained concentrations for Uniform Quartz and Well Graded Quartz (Table 4.1) are similar; this similarity suggests that the differences in immobile zones in the uniform and well graded sands are not large enough to yield differences in observed concentration gradients or overall retention levels despite order-of-magnitude differences in α. The extended tailing behaviour (Figure 4.2) and pore-space nAg distribution near grain-grain contacts for the uniform and well graded quartz sands were also similar. The similarity in behaviour of the uniform quartz and well graded quartz does not necessarily suggest that immobile zones are independent of grain size distribution. Rather, it is hypothesized that the differences in grain size distribution (Table 4.1) between uniform quartz and well graded quartz were not significant enough to quantify differences in immobile zone extent and frequency. The grain size distribution of the well graded quartz was limited by the resolution of the SXCMT datasets and the diameter of the experimental column.

To account for the influence of differing injection concentrations (Table 4.1, C_o) and breakthrough curve behaviour (Figure 4.2) on pore-scale gradient formation, the concentration gradients were plotted as a function of average SXCMT-determined [nAg] (see Figure 4.8). The average SXCMT-determined [nAg] was calculated by averaging every [nAg] voxel value in each dataset, excluding the voxels that were <17µm distance from a grain surface. Figure 4.8 illustrates that in all three experiments dC/dr increased linearly as nanoparticle concentration increased. This indicates that in all three experiments concentration gradient formation depended strongly on average pore-space nanoparticle concentration. The similar gradient vs. concentration trend in Figure 4.8 for all three experiments reinforce the results of Figures 4.2 to 4.7 that all three experiments were similarly impacted by immobile zones, and that this impact was independent of surface chemistry and grain size distribution.
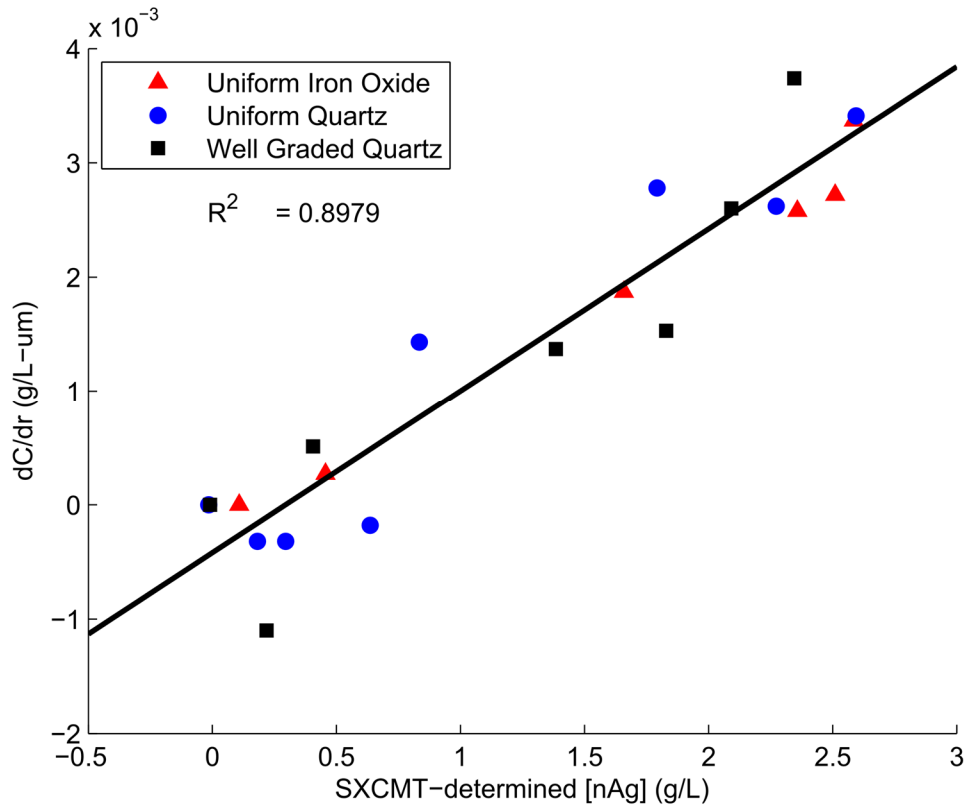
Figure 4.8: dC/dr from Figure 4.7 plotted vs. average SXCMT-determined silver nanoparticle concentration. A line has been fit to all three experiments and overlain in black.

4.4 Conclusions

This study examined the impact of immobile zones on the transport and retention of silver nanoparticles through three sand columns: uniform quartz (unfavorable), uniform iron oxide (favorable) and well graded quartz (unfavorable). Four major findings were drawn from this study: (1) Extended tailing during the elution phase occurred for all three sand types, representing independence from surface chemistry, (2) Numerical simulations of fluid flow through a uniform quartz SXCMT dataset predict the existence of immobile zones near grain-grain contacts, (3) SXCMT-datasets of pore-scale nanoparticle distribution revealed significantly below-average concentrations near grain-grain contacts, and (4) The pore-scale nanoparticle concentration gradients towards the grain surfaces were independent of surface chemistry and grain size distribution and varied linearly with average nanoparticle concentration in the SXCMT-datasets.

A version of this chapter has been published [*Molnar et al.*, 2015]

These observations highlight the impact immobile zones may have on nanoparticle transport and retention. While surface chemistry was observed to control nanoparticle retention at the grains' surfaces, immobile zones impacted the transport of nanoparticles to the surface. Since the observed tailing was independent of surface chemistry, this suggests that (i) immobile zones are likely acting as sources of temporary hydraulic retention, and (ii) diffusive flux between mobile and immobile zones was driving the temporary retention, not torque-induced rolling as is typically suggested. It should be emphasized that the temporary hydraulic retention occurring within this study does not suggest that filtration (i.e., retention by the collector surface) is insignificant for nanoparticles. The high, irreversible, attachment rates onto the iron oxide sand demonstrates that retention by the collector surface is a major component of overall retention in favorable conditions. Since the measured pore-scale concentration gradients were independent of surface chemistry, this revealed that higher retention rates did not create higher diffusive flux rates towards the grains' surfaces. This suggests that diffusive transport through the immobile zones was limiting the overall rate of nanoparticle transport towards the surfaces and thus limiting the overall rate of nanoparticle retention. This could explain why CFT typically over predicts nanoparticle retention: single-collector models in CFT are unable to account for immobile zones as they do not contain any grain-grain contacts. These implications, widely applicable to nano-sized colloids, are likely less important for micron-sized colloids (e.g., bacteria) as the latter exhibit limited Brownian motion relative to the nanoparticles employed in this study.

Accurate prediction of nanoparticle transport will therefore likely require incorporation of immobile zones into continuum-scale and CFT-scale transport models. Incorporating immobile zones may help CFT models accurately predict η for nanoparticles and, by better understanding nanoparticle transport to the collector surface and temporary retention, may also aid the development of models that can predict nanoparticle retention in unfavorable conditions. Incorporating immobile zones into these models should be considered a future research opportunity.

A version of this chapter has been published [*Molnar et al.*, 2015]

It is acknowledged that it was not possible to directly observe individual nanoparticles in real-time within the three-dimensional porous media, either in the pore space or directly on the grains' surfaces as this exceeds both the spatial and temporal resolutions available via SXCMT. The study instead relied on statistical averages of pore-space nanoparticle concentrations that were mapped by a quantitative SXCMT technique, the strength of which is the more than 12 million data values (i.e., voxels) available for averaging. While this technique is limited to quantifying nanoparticle concentrations more than 17µm from the grain surface, it nevertheless provides unprecedented quantification of spatially averaged nanoparticle pore-space concentration gradients. It is also acknowledged that immobile zones are not directly observed, however the weight of combined evidence from pore velocity modelling, column-scale elution behaviour, and pore scale concentrations makes a compelling case about the impact of immobile zones on nanoparticle transport and retention.

A version of this chapter has been published [*Molnar et al.*, 2015]

4.5 References

Abraham, P. M., S. Barnikol, T. Baumann, M. Kuehn, N. P. Ivleva, and G. E. Schaumann (2013), Sorption of Silver Nanoparticles to Environmental and Model Surfaces, *Environ. Sci. Technol.*, *47*(10), 5083-5091.

Baalousha, M., and J. R. Lead (2009), *Overview of Nanoscience in the Environment*, 1-29 pp., John Wiley & Sons, Ltd.

Bennett, P., F. He, D. Zhao, B. Aiken, and L. Feldman (2010), In situ testing of metallic iron nanoparticle mobility and reactivity in a shallow granular aquifer, *Journal of Contaminant Hydrology*, *116*(1–4), 35-46.

Bergendahl, J., and D. Grasso (2000), Prediction of colloid detachment in a model porous media: hydrodynamics, *Chemical Engineering Science*, *55*(9), 1523-1532.

Berkowitz, B., A. Cortis, M. Dentz, and H. Scher (2006), Modeling non-Fickian transport in geological formations as a continuous time random walk, *Rev. Geophys.*, *44*(2), 49.

Bhattacharjee, S., J. Y. Chen, and M. Elimelech (2000), DLVO interaction energy between spheroidal particles and a flat surface, *Colloids and Surfaces A: Physicochemical and Engineering Aspects*, *165*(1–3), 143-156.

Bijeljic, B., P. Mostaghimi, and M. J. Blunt (2011), Signature of Non-Fickian Solute Transport in Complex Heterogeneous Porous Media, *Physical Review Letters*, *107*(20), 204502.

Bijeljic, B., A. Raeini, P. Mostaghimi, and M. J. Blunt (2013a), Predictions of non-Fickian solute transport in different classes of porous media using direct simulation on pore-scale images, *Phys. Rev. E*, *87*(1), 013011.

Bijeljic, B., P. Mostaghimi, and M. J. Blunt (2013b), Insights into non-Fickian solute transport in carbonates, *Water Resour. Res.*, *49*(5), 2714-2728.

Boccardo, G., D. L. Marchisio, and R. Sethi (2014), Microscale simulation of particle deposition in porous media, *Journal of Colloid and Interface Science*, *417*(0), 227-237.

Bradford, S. A., M. Bettahar, J. Simunek, and M. T. van Genuchten (2004), Straining and attachment of colloids in physically heterogeneous porous media, *Vadose Zone J.*, *3*(2), 384-394.

Bradford, S. A., J. Simunek, and S. L. Walker (2006), Transport and straining of E. coli O157:H7 in saturated porous media, *Water Resour. Res.*, *42*(12), W12S12.

Bradford, S. A., S. Torkzaban, F. Leij, im, J. nek, and M. T. van Genuchten (2009), Modeling the coupled effects of pore space geometry and velocity on colloid transport and retention, *Water Resour. Res.*, *45*(2), W02414.

Bradford, S. A., S. Torkzaban, and A. Wiegmann (2011), Pore-Scale Simulations to Determine the Applied Hydrodynamic Torque and Colloid Immobilization, *Vadose Zone J.*, *10*(1), 252-261.

Cardenas, M. B. (2008), Three-dimensional vortices in single pores and their effects on transport, *Geophysical Research Letters*, *35*(18), L18402.

Cortis, A., Y. Chen, H. Scher, and B. Berkowitz (2004), Quantitative characterization of pore-scale disorder effects on transport in ``homogeneous'' granular media, *Phys. Rev. E*, *70*(4), 041108.

A version of this chapter has been published [*Molnar et al.*, 2015]

Cortis, A., T. Harter, L. Hou, E. R. Atwill, A. I. Packman, and P. G. Green (2006), Transport of Cryptosporidium parvum in porous media: Long-term elution experiments and continuous time random walk filtration modeling, *Water Resour. Res.*, *42*(12), n/a-n/a.

Cullen, E., D. M. O'Carroll, E. K. Yanful, and B. Sleep (2010), Simulation of the subsurface mobility of carbon nanoparticles at the field scale, *Adv. Water Resour.*, *33*(4), 361-371.

Edery, Y., A. Guadagnini, H. Scher, and B. Berkowitz (2013), Reactive transport in disordered media: Role of fluctuations in interpretation of laboratory experiments, *Adv. Water Resour.*, *51*(0), 86-103.

Edery, Y., A. Guadagnini, H. Scher, and B. Berkowitz (2014), Origins of anomalous transport in heterogeneous media: Structural and dynamic controls, *Water Resour. Res.*, *50*(2), 1490-1505.

El Badawy, A. M., A. Aly Hassan, K. G. Scheckel, M. T. Suidan, and T. M. Tolaymat (2013), Key Factors Controlling the Transport of Silver Nanoparticles in Porous Media, *Environ. Sci. Technol.*

Faure, B., G. Salazar-Alvarez, and L. Bergström (2011), Hamaker Constants of Iron Oxide Nanoparticles, *Langmuir*, *27*(14), 8659-8664.

Fernández-Varea, J. M., and R. Garcia-Molina (2000), Hamaker Constants of Systems Involving Water Obtained from a Dielectric Function That Fulfills the f Sum Rule, *Journal of Colloid and Interface Science*, *231*(2), 394-397.

Haggerty, R., S. A. McKenna, and L. C. Meigs (2000), On the late-time behavior of tracer test breakthrough curves, *Water Resour. Res.*, *36*(12), 3467-3479.

Hahn, M. W., and C. R. O'Melia (2004), Deposition and reentrainment of Brownian particles in porous media under unfavorable chemical conditions: Some concepts and applications, *Environ. Sci. Technol.*, *38*(1), 210-220.

Happel, J. (1958), VISCOUS FLOW IN MULTIPARTICLE SYSTEMS - SLOW MOTION OF FLUIDS RELATIVE TO BEDS OF SPHERICAL PARTICLES, *Aiche J.*, *4*(2), 197-201.

Jaisi, D. P., and M. Elimelech (2009), Single-Walled Carbon Nanotubes Exhibit Limited Transport in Soil Columns, *Environ. Sci. Technol.*, *43*(24), 9161-9166.

Johnson, P. R., and M. Elimelech (1995), DYNAMICS OF COLLOID DEPOSITION IN POROUS-MEDIA - BLOCKING BASED ON RANDOM SEQUENTIAL ADSORPTION, *Langmuir*, *11*(3), 801-812.

Johnson, P. R., N. Sun, and M. Elimelech (1996), Colloid transport in geochemically heterogeneous porous media: Modeling and measurements, *Environ. Sci. Technol.*, *30*(11), 3284-3293.

Johnson, W. P., E. Pazmino, and H. L. Ma (2010), Direct observations of colloid retention in granular media in the presence of energy barriers, and implications for inferred mechanisms from indirect observations, *Water Research*, *44*(4), 1158-1169.

Johnson, W. P., and M. Hilpert (2013), Upscaling colloid transport and retention under unfavorable conditions: Linking mass transfer to pore and grain topology, *Water Resour. Res.*, *49*(9), 5328-5341.

Ko, C.-H., and J. Y. Chen (2000), Dynamics of Silica Colloid Deposition and Release in Packed Beds of Aminosilane-Modified Glass Beads, *Langmuir*, *16*(17), 6906-6912.

Kocur, C. M., D. M. O'Carroll, and B. E. Sleep (2013), Impact of nZVI stability on mobility in porous media, *Journal of Contaminant Hydrology*, *145*(0), 17-25.

Kocur, C. M., et al. (2014), Characterization of nZVI Mobility in a Field Scale Test, *Environ. Sci. Technol.*, *48*(5), 2862-2869.

Krol, M. M., A. J. Oleniuk, C. M. Kocur, B. E. Sleep, P. Bennett, Z. Xiong, and D. M. O'Carroll (2013), A Field-Validated Model for In Situ Transport of Polymer-Stabilized nZVI and Implications for Subsurface Injection, *Environ. Sci. Technol.*, *47*(13), 7332-7340.

Kuznar, Z. A., and M. Elimelech (2007), Direct microscopic observation of particle deposition in porous media: Role of the secondary energy minimum, *Colloid Surf. A-Physicochem. Eng. Asp.*, *294*(1-3), 156-162.

Landkamer, L. L., R. W. Harvey, T. D. Scheibe, and J. N. Ryan (2013), Colloid transport in saturated porous media: Elimination of attachment efficiency in a new colloid transport model, *Water Resour. Res.*, *49*(5), 2952-2965.

Lecoanet, H. F., J.-Y. Bottero, and M. R. Wiesner (2004), Laboratory Assessment of the Mobility of Nanomaterials in Porous Media, *Environ. Sci. Technol.*, *38*(19), 5164-5169.

Lecoanet, H. F., and M. R. Wiesner (2004), Velocity effects on fullerene and oxide nanoparticle deposition in porous media, *Environ. Sci. Technol.*, *38*(16), 4377-4382.

Li, X. Q., T. D. Scheibe, and W. P. Johnson (2004), Apparent Decreases in Colloid Deposition Rate Coefficients with Distance of Transport under Unfavorable Deposition Conditions: A General Phenomenon, *Environ. Sci. Technol.*, *38*(21), 5616-5625.

Li, X. Q., P. F. Zhang, C. L. Lin, and W. P. Johnson (2005), Role of hydrodynamic drag on microsphere deposition and re-entrainment in porous media under unfavorable conditions, *Environ. Sci. Technol.*, *39*(11), 4012-4020.

Li, X. Q., Z. L. Li, and D. X. Zhang (2010a), Role of Low Flow and Backward Flow Zones on Colloid Transport in Pore Structures Derived from Real Porous Media, *Environ. Sci. Technol.*, *44*(13), 4936-4942.

Li, Y., Y. Wang, K. D. Pennell, and L. M. Abriola (2008), Investigation of the Transport and Deposition of Fullerene (C60) Nanoparticles in Quartz Sands under Varying Flow Conditions, *Environ. Sci. Technol.*, *42*(19), 7174-7180.

Li, Z., D. X. Zhang, and X. Li (2010b), Tracking Colloid Transport in Porous Media Using Discrete Flow Fields and Sensitivity of Simulated Colloid Deposition to Space Discretization, *Environ. Sci. Technol.*, *44*(4), 1274-1280.

Li, Z., D. X. Zhang, and X. Li (2012), Tracking colloid transport in real pore structures: Comparisons with correlation equations and experimental observations, *Water Resour. Res.*, *48*(5), W05533.

Liang, Y., S. A. Bradford, J. Simunek, H. Vereecken, and E. Klumpp (2013), Sensitivity of the transport and retention of stabilized silver nanoparticles to physicochemical factors, *Water Research*, *47*(7), 2572-2582.

A version of this chapter has been published [*Molnar et al.*, 2015]

Lin, S. H., Y. W. Cheng, Y. Bobcombe, K. L. Jones, J. Liu, and M. R. Wiesner (2011), Deposition of Silver Nanoparticles in Geochemically Heterogeneous Porous Media: Predicting Affinity from Surface Composition Analysis, *Environ. Sci. Technol.*, *45*(12), 5209-5215.

Liu, X. (2008), The mobility of engineered multi-walled carbon nanotubes in porous media, University of Western Ontario, London, Ontario.

Liu, X. Y., D. M. O'Carroll, E. J. Petersen, Q. G. Huang, and C. L. Anderson (2009a), Mobility of Multiwalled Carbon Nanotubes in Porous Media, *Environ. Sci. Technol.*, *43*(21), 8153-8158.

Liu, Y., D. Janjaroen, M. S. Kuhlenschmidt, T. B. Kuhlenschmidt, and T. H. Nguyen (2009b), Deposition of Cryptosporidium parvum Oocysts on Natural Organic Matter Surfaces: Microscopic Evidence for Secondary Minimum Deposition in a Radial Stagnation Point Flow Cell, *Langmuir*, *25*(3), 1594-1605.

Long, W., and M. Hilpert (2009), A Correlation for the Collector Efficiency of Brownian Particles in Clean-Bed Filtration in Sphere Packings by a Lattice-Boltzmann Method, *Environ. Sci. Technol.*, *43*(12), 4419-4424.

Long, W., H. Huang, J. Serlemitsos, E. Liu, A. H. Reed, and M. Hilpert (2010), Pore-scale study of the collector efficiency of nanoparticles in packings of nonspherical collectors, *Colloids and Surfaces A: Physicochemical and Engineering Aspects*, *358*(1–3), 163-171.

Ma, H., J. Pedel, P. Fife, and W. P. Johnson (2009), Hemispheres-in-Cell Geometry to Predict Colloid Deposition in Porous Media, *Environ. Sci. Technol.*, *43*(22), 8573-8579.

Mattison, N. T., D. M. O'Carroll, R. Kerry Rowe, and E. J. Petersen (2011), Impact of Porous Media Grain Size on the Transport of Multi-walled Carbon Nanotubes, *Environ. Sci. Technol.*, *45*(22), 9765-9775.

Molnar, I. L., D. M. O'Carroll, and J. I. Gerhard (2011), Impact of surfactant-induced wettability alterations on DNAPL invasion in quartz and iron oxide-coated sand systems, *Journal of Contaminant Hydrology*, *119*(1-4), 1-12.

Molnar, I. L., C. S. Willson, D. M. O'Carroll, M. L. Rivers, and J. I. Gerhard (2014), Method for Obtaining Silver Nanoparticle Concentrations within a Porous Medium via Synchrotron X-ray Computed Microtomography, *Environ. Sci. Technol.*, *48*(2), 1114-1122.

Molnar, I. L., J. I. Gerhard, C. S. Willson, and D. M. O'Carroll (2015), The impact of immobile zones on the transport and retention of nanoparticles in porous media, *Water Resour. Res.*

Nelson, K. E., and T. R. Ginn (2011), New collector efficiency equation for colloid filtration in both natural and engineered flow conditions, *Water Resour. Res.*, *47*, 17.

O'Carroll, D., B. Sleep, M. Krol, H. Boparai, and C. Kocur (2013), Nanoscale zero valent iron and bimetallic particles for contaminated site remediation, *Adv. Water Resour.*, *51*(0), 104-122.

Pazmino, E. F., J. Trauscht, and W. P. Johnson (2014a), Release of Colloids from Primary Minimum Contact under Unfavorable Conditions by Perturbations in Ionic Strength and Flow Rate, *Environ. Sci. Technol.*, *48*(16), 9227-9235.

A version of this chapter has been published [*Molnar et al.*, 2015]

Pazmino, E. F., J. Trauscht, B. Dame, and W. P. Johnson (2014b), Power Law Size-Distributed Heterogeneity Explains Colloid Retention on Soda Lime Glass in the Presence of Energy Barriers, *Langmuir*, *30*(19), 5412-5421.

Pensini, E., C. M. Yip, D. O'Carroll, and B. E. Sleep (2013), Carboxymethyl cellulose binding to mineral substrates: Characterization by atomic force microscopy-based Force spectroscopy and quartz-crystal microbalance with dissipation monitoring, *Journal of Colloid and Interface Science*, *402*(0), 58-67.

Petosa, A. R., D. P. Jaisi, I. R. Quevedo, M. Elimelech, and N. Tufenkji (2010), Aggregation and Deposition of Engineered Nanomaterials in Aquatic Environments: Role of Physicochemical Interactions, *Environ. Sci. Technol.*, *44*(17), 6532-6549.

Phenrat, T., J. E. Song, C. M. Cisneros, D. P. Schoenfelder, R. D. Tilton, and G. V. Lowry (2010a), Estimating Attachment of Nano- and Submicrometer-particles Coated with Organic Macromolecules in Porous Media: Development of an Empirical Model, *Environ. Sci. Technol.*, *44*(12), 4531-4538.

Phenrat, T., H. J. Kim, F. Fagerlund, T. Illangasekare, and G. V. Lowry (2010b), Empirical correlations to estimate agglomerate size and deposition during injection of a polyelectrolyte-modified Fe-0 nanoparticle at high particle concentration in saturated sand, *Journal of Contaminant Hydrology*, *118*(3-4), 152-164.

Pinchuk, A. O. (2012), Size-Dependent Hamaker Constant for Silver Nanoparticles, *The Journal of Physical Chemistry C*, *116*(37), 20099-20102.

Qiu, C. Q., J. Han, H. Gao, L. P. Wang, and Y. Jin (2012), Pore-Scale Numerical and Experimental Investigation of Colloid Retention at the Secondary Energy Minimum, *Vadose Zone J.*, *11*(1).

Rajagopalan, R., and C. Tien (1976), TRAJECTORY ANALYSIS OF DEEP-BED FILTRATION WITH SPHERE-IN-CELL POROUS-MEDIA MODEL, *Aiche J.*, *22*(3), 523-533.

Rivers, M. L., D. T. Citron, and Y. B. Wang (2010), Recent developments in computed tomography at GSECARS, in *Developments in X-Ray Tomography Vii*, edited by S. R. Stock, Spie-Int Soc Optical Engineering, Bellingham.

Ross, S., and I. D. Morrison (1988), *Colloidal systems and interfaces*, Wiley, New York.

Ryan, J. N., R. W. Harvey, D. Metge, M. Elimelech, T. Navigato, and A. P. Pieper (2002), Field and Laboratory Investigations of Inactivation of Viruses (PRD1 and MS2) Attached to Iron Oxide-Coated Quartz Sand, *Environ. Sci. Technol.*, *36*(11), 2403-2413.

Saiers, J. E., and J. N. Ryan (2005), Colloid deposition on non-ideal porous media: The influences of collector shape and roughness on the single-collector efficiency, *Geophysical Research Letters*, *32*(21), L21406.

Scheibe, T. D., Z. S. Hou, B. J. Palmer, and A. M. Tartakovsky (2013), Pore-scale simulation of intragranular diffusion: Effects of incomplete mixing on macroscopic manifestations, *Water Resour. Res.*, *49*(7), 4277-4294.

Scheven, U. M., D. Verganelakis, R. Harris, M. L. Johns, and L. F. Gladden (2005), Quantitative nuclear magnetic resonance measurements of preasymptotic dispersion in flow through porous media, *Phys. Fluids*, *17*(11), 117107.

A version of this chapter has been published [*Molnar et al.*, 2015]

Shen, C., B. Li, Y. Huang, and Y. Jin (2007), Kinetics of Coupled Primary- and Secondary-Minimum Deposition of Colloids under Unfavorable Chemical Conditions, *Environ. Sci. Technol.*, *41*(20), 6976-6982.

Taghavy, A., A. Mittelman, Y. Wang, K. D. Pennell, and L. M. Abriola (2013), Mathematical Modeling of the Transport and Dissolution of Citrate-Stabilized Silver Nanoparticles in Porous Media, *Environ. Sci. Technol.*, *47*(15), 8499-8507.

Tong, M., and W. P. Johnson (2006), Excess Colloid Retention in Porous Media as a Function of Colloid Size, Fluid Velocity, and Grain Angularity, *Environ. Sci. Technol.*, *40*(24), 7725-7731.

Torkzaban, S., S. A. Bradford, and S. L. Walker (2007), Resolving the coupled effects of hydrodynamics and DLVO forces on colloid attachment in porous media, *Langmuir*, *23*(19), 9652-9660.

Torkzaban, S., S. S. Tazehkand, S. L. Walker, and S. A. Bradford (2008), Transport and fate of bacteria in porous media: Coupled effects of chemical conditions and pore space geometry, *Water Resour. Res.*, *44*(4).

Tufenkji, N., and M. Elimelech (2004a), Correlation equation for predicting single-collector efficiency in physicochemical filtration in saturated porous media, *Environ. Sci. Technol.*, *38*(2), 529-536.

Tufenkji, N., and M. Elimelech (2004b), Deviation from the classical colloid filtration theory in the presence of repulsive DLVO interactions, *Langmuir*, *20*(25), 10818-10828.

Tufenkji, N., and M. Elimelech (2005), Breakdown of colloid filtration theory: Role of the secondary energy minimum and surface charge heterogeneities, *Langmuir*, *21*(3), 841-852.

Tufenkji, N. (2007), Modeling microbial transport in porous media: Traditional approaches and recent developments, *Adv. Water Resour.*, *30*(6–7), 1455-1469.

Uyusur, B., C. J. G. Darnault, P. T. Snee, E. Koken, A. R. Jacobson, and R. R. Wells (2010), Coupled effects of solution chemistry and hydrodynamics on the mobility and transport of quantum dot nanomaterials in the vadose zone, *Journal of Contaminant Hydrology*, *118*(3-4), 184-198.

Wang, W., S. Efrima, and O. Regev (1998), Directing oleate stabilized nanosized silver colloids into organic phases, *Langmuir*, *14*(3), 602-610.

Yao, K.-M., M. T. Habibian, and C. R. O'Melia (1971), Water and waste water filtration. Concepts and applications, *Environ. Sci. Technol.*, *5*(11), 1105-1112.

Chapter 5

5 The impact of pore geometry and fluid velocity on the transport of nanoparticles in porous media

5.1 Introduction

Predicting the transport of Engineered Nanoparticles (ENPs) through the subsurface environment is necessary to protect groundwater resources and to efficiently remediate contaminated industrial sites. ENPs' are widely used in both industrial processes and consumer products [*Petosa et al.*, 2010]; their prevalence suggests that they may eventually be released to the subsurface environment and, if mobile in the subsurface, pose risks to municipal drinking water supplies or recreational surface water bodies. Bi-metallic engineered nanoparticles, such as nano-Zero-Valent-Iron (nZVI), are also being purposely injected into the subsurface environment at contaminated industrial sites to degrade industrial contaminants [*O'Carroll et al.*, 2013]. As a result, accurately predicting the transport of engineered nanoparticles through soil is valuable for both groundwater source zone protection and designing efficient site-remediation schemes.

However, current modelling approaches cannot adequately simulate nanoparticle transport through soil. The classic approach to continuum-scale modelling of nanoparticle transport typically employs the Advective-Dispersive equation which predicts a symmetric breakthrough concentration curve and a log-linear concentration profile of retained nanoparticles [*Molnar et al.*, 2015b]. While variations of this approach have been successfully employed to describe anomalous experimental transport behaviour arising from phenomena such as 'site blocking' [*Li et al.*, 2008; *Liu et al.*, 2009], a significant portion of nanoparticle transport experiments exhibit some degree of 'anomalous' behaviour that cannot be adequately explained, or described, by current models.

The observed 'anomalous' behaviours may involve concentration profiles of retained nanoparticles that are either hyperexponential [*Jiang et al.*, 2012a; *Jiang et al.*, 2012b;

Kasel et al., 2013; *Lanphere et al.*, 2013; *Liang et al.*, 2013a; *Liang et al.*, 2013b; *Wang et al.*, 2013a; *Wang et al.*, 2013b; *Wang et al.*, 2014a; *Wang et al.*, 2008; *Wang et al.*, 2012] or non-monotonic [*Chen et al.*, 2011; *Kasel et al.*, 2013; *Lanphere et al.*, 2013; *Li et al.*, 2008; *Liang et al.*, 2013a; *Liang et al.*, 2013b; *Solovitch et al.*, 2010; *Wang et al.*, 2013b; *Wang et al.*, 2014a; *Wang et al.*, 2008; *Wang et al.*, 2014b]. In addition, breakthrough concentration curves will often exhibit non-symmetrical extended tailing behaviour during the elution phase of a transport experiment [*Jiang et al.*, 2012a; *Jiang et al.*, 2012b; *Joo et al.*, 2009; *Kanel et al.*, 2015; *Molnar et al.*, 2015a; *Uyusur et al.*, 2010]. While these anomalous behaviours are similar to what is often observed for larger micron-sized colloids [*Molnar et al.*, 2015b], it is unknown if the processes governing the anomalous transport of nanoparticles are also responsible for the anomalous transport of micron-sized colloids. Nanoparticles may not be governed by the same processes as micon-sized colloids as nanoparticles possess unique physicochemical properties – such as a large degree of Brownian motion – due to their small size and large specific surface areas.

Despite a recent attempt at developing an empirical approach to predicting nanoparticle transport behaviour [*Goldberg et al.*, 2015], current nanoparticle transport models cannot adequately describe, or predict these anomalous behaviours. This inability to describe nanoparticle transport has led some to suggest that existing transport models do not capture pore-scale processes governing nanoparticle transport and retention [*Goldberg et al.*, 2014]. As such, a better understanding of the pore-scale processes governing nanoparticle transport is required to develop continuum-scale models which can simulate the observed 'anomalous' transport behaviour and, in addition, rigorous mechanistic approaches are needed to predict the continuum-scale models' parameters.

The classic Advective-Dispersive equation, when applied to nanoparticle transport through soil, typically contains a first-order kinetic rate term which describes nanoparticle retention (the first-order kinetic retention rate coefficient is denoted by k_{att}). The most commonly employed mechanistic model to predict k_{att} is Colloid Filtration Theory (CFT). CFT has been applied to a predict nanoparticle k_{att} for a wide range of nanoparticles and environmental conditions [*El Badawy et al.*, 2013; *Jaisi and Elimelech*,

2009; *Krol et al.*, 2013; *Lecoanet et al.*, 2004; *Lin et al.*, 2011; *Liu et al.*, 2009; *Mattison et al.*, 2011; *Phenrat et al.*, 2010a; *Phenrat et al.*, 2010b; *Ryan et al.*, 2002; *Taghavy et al.*, 2013; *Tong and Johnson*, 2006; *Wang et al.*, 2012]. CFT has two distinct components: a mechanistic particle transport model and an η-correlation equation. The mechanistic model employs a force/torque balance to determine colloid trajectories and attachment in the presence of a collector (or assemblage of collectors). This mechanistic model is run for a large number of colloids over a wide range of conditions and the fraction of approaching colloids which contact the collector surface (denoted as η and termed 'contact efficiency') under each condition is determined. The results from the mechanistic model are fit to a simplified 'η-correlation equation' which provides a simple tool for end-users to estimate η based on environmental conditions and particle type. The CFT-predicted η is then upscaled into the continuum-scale k_{att} and incorporated into a variation of the classical advective-dispersive equation.

There are a number of different CFT mechanistic models that employ different force/torque balances, environmental conditions, model geometries and η-correlation equations [*Cushing and Lawler*, 1998; *Ma et al.*, 2009; *Nelson and Ginn*, 2011; *Rajagopalan and Tien*, 1976; *Tufenkji and Elimelech*, 2004; *Yao et al.*, 1971]. These models are generally successful at predicting η and k_{att} for micron-sized colloids in favorable Derjaguin-Landau-Verwey-Overbeek (DLVO) conditions [*Molnar et al.*, 2015b]. DLVO conditions can include 'favorable conditions' wherein attractive forces (such as van der Waals and electrostatic attractive forces) between the colloid and grain dominate at all separation distances and there is no repulsive energy barrier preventing attachment of the colloid onto the grain. Unfavorable conditions refer to when repulsive DLVO forces (such as electrostatic repulsion) dominate at small separation distances, creating a potentially significant repulsive energy barrier that might prevent colloid deposition on to the collector surface. Soil/nanoparticle systems in unfavorable conditions exhibit relatively low nanoparticle retention rates compared to favorable conditions [*Petosa et al.*, 2010].

While the mechanistic models in CFT generally provide an excellent description of colloid retention for micron-sized colloids in porous media under favorable DLVO

conditions, mechanistic models and related correlation equations over predict nanoparticle retention in favorable DLVO conditions [*Molnar et al.*, 2015a; *Nelson and Ginn*, 2011]. Applying these over predicted η values to nanoparticle transport at the field-scale may result in over-predicting retention rates, under-predicting nanoparticle mobility and, thus, under-predicting the risk released nanoparticles would pose to nearby drinking water sources.

For unfavorable conditions, CFT mechanistic models and correlation equations are unable to predict experimental colloid retention rates. The most common approach to adapting CFT for use in unfavorable conditions is to employ an additional parameter (commonly denoted by α) termed 'attachment efficiency' which is determined by fitting an advective-dispersion-k_{att} model to experimental results. However, attempts at predicting α for unfavorable conditions, or even the studies that attempt to identify the influence of various parameters on α, are limited by the implicit assumption that CFT is able to accurately predict η.

It is likely that many of the pore-scale processes which yield the previously discussed anomalous nanoparticle transport behaviour also impact CFT's ability to accurately predict η and k_{att}. Thus understanding which pore-scale processes are not adequately represented by CFT will not only improve CFT's ability to predict k_{att}, but will also identify the processes which are potentially responsible for anomalous transport behaviour.

For instance, it has been hypothesized by pore-scale nanoparticle transport studies that CFT's over prediction of η was partially linked to the mechanistic models' pore and grain geometry which relies on a series of simplifying assumptions[*Boccardo et al.*, 2014; *Long and Hilpert*, 2009; *Molnar et al.*, 2015a]. The geometry typically assumes a perfectly spherical collector (or 'grain') surrounded by a spherical shell of fluid – termed the Happel-sphere-in-cell geometry (HSIC) [*Happel*, 1958; *Nelson and Ginn*, 2005; *Nelson and Ginn*, 2011; *Rajagopalan and Tien*, 1976; *Tufenkji and Elimelech*, 2004]. The HSIC geometry also assumes that there are no grain-grain contacts, which are ubiquitous in nature, which leaves it unable to account for any processes linked to that feature.

Molnar et al. [2015a] demonstrated how CFT's overprediction of η could be partially linked to 'immobile zones' (regions of relatively low fluid velocity) near grain-grain contacts as these immobile zones were limiting the rate at which nanoparticles could diffuse to the surface. While this immobile zone process was identified via comparisons to CFT, it was then shown to be responsible for anomalous extended tailing behaviour [*Molnar et al.*, 2015a].

However, the influence of other assumptions within the Happel-sphere-in-cell geometry on the accuracy of mechanistic CFT models and anomalous nanoparticle transport behaviour remains unclear. These other assumptions include whether the average flow field through a realistic porous medium can be approximated by the analytical solution of creeping flow through the Happel fluid envelope; or if approximating the entirety of the soil's pore-space as spherical shell of fluid is appropriate. The latter approximation carries the implicit assumption that all nanoparticles are flowing through the narrow fluid envelope. This assumption is fundamental to the Happel-sphere geometry and it remains unclear if this assumption is valid for nanoparticle transport through real media.

However, attempts at better understanding the processes governing anomalous transport behaviour and inaccurate CFT predictions are limited due to the difficulties of experimentally observing nanoparticles within realistic pore spaces. Column-scale transport studies are typically limited to inferring transport and retention mechanisms, due to their inability to observe nanoparticle behaviour within real pore spaces [*Molnar et al.*, 2015b]. Pore-scale studies of nanoparticle transport, which have provided valuable information on nanoparticle flow and transport, are typically limited to relatively simple two-dimensional micro-model systems which may not adequately incorporate all governing processes in real soil pore spaces. For instance, laser scanning cytometry was employed by May et al. [2012; 2013] to observe nanoparticle retention and re-entrainment during flow through a two-dimensional micro-model.

Other imaging techniques, X-ray Computed Microtomography (XCMT) in particular, have yielded significant insights into the pore-scale processes which govern the transport of contaminants such as NAPL's and micron-sized colloids. However XCMT has yet to

be widely applied to nanoparticle transport. XCMT imaging has been performed for micron-sized colloids as they can be easily observed due to their relatively high density and large particle diameter which can be larger than the XCMT resolution. This has been used to experimentally examine the deposition patterns of micron-sized colloids and colloidal aggregates which were then linked to reductions in the permeability of the porous medium [*Chen et al.*, 2008; *Chen et al.*, 2009; *Gaillard et al.*, 2007]. It was observed that colloids in unfavorable conditions will experience significant retention at grain-grain contacts (termed 'wedging') [*Li et al.*, 2006a; b]. Recently, Molnar et al. [2014] developed a quantitative-Synchrotron X-ray Computed Microtomography technique (qSXCMT) to accurately determine the changing pore-scale concentrations of nanoparticles in packed soil columns during nanoparticle transport experiments. Molnar et al. [2015a] employed qSXCMT to determine, as described above, that regions of low fluid velocity (termed 'immobile zones') were limiting nanoparticle rates in the soil and responsible for extended tailing behaviour.

In this study, qSXCMT is employed to determine, for the first time, the averaged distribution of nanoparticle mass flux within a soil's pore spaces. To do this, qSXCMT was coupled with CFD to characterize the averaged pore-scale nanoparticle distribution and flow field during a real 1-dimensional column nanoparticle transport experiment. The column experiment injected a silver nanoparticle solution into a uniform quartz sand in unfavorable DLVO conditions and was imaged via qSXCMT at regular intervals during nanoparticle injection and elution. First, this study characterized the distribution of pore space within the soil and examined how well bulk-measured lab properties (i.e., soil sieve analysis) described the real pore and grain geometry. Then, the distribution of fluid velocity through the soil was ascertained via CFD modelling and compared to analytical solutions for creeping flow around the idealized Happel Sphere in Cell geometry commonly employed by CFT mechanistic models. Next, the distribution of nanoparticle mass within the pore space was determined and coupled with the CFD-simulated velocity distribution to estimate the distribution of silver nanoparticle mass flux and mass flow rates. The implications of these findings are discussed in the context of anomalous nanoparticle transport behaviour as well as colloid filtration theory mechanistic models.

5.2   Materials and Methods

A silver nanoparticle (nAg) transport experiment was undertaken at the GeoSoilEnviro Center of Advanced Radiation Sources (GSECARS) 13-BM-D beamline during an allotted 24-hour SXCMT time slot at the Advanced Photon Source (APS) at the Argonnne National Lab. The experimental method is described in detail in [*Molnar et al.*, 2015a]; a summary of the relevant details are provided here. Note that the nAg transport experiment and corresponding SXCMT datasets examined here were also used in Molnar et al. [2015a], there described as the 'Uniform Quartz' dataset. The analysis presented here is entirely new; this paper does not re-use or re-present any results from the Molnar et al. [2015a] study

5.2.1   Materials

Silver nanoparticles were synthesized by reducing silver nitrate (0.1N, Alfa Aesar) with sodium borohydride (Granulated, 97+%, Alfa Aesar) and electrosterically stabilized with a 1% solution of carboxymethylcellulose 90k (CMC90k) [*Molnar et al.*, 2014; *Molnar et al.*, 2015a]. The synthesis procedure occurred at the GSECARS wet lab the day before the allotted synchrotron beam time. The synthesized silver nanoparticles had an average hydrodynamic diameter (d_{50}) of 29.8 nm, a zeta potential of -27.97 mV and the final CMC90k stabilized solution had a viscosity of 14 cP.

The porous medium employed for the transport experiment was a quartz sand (Unimin Accusand) that had been cleaned by rinsing with Nitric Acid (Environmental grade, Alfa Aesar) followed by rinsing with deionized water and left to dry overnight. The sand was sieved to achieve a specific grain size distribution (see Table 5.1) and was then wet-packed into a small aluminum column (ID: 5.6 mm, length: 5 cm). The solution used for wet packing contained no nanoparticles but was controlled to the same viscosity (i.e. 1% CMC90k solution at 14 cP) and ionic strength (120 mM) as the nAg solution. The porosity of the column (see Table 5.1) was determined by measuring the specific gravity of the sand (2.65 g/cm^3) and weighing the amount of sand packed into the column.

5.2.2   Silver nanoparticle transport experiment

The packed column was loaded into the GSECARS 13-BM-D imaging hutch and a pre-injection image was collected. Following the pre-injection imaging, the silver nanoparticle solution was injected into the column with a syringe pump at a rate of 0.11 mL/min (see Table 5.1 for overview of associated hydraulic parameters). The flow direction was upwards through the column. A total of 3 pore volumes (PV's) of nAg solution was injected into the column and qSXCMT imaging occurring at 0.25, 0.5, 0.75, 1 and 2 PV's of injection. All flow through the column was stopped during qSXCMT imaging. The concentration of silver nanoparticles in the injection solution was measured at the beginning and end of the nAg injection period via acid-digestion and ICP-OES analysis. The average silver nanoparticle concentration being injected into the column was determined to be 2.48 g/L (+/- 0.06 g/L).

After 3 PV's of injecting the nAg solution, the input was switched to a 1% CMC90k solution with no silver nanoparticles – controlled to the same pH and ionic strength as the wet packing and nAg solutions – to flush the nanoparticles out the column. The column was imaged after 1 and 2 PV's of elution and elution continued for an additional 5 PV's (7 PV's of elution total) with no additional qSXCMT imaging. During injection and elution, samples were collected from the column's effluent and analyzed for total silver concentration via ICP-OES and acid-digestion. The results from the effluent sampling are presented elsewhere [*Molnar et al.*, 2015a] and will not be discussed here.

It should be noted that the results of this study are presented in terms of SXCMT pore volumes (SXCMT-PV's) injected, not total column pore volumes. An SXCMT-PV is defined as the pore space between the bottom of the column and the center of the imaging window whereas a total column pore volume (PV's) refers to the pore volume of the entire column (approximately 0.4 mL). Thus '1 SXCMT-PV's injected' refers to when the advective front of the injected nAg solution reaches the center of the SXCMT imaging window. qSXCMT imaging occurred at 0.4, 0.9, 1.3, 1.8, 3.6, 7.2 and 8.9 SXCMT-PV's corresponding to 0.25, 0.5, 0.75, 1, 2, 4 and 5 total column pore volumes. The column was imaged at its midpoint which was 2.55 cm above the base of the porous medium. The length of column section imaged (referred to as the 'SXCMT imaging

window') was 0.51 cm and extended from 2.55 cm to 3.06 cm above the base of the column.

Table 5.1: Overview of soil and hydraulic properties of the uniform quartz column experiment[a]

Porous Medium	Porosity (%)	Sieved Grain Size (µm)	Pore Water Velocity (cm/min)	Volumetric Flow Rate (mL/min)	Co Average (g/L)	Reynold's Number
Uniform Quartz	33	420 – 600	1.38	0.11	2.48	0.0079

[a]These are column-scale properties, determined via lab techniques during experimentation.

5.2.3   SXCMT imaging, reconstruction and analysis

The specific imaging procedure required for qSXCMT imaging of silver nanoparticles in a porous medium is discussed in detail elsewhere [*Molnar et al.*, 2014; *Molnar et al.*, 2015a]. Briefly, during qSXCMT imaging all flow through the column was stopped and all hydraulic valves were closed. Each collected image (i.e., 0 PV, 0.25 PV etc…) required approximately 40 minutes of imaging time during which time the fluid in the column was stagnant. During this 40 minutes of imaging time, the column was imaged at 4 separate energies below and above the Ag k-edge (25.514 keV). The imaged energies were: 25.414, 25.614, 25.714 and 25.814 keV. For each energy, 1440 2-dimensional projections were captured as the column rotated 180°. The voxel resolution of the collected images was determined to be 9.87 µm/voxel. Image reconstruction produced a 3-dimensional dataset of x-ray linear mass attenuation values averaged over a 9.87×9.87×9.87 µm voxel. So each imaged time-step (e.g., 0 PV, 0.25 PV, 0.5 PV etc…) had 4 corresponding 3-dimensional datasets of x-ray linear mass attenuation values.

Sub-volumes of 350×350×450 voxels were cropped from each of the 4 reconstructed datasets at each time-step to remove edge effects and column (i.e., aluminum) material. The reconstructed 25.614 keV sub volumes for each time-step underwent a segmentation into water and solid (i.e., grain) using an indicator kriging technique [*Bhattad et al.*, 2010; *Oh and Lindquist*, 1999]. Grain characteristics and pore-network structure within each segmented image were then extracted and characterized using the method of

Thompson et al. [2006; 2008]. This method assigns a unique identifier to every pore and grain within the segmented sub-volumes as well as topological properties. The three-dimensional segmented sub-volume of the pre-injection dataset presented in Figure 5.1A to illustrate the structure of the porous medium within the SXCMT imaging window. A two-dimensional slice of the raw reconstructed gray values from the same dataset is also presented in Figure 5.1B to illustrate the internal structure of the medium within the SXCMT imaging window. In addition, the distances between every pore space voxel and the closest grain surface voxel was identified and measured using the unique pore and grain identifiers. The algorithm used to find the closest grain surface voxel for each pore space voxel, and measure the distance between the two, is detailed in Appendix 10.1.
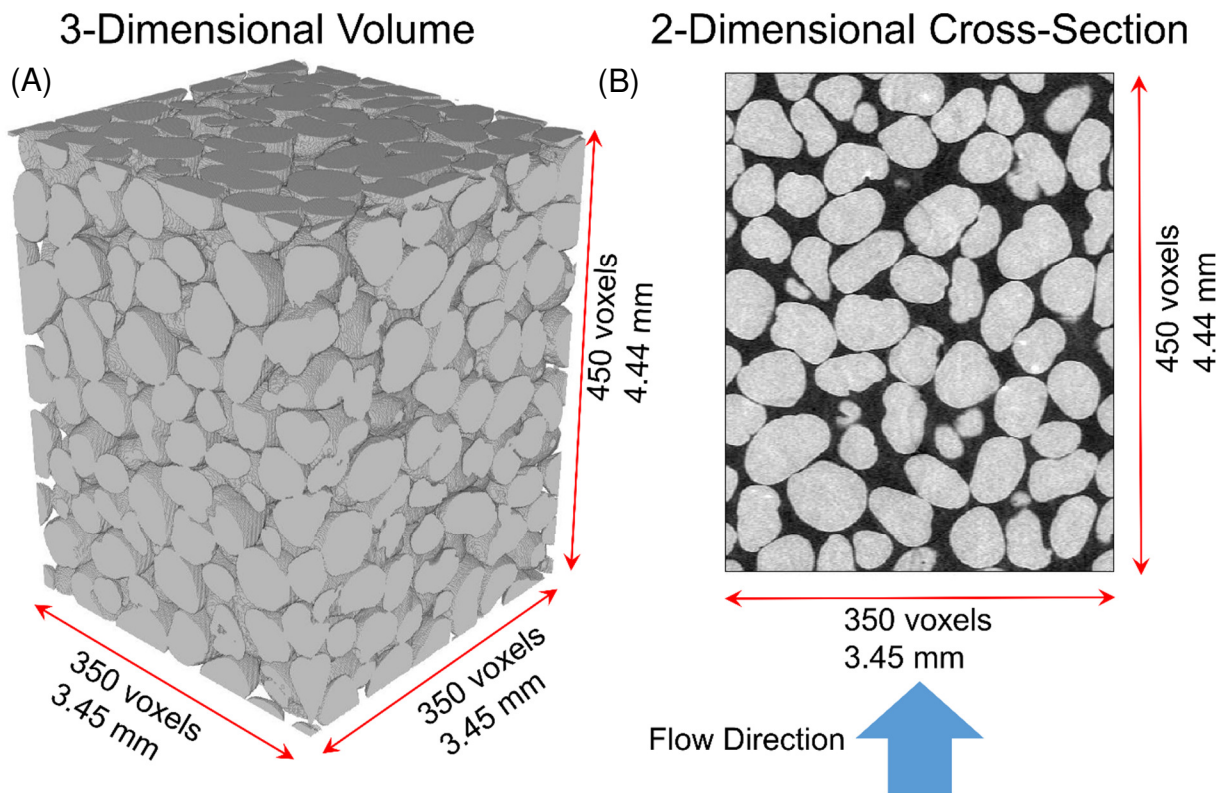
Figure 5.1: Images of the pre-injection uniform quartz SXCMT dataset. A:The 3-dimensional segmented sub volume is presented to illustrate the overall structure of the medium. B: A representative 2-dimensional gray-value (i.e., non-segmented) slice is presented to illustrate the internal structure of the medium. The grains are coloured gray while the pore space is either transparent (left, segmented) or black (right, gray value). Flow direction is upwards (indicated by the blue arrow).

5.2.4 Quantifying silver nanoparticle concentrations within the SXCMT sub-volumes

The method of Molnar et al. [2014] was employed to convert the 4 sub-volumes of x-ray linear mass attenuation to SXCMT-determined nanoparticle concentrations. For each time-step, the below k-edge sub-volume (25.414 keV) was subtracted from the three above k-edge subvolumes to create three difference images (25.614-25.414 keV, 25.714-25.414 keV and 25.814-25.414 keV). A modified form of Beer's law was employed to calculate the SXCMT-determined concentration for every pore space voxel in each of the three difference datasets. The SXCMT-determined concentrations in the three difference datasets were then averaged together and calibrated using the procedure described in Molnar et al. [2015a] to create a single dataset of SXCMT-determined concentration for each time-step.

This qSXCMT procedure does not accurately determine nanoparticle concentration on a voxel-by-voxel basis due to noise associated with SXCMT imaging and reconstruction and is unable to determine concentrations of nanoparticles retained on the soil surface. However, analyzing the approximately 16 million voxels with various averaging techniques can accurately quantify average changes in nanoparticle concentrations within the bulk pore space in space and time [*Molnar et al.*, 2014; *Molnar et al.*, 2015a].

Moreover, this qSXCMT method is currently unable to accurately determine nanoparticle concentrations within 17.3 μm of the grain surface due to a noted 'shadow zone' effect caused by x-ray refraction occurring at the grain/pore interface (this width is experiment specific and should not be taken as a general value) [*Molnar et al.*, 2014]. Thus, all pore-space voxels within the 'shadow zone' in each SXCMT-determined concentration dataset are discarded during this quantification and calibration process.

5.2.5 Fluid Dynamics Modeling within the SXCMT datasets

Computational Fluid Dynamics (CFD) modelling was employed to determine the uniform quartz's fluid flow field in the 0 PV (i.e., pre-injection) SXCMT dataset. A single dataset was employed for CFD modeling (0 PV) as it was assumed that the flow field did not change throughout the injection or elution period; this is supported by the fact that the

extracted pore network statistics were similar for all time steps. For CFD modeling, a sub-section of the total SXCMT-dataset had to be created due to the large computational cost of obtaining a mesh-independent solution. The cropped sub-volume was approximately 150×150×350 voxels (1.48×1.48×3.45 mm). The porosity of the cropped CFD sub-volume (32%) is close to the porosity of the total column (33%) and the sub-volume illustrated in Figure 5.1 (29%).

CFD modeling was conducted in ANSYS FLUENT 13.0 which solves the continuity (eq. 5.1) and Navier-Stokes equations (eq. 5.2):

$$\nabla v = 0 \qquad\qquad\qquad 5.1$$

$$\rho v \cdot \nabla v = -\nabla p + \mu \nabla^2 v \qquad\qquad\qquad 5.2$$

where v is fluid velocity, ρ is the fluid density, p is pressure and μ is the fluid viscosity. FLUENT solves eq. 5.1 and eq. 5.2 using a finite-volume method on an unstructured grid. The cropped sub-volume was meshed in ICEM-CFD 13.0. The meshed volume was qualitatively compared to the gray-scale (i.e., raw) cropped sub-volume and segmented cropped sub-volume to ensure that the geometry of the pore and grain network was retained during the segmentation and meshing procedures.

Constant pressure boundary conditions were applied at the inlet and outlet boundaries. The pressure drop was varied until the average upwards vertical velocity matched the pore water velocity in Table 5.1. The grain surfaces were set to 'no flow' boundaries and the sides of the domain were set to 'perfect slip' to allow flow parallel to the sides of the domain, but not across it. Convergence of the simulation was determined by tracking fluid mass flow rates and average velocity within the dataset. Confidence in the simulated flow field was developed by back calculating soil permeability based on the pressure drop applied across the inlet/outlet boundaries, the solution viscosity (14 cP) and the resulting average fluid velocity. The simulated permeability (1.4×10^{-6} cm^2) is consistent with those experimentally determined for similarly sized sands (e.g., 6.4×10^{-7} cm^2 [*O'Carroll et al.*, 2004]). However, it is important to note that this only ensures that the

average simulated flow properties are approximately consistent with the average experimental flow. This was deemed sufficient as this study focuses on average behavior and does not compare nanoparticle concentrations and simulated flow behaviour on a voxel-by-voxel basis.

5.2.6　Fluid Dynamics within the Happel Sphere-in-Cell Geometry

An analytical solution was employed to solve for the fluid flow through the Happel Sphere-in-Cell geometry. The flow regime through this geometry is assumed to be creeping flow and is described via the continuity (eq. 5.1) and Stokes flow (eq. 5.3) equations:

$$\nabla p = \mu \nabla^2 v \qquad\qquad 5.3$$

The solution to the velocity vectors in the Happel Sphere-in-Cell geometry are not explicitly published in any of the mechanistic model papers [*Elimelech*, 1994; *Nelson and Ginn*, 2005; *Nelson and Ginn*, 2011; *Rajagopalan and Tien*, 1976; *Tufenkji and Elimelech*, 2004]. However, the general stream function and Happel-specific coefficients published in Elimelech [1994] can be used to explicitly solve for v_r and v_θ in the Happel geometry:

$$v_r = U cos\theta \left[k_1 \left(\frac{a_s}{x}\right)^3 + k_2 \frac{a_s}{x} + k_3 + k_4 \left(\frac{x}{a_s}\right)^2 \right] \qquad\qquad 5.4$$

$$v_\theta = -U sin\theta \left[-\frac{1}{2}k_1 \left(\frac{a_s}{x}\right)^3 + \frac{1}{2}k_2 \frac{a_s}{x} + k_3 \right.$$
$$\left. + 2k_4 \left(\frac{x}{a_s}\right)^2 \right] \qquad\qquad 5.5$$

$$k_1 = \frac{1}{w} \qquad\qquad 5.6$$

$$k_2 = -\frac{(3 + 2p^5)}{w} \qquad\qquad 5.7$$

$$k_3 = \frac{(2 + 3p^5)}{w} \qquad\qquad 5.8$$

$$k_4 = -\frac{p^5}{w} \qquad\qquad 5.9$$

$$w = 2 - 3p + 3p^5 - 2p^6 \qquad\qquad 5.10$$

$$p = (1 - n)^{\frac{1}{3}} \qquad\qquad 5.11$$

where v_r and v_θ are the fluid velocities in the radial and tangential directions, U is the approach (i.e., Darcy) velocity, a_s is the radius of the spherical collector and x is the distance away from the collector surface and n is the porosity. The variables k_1, k_2, k_3 and k_4 are functions of w and p, which are dimensionless functions of porosity. It should be noted that the velocity vectors in 5.4 and 5.5 are only definable between x = 0 and x = r (i.e., within the Happel fluid envelope) where r is given by:

$$r = a_s(1 - n)^{-1/3} - a_s \qquad\qquad 5.12$$

In the analysis within this paper this analytical solution to the velocity vectors in the Happel Sphere model is combined to calculate the magnitude of the velocity over a range of θ and r values (i.e., $v = \sqrt{v_r^2 + v_\theta^2}$).

5.3   Results and Discussion

The results and discussion presented within this study is divided into three separate sections. The first compares the Happel Sphere-in-Cell model geometry to the pore and grain network extracted from the SXCMT datasets. The second compares the analytical solutions of fluid flow through the Isolated Sphere and Happel Sphere-in-Cell geometries to the CFD-simulated flow field in the SXCMT-CFD dataset. The third examines the distributions of nAg mass, mass flux and mass flow through the SXCMT-determined concentration datasets. In all three of the subsections, the results and discussions highlight whether the Happel Sphere-in-Cell geometry is appropriate for approximating nanoparticle transport through the imaged pore geometry.

5.3.1   Happel Sphere vs. SXCMT pore and grain geometry

The porosity of the SXCMT-dataset (29%) is lower than the overall packed column (33%), however the values are similar enough that the pore and grain network statistics can be taken as approximately equivalent to the pore and network throughout the experimental column. The grain and pore network statistics were compiled by examining 329 uniquely identified sand grains, 2,139 pore bodies and 26,362 pore throats (the narrow region connecting two larger pore bodies) . The total number of unique grains and pores within the dataset is significantly larger (619 grains and 3802 pores), however the extra grains and pores were excluded from the pore network analysis as they were only partially present within the dataset. The grains within the dataset were significantly non-spherical, as the average length of each grain's longest axis was longer than the length of the grain's shortest axis (the inscribed radius) by a factor of 1.64 (the Grain Aspect Ratio). This average grain aspect ratio is consistent with one previously published [*Willson et al.*, 2012], suggesting that the characteristics of the sand employed in this study is typical of sandy media. The average grain aspect ratio is qualitatively consistent with the images of the SXCMT dataset in Figure 5.1. The average pore inscribed radii is 59.4 μm and the average throat inscribed radii is 39.9μm.

Employing any CFT-HSIC mechanistic model (or η-correlation equation) to describe the silver nanoparticle transport experiment assumes that all fluid flow and nanoparticle

transport is occurring within a fluid envelope surrounding a spherical collector (illustrated in Figure 5.2). The width of this fluid envelope (r, illustrated in Figure 5.2) is defined so that the porosity of the Happel Sphere-in-Cell (HSIC) geometry (the volume ratio of fluid envelope:spherical collector) is equivalent to the macroscopic porosity of the porous medium and is calculated from eq. 5.12. This definition of the fluid envelope, along with eq. 5.12, is used throughout the CFT literature [*Elimelech*, 1994; *Nelson and Ginn*, 2005; *Nelson and Ginn*, 2011; *Rajagopalan and Tien*, 1976; *Tufenkji and Elimelech*, 2004] as it is a relatively simple method for accounting for porosity as well as the influence of neighbouring collectors on the fluid velocity.

Applying eq. 5.12 to calculate the dimensions of the Happel Sphere-in-Cell geometry (Figure 5.2) requires bulk measurements of the soil's properties from lab-scale analyses. Sieve analysis of the uniform quartz sand mixture (detailed in Table 5.1) determined the average radius of the sand ($a_s = 255$ µm), and the porosity of the packed column (as listed in Table 5.1, 33%) was determined during packing. From these values, and eq. 5.12, the calculated width of the HSIC fluid envelope was 36µm. Thus the HSIC geometry, applied to the transport experiment examined within this study, approximates all the pore space as being within a 36µm-thick fluid envelope.
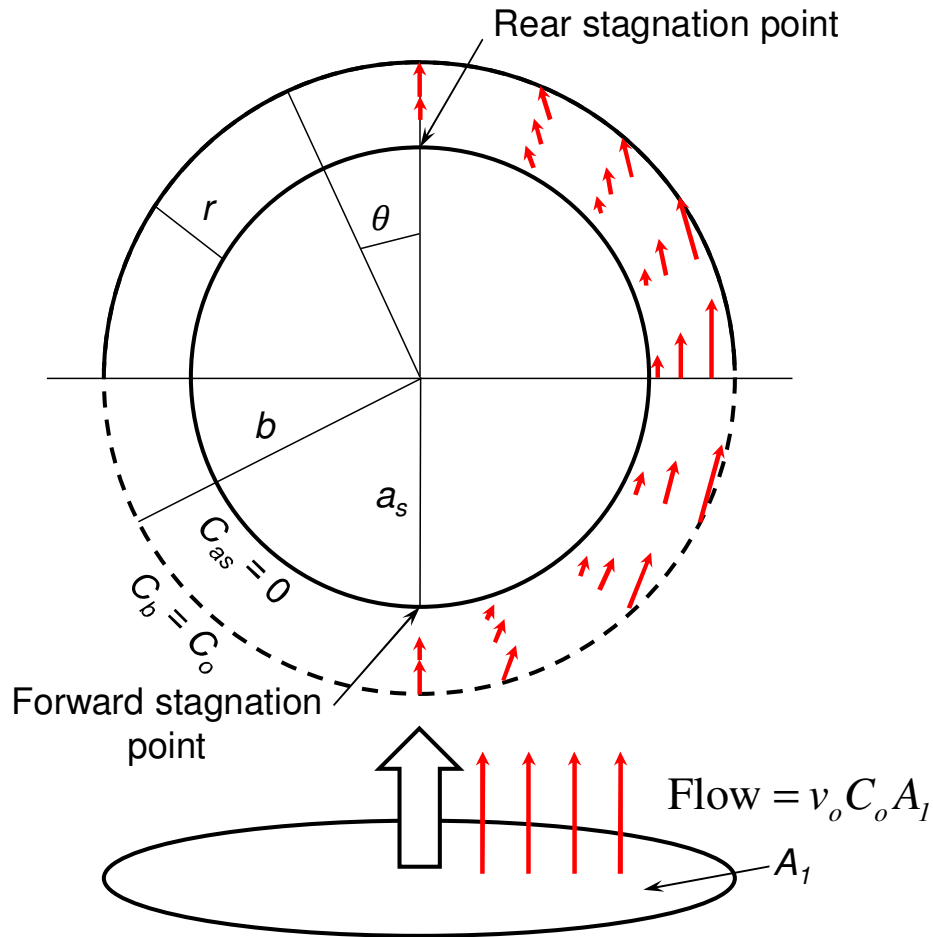
Figure 5.2 Overview of the standard 'Happel Sphere in Cell' geometry commonly employed by Colloid Filtration Theory mechanistic models (reproduced from Molnar et al. [2015b]). Colloid radius: a_s, radius of fluid film: b, thickness of fluid film: r. The red arrows on the right side of the geometry approximate the fluid velocity vectors from the analytical stokes flow solution in eq.'s 5.4 and 5.5. C_b and C_{as}: the concentration boundary conditions employed by Tufenkji and Elimelech [2004], these boundary conditions do not apply to mechanistic models employing discrete particle tracking. The angle θ represents the angle away from the axis running through the collector's center of mass in the direction of flow.

The width of the HSIC envelope, 36μm, is closer in size to the average pore throat inscribed radii than the average pore body inscribed radii in the SXCMT dataset. This suggests that a majority of the uniquely identified pore bodies have some volume of pore fluid that is at least 23μm further away from a grain surface than considered by HSIC. The difference between pore body width and HSIC fluid envelope width is illustrated by Figure 5.3.

The relative widths of the HSIC fluid envelope (r) and collector radii (a_s) are drawn to scale for:
a_s = 255 μm, r = 36 μm and n = 0.33
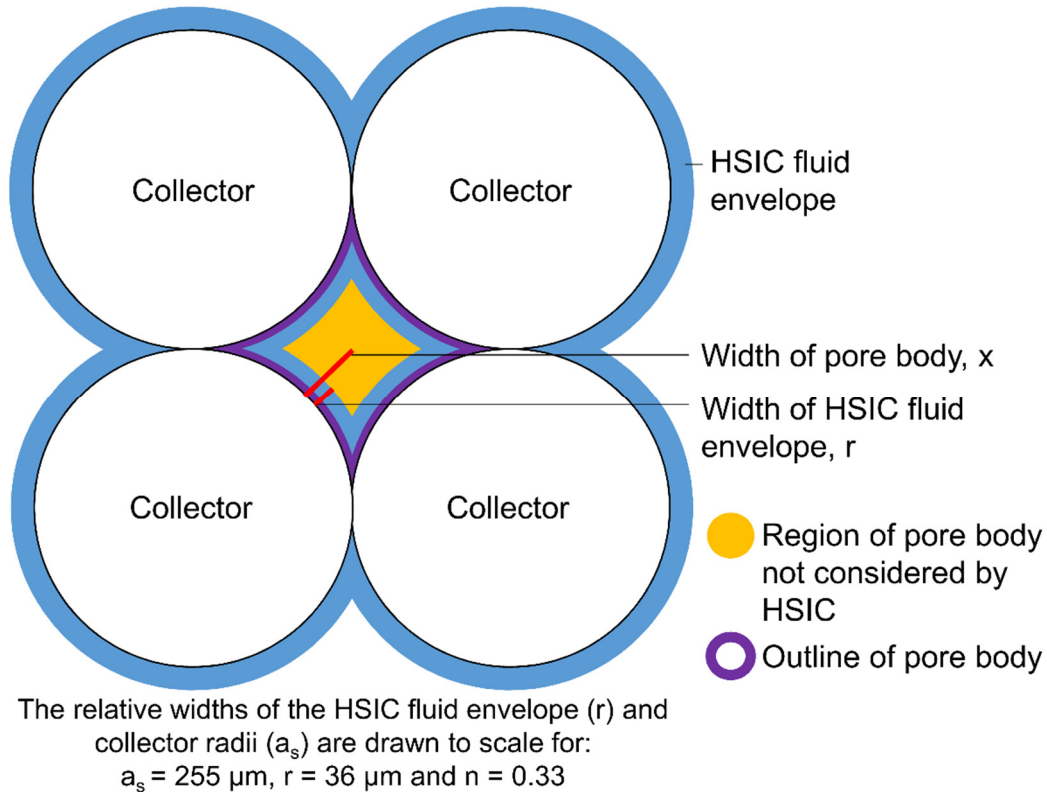
Figure 5.3: A depiction of how a pore body (outlined in purple) surrounded by a four circular collectors will have a portion of pore space that is within the region considered by the HSIC's fluid envelope (blue) and a portion of pore space that is outside of the region considered by the HSIC fluid envelope (outlined in orange).

The difference between the SXCMT dataset's pore geometry and the HSIC is further highlighted by plotting the pore network statistics as a cumulative percentage in Figure 5.4. The average Grain Effective Radius (defined as the average of the grain's short axis radius and long axis radius) within the SXCMT dataset is consistent with the radius of the spherical collector in the HSIC geometry. This is to be expected as the radius of the HSIC collector is determined by the results of the laboratory sieve analysis. The consistency between the HSIC collector radius and the average Grain Effective Radius suggests that 1) the image segmentation routine accurately identified the boundary of the soil/grain interface and 2) the grains within the SXCMT dataset are representative of the overall sand mixture used to pack the column. In addition, the distribution of grain effective radii within the SXCMT dataset ranges from roughly 200 – 300 μm (i.e., grain effective diameter = 400 – 600 μm) and is consistent with the sieve analysis in Table 5.1. The

grain effective radius tailing towards 0 μm in Figure 5.4 is likely due to the fact that the cropping procedure for the network analysis could not remove all partial grains from the statistics analysis.

The distribution of pore bodies in Figure 5.4 suggests that of the uniquely identified 2,139 pore bodies, approximately 80% have a radius equal to, or larger than, the width of the HSIC fluid envelope (36μm). This means that within 80% of pores, some fraction of nanoparticles will be further away from the grain surface than expected by CFT-HSIC models. For example, the largest pore within the dataset has an inscribed radii of 160 μm and therefore nanoparticles can be upwards of 124μm further away from a grain surface than expected by CFT-HSIC models. This trend is consistent with pore throats as well, of the 26,362 uniquely identified pore throats approximately 50% are larger than the HSIC fluid envelope and can range up to 130 μm in radius.

Figure 5.4: Cumulative size distributions of the grains (black circles), pores (blue triangles) and pore throats (red squares) within the pore network of the 1.8 SXCMT-PV dataset. The dataset was cropped 175 μm on each side to minimize edge effects from grains, pores and throats that were partially in the SXCMT dataset. Inscribed radius refers to the radius of the largest sphere that can

be drawn entirely within the body. Effective radius is an average of the inscribed radius and the length of the grain's longest axis. Effective radius is not definab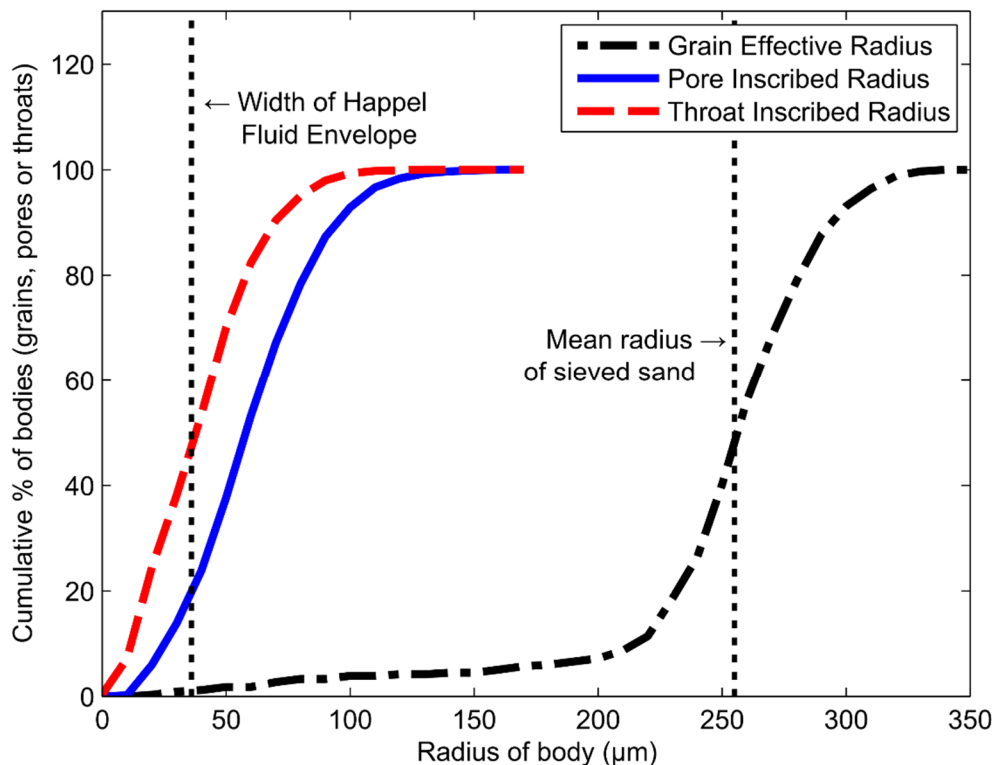le for pore or throat bodies and is not plotted for them. The leftmost vertical dotted black line represents the width of the Happel fluid envelope (*r* from Figure 5.2). The rightmost vertical dotted black line represents the average radius of sand packed into the experimental column as measured by soil sieve analysis.

Figure 5.5A illustrates how the volume of pore space in the 0 SXCMT-PV dataset changes as a function of distance from the nearest grain surface for the HSIC geometry and the SXCMT-dataset. For the SXCMT-dataset used in the pore space analysis, the distance between every pore space voxel and the nearest grain surface was measured. The pore space voxels were then sorted in to bins representing 9.87 μm intervals from the grain surface (i.e., intervals corresponding to the length of 1 voxel). The number of voxels in each bin was divided by the total number of pore space voxels (approximately 16,000,000) to determine the percentage of pore space within each 9.87 μm bin from the grain surface. Two SXCMT-datasets are plotted, the full SXCMT dataset and the smaller SXCMT-CFD dataset. A comparison of the two datasets in Figure 5.5A indicates that the overall geometry of the pore space is the same for the SXCMT-determined concentration datasets and the SXCMT-CFD dataset. To determine the distribution of pore space in the HSIC geometry, the volume of thin fluid shells were calculated in 9 μm intervals using the geometric equation for volume of a sphere (9 μm intervals were used instead of the SXCMT resolution of 9.87 so that 4 data points would not over-estimate the volume of HSIC pore space).

Figure 5.5 reveals that the volume of pore space in the SXCMT datasets decreases with each increment of distance from a grain surface, indicating that there is more pore space near the grain surface than at the centers of the pores (this is qualitatively illustrated in Figure 5.3). This decreasing trend in the real porous media is the opposite of what is encountered within the HSIC geometry. Within the HSIC geometry, pore volume increases with increasing distance from a grain surface. The trend of increasing pore space with distance arises from the HSIC conceptual model where a collector is surrounded by a sphere of fluid (illustrated in Figure 5.2). Given that the volume of a sphere is a cubed function of radius, the pore space volume in the HSIC geometry is greatest near the edges of the sphere. In Figure 5.5B, these trends are plotted as a cumulative percentage of total pore space (the total percentage of pore space that is closer

to the grain surface than a certain distance). It demonstrates that the cumulative distribution of the near-grain pore space is similar between the SXCMT datasets and the HSIC geometry. In fact, 50% of all pore space in both the porous media and HSIC model is approximately 20-25 μm from a grain surface. However, Figure 5.5B highlights that 25% of the entire pore space is further away from the grain surface than expected by the HSIC geometry. The difference in maximum pore size between Figure 5.4 and 5.5 is due to the fact that no cropping was performed for Figure 5.5.

The trends in pore size and pore space distribution highlighted in Figures 5.4 and 5.5 suggests that the HSIC model, purely on the basis of pore geometry, will treat flow and transport processes as being much closer to the grain surface than they would be within the medium-to-larger pores in the SXCMT dataset. This is because the HSIC geometry approximates all pore space as being $0 - 36$ μm away from a grain surface despite the pore space distribution in the SXCMT dataset ranging from $0 - 197$ μm away from a grain surface in Figure 5.5. Thus flow and transport processes such as the diffusive flux of nanoparticles towards grain surface, which could be occurring upwards of 197 μm, away from a grain surface will be treated by HSIC as being within 36 μm of a grain surface. Approximately 80% of all uniquely identified pore bodies are affected by this pore space compression, and 25% of the total pore space in the SXCMT-dataset is treated by the HSIC geometry as being much closer to a grain surface than it actually is. Given the similarities in grain shape between this study and a previous study [*Willson et al.*, 2012], this trend is likely widely present in sand media.

Overall, these results suggest that there is a significant volume of pore space further from the grain surface than allowable within the HSIC geometry. The next section will examine the distribution of flow velocities within the SXCMT-CFD dataset which will be compared to the analytical solution of flow around the HSIC envelope.
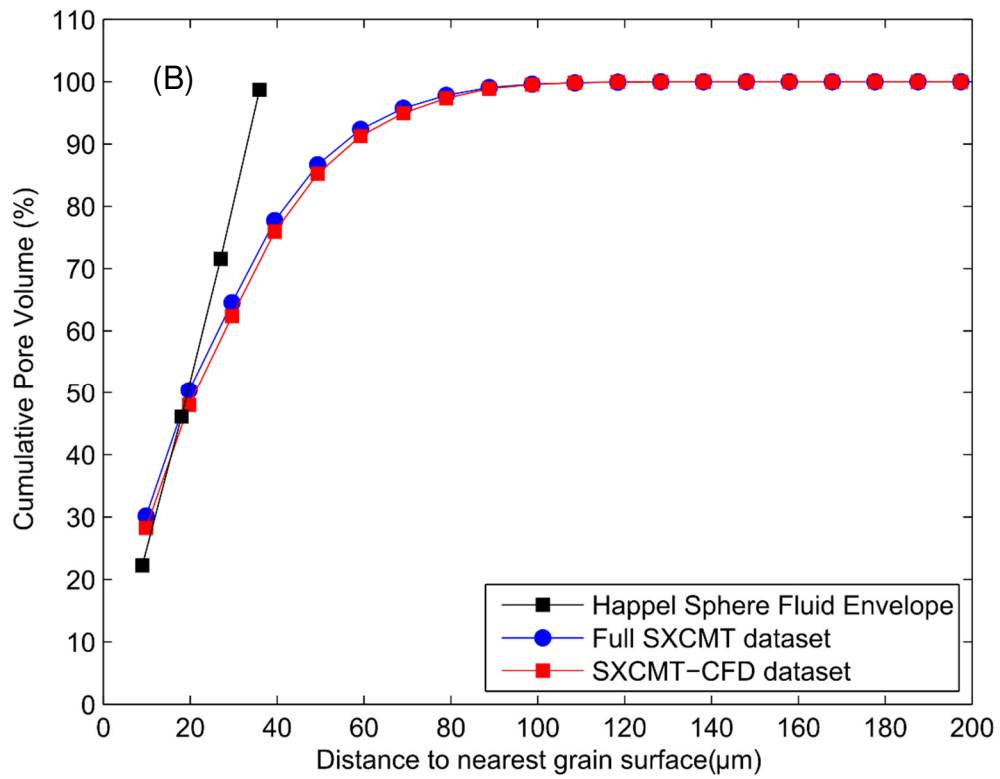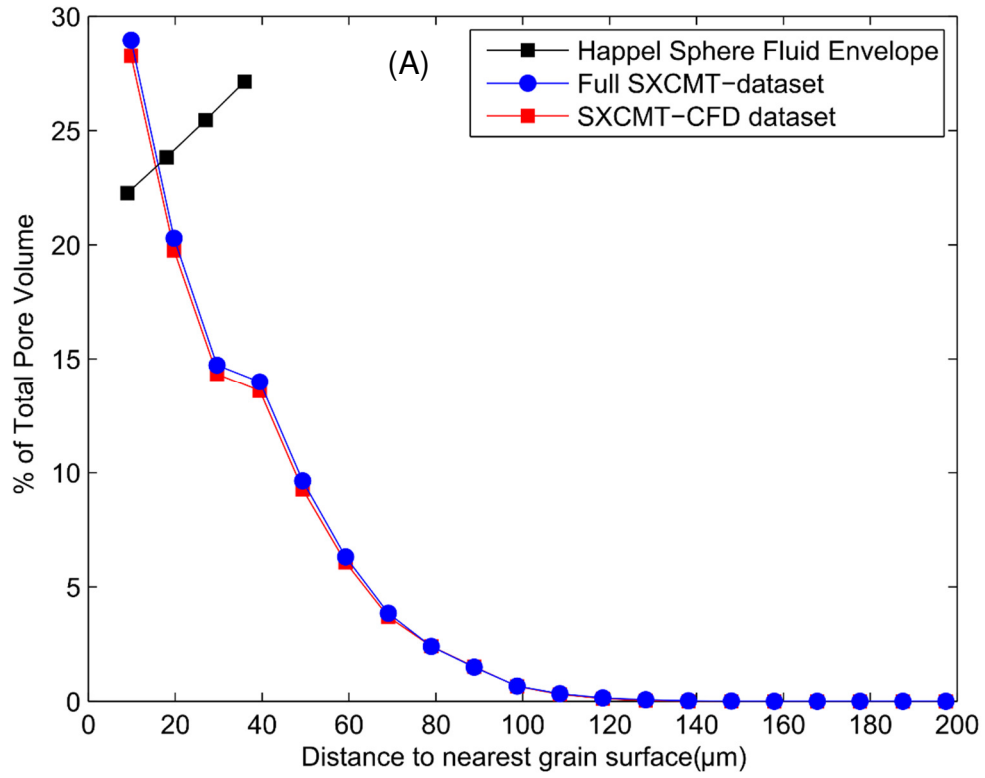
Figure 5.5A: The percentage of pore space as a function of distance from the nearest grain surface for the Happel sphere geometry (black squares), the full SXCMT-dataset (blue circle) and the SXCMT-CFD dataset (red square). Percentage refers to the amount of the geometries' pore space that is within a certain range of the grain's surface.

Figure 5.5B: The cumulative percentage of pore space as a function of distance from the nearest grain surface. Cumulative percentage refers to the amount of the geometries' pore space that is between the grain surface and a certain distance. For instance, the top image indicates that 20% of the SXCMT dataset's pore space is within 17 - 25μm of a grain surface. The bottom image indicates that 50% of the SXCMT dataset's pore space is 0 – 25 μm from a grain surface.

5.3.2   Happel sphere vs. SXCMT flow field

One of the major assumptions within the mechanistic CFT-HSIC model is that the fluid flow may be described by an analytical solution of the Stokes flow equation [*Nelson and Ginn*, 2011; *Rajagopalan and Tien*, 1976; *Tufenkji and Elimelech*, 2004]. This solution is subject to certain flow boundary conditions described by Rajagopalan and Tien [1976]. By employing these analytical solutions in a mechanistic model, creeping flow is assumed (i.e., Re << 1) where the inertial component of flow is negligible relative to viscous forces. The Reynold's number (Re) for the uniform quartz transport experiment (Table 5.1) indicates that flow is within the creeping regime.

Simulated velocity contours and streamlines in SXCMT-CFD subvolume

Averaged CFD-simulated flow through SXCMT-CFD subvolume

Creeping flow through a Happel-sphere-in-cell model [Rajagopalan and Tien, 1976]

(A) (B) (C)
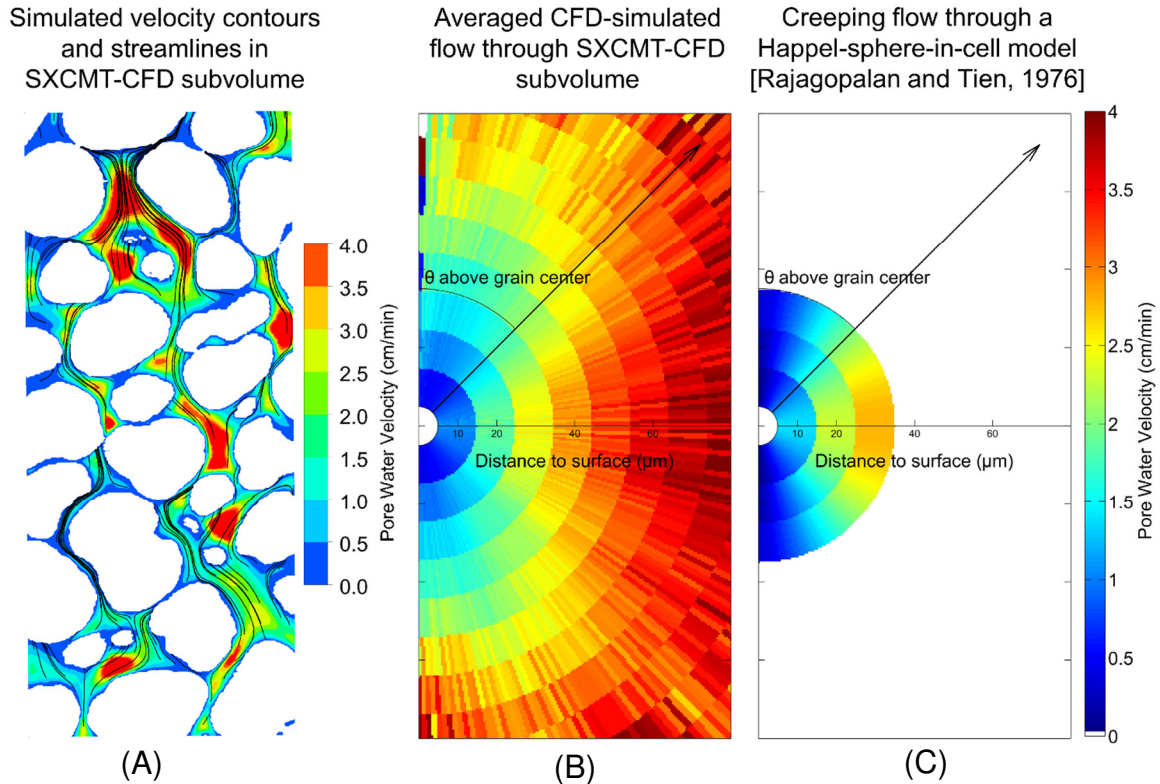
Figure 5.6A Contour plot of CFD-simulated pore water velocity magnitude overlain with black streamlines overlain for a representative cross-section within the SXCMT-CFD subvolume. B: pore water velocity magnitude around the SXCMT-CFD dataset. C: Pore water velocity magnitude around the Happel sphere in cell. The direction of flow is upwards. The velocity contours in the middle and right images are plotted as a function of distance away from a grain surface and angle away from the downstream side of a grain (θ, illustrated in Figure 5.2) to illustrate how the pore water velocity in the left image and in the HSIC image changes from the downstream to the upstream side of a grain at a variety of distances. Further details on this figure are discussed in text.

A volume-averaging technique was employed on the three-dimensional CFD-simulated velocities in the SXCMT-CFD dataset (see Figure 5.6Afor a representative cross-section of velocity contours) to examine how specific pore and grain features influenced velocity within the porous media. The average pore water velocity in the SXCMT-CFD dataset was plotted in Figure 5.6 as a function of distance from the nearest grain surface and angle from the downstream side of a grain (i.e., θ illustrated in Figure 5.2 which was measured from each grain's center of mass). This created a velocity plot which represents the average fluid velocity around every grain in the SXCMT-CFD dataset. All voxels were sorted into 9.87 μm×1° bins and averaged to calculate an average velocity for every definable distance and angle around a grain. The averaged velocity in each bin represents the average velocity within the SXCMT-CFD dataset at that particular distance and

angle. For the analytical solution for flow through the HSIC model, a similar process was used. Eq.'s 5.4 – 5.11 were solved in increments of 9.87 μm (for distance) and 1º (for angle) and a nearest neighbor interpolation routine was used to generate a radial surface plot (Figure 5.6C).

The CFD-simulated flow field in the SXCMT-CFD dataset illustrated in Figures 5.6A and 5.6B has a number of important features. At all distances, velocity in the SXCMT-CFD dataset is a function of angle with the highest velocities observed near the midpoint of the grain ($\theta = 90$º) and relatively low velocity regions near the upstream (bottom) and downstream (top) sides of the grain. The velocity distribution around the grain is also symmetric: the distribution on the upstream and downstream sides of the grains are similar for all distances. This indicates that there is little to no flow separation occurring on the downstream sides of the grains which is consistent with the typical definition of creeping flow. In addition, the average velocity increases with distance from a grain surface, consistent with highest velocities occurring in the centres of pores.

The flow field around the HSIC model (Figure 5.6C) is in excellent qualitative agreement with the CFD-simulated flow field in the SXCMT-CFD dataset (Figure 5.6B) within 36 μm of a surface. The major velocity features in the SXCMT-CFD dataset are captured by the HSIC flow field, including the relatively low-velocity regions on the upstream and downstream sides of the grains as well as the increase in velocity at $\theta = 90$º and the symmetric flow behaviour. However, the HSIC model over-estimates the extent to which velocity is lower in the upstream and downstream regions; the velocities in the SXCMT-CFD dataset at 0º and 180º near 20 μm are higher than the velocities in the HSIC fluid envelope. The difference between these velocities increases with increasing distance, at 0º and 180º near 30 μm the difference is larger than the difference at 20 μm.

To more quantitatively examine the distribution of velocities within the CFD-simulated SXCMT-CFD dataset, Figure 5.7 plots the velocity distribution in Figure 5.6 as a one-dimensional function of distance to the nearest grain where the velocity was averaged over all angles for each particular distance interval. As expected, the velocity is a strong function of distance from the nearest grain surface. In addition, the average pore water

velocities within the centers of the largest pores (~100 μm) may be as large as 2.5× the average pore water velocity (1.38 cm/min, Table 5.1). This trend is qualitatively consistent with the velocity contour plot illustrated in Figure 5.6A. The local (i.e., not averaged) velocities within the SXCMT-CFD dataset can be even higher; simulated velocities upwards of ten times the average pore water velocity were observed. The increasing size of the error bars with distance from the grain surface on the SXCMT-CFD line in Figure 5.7 is due to the decreasing volume of pore space with distance (Figure 5.5); there are fewer pore space voxels in the centers of larger pores which results in larger 95% confidence intervals.

The average velocity within the HSIC fluid envelope is also a strong function of distance from the nearest grain surface. In addition, the velocities as a function of distance from the nearest grain surface within the HSIC model and SXCMT-CFD dataset are very similar within the region of pore space encompassed by the HSIC fluid envelope. However, the magnitude of CFD-simulated velocities in the SXCMT-CFD dataset can be much larger than velocities within the HSIC model. Thus nanoparticles and colloids may be experiencing significantly higher fluid velocities than expected within Colloid Filtration Theory. These larger-than-expected velocities will impact the force and torque balances employed by the CFT mechanistic models. For instance, Figure 5.7 suggests that the inertial forces acting on colloids in the centers of pores will be much greater than the inertial forces considered within the CFT-HSIC models.

To the best of the authors' knowledge this represents one of the first comparisons between a CFD-simulated velocities in a real sand media and the Happel Sphere in Cell model. The observed trend of increasing velocity in both HSIC and SXCMT-CFD datasets matches expectations, in a viscous solution fluid velocity always increases with distance from a no-slip wall. In addition, the flow field in both SXCMT-CFD and HSIC datasets are essentially solutions to the same equation (Navier-Stokes equation), however inertia is explicitly ignored in HSIC and is not significant in the SXCMT-CFD dataset, so similar trends and behaviours were expected. It was surprising, however, that the irregular shape of the sand grains and their complex structure (e.g. grain-grain contacts, regions of fluid expansion and contraction, differing pore sizes) resulted in nearly

identical fluid velocities in both 1-dimension (Figure 5.7) and similar velocities in a radial surface plot (Figure 5.6).
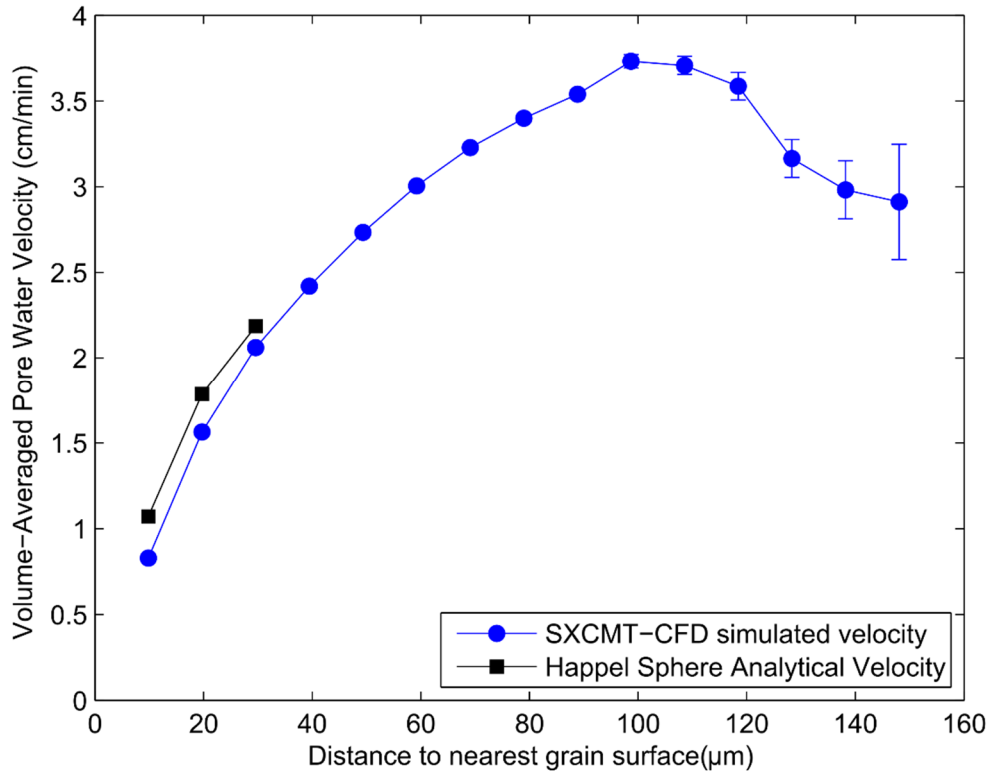
Figure 5.7: The average pore water velocity magnitude as a function distance from the nearest grain surface for both the Happel sphere geometry (black squares) and the SXCMT-CFD dataset (blue circles). The velocity contours presented in Figure 5.6 were employed to create this plot; at each 9.87 µm distance interval the velocities were averaged over all 1º bins (i.e., each datapoint represents velocity averaged over 0 – 180 º) and weighted by the fraction of pore volume in each 1 º bin. The error bars on the SXCMT-CFD dataset line represent 95% confidence intervals calculated at each datapoint.

5.3.3   Nanoparticle mass distribution in qSXCMT datasets

Figure 5.8 presents the distribution of nanoparticle mass within the SXCMT dataset as a function of distance to the nearest grain surface for each imaged timestep. The mass distribution curves were calculated by first determining the nanoparticle mass in each voxel. The nanoparticle mass in each voxel was calculated by multiplying each voxel's SXCMT-determined concentration by the volume of the voxel, approximately 961.5 µm³. This calculation was repeated for every voxel outside of the SXCMT 'shadow zone' (i.e.,

> 17.3µm from a grain surface). Then the distance between every pore space voxel and the nearest grain surface in each SXCMT dataset was measured and then sorted into bins representing 9.87 µm intervals from the grain surface. The nanoparticle mass in each bin was summed and plotted as a function of nAg mass versus distance to the nearest grain surface (Figure 5.8, top).

As illustrated in Figure 5.8A, most nanoparticle mass is located near the grain surface, this is expected as the near surface regions possess the largest volume of pore space (volume pore space with distance is shown in Figure 5.5). While the qSXCMT method is currently unable to quantify nanoparticle concentrations and mass closer than 17.3 µm (corresponding to 25% of the total pore space, Figure 5.5), based on the trend of pore volume in Figure 5.5 it is hypothesized that the total mass of nanoparticles continues increasing with decreasing distance to the grain surface. The term 'quantifiable mass' is used throughout this section to explicitly refer to mass, or mass flow, that is outside of the SXCMT 'shadow zone' and can be accurately quantified via the qSXCMT procedure.

The general shape of the mass distribution curve in Figure 5.8A is approximately consistent with the shape of the pore space volume curve in Figure 5.5A. To quantitatively compare the distributions of mass and pore space volume, Figure 5.8B plots the cumulative percentage of quantifiable nanoparticle mass as a function of distance to the nearest grain surface. This represents the total percentage of quantifiable nanoparticle mass that is closer to the grain surface than a certain distance. This suggests that at every time-step, only 60% of all quantifiable nanoparticle mass is within the fluid region encompassed by the HSIC fluid envelope.
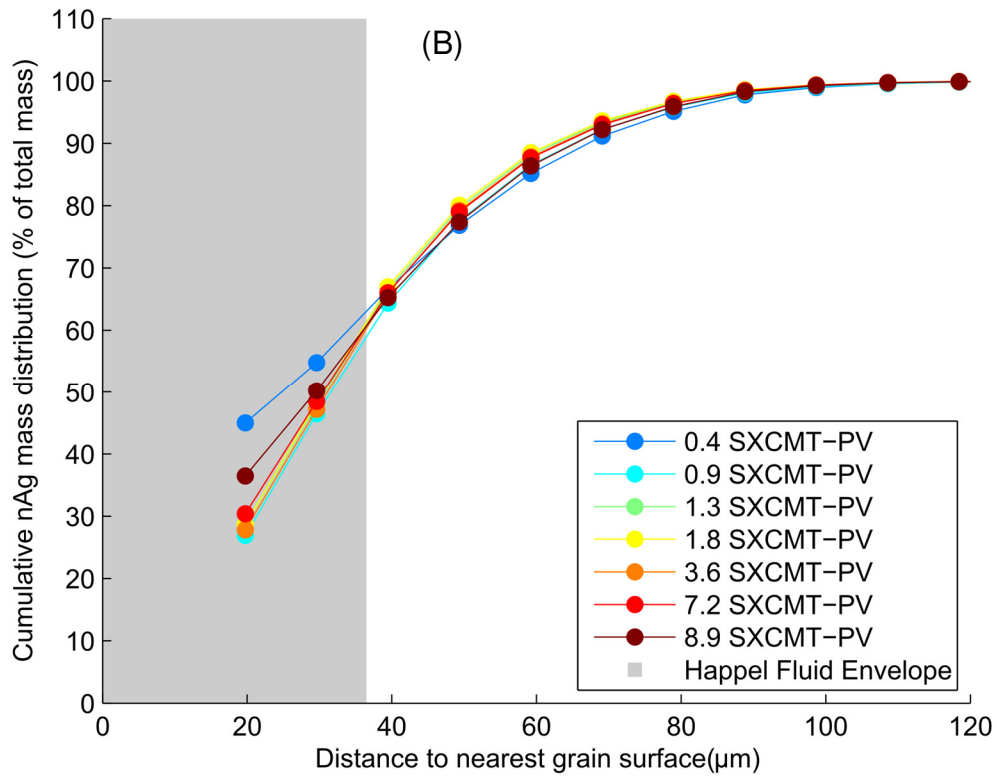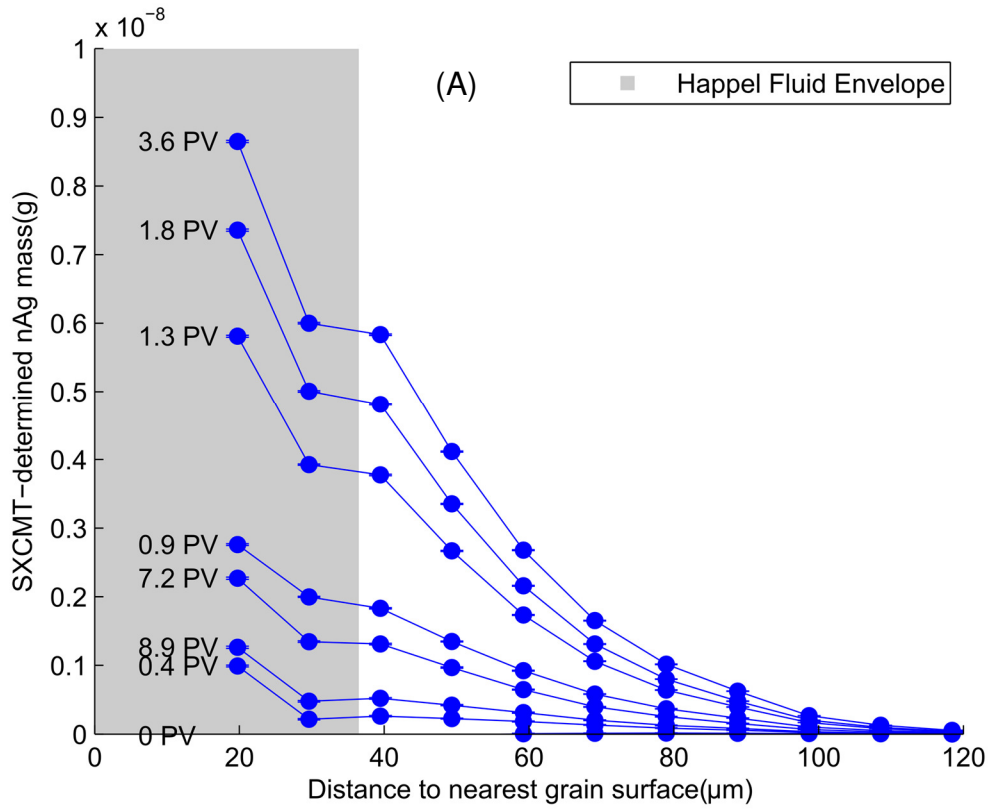
Figure 5.8A: The SXCMT-determined nAg mass plotted as a function of distance from the nearest grain surface (top) for each imaged time-step/SXCMT-PV. The gray box represents the thickness *r* of the Happel Sphere-in-Cell fluid envelope. To avoid cluttering the figure, 'PV' is used instead of 'SXCMT-PV's'.

Figure 5.8B: The cumulative percentage of SXCMT-determined nAg mass for each imaged time-step/SXCMT-PV as a function of distance from the nearest grain surface. Cumulative percentage refers to the total percentage of nAg mass that is between the grain surface and a certain distance from the surface.

Figure 5.5 can be employed to estimate the nanoparticle mass distribution in the pore space region that cannot be quantified by qSXCMT. The 'shadow zone' region which accounts for 25% of all pore space voxels. This suggests that, assuming a strictly per-volume ratio, only 75% of the total nanoparticle mass can be quantified via qSXCMT at each time step. Incorporating these mass estimates into the cumulative percentages in Figure 5.8B yields an adjusted estimate of approximately 70% of total nanoparticle mass encompassed within the HSIC fluid envelope region and 30% of nanoparticle mass outside of the HSIC envelope. The percentage of nanoparticle mass outside the HSIC envelope (30%) is statistically greater than the pore volume outside the HSIC envelope (25%). This indicates that nanoparticles are not uniformly distributed throughout the pore space and that the relatively small pore-scale concentration gradients identified by Molnar et al. [2015a] significantly affects the overall mass distribution through the pore space.

The nanoparticle mass flux rates (mass flow per unit area) through the pore space as a function of distance to the nearest grain surface was estimated from volume-averaged distributions of velocity and concentration as functions of distance to nearest grain surface. Specifically, the CFD-simulated velocity distribution in Figure 5.7 was separated into its component velocities (v_x, v_y and v_z). These component velocities were multiplied by the one dimensional concentration distributions from Molnar et al. [2015a] to yield estimated mass flux distributions in the x, y and z directions (q_x, q_y and q_z) as a function of distance from the nearest grain surface. These component mass flux distributions were summed to determine an overall mass flux distribution ($q = q_x + q_y + q_z$) as a function of distance to the nearest grain surface. This mass flux distribution is illustrated in Appendix

10, Figure 10.1. Molnar et al. [2015a] reported nanoparticle concentrations as a function of distance from the grain surface in 9.87 μm intervals for each imaged time-step.

Due to the high velocities and higher concentrations in the centers of the larger pores, mass flux rates were the highest at the centers of the pores for the time-steps between 0.9 and 3.6 SXCMT-PV's and, to a lesser extent, 7.2 SXCMT-PV's. The mass flux rates do not appreciably change with distance from the grain surface for the early time-step of 0.4 SXCMT-PV and the last time-step of 8.9 SXCMT-PV's; this is likely due to the minimal concentration gradients noted by Molnar et al. [2015a] at the very early and late time-steps in this transport experiment.

The average mass flux distributions were employed to estimate the total quantifiable nanoparticle mass flow rate occurring at each 9.87 μm interval from the grain surface. Component mass flow rates in the x, y and z directions (Q_x, Q_y and Q_z) were estimated by multiplying the distribution of component mass flux rates (q_x, q_y and q_z) by the number of voxels within each 9.87 μm distance interval and by the area of a voxel face (9.87×9.87 μm). The component mass flow rates were then summed to yield the single nanoparticle mass flow rate distribution ($Q = Q_x + Q_y + Q_z$) plotted in Figure 5.9.

Figure 5.9A represents the total quantifiable mass flow occurring at each 9.87 μm distance interval from the grain surface. As can be seen in Figure 5.9 (top), the mass flow rate distribution is qualitatively different from the distribution of pore space. The nanoparticle mass flow rate exhibits a bi-modal distribution with one peak near the grain surface and a second peak 40 μm from the grain surface. The location of this second peak mass flow rate was unexpected as it does not occur at a region of peak nanoparticle mass, mass flux or fluid velocity. This second peak is likely due to an optimal combination of several factors such as nanoparticle concentration distribution, fluid velocity distribution, the complex distribution of small, medium and large pores illustrated in Figure 5.4 and the overall distribution of pore space illustrated in Figure 5.5.

Figure 5.9 B plots the cumulative percentage of quantifiable nanoparticle mass flow as a function of distance to the nearest grain surface (the total percentage of quantifiable mass flow that is closer to the grain surface than a certain distance). The cumulative percentage

at the edge of the HSIC fluid envelope can be used to compare the distributions of pore space volume, nanoparticle mass and nanoparticle mass flow. Accounting for the pore space volume within the SXCMT 'shadow zone' on a per-volume basis, approximately 37% of total nanoparticle mass flow is occurring further away from the grain surface than considered by the HSIC model. Moreover, more mass flow is occurring further away from the grain surface than would be expected by either the pore space volume distribution (25%) or the distribution of nanoparticle mass (30%). The distribution of velocity in Figure 5.7 is primarily responsible for the distribution of mass flow that favours the centers of pores.

Figure 5.9A: The estimated nAg mass flow rate as a function of distance from the nearest grain surface for each imaged time-step/SXCMT-PV. The gray box represents the thickness *r* of the Happel Sphere-in-Cell fluid envelope. To avoid cluttering the figure, 'PV' is used instead of 'SXCMT-PV's'.

Figure 5.9B: The cumulative percentage of estimated nAg nanoparticle mass flow for each imaged time-step/SXCMT-PV as a function of distance from the nearest grain surface. Cumulative percentage refers to the total percentage of nAg mass flow occurring between the grain surface and a certain distance from the surface.

5.4 Discussion

The 'compression' of the pore space by the HSIC geometry in CFT, illustrated in Figure 5.3, may be impacting the accuracy of CFT's predictions for nanoparticle transport. Figures 5.5, 5.8 and 5.9 indicate that large percentages of pore space (25%), nanoparticle mass (30%) and mass flow (37%) are further away from the grain surface than is considered by the HSIC model. These percentages remain consistent for all time-steps through the transport experiment. The degree to which CFT's prediction of colloid retention is affected by these percentages depends on the primary process governing

colloid transport. Micron-sized colloids rely on interception (commonly denoted by η_I) to contact the grain surface [e.g. *Rajagopalan and Tien*, 1976; *Yao et al.*, 1971].

Interception is when colloids are flowing along a fluid streamline which passes within 1 colloid radius of the collector surface, the colloids then contact the collector surface by virtue of their size and, if energetically favorable, attach to the collector. The micron-sized colloids exhibit only a minimal degree of Brownian motion – the diffusive behaviour of particles arising from collisions with surrounding molecules – and are not expected to diffuse across a significant number of streamlines. This strong interception behaviour, coupled with weak diffusive transport, suggests that only colloids on specific trajectories will be contacting and attaching to the collector; the 'critical trajectory' refers to the trajectory beyond which colloids will no longer intercept the grain surface. Rajagopalan and Tien [1976] employ this concept to simplify their calculations by only considering colloids within the critical trajectory. As a result, micron-size colloid transport and retention is unlikely to be adversely affected by approximating the pore space, which extends out to 197 μm, as only being 36 μm thick. Colloids further than 36 μm away from a grain surface are likely outside of the grain's critical trajectory and are unlikely to interact with a collector surface so the approximation does not affect their likelihood of contacting a surface. In addition, the strong interception behaviour coupled with the HSIC's reasonable approximation of near-surface pore space (Figure 5.5B) suggests that this geometry can be appropriate for predicting micron-sized colloid retention rates.

Interception is not a dominant mechanism for nanoparticles. Due to nanoparticles' small radii there are only a small number of trajectories which will bring nanoparticles within 1 colloid radius of the collector. Nanoparticles rather rely on diffusive transport to come into contact with collector surfaces (commonly denoted by η_D). The classical analytical solution to 1-dimensional colloid diffusion arising from Brownian motion is given by [*Einstein*, 1956]:

$$f(x,t) = \frac{N}{\sqrt{4\pi D}} \frac{e^{-\frac{x^2}{4Dt}}}{\sqrt{t}} \qquad\qquad 5.13$$

$$D = \frac{k_b T}{6\pi\mu a_p} \qquad\qquad 5.14$$

where $f(x,t)$ is the number of colloids which diffuse a distance x over time t from an origin point which initially contained N colloids, D is the diffusivity coefficient calculated from the Stokes-Einstein equation (eq. 5.14), k_b is the Boltzmann constant, T is the absolute temperature, μ is the fluid viscosity and a_p is the colloid radius. It should be noted that $f(x,t)$ can be used interchangeably with $c(x,t)$ where c is the concentration of colloids. If $f(x,t)$ is employed to describe the number of nanoparticles that have to diffused to a region on a collector surface, the value of x would range from 0–36 μm in the HSIC geometry and 0–197 μm in the uniform quartz porous medium. eq.'s 5.13 and 5.14 predict that the numbers of nanoparticles reaching the collector surface via diffusion decreases with increasing initial distance from a collector surface for a given time t. Thus, the fraction of nanoparticles diffusing distances of 0 – 36 μm across the HSIC envelope will be much larger than in the porous medium where diffusive distance can range from 0 – 197 μm. Given that 80% of the pore bodies have larger radii than the HSIC envelope and 25% of the total pore space – as well as 30% of the nanoparticle mass and 37% of the nanoparticle mass flow – is further away from the grain surface than expected by HSIC, approximating all nanoparticles as being within the 36μm HSIC envelope will over-estimate η and nanoparticle retention rates. This hypothesis is supported by previous studies which have shown that the HSIC-CFT models can over-predict η and k_att [*Long and Hilpert*, 2009; *Molnar et al.*, 2015a; *Nelson and Ginn*, 2011].

The pore-scale distribution and behaviour of nanoparticles within real porous media is currently poorly understood [*Molnar et al.*, 2015b], so it is unclear how much the extended diffusive distances (0–36 μm vs 0–197 μm) has on over-predicted retention rates as opposed to other proposed mechanisms (e.g., immobile zones) [*Molnar et al.*,

2015a]. Furthermore, while eq. 5.13 clearly illustrates how larger pore bodies can decrease the number of nanoparticles reaching grain surfaces relative to the HSIC model, it is unclear to what extent other fluid and nanoparticle parameters influence the 'diffusive error' arising from approximating larger pore bodies as a thin HSIC fluid envelope. These fluid and nanoparticles parameters, however, can be estimated by:

$$f_{x/r} = \frac{f(x,t)}{f(r,t)} \qquad 5.15$$

where $f(x,t)$ is the number of nanoparticles diffusing distance x during time t (as illustrated by Figure 5.3), and $f(r,t)$ is the number of nanoparticles diffusing across the width r of the HSIC envelope during time t (in Figure 5.3). The closer $f_{x/r}$ is to 1, the smaller the error associated with diffusion across the HSIC geometry versus actual geometry (termed 'diffusive error). While there will be a fraction of nanoparticles diffusing distances further than x or r, the relationship governing $f_{x/r}$ can be used to qualitatively examine what fluid parameters would minimize or exacerbate the diffusive error associated with the HSIC fluid envelope. 5.13 can be substituted twice into 5.15 (for both x and r) to yield:

$$f_{x/r} = e^{\frac{r^2-x^2}{4Dt}} \qquad 5.16$$

The relationship in 5.16 illustrates that the diffusive error associated with the HSIC envelope increases not only with increasing distance x, but also increases with lower nanoparticle diffusivities (D) and shorter times.

The diffusive error (i.e., $f_{x/r} \ll 1$) is expected to be significant for many nanoparticle flow and transport scenarios. Many nanoparticle solutions, especially nZVI, are stabilized with viscous polymer solutions to prevent rapid aggregation and settling [*El Badawy et al.*, 2013; *He and Zhao*, 2005; *He et al.*, 2007; *Hotze et al.*, 2010; *O'Carroll et al.*, 2013]. For instance, nZVI solutions may have viscosities between 1.3×10^{-2} Pa·s [*Krol et al.*, 2013] to upwards of 1.942 Pa·s [*Quinn et al.*, 2005]. Nanoparticles contained within these stabilized solutions will have significantly lower diffusivity coefficients than non-

polymer stabilized nanoparticles and, as suggested by eq. 5.16, will have larger diffusive errors within the CFT-HSIC models. Unlike micron-sized colloids, which also have small diffusivity coefficients, stabilized nanoparticles do not experience enough interception – which, as discussed, is typically accurately predicted by CFT – to off-set the increase in error described by eq. 5.16.

The high simulated velocities in Figure 5.7 may influence the time available for nanoparticles to diffuse to the collector surface before being flushed from the pore space. As described in eq. 5.16, decreasing the time available increases the error associated with diffusion across the HSIC fluid envelope. If nanoparticles are being transported at high velocities through the centers of pores then these nanoparticles may not be able to diffuse across enough streamlines to reach the relatively low near-surface velocities before being flushed from the pore. While HSIC's velocity field is in excellent comparison with the near-surface CFD-simulated field in the SXCMT-CFD dataset (which comprises 75% of the total pore space in the SXCMT-CFD dataset), HSIC under-predicts the fluid velocities that nanoparticles may be exposed to. This under-prediction of fluid velocities through the pore centers supports the hypothesis that the CFT's over-prediction of η arises, at least partially, due to the HSIC geometry under-predicting the distances across which nanoparticles must diffuse to reach the grain surfaces.

The results presented in Figure 5.4, 5.5, 5.8 and 5.9 as well as eq.'s 5.13 and 5.16 suggest that nanoparticle transport studies which employ η-correlation equations from Colloid Filtration Theory to estimate η [e.g., *El Badawy et al.*, 2013; *Jaisi and Elimelech*, 2009; *Krol et al.*, 2013; *Lecoanet et al.*, 2004; *Lin et al.*, 2011; *Liu et al.*, 2009; *Mattison et al.*, 2011; *Phenrat et al.*, 2010a; *Phenrat et al.*, 2010b; *Ryan et al.*, 2002; *Taghavy et al.*, 2013; *Tong and Johnson*, 2006] are over-predicting η due to the CFT-HSIC geometry's inability to consider nanoparticle mass flow outside the thin fluid envelope. The fraction of nanoparticle mass flow occurring outside of the HSIC fluid envelope (37%) is approximately consistent with the over-predictions of η for nanoparticles reported in the literature. Nelson and Ginn [2011] note that CFT-predicted k_{att} values (when $\alpha = 1$) were typically larger than experimental observations by a factor of ~ 2. Molnar et al. [2015a] observed that applying a CFT-HSIC correlation equation to nanoparticles flowing

through an iron oxide sand (structurally identical to the media employed within this study, but coated with iron oxide to achieve α=1) over-predicted η by approximately 33%.

In favorable DLVO conditions where α = 1 (i.e., attachment efficiency = 1) this over-prediction of η will result in over-predictions of the nanoparticle kinetic retention rate coefficient k_{att} and over-predictions of the overall rate of nanoparticle retention. This may result in under-predictions of nanoparticle mobility under-predictions of nanoparticle risk to nearby drinking water supplies. In unfavorable DLVO conditions where α < 1, a-priori estimations of η are required to determine α. CFT-HSIC over-predictions of η will then result in under-estimations of α. Numerous studies have tried to identify trends in nanoparticle α [*Bai and Tien*, 1999; *Elimelech and Omelia*, 1990; *Kocur et al.*, 2013; *Lin et al.*, 2011; *Petosa et al.*, 2010; *Tiraferri and Sethi*, 2009; *Tong and Johnson*, 2006] but with generally limited success. This limited success in describing α for nanoparticle transport may be due, in part, to the inability to accurately predict η with CFT-HSIC mechanistic models and correlation equations.

5.5 Conclusions

This study examined experimentally-collected pore-scale datasets of nanoparticle distribution during a silver nanoparticle- quartz sand transport experiment. The pore-scale silver nanoparticle distributions were imaged via quantitative Synchrotron X-Ray Computed Microtomography (qSXCMT). This examination yielded some of the first ever data on pore-scale nanoparticle transport through real porous media. In addition, this data was employed to perform the first systematic examination of how well the Happel Sphere-in-Cell (HSIC) geometry, commonly employed for Colloid Filtration Theory mechanistic models, approximated the pore-scale processes governing nanoparticle flow and transport.

Four major findings were drawn from this study: (1) The distribution of pore space ranged from 0 – 197 μm from a grain surface, with most of the pore space close to the grain surface, 25% of this pore space was further away from the grain surface than allowable within the HSIC model, (2) Numerical simulations of fluid flow through the

SXCMT-CFD dataset indicated that velocity was a strong function of distance from the grain surface and could be upwards of ten times the average pore water velocity. These numerical simulations compared well with analytical solutions of fluid flow through the HSIC fluid envelope although the HSIC velocities predicted were much less than those in the centers of the larger pores, (3) SXCMT-datasets revealed that nanoparticle mass and mass flow distributions were larger in centers of pores than expected from the pore volume distribution. The distribution of mass and mass flow that favoured pore centers is associated with previously observed concentration gradients and the simulated velocity distributions. Approximately 30% of all nanoparticle mass and 37-38% of all nanoparticle mass flow was occurring further away from the grain surface than expected by the HSIC geometry. (4) The diffusive behaviour of nanoparticles, coupled with the larger-than-expected distances from the grain surface, suggests that a significant fraction of nanoparticles are less likely to diffuse far enough to contact a grain surface than expected by HSIC geometry (termed 'diffusive error'), likely contributing to CFT's over-predictions of η for nanoparticle

5.6 References

Bai, R., and C. Tien (1999), Particle Deposition under Unfavorable Surface Interactions, *Journal of Colloid and Interface Science*, *218*(2), 488-499.

Bhattad, P., C. S. Willson, and K. E. Thompson (2010), Segmentation of low-contrast three-phase X-Ray Computed Tomography images of porous media, paper presented at Proceedings of the GeoX 2010: 3rd International Workshop on X-ray CT for Geomaterials, New Orleans, LA.

Boccardo, G., D. L. Marchisio, and R. Sethi (2014), Microscale simulation of particle deposition in porous media, *Journal of Colloid and Interface Science*, *417*(0), 227-237.

Chen, C., A. I. Packman, and J.-F. Gaillard (2008), Pore-scale analysis of permeability reduction resulting from colloid deposition, *Geophys. Res. Lett.*, *35*(7), L07404.

Chen, C., B. L. T. Lau, J.-F. Gaillard, and A. I. Packman (2009), Temporal evolution of pore geometry, fluid flow, and solute transport resulting from colloid deposition, *Water Resour. Res.*, *45*(6), W06416.

Chen, G., X. Liu, and C. Su (2011), Transport and Retention of TiO2 Rutile Nanoparticles in Saturated Porous Media under Low-Ionic-Strength Conditions: Measurements and Mechanisms, *Langmuir*, *27*(9), 5393-5402.

Cushing, R. S., and D. F. Lawler (1998), Depth Filtration: Fundamental Investigation through Three-Dimensional Trajectory Analysis, *Environ. Sci. Technol.*, *32*(23), 3793-3801.

Einstein, A. (1956), *Investigations on the Theory of the Brownian Movement*, Dover Publications, Mineola, N.Y.

El Badawy, A. M., A. Aly Hassan, K. G. Scheckel, M. T. Suidan, and T. M. Tolaymat (2013), Key Factors Controlling the Transport of Silver Nanoparticles in Porous Media, *Environ. Sci. Technol.*

Elimelech, M., and C. R. Omelia (1990), EFFECT OF PARTICLE-SIZE ON COLLISION EFFICIENCY IN THE DEPOSITION OF BROWNIAN PARTICLES WITH ELECTROSTATIC ENERGY BARRIERS, *Langmuir*, *6*(6), 1153-1163.

Elimelech, M. (1994), PARTICLE DEPOSITION ON IDEAL COLLECTORS FROM DILUTE FLOWING SUSPENSIONS - MATHEMATICAL FORMULATION, NUMERICAL-SOLUTION, AND SIMULATIONS, *Sep. Technol.*, *4*(4), 186-212.

Gaillard, J.-F., C. Chen, S. H. Stonedahl, B. L. T. Lau, D. T. Keane, and A. I. Packman (2007), Imaging of colloidal deposits in granular porous media by X-ray difference micro-tomography, *Geophys. Res. Lett.*, *34*(18), L18404.

Goldberg, E., M. Scheringer, T. D. Bucheli, and K. Hungerbühler (2014), Critical Assessment of Models for Transport of Engineered Nanoparticles in Saturated Porous Media, *Environ. Sci. Technol.*, *48*(21), 12732-12741.

Goldberg, E., M. Scheringer, T. D. Bucheli, and K. Hungerbuhler (2015), Prediction of nanoparticle transport behavior from physicochemical properties: machine learning provides insights to guide the next generation of transport models, *Environmental Science: Nano*, *2*(4), 352-360.

Happel, J. (1958), VISCOUS FLOW IN MULTIPARTICLE SYSTEMS - SLOW MOTION OF FLUIDS RELATIVE TO BEDS OF SPHERICAL PARTICLES, *Aiche J.*, *4*(2), 197-201.

He, F., and D. Zhao (2005), Preparation and Characterization of a New Class of Starch-Stabilized Bimetallic Nanoparticles for Degradation of Chlorinated Hydrocarbons in Water, *Environ. Sci. Technol.*, *39*(9), 3314-3320.

He, F., D. Zhao, J. Liu, and C. B. Roberts (2007), Stabilization of Fe−Pd Nanoparticles with Sodium Carboxymethyl Cellulose for Enhanced Transport and Dechlorination of Trichloroethylene in Soil and Groundwater, *Industrial & Engineering Chemistry Research*, *46*(1), 29-34.

Hotze, E. M., T. Phenrat, and G. V. Lowry (2010), Nanoparticle Aggregation: Challenges to Understanding Transport and Reactivity in the Environment, *Journal of Environmental Quality*, *39*(6), 1909-1924.

Jaisi, D. P., and M. Elimelech (2009), Single-Walled Carbon Nanotubes Exhibit Limited Transport in Soil Columns, *Environ. Sci. Technol.*, *43*(24), 9161-9166.

Jiang, X., M. Tong, R. Lu, and H. Kim (2012a), Transport and deposition of ZnO nanoparticles in saturated porous media, *Colloids and Surfaces A: Physicochemical and Engineering Aspects*, *401*(0), 29-37.

Jiang, X., M. Tong, and H. Kim (2012b), Influence of natural organic matter on the transport and deposition of zinc oxide nanoparticles in saturated porous media, *Journal of Colloid and Interface Science*, *386*(1), 34-43.

Joo, S. H., S. R. Al-Abed, and T. Luxton (2009), Influence of Carboxymethyl Cellulose for the Transport of Titanium Dioxide Nanoparticles in Clean Silica and Mineral-Coated Sands, *Environ. Sci. Technol.*, *43*(13), 4954-4959.

Kanel, S., J. Flory, A. Meyerhoefer, J. Fraley, I. Sizemore, and M. Goltz (2015), Influence of natural organic matter on fate and transport of silver nanoparticles in saturated porous media: laboratory experiments and modeling, *J. Nanopart. Res.*, *17*(3), 1-13.

Kasel, D., S. A. Bradford, J. Šimůnek, M. Heggen, H. Vereecken, and E. Klumpp (2013), Transport and retention of multi-walled carbon nanotubes in saturated porous media: Effects of input concentration and grain size, *Water Research*, *47*(2), 933-944.

Kocur, C. M., D. M. O'Carroll, and B. E. Sleep (2013), Impact of nZVI stability on mobility in porous media, *Journal of Contaminant Hydrology*, *145*(0), 17-25.

Krol, M. M., A. J. Oleniuk, C. M. Kocur, B. E. Sleep, P. Bennett, Z. Xiong, and D. M. O'Carroll (2013), A Field-Validated Model for In Situ Transport of Polymer-Stabilized nZVI and Implications for Subsurface Injection, *Environ. Sci. Technol.*, *47*(13), 7332-7340.

Lanphere, J. D., C. J. Luth, and S. L. Walker (2013), Effects of Solution Chemistry on the Transport of Graphene Oxide in Saturated Porous Media, *Environ. Sci. Technol.*, *47*(9), 4255-4261.

Lecoanet, H. F., J.-Y. Bottero, and M. R. Wiesner (2004), Laboratory Assessment of the Mobility of Nanomaterials in Porous Media, *Environ. Sci. Technol.*, *38*(19), 5164-5169.

Li, X. Q., C. L. Lin, J. D. Miller, and W. P. Johnson (2006a), Pore-scale observation of microsphere deposition at grain-to-grain contacts over assemblage-scale porous

media domains using X-ray microtomography, *Environ. Sci. Technol.*, *40*(12), 3762-3768.

Li, X. Q., C. L. Lin, J. D. Miller, and W. P. Johnson (2006b), Role of grain-to-grain contacts on profiles of retained colloids in porous media in the presence of an energy barrier to deposition, *Environ. Sci. Technol.*, *40*(12), 3769-3774.

Li, Y., Y. Wang, K. D. Pennell, and L. M. Abriola (2008), Investigation of the Transport and Deposition of Fullerene (C60) Nanoparticles in Quartz Sands under Varying Flow Conditions, *Environ. Sci. Technol.*, *42*(19), 7174-7180.

Liang, Y., S. A. Bradford, J. Simunek, M. Heggen, H. Vereecken, and E. Klumpp (2013a), Retention and Remobilization of Stabilized Silver Nanoparticles in an Undisturbed Loamy Sand Soil, *Environ. Sci. Technol.*, *47*(21), 12229-12237.

Liang, Y., S. A. Bradford, J. Simunek, H. Vereecken, and E. Klumpp (2013b), Sensitivity of the transport and retention of stabilized silver nanoparticles to physicochemical factors, *Water Research*, *47*(7), 2572-2582.

Lin, S. H., Y. W. Cheng, Y. Bobcombe, K. L. Jones, J. Liu, and M. R. Wiesner (2011), Deposition of Silver Nanoparticles in Geochemically Heterogeneous Porous Media: Predicting Affinity from Surface Composition Analysis, *Environ. Sci. Technol.*, *45*(12), 5209-5215.

Liu, X. Y., D. M. O'Carroll, E. J. Petersen, Q. G. Huang, and C. L. Anderson (2009), Mobility of Multiwalled Carbon Nanotubes in Porous Media, *Environ. Sci. Technol.*, *43*(21), 8153-8158.

Long, W., and M. Hilpert (2009), A Correlation for the Collector Efficiency of Brownian Particles in Clean-Bed Filtration in Sphere Packings by a Lattice-Boltzmann Method, *Environ. Sci. Technol.*, *43*(12), 4419-4424.

Ma, H., J. Pedel, P. Fife, and W. P. Johnson (2009), Hemispheres-in-Cell Geometry to Predict Colloid Deposition in Porous Media, *Environ. Sci. Technol.*, *43*(22), 8573-8579.

Mattison, N. T., D. M. O'Carroll, R. Kerry Rowe, and E. J. Petersen (2011), Impact of Porous Media Grain Size on the Transport of Multi-walled Carbon Nanotubes, *Environ. Sci. Technol.*, *45*(22), 9765-9775.

May, R., S. Akbariyeh, and Y. Li (2012), Pore-Scale Investigation of Nanoparticle Transport in Saturated Porous Media Using Laser Scanning Cytometry, *Environ. Sci. Technol.*, *46*(18), 9980-9986.

May, R., and Y. S. Li (2013), The effects of particle size on the deposition of fluorescent nanoparticles in porous media: Direct observation using laser scanning cytometry, *Colloid Surf. A-Physicochem. Eng. Asp.*, *418*, 84-91.

Molnar, I. L., C. S. Willson, D. M. O'Carroll, M. L. Rivers, and J. I. Gerhard (2014), Method for Obtaining Silver Nanoparticle Concentrations within a Porous Medium via Synchrotron X-ray Computed Microtomography, *Environ. Sci. Technol.*, *48*(2), 1114-1122.

Molnar, I. L., J. I. Gerhard, C. S. Willson, and D. M. O'Carroll (2015a), The impact of immobile zones on the transport and retention of nanoparticles in porous media, *Water Resour. Res.*

Molnar, I. L., W. P. Johnson, J. I. Gerhard, C. S. Willson, and D. M. O'Carroll (2015b), Predicting colloid transport through saturated porous media: A critical review *Water Resour. Res.*, *51*(50th anniversary special collection), 6804-6845.

166

Nelson, K. E., and T. R. Ginn (2005), Colloid Filtration Theory and the Happel Sphere-in-Cell Model Revisited with Direct Numerical Simulation of Colloids, *Langmuir*, *21*(6), 2173-2184.

Nelson, K. E., and T. R. Ginn (2011), New collector efficiency equation for colloid filtration in both natural and engineered flow conditions, *Water Resour. Res.*, *47*, 17.

O'Carroll, D., B. Sleep, M. Krol, H. Boparai, and C. Kocur (2013), Nanoscale zero valent iron and bimetallic particles for contaminated site remediation, *Adv. Water Resour.*, *51*(0), 104-122.

O'Carroll, D. M., S. A. Bradford, and L. M. Abriola (2004), Infiltration of PCE in a system containing spatial wettability variations, *Journal of Contaminant Hydrology*, *73*(1-4), 39-63.

O'Carroll, D., B. Sleep, M. Krol, H. Boparai, and C. Kocur (2013), Nanoscale zero valent iron and bimetallic particles for contaminated site remediation, *Adv. Water Resour.*, *51*(0), 104-122.

Oh, W., and W. B. Lindquist (1999), Image thresholding by indicator kriging, *Ieee Transactions on Pattern Analysis and Machine Intelligence*, *21*(7), 590-602.

Petosa, A. R., D. P. Jaisi, I. R. Quevedo, M. Elimelech, and N. Tufenkji (2010), Aggregation and Deposition of Engineered Nanomaterials in Aquatic Environments: Role of Physicochemical Interactions, *Environ. Sci. Technol.*, *44*(17), 6532-6549.

Phenrat, T., H. J. Kim, F. Fagerlund, T. Illangasekare, and G. V. Lowry (2010a), Empirical correlations to estimate agglomerate size and deposition during injection of a polyelectrolyte-modified Fe-0 nanoparticle at high particle concentration in saturated sand, *Journal of Contaminant Hydrology*, *118*(3-4), 152-164.

Phenrat, T., J. E. Song, C. M. Cisneros, D. P. Schoenfelder, R. D. Tilton, and G. V. Lowry (2010b), Estimating Attachment of Nano- and Submicrometer-particles Coated with Organic Macromolecules in Porous Media: Development of an Empirical Model, *Environ. Sci. Technol.*, *44*(12), 4531-4538.

Quinn, J., et al. (2005), Field Demonstration of DNAPL Dehalogenation Using Emulsified Zero-Valent Iron, *Environ. Sci. Technol.*, *39*(5), 1309-1318.

Rajagopalan, R., and C. Tien (1976), TRAJECTORY ANALYSIS OF DEEP-BED FILTRATION WITH SPHERE-IN-CELL POROUS-MEDIA MODEL, *Aiche J.*, *22*(3), 523-533.

Ryan, J. N., R. W. Harvey, D. Metge, M. Elimelech, T. Navigato, and A. P. Pieper (2002), Field and Laboratory Investigations of Inactivation of Viruses (PRD1 and MS2) Attached to Iron Oxide-Coated Quartz Sand, *Environ. Sci. Technol.*, *36*(11), 2403-2413.

Solovitch, N., J. Labille, J. Rose, P. Chaurand, D. Borschneck, M. R. Wiesner, and J.-Y. Bottero (2010), Concurrent Aggregation and Deposition of TiO2 Nanoparticles in a Sandy Porous Media, *Environ. Sci. Technol.*, *44*(13), 4897-4902.

Taghavy, A., A. Mittelman, Y. Wang, K. D. Pennell, and L. M. Abriola (2013), Mathematical Modeling of the Transport and Dissolution of Citrate-Stabilized Silver Nanoparticles in Porous Media, *Environ. Sci. Technol.*, *47*(15), 8499-8507.

Thompson, K. E., C. S. Willson, and W. L. Zhang (2006), Quantitative computer reconstruction of particulate materials from microtomography images, *Powder Technology*, *163*(3), 169-182.

Thompson, K. E., C. S. Willson, C. D. White, S. L. Nyman, J. P. Bhattacharya, and A. H. Reed (2008), Application of a new grain-based reconstruction algorithm to microtomography images for quantitative characterization and flow modeling, *Spe Journal*, *13*(2), 164-176.

Tiraferri, A., and R. Sethi (2009), Enhanced transport of zerovalent iron nanoparticles in saturated porous media by guar gum, *J. Nanopart. Res.*, *11*(3), 635-645.

Tong, M., and W. P. Johnson (2006), Excess Colloid Retention in Porous Media as a Function of Colloid Size, Fluid Velocity, and Grain Angularity, *Environ. Sci. Technol.*, *40*(24), 7725-7731.

Tufenkji, N., and M. Elimelech (2004), Correlation equation for predicting single-collector efficiency in physicochemical filtration in saturated porous media, *Environ. Sci. Technol.*, *38*(2), 529-536.

Uyusur, B., C. J. G. Darnault, P. T. Snee, E. Koken, A. R. Jacobson, and R. R. Wells (2010), Coupled effects of solution chemistry and hydrodynamics on the mobility and transport of quantum dot nanomaterials in the vadose zone, *Journal of Contaminant Hydrology*, *118*(3-4), 184-198.

Wang, D., W. Zhang, X. Hao, and D. Zhou (2013a), Transport of Biochar Particles in Saturated Granular Media: Effects of Pyrolysis Temperature and Particle Size, *Environ. Sci. Technol.*, *47*(2), 821-828.

Wang, D., W. Zhang, and D. Zhou (2013b), Antagonistic Effects of Humic Acid and Iron Oxyhydroxide Grain-Coating on Biochar Nanoparticle Transport in Saturated Sand, *Environ. Sci. Technol.*, *47*(10), 5154-5161.

Wang, D., L. Ge, J. He, W. Zhang, D. P. Jaisi, and D. Zhou (2014a), Hyperexponential and nonmonotonic retention of polyvinylpyrrolidone-coated silver nanoparticles in an Ultisol, *Journal of Contaminant Hydrology*, *164*(0), 35-48.

Wang, Y., Y. Li, J. D. Fortner, J. B. Hughes, L. M. Abriola, and K. D. Pennell (2008), Transport and Retention of Nanoscale C60 Aggregates in Water-Saturated Porous Media, *Environ. Sci. Technol.*, *42*(10), 3588-3594.

Wang, Y., Y. Li, J. Costanza, L. M. Abriola, and K. D. Pennell (2012), Enhanced Mobility of Fullerene (C60) Nanoparticles in the Presence of Stabilizing Agents, *Environ. Sci. Technol.*, *46*(21), 11761-11769.

Wang, Y., M. D. Becker, V. L. Colvin, L. M. Abriola, and K. D. Pennell (2014b), Influence of Residual Polymer on Nanoparticle Deposition in Porous Media, *Environ. Sci. Technol.*, *48*(18), 10664-10671.

Willson, C., N. Lu, and W. Likos (2012), Quantification of Grain, Pore, and Fluid Microstructure of Unsaturated Sand from X-Ray Computed Tomography Images, *Geotechnical Testing Journal*, *35*(6), 1-13.

Yao, K.-M., M. T. Habibian, and C. R. O'Melia (1971), Water and waste water filtration. Concepts and applications, *Environ. Sci. Technol.*, *5*(11), 1105-1112.

Chapter 6

6 Conclusions

6.1 Summary

The work presented in this thesis demonstrates that the transport and retention of nanoparticles in soil is sensitive to pore-scale properties such as variations in fluid velocity and the distribution of mass flow rates. The link between these pore-scale properties and nanoparticle transport and retention was examined by employing Synchrotron X-ray Computed Microtomography (SXCMT). The use of SXCMT to examine the pore-scale transport and behaviour of environmental contaminants has been well documented [e.g., *Al-Raoush and Willson*, 2005; *Blunt et al.*, 2013; *Wildenschild and Sheppard*, 2013]. However SXCMT techniques had not been previously extended to nanoparticle/soil systems as nanoparticles were orders of magnitude smaller than the resolution of SXCMT systems and could not be visually observed. It was conjectured that Beer's law could be applied directly to reconstructed SXCMT datasets to mathematically determine the concentrations of silver nanoparticles for every pore space voxel. This method would be able to directly quantify the distribution nanoparticles within a water saturated soil's pore space during transport.

This approach to determining pore-scale distributions of silver nanoparticles was validated by examining the distribution of silver nanoparticles in static and quasi-dynamic systems of representative packed glass bead columns. In the systems tested, the SXCMT method was able to accurately quantify the spatial distributions of static silver nanoparticle/glass bead systems and temporal changes in the spatial distributions of the quasi-dynamic silver nanoparticle/glass bead systems. In addition, the factors affecting the quality of the SXCMT-determined results were investigated: 1) The acquisition of additional datasets reduced the standard deviation of SXCMT-determined concentrations; 2) X-ray interactions (i.e., absorption, refraction and reflection) with the soil/water media, column material and scintillator crystal significantly impacted the accuracy of the

SXCMT-determined concentrations; 3) By treating the approximately 20×10^6 voxels within each data set statistically (i.e., averaging), a high level of confidence in the SXCMT-determined mean concentrations can be obtained.

The validated SXCMT method was then employed to examine pore-scale silver nanoparticle distributions during transport through three sand columns: uniform iron oxide, uniform quartz and well graded quartz. Extended tailing was observed during the elution phase of all experiments suggesting that hydraulic retention in immobile zones, not detachment from grains, was the source of tailing. A numerical simulation of fluid flow through an SXCMT dataset predicted the presence of immobile zones near grain-grain contacts. SXCMT-determined silver nanoparticle concentrations observed that significantly lower nanoparticle concentrations existed near grain-grain contacts throughout the duration of all experiments. In addition, the SXCMT-determined pore-scale concentration gradients were found to be independent of surface chemistry and grain size distribution, suggesting that immobile zones limit the diffusive transport of nanoparticles towards the collectors.

The simulated CFD datasets were then coupled directly with the uniform quartz SXCMT-determined silver nanoparticle datasets to estimate the distribution of silver nanoparticle mass flow rates during transport. It was found that the distribution of mass flow rates depended on the pore-scale distribution of several properties: nanoparticle concentration, fluid velocity and pore-scape geometry. The nanoparticle concentrations and fluid velocities were highest in the centers of the largest pores, yielding high rates of mass flux in those areas. However, the volume of pore space decreased with increasing distance from the grain surfaces; thus the regions with high mass flux rates occurred in only a small percentage of the total pore space. When these factors were combined, it was found that mass flow rates decreased with increasing distance from the grain surfaces.

6.2   Implications

These results presented in this thesis have substantial implications for both employing SXCMT to the study pore-scale transport of contaminants and for nanoparticle transport through the subsurface. As SXCMT is being increasingly employed to examine the

transport of contaminants, the ability to quantify elemental pore-scale distribution of contaminants in real soil pore spaces over time will open up new avenues of contaminant transport research.

Current approaches for modelling nanoparticle transport are unable to describe and accurately predict nanoparticle transport behaviour and retention rates. It was shown that immobile zones yielded extended tailing behaviour that is typically not describable by standard continuum-scale nanoparticle transport models. In addition, Colloid filtration theory (CFT) – a mechanistic approach to predicting colloid retention rates for continuum-scale transport models – is widely applied to nanoparticle transport and is known to over-predict retention rates in even simple systems. CFT was unable to account for the phenomena observed within this study (immobile zones, mass flow through large pore centers) and it is hypothesized that these phenomena are at least partially responsible for CFT's inability to accurately predict nanoparticle retention rates. If these observed phenomena are widely present in the subsurface, then Colloid Filtration Theory and the standard continuum-scale transport modelling approach may be insufficient to describe field-scale nanoparticle transport and their uses should be reconsidered.

6.3   Recommendations for Future Work

Numerous simplifications and assumptions were employed in this study that may limit the direct applicability of these results to field-scale nanoparticle transport. These assumptions and simplifications include: employing homogeneous sand packed columns with no organic carbon content or micro-organisms, freshly synthesized silver nanoparticles which may be different from nanoparticles that have undergone aging and transformations within the natural environment and a simple aqueous solution with a high ionic strength which may not be representative of actual groundwater. As such, future research on the pore-scale processes governing field-scale nanoparticle transport needs to be expanded to consider more realistic nanoparticles, soils and groundwater.

In addition, this thesis highlighted several pore-scale phenomena impacting silver nanoparticle transport and discussed how current nanoparticle transport modelling approaches do not adequately describe or predict the impact of these phenomena on

nanoparticle transport through soil. As such, future research should also focus on further developing our understanding of these phenomena and developing nanoparticle-specific modelling approaches.

Specifically, future research should:

1. Examine the pore-scale aggregation and transport of silver nanoparticles which have undergone aging and transformation in the environment. Silver nanoparticles react with to common subsurface constituents such as chloride and oxygen, the possibility exists that these reactions will alter how the silver nanoparticles interact with phenomena such as immobile and other processes, such as aggregation and straining, may become more dominant.

2. Identify how silver nanoparticles interact with iron oxide surfaces. In this thesis it was shown that silver nanoparticles interacted with iron oxide surfaces in a way that rendered them non-digestible to even highly acidic (pH ~ 0) solutions. This interaction between silver nanoparticles and iron oxides has, to the best of the author's knowledge, not been previously researched and, given the widespread presence of iron oxide in the subsurface, should be examined in greater detail.

3. Examine how the presence of microbes in the subsurface alters nanoparticle transport behaviour. Silver nanoparticles possess strong anti-microbial properties, suggesting that they actively interact with nearby microbes. Microbes are ubiquitous throughout subsurface soils and groundwater resources and it is likely that their presence will alter the transport and ultimate fate of silver nanoparticles in soils.

4. Develop mathematical approaches to incorporate pore-scale phenomena into continuum-scale transport models and to predict the required parameters. Currently, continuum-scale transport models require extra parameters and coefficients to incorporate phenomena such as immobile zones and these parameters are typically determined by fitting to experimental data. The SXCMT method developed and presented in this thesis will provide a valuable path forward for developing the mathematical relationships, and methods for predicting the parameters, required to incorporate nanoparticle interactions with these phenomena into continuum-scale models.

5. Develop nanoparticle-specific mechanistic approaches to predicting nanoparticle retention rates in soils. As shown in this study, Colloid Filtration Theory is not well suited to predicting nanoparticle retention rates as it is incapable of including processes that impact experimental nanoparticle retention rates such as immobile zones and mass flow through larger pores. There are several promising CFT approaches to predicting nanoparticle retention rates in soils [*Long and Hilpert*, 2009; *Long et al.*, 2010] that should be further developed.

6. In addition, there are likely numerous other pore-scale processes and phenomena that are responsible for the 'anomalous' transport behaviour of nanoparticles such as bi-modal breakthroughs, and non-log linear retention profiles. While the results presented in this thesis partially explain at least two of the anomalous behaviours – extended tailing and lower-than-expected retention rates – the SXCMT method presented and validated in this thesis should be employed to further investigate the potential causes of the remaining anomalous behaviours.

7. The SXCMT method developed and validated in this thesis remains the only method that can accurately determine high resolution distributions of nanoparticle concentrations within real soil pore spaces. As such, it should be further developed to improve the accuracy, uncertainty, limits, and range of nanoparticles that can be examined with this method. For instance, other reconstruction algorithms, such as algebraic or statistical reconstruction techniques, may provide higher quality reconstructed datasets than the reconstruction algorithm employed within this thesis (filtered back projection with a radon transform). It is also likely that as X-ray Microtomography technology evolves and the component parts improve (e.g., CCD detectors and scintillator crystals) this SXCMT method will become capable of delivering higher quality SXCMT-determined concentration datasets and may also partially eliminate some of the SXCMT imaging artifacts (such as the 'shadow zone') which limited the analyses within this thesis.
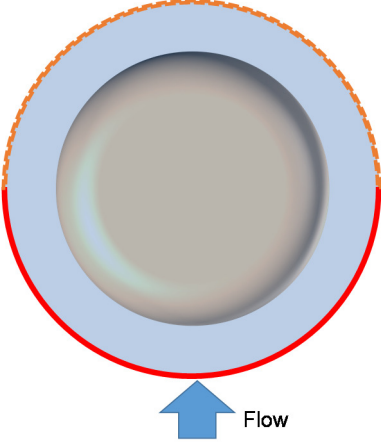
6.4   References

Al-Raoush, R. I., and C. S. Willson (2005), A pore-scale investigation of a multiphase porous media system, *Journal of Contaminant Hydrology*, *77*(1-2), 67-89.

Blunt, M. J., B. Bijeljic, H. Dong, O. Gharbi, S. Iglauer, P. Mostaghimi, A. Paluszny, and C. Pentland (2013), Pore-scale imaging and modelling, *Adv. Water Resour.*, *51*(0), 197-216.

Long, W., and M. Hilpert (2009), A Correlation for the Collector Efficiency of Brownian Particles in Clean-Bed Filtration in Sphere Packings by a Lattice-Boltzmann Method, *Environ. Sci. Technol.*, *43*(12), 4419-4424.

Long, W., H. Huang, J. Serlemitsos, E. Liu, A. H. Reed, and M. Hilpert (2010), Pore-scale study of the collector efficiency of nanoparticles in packings of nonspherical collectors, *Colloids and Surfaces A: Physicochemical and Engineering Aspects*, *358*(1–3), 163-171.

Wildenschild, D., and A. P. Sheppard (2013), X-ray imaging and analysis techniques for quantifying pore-scale structure and processes in subsurface porous medium systems, *Adv. Water Resour.*, *51*(0), 217-246.

7 Appendix A: Supplementary Material for "Predicting colloid transport through saturated porous media: A critical review"

7.1 Overview of the geometries and equations of select CFT models

Table 7.1 Overview of the geometries and equations governing selected mechanistic Happel sphere models

Model Name	Rajagopalan and Tien [1976]	Tufenkji and Elimelech [2004]	Nelson and Ginn [2011]
Model type	Lagrangian[a]	Eulerian	Lagrangian
Model Geometry[*]			

Particle boundary conditions	── Injection boundary(Lagrangian only)[+] Constant concentration (C = C$_o$) (Eulerian only) ─ ·─ Free exit boundary (Lagrangian only) Constant Concentration (C = C$_o$) (Eulerian only) ● Perfect sink (C = 0)		
Fluid flow equation	Stokes (creeping) flow[b]: $\nabla p = \mu \nabla^2 v$ Continuity: $\nabla v = 0$		
Governing colloid transport equation[c]	$F_G + F_{LO} + F_{DL} + F_D + F_I = 0$ $t_G + t_{LO} + t_{DL} + t_D + t_I = 0$	$\nabla(uC) = \nabla(D_{BM}^r \cdot \nabla C) - \nabla\left(\frac{D_{BM}^r \cdot F}{k_B T}\right) C$	$m\frac{du}{dt} = F_H + F_e + F_B$
η correlation[d]	$\eta \approx \gamma^2 \left[4A_s^{1/3} N_{Pe}^{-2/3} + A_s N_{LO}^{1/8} N_R^{15/8} + 0.00338 A_s N_G^{1.2} N_R^{-0.4} \right]$	$\eta \approx 2.4 A_s^{1/3} N_R^{-0.081} N_{Pe}^{-0.715} N_{vdW}^{0.052} + 0.55 A_s N_R^{1.675} N_A^{0.125} + 0.22 N_R^{-0.24} N_G^{1.11} N_{vdW}^{0.053}$	$\eta \approx$ $\gamma^2 \left[2.4 A_s^{\frac{1}{3}} \left(\frac{N_{Pe}}{N_{Pe}+16}\right)^{0.75} N_{Pe}^{-0.68} N_{LO}^{0.015} N_{Gi}^{0.8} + A_s N_{LO}^{1/8} N_R^{15/8} + 0.7 \left(\frac{N_{Gi}}{N_{Gi}+0.9}\right) N_G N_R^{-0.05} \right]$
Kinetic retention rate equation	$k = \frac{3}{2}\frac{(1-n)^{1/3} U}{d_c n}\eta\alpha$	$k = \frac{3}{2}\frac{(1-n) U}{d_c n}\eta\alpha$	$k = \frac{3}{2}\frac{(1-n)^{1/3} U}{d_c n}\eta\alpha$

[a] Rajagopalan and Tien [1976] only employed a Lagrangian model for colloid interception and sedimentation. An analytical solution (not shown here) was employed for diffusion.

[b] Assumes steady-state conditions (i.e., $\frac{\partial V}{\partial t} = 0$) and negligible external forces. Subject to boundary conditions outlined in each model.

[c] The force/torque equations for each model are listed below in their respective tables.

[d] The η correlation equation originally presented in Rajagopalan and Tien [1976] is incorrect. Here we are presenting the Logan et al [1995] corrected version.

[+] Trajectory simulations employ random starting locations at upstream (labelled 'injection') collector boundary

[*] The illustrated models typically considered downwards flow (with gravity).

Table 7.2 Overview of the geometries and equations governing selected mechanistic non-Happel sphere models

Model Name	*Yao et al [1971]*	*Hemisphere-in-Cell [Ma et al., 2013][a]*	*Long and Hilpert [2009]*
Model type	Eulerian	Lagrangian	Eulerian
*Model Geometry**			
Particle boundary conditions	Constant concentration ($C = C_o$); Perfect sink ($C = 0$)	Injection boundary[+]; Free exit boundary; Perfect sink ($C = 0$); Perfect sink is replaced with surface friction in Ma et al. [2011]	$dC/dz = 0$; Constant concentration ($C = C_o$); Perfect sink ($C = 0$)

	Stokes (creeping) flow[b,c]:	Navier-Stokes[b]:
Fluid flow equation	$\nabla p = \mu \nabla^2 v$ Continuity: $\nabla v = 0$	$\rho v \cdot \nabla v = -\nabla p + \mu \nabla^2 v$ Continuity: $\nabla v = 0$
Governing colloid transport equation[c]	$\dfrac{\partial C}{\partial t} + v\nabla C = D_{BM}\nabla^2 C +$ $\left(1 - \dfrac{\rho_f}{\rho_p}\right)\dfrac{mg}{3\pi\mu d_p}\dfrac{\partial C}{\partial Z}$	$(m + m^*)\dfrac{du}{dt} = F_D + F_G + F_L + F_{EDL} + F_{vdW} + F_B$ $\nabla(vC) = \nabla(D_{BM}\cdot\nabla C) - \nabla\left(\dfrac{D_{BM}\cdot F}{k_B T}\right)C$
η correlation[d]	$\eta \approx \dfrac{3}{2}\left(\dfrac{d_p}{d_c}\right)^2 +$ $\dfrac{(\rho_p - \rho_f)gd_p^2}{18\mu v} +$ $0.9\left(\dfrac{k_B T}{\mu d_p d_c v}\right)^{2/3}$	$\eta \approx \gamma^2\left[\dfrac{8 + 4(1-\gamma)A_s^{1/3}N_{Pe}^{1/3}}{8 + (1-\gamma)N_{Pe}^{0.97}}N_{Lo}^{0.015}N_{Gi}^{0.8}N_R^{0.028} +\right.$ $\left. A_s N_R^{15/8}N_{Lo}^{1/8} + 0.7N_R^{-0.05}N_G\dfrac{N_{Gi}}{N_{Gi}+0.9}\right]$ [e] $\eta \approx (15.56 \pm$ $0.21)\dfrac{(1-n)^3}{n^2}N_{Pe}^{-0.65\pm0.023}N_R^{0.19\pm0.03} +$ $0.55A_s N_R^{0.1675}N_A^{0.125} +$ $0.22N_R^{-0.24}N_G^{1.11}N_{vdW}^{0.053}$
Kinetic retention rate equation	$k = \dfrac{3}{2}\dfrac{(1-n)U}{d_c n}\eta\alpha$	$k = \dfrac{3(1-n)}{2d_c}\eta v\left[\dfrac{3-n}{3-3n} - \dfrac{2(3-n)}{\pi(3-3n)}\cos^{-1}\left(\dfrac{3-3n}{3-n}\right)^{\frac{1}{2}} +\right.$ $\left. \dfrac{2}{\pi}\sqrt{2\left(\dfrac{3-n}{3-3n}\right)^{0.5} - 1}\right]$ $k = \dfrac{3}{2}\dfrac{(1-n)U}{d_c n}\eta\alpha$

[a] There are a number of iterations of the Hemisphere-in-Cell model [*Ma et al.*, 2009; *Ma and Johnson*, 2010; *Ma et al.*, 2011; *Ma et al.*, 2013]. Here we are specifically presenting the η correlation for Ma et al. [2013]. Many of the model details relevant to these tables remain the same between the iterations and, unless noted otherwise, it is not necessary to differentiate between the specific iterations.

[b] Assumes steady-state conditions (i.e., $\dfrac{\partial v}{\partial t} = 0$) and negligible external forces. Subject to boundary conditions outlined in each model.
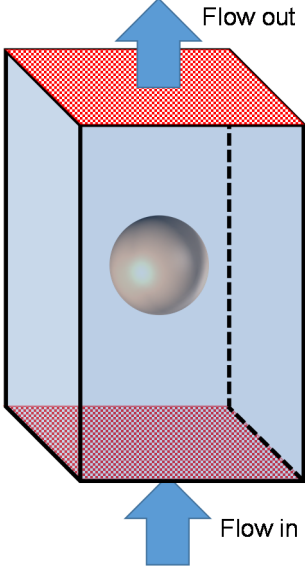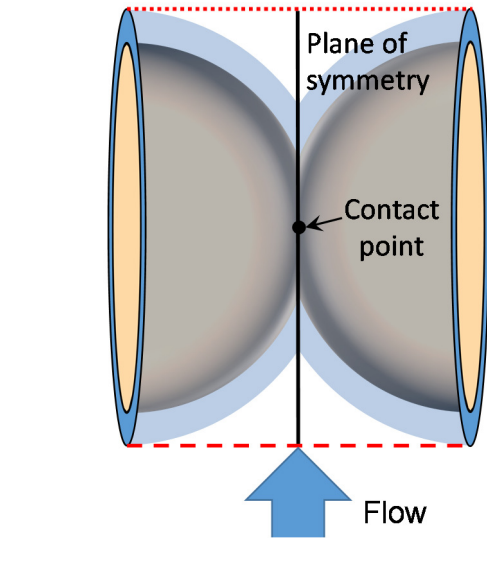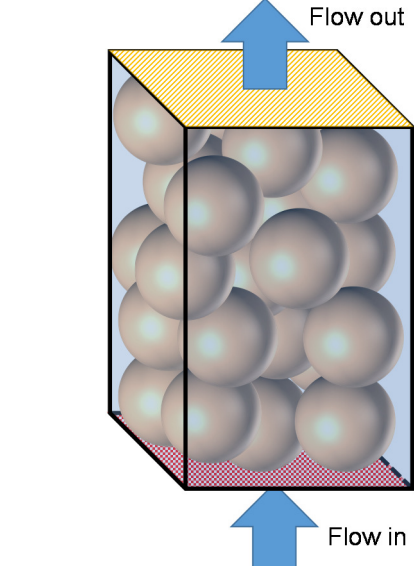
[c] The force/torque equations for each model are listed below in their respective tables. Yao 1971 does not include forces or torques therefore none

are reported here.

[d] Long and Hilpert [2009] adopts the governing equations (in addition to the force balance) from Elimelech[1994] but without van der Waals, anisotropic diffusion or lubrication. The reader is referred to the Tufenkji and Elimelech [2004] table below for further information on the Long and Hilpert [2009] force/torque balance.

[e] In regimes of either pure diffusion or sedimentation mass transfer use the asymptotes described in Ma et al. [2013].

[+] Trajectory simulations employ random starting locations at upstream (labelled 'injection') collector boundary

[*] The illustrated models typically considered downwards flow (with gravity).

Table 7.3: Force/torque equations for Rajagopalan and Tien [1976]

	Force	*Torque*
Inertia	$F_I = m\left(\dfrac{du}{dt} + u \cdot \nabla u\right)$	$t_I = 0$
Gravity	$F_G = \dfrac{4}{3}\pi a_p{}^3\left(\rho_p - \rho_f\right)g[-\cos(\theta)\,e_r + \sin(\theta)e_\theta]$	$t_G = 0$
London	$F_{LO} = \left[\dfrac{-2H\alpha_{rtd}a_p^3}{3\delta^2(2a_p+\delta)^2}\right]e_r$	$t_{LO} = 0$
Electrostatic Double Layer	$F_{DL} = \left\{\left[\dfrac{\varepsilon a_p\kappa(\xi_c^2+\xi_p^2)}{2}\right] \times \left[\left(\dfrac{2\xi_c\xi_p}{\xi_c^2+\xi_p^2}\right) - e^{-\kappa\delta}\right]\left[\dfrac{e^{-\kappa\delta}}{(1-e^{-2\kappa\delta})}\right]\right\}e_r$	$t_{DL} = 0$
Hydrodynamic drag (t = translation, r = rotation, m = movement of fluid around particle)	$(F_D)^t = -6\pi\mu a_p\left[u_r f_r^t e_r + u_\theta f_\theta^t e_\theta\right]$ $(F_D)^r = 6\pi\mu a_p^2 \omega f_\theta^r e_\theta$ $(F_D)^m = 6\pi\mu a_p\{-Ay_r{}^2 f_r^m e_r + [By_r f_{1\theta}^m + Dy_r{}^2 f_{2\theta}^m]e_\theta\}$	$(t_D)^t = 8\pi\mu a_p{}^2 u_\theta g_\phi^t e_\phi$ $(t_D)^r = -8\pi\mu a_p{}^3 \omega g_\phi^r e_\phi$ $(t_D)^m = 8\pi\mu a_p^3\big(Bg_{1\phi}^m + Dy_r g_{2\phi}^m\big)e_\phi$

Table 7.4: Force/torque equations for Tufenkji and Elimelech [2004][1]

	Force
External force in governing equation	$F = F_{col} + F_G$
Colloidal forces	$F_{col} = -\nabla \varphi_T$
Gravity	$F_G = \frac{4}{3}\pi a_p^3 (\rho_p - \rho_f) g$
Hydrodynamic drag[2,3]	$u_r = f_1(\delta^+) f_2(\delta^+) v_r$
	$u_\theta = f_3(\delta^+) v_\theta$
	$D_r = f_1(\delta^+) D_{BM}$
	$D_\theta = f_4(\delta^+) D_{BM}$

[1]The model equations are presented in Elimelech [1994], not Tufenkji and Elimelech [2004]

[2]Elimelech [1994] does not present hydrodynamic force equations. We have reproduced the particle velocity equations with hydrodynamic forces instead.

[3]D_r and D_θ are referred to more generally as D_{BM}^r in the governing colloid transport equation in Table 7.1.

Table 7.5: Force/torque equations for Nelson and Ginn [2011][1,2]

	Equation for θ and r component particle velocities
Particle velocity from streamline	$$u_\theta = [B^+(1+\delta^+) + D^+(1+\delta^+)^2]\left(\frac{U}{r}\right)$$ $$u_r = -A^+(1+\delta^+)^2 U$$
Particle velocity with London van der Waals forces	*n.a. to u_θ* $$u_r = \left[-\frac{\alpha_{rtd}N_{LO}}{(\delta^+)^2(2+\delta^+)^2}\right]U$$
Particle velocity with sedimentation	$$u_\theta = [N_G\sin(\theta)]\left(\frac{U}{r}\right)$$ $$u_r = [-N_G\cos(\theta)]U$$
Particle velocity with hydrodynamic retardation	$$u_\theta = \frac{1}{s_1}[B^+s_2 + D^+(1+\delta^+)s_3]\left(\frac{U}{r}\right)$$ $$u_r = \frac{1}{f_r^t}[-A^+(1+\delta^+)^2 f_r^m]U$$
Total expression for particle velocity	$$u_\theta = \frac{1}{s_1}[B^+s_2 + D^+(1+\delta^+)s_3 + N_G\sin(\theta)]\left(\frac{U}{r}\right)$$ $$u_r = \frac{1}{f_r^t}\left[-A^+(1+\delta^+)^2 f_r^m - N_G\cos(\theta) - \frac{\alpha_{rtd}N_{LO}}{(\delta^+)^2(2+\delta^+)^2}\right]U$$

Particle displacement due to Brownian force vector (F_b) (Cartesian)[3]	$\tilde{R}_x = n_x\sqrt{2D_{BM}\Delta t}$ $\tilde{R}_y = n_y\sqrt{2D_{BM}\Delta t}$ $\tilde{R}_z = n_z\sqrt{2D_{BM}\Delta t}$

[1]Many of these equations are not presented in Nelson and Ginn [2011] but appear instead in Nelson and Ginn [2005].

[2]The Nelson and Ginn [2005; 2011] papers do not present their force/torque equations. Instead, they present the contributions to particle velocity from the individual components. We have reproduced these velocity expressions here along with the final, complete equations for particle velocity.

[3]D_{BM} in this table is a function of both δ^+ and the classic Stokes-Einstein equation, please see Nelson and Ginn [2011] for full details.

Table 7.6: List of force equations for the Hemisphere-in-Cell model [Ma et al., 2009; Ma and Johnson, 2010; Ma et al., 2011; Ma et al., 2013] [1,2]

	Force
Hydrodynamic drag[3]	$F_D^N = \dfrac{6\pi\mu a_p u_N}{f_1} + 6\pi\mu a_p v_N f_2$ $F_D^t = -\dfrac{6\pi\mu a_p u_t}{f_4} + \dfrac{f_3}{f_4} 6\pi\mu a_p v_t$
Gravity	$F_G = \dfrac{4}{3}\pi a_p^3 (\rho_p - \rho_f) g$
Shear lift	$F_L = \dfrac{6.46\mu a_p^3 (\partial v/\partial r)^{3/2}}{\left(\dfrac{\mu}{\rho_f}\right)^{0.5}}$
Electrostatic Double Layer	$F_{EDL} = 4\pi\varepsilon_r\varepsilon_o\kappa\xi_p\xi_c \times \left[\dfrac{\exp(-\kappa\delta)}{1+\exp(-\kappa\delta)} - \dfrac{(\xi_p-\xi_c)^2}{2\xi_p\xi_c}\dfrac{\exp(-2\kappa\delta)}{1-\exp(-2\kappa\delta)} \right]$
van der Waals	$F_{vdW} = -\dfrac{H a_p}{6\delta^2}\dfrac{\lambda(\lambda+22.232\delta)}{(\lambda+11.116\delta)^2}$
Brownian force	$F_B = \mathcal{R}\sqrt{\dfrac{2\zeta k_B T}{\Delta t}}$

[1] The Hemisphere-in-Cell model employs torques that are equivalent to the Rajagopalan and Tien [1976] model. The result of this is that, for colloids in contact with the collector surface, all torque-induced rolling is assumed yield translation along the collector surface (i.e., no slipping or friction) in unfavorable conditions. The only difference is an additional surface friction torque that appears in the Ma et al [2011] iteration of the

Hemisphere-in-Cell model.

[2] Many of the terms in the Hemisphere-in-Cell model and the Rajagopalan and Tien [1976] model are similar, however the Hemisphere-in-Cell flow field has to be solved numerically, this results in references to velocity (*v*) in the force equations as opposed to the A,B and D coefficients employed by Rajagopalan and Tien [1976] from their analytical solution of the flow field.

[3] Superscripts and subscripts N and t refer to directions normal and tangential to collector surface respectively

Table 7.7: Notation for Tables 7.1 to 7.6

A brief note on notation for the above tables: The authors of these mechanistic model studies often use different symbols to represent the same parameter. Wherever possible we have consolidated the symbols representing each parameter into a single consistent symbol. For instance the separation distance between colloid and collector surface has been variously referred to as δ, h and H. In this appendix we use the symbol δ from the Rajagopalan and Tien [1976] paper.

Symbol	Definition	Dimensions (L = length, t = time, m = mass, K = temperature, V = electric potential difference, A = current, N.A. = dimensionless)
a_p	= radius of colloid	L
a_s	= radius of collector	L
A_s	=porosity dependent parameter = $2(1 - \gamma^5)/(2 - 3\gamma + 3\gamma^5 - 2\gamma^6)$	N.A.

A, B, D	= coefficients to correct fluid velocity. Refer to the individual papers for their exact values	A:L^{-1}t^{-1}, B: t^{-1}, D:L^{-1}t^{-1}
A^+, B^+, D^+	= dimensionless versions of the A,B,D coefficients	N.A.
C	= concentration of colloids	m/L^3
C_{in}	= concentration of colloids entering the domain	m/L^3
D_{BM}	= Brownian diffusion coefficient for a sphere in an infinite fluid (from Stokes-Einstein equation: $D_{BM} = \frac{k_B T}{3\pi\mu d_p}$	L^2/t
D_{BM}^r	= diffusion tensor (from D_r, D_θ)	L^2/t
D_r, D_θ	= diffusion coefficient in the radial and angular directions	L^2/t
d_c	= diameter of collector	L
d_p	= diameter of colloid	L

e_r, e_θ, e_ϕ	= unit vectors in the radial and angular directions	N.A.
F	= force vector (subscripts refer to the specific force of interest)	$m \cdot L/t^2$
$f_r^t, f_\theta^t, f_\theta^r,$ $f_r^m, f_{1\theta}^m, f_{2\theta}^m$	= drag correction factors in RT 1976 and NG 2011. Refer to individual papers for exact values.	N.A.
f_1, f_2, f_3, f_4	= corrections for hydrodynamic interactions in TE 2004 and MPFJ. Refer to individual papers for exact values.	N.A.
g	= gravitational acceleration, 9.81 m/s	L/t
$g_\phi^t, g_\phi^r, g_{1\phi}^m, g_{2\phi}^m$	= torque correction factors in RT 1976	N.A.
H	= Hamaker coefficient	$m \cdot L^2/t^2$
k_B	= Boltzmann constant ($\sim 1.38 \times 10^{-23}$ m$^2 \cdot$kg$\cdot$s$^{-2} \cdot$K^{-1})	$L^2 \cdot m/(t^2 \cdot K)$
k	= kinetic retention rate coefficient (also commonly denoted as k_{att}, k_f)	1/t

m	= particle mass (m^* refers to virtual particle mass)	m
N_A	= attraction number = $H/(12\pi\mu a_p^2 U)$	N.A.
N_G	= gravity number = $2a_p^2(\rho_p - \rho_f)g/(9\mu U)$	N.A.
N_{Gi}	= $1/(N_G + 1)$	N.A.
N_{LO}	= London number = $H/(9\pi\mu a_p^2 U)$	N.A.
N_{Pe}	= Peclet number = Ud_c/D_{BM}	N.A.
N_R	= aspect ratio = a_p/a_s	N.A.
N_{vdW}	= van der Waals number = $H/(k_b T)$	N.A.
n	= porosity	N.A.
n_x, n_y, n_z	= random numbers for Brownian force vector	N.A.
p	= fluid pressure	m/(L·t^2)

$\tilde{R}_x, \tilde{R}_y, \tilde{R}_z$	= random displacement for Brownian motion	L
$\mathcal{R}$	= Gaussian random number	N.A.
r	= radial coordinate	L
s_1, s_2, s_3	= drag correction factors in NG 2011	N.A.
T	= temperature	K
t	= time	T
$t_G, t_{LO}, t_{DL}, t_D, t_I$	= torques	$(m \cdot L/t^2) \cdot L$
u	= particle velocity (subscripts r and θ refer to its polar components)	L/t
U	= approach (or darcy) velocity $= v \times n$	L/t
v	= fluid velocity (subscripts refer to its directional components)	L/t

y_r $\qquad = (r - a_s)$ $\qquad$ L

x, y, z $\qquad$ = Cartesian coordinates $\qquad$ L

Greek letters:

α $\qquad$ = sticking (or collision) efficiency $\qquad$ N.A.

α_{rtd} $\qquad$ = retardation correction for London force $\qquad$ L^{-4}

δ $\qquad$ = surface to surface separation between colloid and collector $\qquad$ L

δ^+ $\qquad = \delta/a_p$ $\qquad$ N.A.

ε $\qquad$ = dielectric constant of the medium $\qquad$ N.A.

$\varepsilon_r \varepsilon_o$ $\qquad$ = permittivity of water $\qquad$ $t^4 \cdot A^2/(L^2 \cdot m)/L$

η $\qquad$ = collector contact efficiency $\qquad$ N.A.

ζ $\qquad$ = friction coefficient $\qquad$ m/t

κ	= Debye-Hückel reciprocal length	L^{-1}
ρ_f, ρ_p	= density of fluid and particle	m/L^3
μ	= dynamic (absolute) viscosity of fluid	$m/(L \cdot t)$
ω	= angular velocity	Radians/t
ξ_c, ξ_p	= surface potentials of the collector and particle (it is common practice to use zeta potentials instead of surface potentials)	V
θ	= angle	Radians
ϕ_t	= total interaction energy (i.e., sum of van der Waals and electric double layer forces)	$m \cdot L^2/t^2$
λ	= characteristic wave length	L
γ	$= (1 - n)^{1/3}$	N.A.

7.2   References

Elimelech, M. (1994), PARTICLE DEPOSITION ON IDEAL COLLECTORS FROM DILUTE FLOWING SUSPENSIONS - MATHEMATICAL FORMULATION, NUMERICAL-SOLUTION, AND SIMULATIONS, *Sep. Technol.*, *4*(4), 186-212.

Logan, B., D. Jewett, R. Arnold, E. Bouwer, and C. O'Melia (1995), Clarification of Clean-Bed Filtration Models, *Journal of Environmental Engineering*, *121*(12), 869-873.

Long, W., and M. Hilpert (2009), A Correlation for the Collector Efficiency of Brownian Particles in Clean-Bed Filtration in Sphere Packings by a Lattice-Boltzmann Method, *Environ. Sci. Technol.*, *43*(12), 4419-4424.

Ma, H., J. Pedel, P. Fife, and W. P. Johnson (2009), Hemispheres-in-Cell Geometry to Predict Colloid Deposition in Porous Media, *Environ. Sci. Technol.*, *43*(22), 8573-8579.

Ma, H., and W. P. Johnson (2010), Colloid Retention in Porous Media of Various Porosities: Predictions by the Hemispheres-in-Cell Model, *Langmuir*, *26*(3), 1680-1687.

Ma, H., E. Pazmino, and W. P. Johnson (2011), Surface Heterogeneity on Hemispheres-in-Cell Model Yields All Experimentally-Observed Non-Straining Colloid Retention Mechanisms in Porous Media in the Presence of Energy Barriers, *Langmuir*, *27*(24), 14982-14994.

Ma, H., M. Hradisky, and W. P. Johnson (2013), Extending Applicability of Correlation Equations to Predict Colloidal Retention in Porous Media at Low Fluid Velocity, *Environ. Sci. Technol.*, *47*(5), 2272-2278.

Nelson, K. E., and T. R. Ginn (2005), Colloid Filtration Theory and the Happel Sphere-in-Cell Model Revisited with Direct Numerical Simulation of Colloids, *Langmuir*, *21*(6), 2173-2184.

Nelson, K. E., and T. R. Ginn (2011), New collector efficiency equation for colloid filtration in both natural and engineered flow conditions, *Water Resour. Res.*, *47*, 17.

Rajagopalan, R., and C. Tien (1976), TRAJECTORY ANALYSIS OF DEEP-BED FILTRATION WITH SPHERE-IN-CELL POROUS-MEDIA MODEL, *Aiche J.*, *22*(3), 523-533.

Tufenkji, N., and M. Elimelech (2004), Correlation equation for predicting single-collector efficiency in physicochemical filtration in saturated porous media, *Environ. Sci. Technol.*, *38*(2), 529-536.

Yao, K.-M., M. T. Habibian, and C. R. O'Melia (1971), Water and waste water filtration. Concepts and applications, *Environ. Sci. Technol.*, *5*(11), 1105-1112.

7.3   Mechanistic simulations: Unfavorable conditions

Mechanistic force/torque balance simulations that use mean-field DLVO interactions predict zero attachment even under conditions of modest repulsion (e.g., interaction energy > several kT, see Figure 2.1) between colloids and grain surfaces [*Elimelech and Omelia*, 1990].   Yet, as discussed earlier, unfavorable conditions are observed in numerous environmental scenarios. As a result, we have until recently lacked mechanistic theory to predict colloid attachment and transport in environmental contexts, and there as yet exists no easily-implemented approximating correlation equation for mechanistically-based prediction of colloid attachment under unfavorable conditions.

The inability of mean-field force/torque balances to predict colloid attachment in unfavorable conditions has driven the development of semi-empirical expressions to predict attachment [*Bai and Tien*, 1996; 1999; *Chang et al.*, 2009; *Elimelech*, 1992]. Like the approximating correlation equations for favorable conditions described above, these semi-empirical correlations are composed of dimensionless groups of relevant physicochemical parameters that were fit via coefficients and powers. An example correlation from Elimelech [1992] is provided:

$$\eta_{unf} = 0.0257(N_{col})^{1.19}\eta_{fav} \qquad\qquad 7.1$$

where η_{unf} and η_{fav} are the collector efficiencies in the presence and absence of repulsion, respectively, and N_{col} represents the ratio of attractive to repulsive colloid-collector interactions and is defined as follows:

$$N_{col} = \frac{A_{132}}{\varepsilon_0\varepsilon_r\xi_p\xi_c\ \kappa^{-1}} \qquad\qquad 7.2$$

where A_{132} is the combined Hamaker constant for the colloid, water, and porous media, ε_o and ε_r are the absolute and relative permittivities in vacuum and water, respectively. The parameters ζ_p and ζ_c are the mean-field potentials of the colloid and collector surfaces, and κ^{-1} is the inverse Debye length. The reported fitted coefficient (0.0257) and power (1.19) correspond to the general set of experiments reported by Elimelech (1992). Please

note that throughout this document we do not use subscripting of η to denote whether it represents favorable versus unfavorable conditions, except in circumstances where direct comparison of these two conditions is required.

Semi-empirical correlations coefficients and powers were fit directly to experimental data rather than to mechanistic simulations. They are therefore limited to the experimental conditions from which they were developed, and their relative performance across a larger range of conditions is generally poor when applied outside the experimental conditions under which they were developed. In contrast, the approximating correlation equations for favorable conditions typically show relative errors less than a factor of three (i.e., the error is less than 3× the estimated η) [*Ma et al.*, 2013; *Nelson and Ginn*, 2011]. The relatively greater success of correlation equations developed for favorable conditions may reflect their having been fit to mechanistic simulations, which ideally extends their utility to a larger range of conditions, but may also reflect the greater complexity of colloid transport under unfavorable conditions.

The ratio (η_{unf}/η_{fav}) provides a measure of the effect of repulsion, and is called the collision or attachment efficiency (α). The value of α should therefore range from 0 to unity. Investigators can obtain α by comparing experiments conducted under unfavorable versus favorable conditions, or as more often is the case, by substituting favorable condition correlation equation predictions of η_{fav}. Whereas the latter approach yields reasonable estimates of α for many conditions, it may yield values of $\alpha > 1$ for less unfavorable (nearly favorable) conditions. This reflects the fact that, as described above, the approximating correlation equations for favorable conditions are just that, approximations of the underlying mechanistic models, and so they may introduce error via the approximation. Furthermore, even the underlying mechanistic models may introduce error if the experimental conditions "violate" assumptions in the underlying mechanistic models (e.g., uniformity, spheroidal colloids and collectors, etc.) as is also true for predictions under favorable conditions.

7.3.1.1   Secondary minimum association.

Whereas mean-field mechanistic models do not predict immobilization (attachment) of colloids in the presence of significant repulsion, they do predict the accumulation of colloids in the near-surface fluid domain due to secondary minimum attraction under unfavorable conditions [e.g. *Johnson et al.*, 2007]. The experimentally-observed "skimming" behavior of colloids in the near-surface fluid domain under unfavorable conditions [e.g. *Johnson et al.*, 2010] is predicted by mean-field mechanistic models, for example, in dense and simple cubic packing structures [e.g. *Johnson et al.*, 2007] and impinging jet systems where flow is directed normal to a planar surface and spreads radially from the flow stagnation axis [*Johnson and Hilpert*, 2013].

The influence of secondary minimum interactions is accounted for in mean-field force/torque models underlying CFT but this has received limited attention. The reason being that these models (often performed in the Happel unit cell) were usually run under favorable conditions (absence of repulsive barrier yields absence of secondary minimum) but would need to be run under unfavorable conditions in order for the influence of the secondary minimum to be observed. Furthermore, when these models were run under unfavorable conditions, the primary purpose was to demonstrate lack of immobilization (lack of attachment) for significant repulsion [e.g. *Elimelech and Omelia*, 1990].

The possibility that experimentally-inferred colloid retention at the column scale may include secondary minimum-associated colloids prompted the development of easily-adopted approaches to predict potential colloid retention via this mechanism. Foremost among these is the Maxwell approach [*Franchi and O'Melia*, 2003; *Hahn and O'Melia*, 2004; *Sang et al.*, 2013; *Shen et al.*, 2007; *Tosco et al.*, 2009], which determines the kinetic energy distribution among the colloid population from the Maxwell frequency distribution of their velocities. Retained colloids are those with insufficient kinetic energy to escape from the secondary energy minimum into the bulk fluid domain. The Maxwell approach is a simplified version of CFT in that it does not account for fluid flow, collector geometry, or mechanistic force/torque balance, such that the subsequent

fate (e.g., exit from the collector) of colloids associated with the surface via secondary minimum interactions is not actually determined.

The utility of the Maxwell approach lies in its relative ease of application relative to a full force/torque balance. It must be stressed that although both the Maxwell or mean-field mechanistic force/torque balance approaches predict accumulation in the secondary energy minima they predict no colloid attachment to (i.e., immobilization on) surfaces (except for energy barriers less than several kT).

7.3.1.2   Immobilization.

As mentioned above, mean-field mechanistic models do not predict the experimentally-observed immobilization of a significant fraction of near-surface colloids [e.g. *Johnson et al.*, 2010] on bulk repulsive surfaces. Instead, as stated above, colloids are predicted to skim (spin and translate) outboard of the energy barrier in the near-surface fluid domain. As such, the challenge in prediction of colloid attachment (immobilization) is how to achieve physical contact with the surface when mean-field prediction indicates that it is prevented by the repulsive barrier. A number of strategies have been recently employed to mechanistically predict this immobilization. These strategies can be categorized as: 1) macroscopic heterogeneity, 2) implied physical heterogeneity, and 3) representative discrete heterogeneity.

Heterogeneity has, for at least twenty years, been acknowledged as a potential explanation for the discrepancy between mechanistic predictions and experimental observations in environmental (unfavorable) conditions [*Ryan and Elimelech*, 1996]. Since then, research has confirmed the potential role of heterogeneity in colloid retention in environmental conditions. While our understanding of the processes governing colloid-heterogeneity interactions has evolved considerably, there remain a number of questions regarding the role and significance of heterogeneity at macroscopic and microscopic scales as described below.

7.3.1.2.1   Macroscopic and implied physical heterogeneity

Macroscopic surface heterogeneity (i.e., readily measured surface properties) arises from, for example, the presence of multiple mineral surfaces with different isoelectric points such that some surfaces are positively charged, and some are negatively charged (e.g., iron oxyhydroxides versus silica) at circum-neutral pH. For porous media having macroscopic geochemical heterogeneity, the unfavorable fraction of the surface can be approximated as having $\alpha=0$, and the favorable fraction of surface can be approximated as having $\alpha= 1$. This approach is successful in that a simple linear combination of the binary α values weighted by the corresponding fractions of favorable versus unfavorable surfaces in the porous media yields reasonable prediction of observed retention in macroscopically heterogeneous media [*Chen et al.*, 2001; *Johnson et al.*, 1996; *Loveland et al.*, 2003; *Song et al.*, 1994].

The primary limitation of this approach is that while macroscopic surface heterogeneities are widespread in environmental porous media, there is significant evidence that these heterogeneities may only minimally influence colloid transport in soils. Natural organic matter (NOM) has been shown to sorb strongly to positively charged (i.e., favorable) mineral surfaces such as ferric and aluminum oxyhydroxides and switch their surface charges from positive to negative [*Abudalo et al.*, 2010; *Amirbahman and Olson*, 1993; *Foppen et al.*, 2008; *Gu et al.*, 1995; *Johnson and Logan*, 1996; *Liu et al.*, 2009b; *Mosley et al.*, 2003; *Mylon et al.*, 2004; *Pieper et al.*, 1997; *Wang et al.*, 2012]. The sorption of NOM to surfaces that are favorable for colloid attachment will potentially yield unfavorable attachment conditions. Given the widespread prevalence of NOM throughout environmental media, many macroscopic heterogeneities may be coated by organics that yield unfavorable conditions thereby limiting the relevance of macroscopic heterogeneities in environmental media. A large number of colloid transport studies have demonstrated this NOM 'masking effect' in which the presence of organic matter can increase colloid transport [*Abudalo et al.*, 2010; *Amirbahman and Olson*, 1993; *Foppen et al.*, 2008; *Jiang et al.*, 2012b; *Johnson and Logan*, 1996; *Morales et al.*, 2011; *Mylon et al.*, 2004; *Pelley and Tufenkji*, 2008; *Pieper et al.*, 1997; *Wang et al.*, 2012].

Environmental media coated with NOM cannot be represented by this "patchwise" linear approximation since the entire media would be represented by $\alpha=0$; whereas significant colloid retention is experimentally observed in such media [*Elimelech and Omelia*, 1990; *Johnson et al.*, 2010; *Li et al.*, 2004; *Tong and Johnson*, 2006]. The discrepancy suggests the presence of micro- to nano-scale heterogeneity (i.e., not readily measurable surface properties) on the bulk repulsive surface, which may allow attachment to occur (e.g., Elimelech and O'Melia, 1990) as described below in Appendix 7.3.1.2.2.

The inferred presence of micro- to nano-scale heterogeneity on surfaces has spurred the development of a variety of mechanistic approaches to account for nano- to micro-scale physical and chemical heterogeneity. One approach that capitalizes on the predicted accumulation of colloids in secondary minima, but also provides a mechanism to immobilize a subset of these secondary minimum-associated colloids, is herein called the "implied physical heterogeneity approach" [*Torkzaban et al.*, 2008]. The approach extends surface friction, which is traditionally considered to act at the primary minimum [e.g. *Bergendahl and Grasso*, 2000; *Johnson et al.*, 1971], out to the secondary minimum, which is traditionally considered "non contact" such that the relevant friction in the secondary minimum arises from fluid viscosity [e.g. *Rajagopalan and Tien*, 1976]. Extending surface friction to the secondary minimum replaces the traditionally-assumed relatively weak friction from fluid viscosity with stronger surface friction that immobilizes colloids in zones of low fluid drag (e.g. low velocity or recirculation zones). The approach effectively treats the near-surface fluid domain (see Figure 2.1) as a highly viscous fluid yielding a friction coefficient equal to that of the surfaces in contact. This method is justified on the basis that there can exist roughness, macromolecules, etc. that may effectively extend surface friction to the attractive secondary well [*Johnson et al.*, 2009].

The approach is successful in that it identifies zones on the surface where colloids can be immobilized due to drag forces being less than the extended friction force. However, an important limitation of the approach is that it has not been reconciled with existing work that considers secondary minimum interactions as non–contact forces [*Israelachvili*, 2011], and it does not build on the formal approach provided by the previously existing

body of work accounting for steric forces associated with water structure, roughness, and macromolecules in the near-surface domain [*Israelachvili*, 2011].

With respect to predictions, the implied physical heterogeneity approach predicts attachment only in zones of low fluid drag [*Bradford et al.*, 2011; *Torkzaban et al.*, 2007; *Torkzaban et al.*, 2008]; whereas, experiments demonstrate colloid deposition in high fluid drag zones such as forward flow stagnation zones [*Johnson et al.*, 2010; *Pazmino et al.*, 2014b] under unfavorable conditions. Forward flow stagnation zones are regions where flow impinging normal to the collector surface is converted to tangential flow. Tangential flow is zero on the forward flow stagnation axis that is defined as the center of the impinging flow. Normal flow on this axis decays with decreasing separation distance from the surface to a minimum (taken to be zero) at the forward flow stagnation point on the collector surface. Adjacent to the collector surface outside the forward flow stagnation point, tangential flow and tangential drag force on colloids rapidly increase. As a result the forward flow stagnation zones are not zones of low fluid drag except at the forward flow stagnation point (identified in Figure 2.4). The same principle applies to the rear flow stagnation zone and point, where tangential flow converging on the flow stagnation axis is converted to normal flow away from the grain surface. Simulations utilizing implied physical heterogeneity also predict that colloids will immobilize (attach) at long distances (e.g., multiple tens of nm) from the surface, in which case detachment will occur in response to very slight increases in fluid drag [*Pazmino et al.*, 2014a]. In contrast, direct observation experiments show that detachment requires fluid velocity perturbations significantly higher than the loading velocity [*Pazmino et al.*, 2014a], as further described below.

7.3.1.2.2   Micro- to nano-scale heterogeneity.

The existence of micro- to nano-scale heterogeneity (herein called discrete heterogeneity) on bulk repulsive surfaces is inferred from the observed attachment of colloids under unfavorable conditions lacking macroscopic heterogeneity. The rationale for this inference is that repulsion experienced by colloids from a bulk like-charged surface may be locally eliminated or reduced by the presence of physical asperities (protrusions

associated with roughness) and charge heterogeneity [*Bhattacharjee et al.*, 1998; *Hoek and Agarwal*, 2006]. As illustrated in Figure 7.1, physical asperities reduce repulsion because interaction forces scale directly with radius of curvature [*Israelachvili*, 2011], and the asperity reduces (locally) the radius of curvature associated with colloid-surface interaction. Charge heterogeneity creates local zones of opposite charge (attraction) that scales with the size of these zones, as illustrated in Figure 7.1.
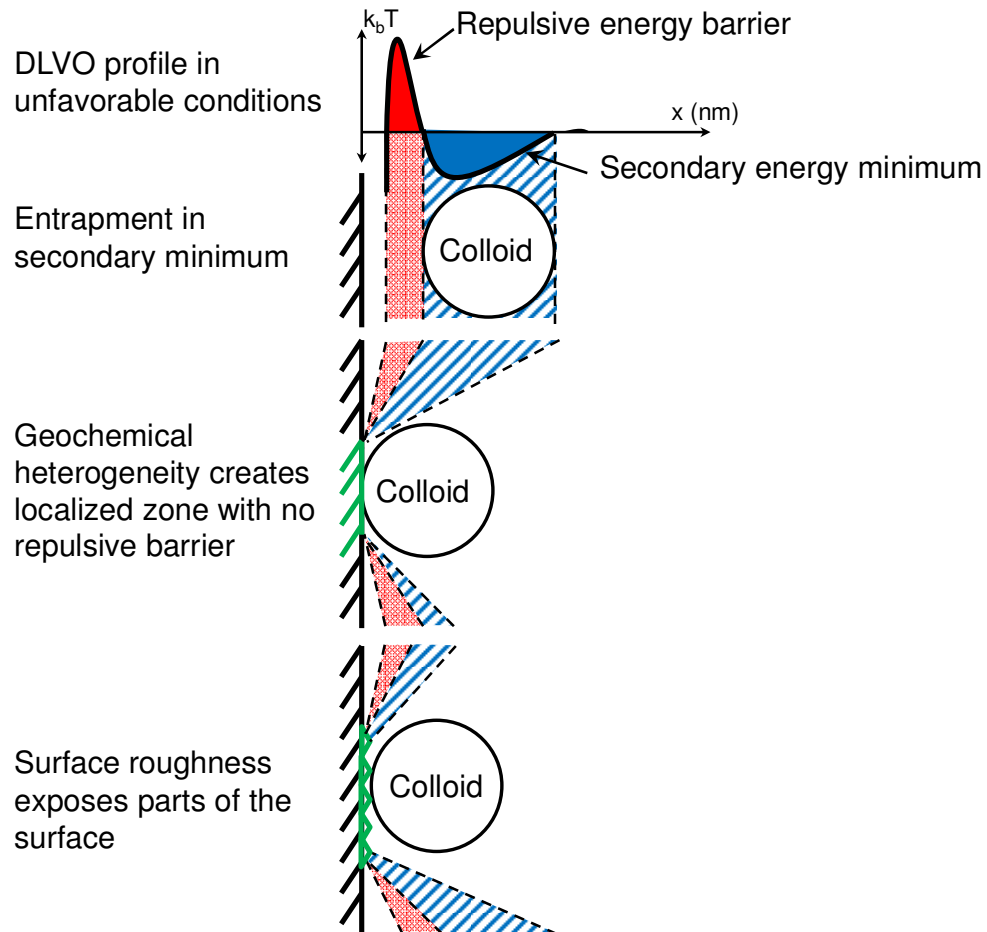

Figure 7.1: The different attachment/retention interactions that may occur when the colloid is near the collector surface. The representative DLVO profile is an approximation of unfavorable deposition conditions with both an electrostatic repulsive energy barrier (red) and an attractive secondary energy minimum (blue). For ease of interpretation, the size of the primary energy barrier is on the same order as the depth of the secondary minimum but there are scenarios where the primary energy barrier may be much larger than what is pictured. In addition, for ease of interpretation the colloids are depicted as being the same size as the heterodomain features they are interacting with; this is not necessarily the case as the size of these features may range from the micro- to nano-scale while colloids may be up to 10 μm in diameter.

Whereas macroscopic heterogeneity (e.g., metal oxyhydroxide coatings on silica) may be removed via acid-base cleaning, nano- to micro-scale heterogeneity from roughness and cation substitution in the mineral matrix are not removed, and in fact may be enhanced, by cleaning approaches [*DiCarlo et al.*, 2010; *Jiang et al.*, 2012a; *Johnson et al.*, 1996; *Litton and Olson*, 1993; *Liu et al.*, 2009a; *Molnar et al.*, 2011; *Tong and Johnson*, 2006]. The sometimes-invoked assumption that colloid retention on cleaned surfaces must occur via straining (due to presumed absence of heterogeneity) has been discussed [*Johnson et al.*, 2011] (see Appendix 7.4.3 for a discussion on successes and opportunities in straining research).

7.3.1.2.3 Representative discrete heterogeneity

Another approach to achieve physical contact between the colloid and the collector surface in spite of significant repulsion between the bulk surfaces is to replace the mean-field colloid-collector interactions with interactions that explicitly recognize the existence of discrete nano- to micro-scale physical and chemical heterogeneity on the collector (or potentially colloid) surface where colloid-collector repulsion is locally reduced or eliminated (herein referred to as heterodomains)[e.g. *Bendersky and Davis*, 2011; *Duffadar and Davis*, 2007; *Shen et al.*, 2013]. Heterodomains differ from the previously discussed macroscopic surface heterogeneities as they are not readily measurable surface properties. These heterodomains, illustrated in Figure 7.1, can bring colloids into physical (e.g., primary minimum) contact with the surface, where surface friction is more generally accepted to be applicable [*Bergendahl and Grasso*, 2000; *Johnson et al.*, 1971], as described in detail in Pazmino et al. [2014b].

Discrete heterogeneity on a collector surface yields different net interactions (attractive versus repulsive) for different colloid sizes [*Pazmino et al.*, 2014b]. Due to curvature of the colloid surface and the rapid decay of colloid-collector interactions with increasing separation distance, the zone of significant colloid-collector interaction (ZOI) is a fraction of the projected area of the colloid. The ZOI area decreases with increasing ionic strength [*Duffadar et al.*, 2009; *Pazmino et al.*, 2014b]. The net colloid-collector interaction is determined by the combination of attractive and repulsive interactions

across the ZOI, which is determined by the fraction of the ZOI that is occupied by heterodomain(s) [*Pazmino et al.*, 2014a; *Pazmino et al.*, 2014b]. Hence, the net colloid-collector interaction (attractive versus repulsive) depends on the interplay of colloid size, heterodomain size, and ionic strength, as shown in Figure 7.2 adapted from Pazmino et al. [2014b]. In the figure, a given heterodomain size and ionic strength condition yields a net interaction force that depends directly on colloid size, as shown by the force curves in Figure 7.2, where blue yields no repulsion and red yields the largest repulsion. This occurs because the radius of the ZOI (R_{ZOI}) increases with colloid size, as shown by spheres in Figure 7.2. The fractional coverage (of ZOI) by heterodomains decreases as the colloid size increases relative to a given heterodomain size, leading to net attractive interaction at all separation distances for the smallest (blue) colloid, and net strong repulsion at intermediate distances (repulsive barrier) for the largest (red) colloid.

Successes of the discrete heterogeneity approach, referring to the incorporation of nanoscale zones of attraction in the DLVO interaction, include: (i) colloid attachment on the open surface, and (ii) wedging in grain to grain contacts for larger colloids both emerge from the force/torque simulations that incorporate discrete nanoscale heterogeneity [*Ma et al.*, 2011]. Quantitative prediction of experimentally-observed attachment of colloids on silica emerges from incorporation of representative discrete nanoscale heterogeneity into mechanistic force/torque balance [*Pazmino et al.*, 2014b]. The approach also predicts the experimentally-observed detachment of colloids (i.e., a fractional release of the attached population) in response to perturbations in ionic strength or fluid velocity. Notably, both the observed and simulated colloid detachment in response to fluid velocity perturbations required perturbations to be significantly greater than the loading velocity. This resulted from colloid immobilization (attachment) in the primary minimum where van der Waals attraction generated strong adhesion [*Pazmino et al.*, 2014a]. This is an important contrast to the implied physical heterogeneity approach, which immobilizes colloids multiple tens of nm from the surface in the secondary minimum, as described above.

The discrete heterogeneity approach represents (to the knowledge of the authors) the first report of an ability to predict attachment quantitatively and detachment (from physical

contact) qualitatively, using the same set of fundamental parameters in force/torque simulations for both predictions [*Pazmino et al.*, 2014a; *Pazmino et al.*, 2014b]. However, there are still challenges to be addressed in the discrete heterogeneity approach; to date discrete heterogeneity cannot be independently measured in ways directly relevant to colloid-surface interaction. For example, zeta potentials are too insensitive to reflect nano- to micro-scale heterogeneity [*Elimelech et al.*, 2000], atomic force microscopy has limited resolution [*Drelich and Wang*, 2011; *Shellenberger and Logan*, 2002; *Taboada-Serrano et al.*, 2005], and surface spectroscopic techniques do not yield information directly applicable to colloid-surface interaction. Whereas there are many opportunities to explore application of the above techniques, at present the discrete heterogeneity approach requires empirical determination of a representative heterogeneity on surfaces. Currently, the published literature reflects representative discrete heterogeneity on silica surfaces only [*Pazmino et al.*, 2014b]. Although silica is an important primary target surface (i.e., the vast majority of colloid transport experiments utilize silica porous media), the approach needs to be extended to other surfaces and conditions to test its general applicability.

The outcomes that emerge from the force/torque simulations utilizing discrete heterogeneity match experimental observations across an array of colloid sizes, fluid velocities, and ionic strength values. The discrete heterogeneity approach, by developing a representative heterogeneity for a surface, provides a mechanism to represent differences in heterogeneity among different mineral types and different pH conditions. These changes are not captured by mean-field parameters such as bulk surface zeta potential [*Elimelech et al.*, 2000].

Representative discrete heterogeneity provides a potential platform for mechanistic representation of blocking or ripening, both of which begin with a limited number of colloid attachment sites. Heterodomains (representative heterogeneity) would serve as these initial attachment sites, with subsequent decrease (blocking) or increase (ripening) in the number of attachment sites with increased colloid attachment, depending on whether colloid-colloid interactions are repulsive or attractive, respectively.

As explained above, for a given heterogeneous surface, the net interaction (attractive versus repulsive) depends on colloid size and surface properties. As such, slight differences in colloid size and/or surface properties may generate effective heterogeneity in "stickiness" among the colloid population. Demonstrating this effect may yield a mechanistic explanation for the apparent heterogeneity in retention rate coefficients among apparently uniform populations, which is thought to drive the observed non log-linear profiles of retained colloids observed under unfavorable conditions [*Albinger et al.*, 1994; *Baygents et al.*, 1998; *Bolster et al.*, 1999; *Bolster et al.*, 2000; *Harvey et al.*, 1995; *Hendry et al.*, 1997; *Li et al.*, 2004; *Liang et al.*, 2013; *Schijven et al.*, 1999; *Simoni et al.*, 1998; *Tong and Johnson*, 2007; *Tufenkji and Elimelech*, 2004; *Tufenkji et al.*, 2004; *Tufenkji and Elimelech*, 2005a; b; *Wang et al.*, 2014].
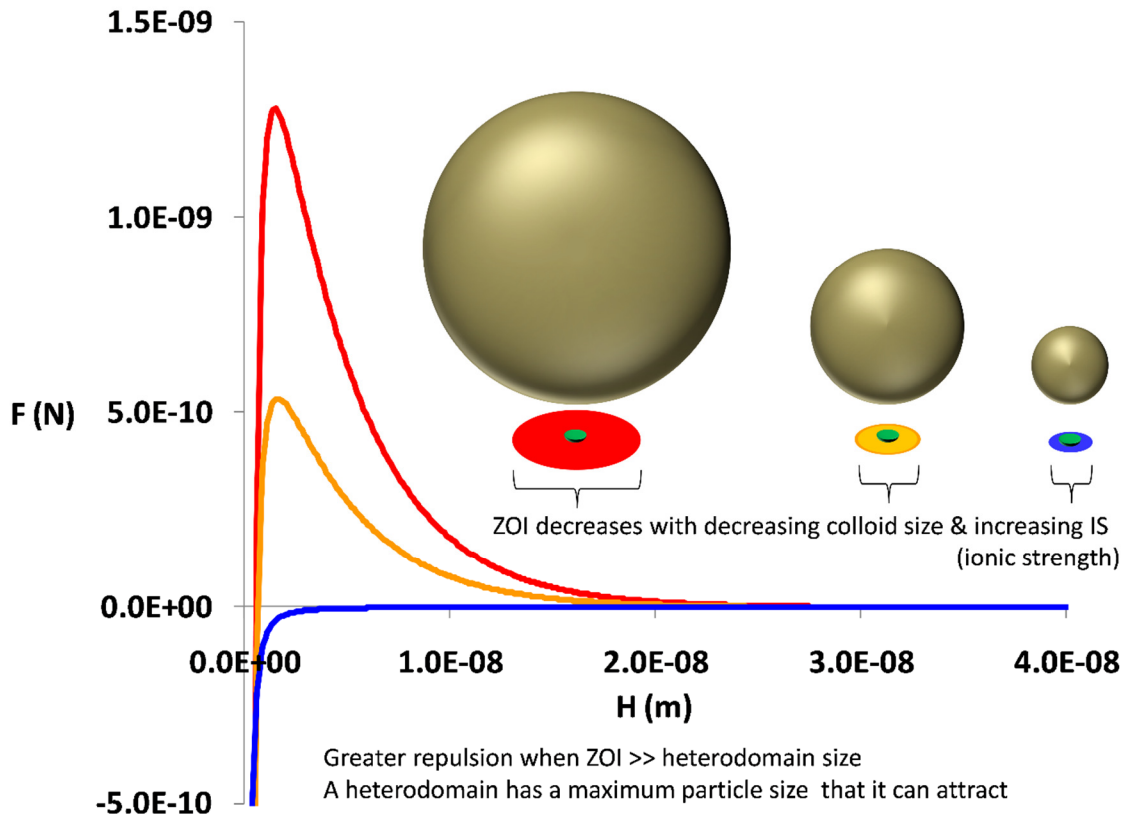
Figure 7.2: Colloidal force profiles as a function of colloid-collector separation distance (H) for 1.95, 1.1 and 0.25 μm colloids. The height of the energy barrier corresponds to the size of the colloid. The largest colloid – 1.95 μm – has the largest energy barrier, the medium colloid – 1.1 μm– has the smaller energy barrier and the smallest colloid – 0.25 μm – has no energy barrier. The projected colored circle represents the ZOI, the inner circle represents an 80-nm radius heterodomain. The ZOI color corresponds to the force profile. The repulsive force is greatest for the lowest ZOI coverage by heterodomain(s). Varied heterodomain size relative to ZOI would have the same effect, as would varied IS for a given colloid and heterodomain size (increased IS yields decreased radius of ZOI). Adapted from Pazmino et al., [2014b].

7.4 Upscaling from pore to continuum scale

The parameter η describes the efficiency of colloid delivery to the surface (favorable conditions) or the near surface fluid domain (unfavorable conditions) at the pore scale. Its implementation into continuum scale models (upscaling) is performed under the simple assumption that the control volume considered in the continuum model is represented by a collection of identical pore scale collectors comprising the same volume and having the same porosity as the control volume [*Johnson and Hilpert*, 2013; *Logan et*

al., 1995; *Nelson and Ginn*, 2011]. Under this assumption the equation expressing η as a rate constant (k) for the Happel sphere in cell geometry is:

$$k = -\frac{3(1-\theta)^{1/3}}{2d_c}\ln(1-\eta)v \qquad\qquad 7.3$$

Where d_c is the average collector diameter, v is velocity and θ is porosity. The functional form of k is not the same for all η correlations, it is a function of the conceptual model employed; the Hemisphere-in-cell [*Ma et al.*, 2009] and constricted tube [*Paraskeva et al.*, 1991] geometries have different relationships for k.

7.4.1   Opportunities in secondary minimum interactions

The $k - \eta$ relationship (eq. 7.3) describes colloid delivery to the near-surface fluid, which under favorable conditions is practically equivalent to attachment. Under unfavorable conditions, the fate of near surface colloids is less straightforward. While a fraction of near-surface (secondary minimum-associated) colloids may attach in response to local attraction emanating from heterogeneity, the complement may translate across the surface until they return to the bulk fluid.

While eq. 7.3 is specifically for porous media, it is worthwhile mentioning that it is possible to link the observed deposition rates in impinging jet systems to mechanistically-predicted collector efficiencies in pore scale models [*Pazmino et al.*, 2014b]. In contrast, comparison of k between these systems requires relating the flow fields between them, and this likely requires incorporating discrete heterogeneity representations into Happel sphere in cell geometry.

Additionally, the presence of secondary minima in unfavorable conditions may yield an indefinite residence time of colloids in the near-surface fluid domain. Secondary minimum interactions will influence the average velocity of the colloid population to an extent depending on η as well as the depth of the secondary minimum, since velocity in the near surface fluid is far lower than the average pore water velocity. Furthermore, secondary minimum-associated colloids may be effectively retained in the control

volume (e.g., packed column in experiments) if elution does not occur prior to termination of the observation. Currently there exists no relationship to quantitatively account for the influence of secondary minimum association on the concentration and timing of colloid elution. Developing such a relationship will require identifying the frequency with which colloids transfer between the bulk and near surface fluid domains, as discussed below.

7.4.2   Opportunities in the role of topology

The fact that mechanistic simulations and upscaling provide good prediction at the continuum scale under favorable conditions suggests that mixing of near surface and bulk fluid must occur between subsequent collectors (grains) in the control volume [Johnson and Hilpert, 2013]. This is inferred on the basis that under favorable conditions in the absence of mixing, the near-surface fluid would become depleted of colloids, increasingly so with each subsequent collector, yielding decreasing k with increased transport distance [*Johnson and Hilpert*, 2013]. The log-linear profiles of retained colloids that are typically observed under favorable conditions indicate that k remains constant with transport distance. Hence, mixing of near-surface and bulk fluid between subsequent collectors is reasonably inferred. In contrast, absence of mixing between collectors under unfavorable conditions would yield increasing excess of colloids in the near-surface fluid (via secondary minimum attraction), increasingly so with each subsequent collector, such that k would increase with increased transport distance [*Johnson and Hilpert*, 2013]. Whereas k does vary with transport distance under unfavorable conditions (e.g., hyper-exponential and non-monotonic profiles of retained colloids), it does not strictly increase with transport distance.

Nevertheless, the association of distance-varying k and extended tailing with unfavorable conditions suggests a relationship with colloid accumulation in the near surface under unfavorable conditions. Johnson and Hilpert [2013] speculated that incomplete mixing of bulk and near-surface fluid between subsequent grains may at least partially drive the observed extended tailing (and non-log-linear retained profiles) under unfavorable conditions. This, in addition to the above-described potential influence of discrete

heterogeneity on amplifying heterogeneity among the colloid population, provide potent mechanisms to potentially explain these critical phenomena observed under unfavorable conditions.

Since colloid transfer from the bulk to the near-surface fluid occurs at forward flow stagnation points, and colloid transfer from the near-surface to the bulk fluid occurs largely at rear flow stagnation zones (less so for Brownian-dominated colloids) [*Johnson and Hilpert*, 2013], the degree of mixing between collectors is a topological issue that depends on the alignment of the local flow field with the grain-to-grain contacts [*Johnson and Hilpert*, 2013]. Whereas experimental evidence that topology (degree of alignment of flow field and grain-to-grain contacts) governs retention at the continuum scale has been provided [*Johnson and Hilpert*, 2013], the opportunity exists for many additional studies to explore experimentally and theoretically the relationship of observed profiles of retained colloids to topology (as governed by packing structure). Such information can guide development of upscaling techniques for non-uniform media.

An additional mechanism potentially driving extended tailing under unfavorable conditions is provided by recent pore-scale modeling studies that suggest the possibility of indefinite colloid retention under unfavorable conditions in low-flow/recirculation zones associated with grain-grain contacts (discussed in Section 4.1.1) [*Cardenas*, 2008; *Li et al.*, 2010a; *Li et al.*, 2010b; 2012; *Torzkaban et al.*, 2008]. Temporary hydraulic retention of colloids in these regions could drive long-term tailing as colloids slowly exit the immobile zones via Brownian motion [*Molnar et al.*, 2015]. More generally, solute transport demonstrates diffusive mass transfer between advective and non-advective zones [e.g. *Berkowitz et al.*, 2006; *Haggerty and Gorelick*, 1995; *Haggerty et al.*, 2000; *Scheibe et al.*, 2013]. There is opportunity to distinguish the influence of near-surface residence from the influence of mass transfer between bulk advective versus non-advective zones in colloid transport. This is particularly true for nanoparticles, for which it is not yet demonstrated whether their diffusivity will allow them to enter bulk non-advective domains and whether this entry would require skimming along the secondary minima (as required by micron-sized colloids) or direct diffusive mass transfer that could occur in both favorable and unfavorable conditions.

7.4.3   Opportunities in straining.

Another critical aspect of non-uniformity of porous media is the expectation that a fraction of the pore throats will be too small for colloids to pass (i.e., straining) [*Bradford et al.*, 2002; *Bradford et al.*, 2003; *Bradford et al.*, 2004; *Bradford et al.*, 2006a; *Bradford et al.*, 2006b; *Bradford et al.*, 2013; *Shen et al.*, 2008; *Tufenkji et al.*, 2004]. The process of straining is not included in CFT because, while both filtration and straining lead to attachment, straining has no dependence on diffusion, sedimentation and limited dependence on colloid-surface interaction. Early work on straining [*Herzig et al.*, 1970; *McDowell-Boyer et al.*, 1986; *Sakthivadivel*, 1966; 1969] identified the ratio of mean particle:collector diameter (d_p/d_c) as the critical factor in determining straining. These early works presented a range of critical d_p/d_c ratios required for straining, such as >5% [*Sakthivadivel*, 1966; 1969] and >18% [*Matthess et al.*, 1985]. These large critical ratios suggest that only the largest (i.e., d_p~10μm) colloids in fine textured soils would be strained. However, there has recently been a large volume of research published inferring (see Section 3 for a discussion on the limitations of inferred transport behaviour) colloid straining as a significant removal mechanism for a wide range of colloid and collector sizes [*Bradford et al.*, 2002; *Bradford et al.*, 2003; *Bradford et al.*, 2004; *Bradford et al.*, 2005; *Bradford et al.*, 2006a; *Bradford et al.*, 2006b; *Bradford et al.*, 2013; *Chowdhury et al.*, 2011; *Du et al.*, 2013; *Foppen et al.*, 2005; *Gaillard et al.*, 2007; *Porubcan and Xu*, 2011; *Raychoudhury et al.*, 2014; *Sagee et al.*, 2012; *Shen et al.*, 2008; *Tufenkji et al.*, 2004; *Xu et al.*, 2006a; *Xu et al.*, 2008; *Xu and Saiers*, 2009]. These studies have inferred that d_p/d_c ratios can be much lower than originally reported (as low as 0.01%)[*Bradford et al.*, 2002; *Bradford et al.*, 2003; *Bradford et al.*, 2004; *Raychoudhury et al.*, 2014; *Shen et al.*, 2008; *Tosco and Sethi*, 2010; *Xu et al.*, 2008; *Xu et al.*, 2006b]. In addition, a number of studies have suggested that straining is not strictly a function of pore throat and colloid size by suggesting that flow velocity [*Bradford et al.*, 2006a; *Du et al.*, 2013], input concentration[*Bradford and Bettahar*, 2006], ionic strength [*Shen et al.*, 2008] and colloid shape [*Xu et al.*, 2008] can influence straining behavior. However, many of these studies base their evidence for straining on a-priori assumptions that may not be correct (e.g. that acid washed sand possesses no macroscopic surface impurities ergo straining is

predominant) [*Johnson et al.*, 2011]. These a-priori assumptions have led to, for instance, a number of studies suggesting that even nano-sized colloids (with d_p/d_c ratios orders of magnitude lower than suggested in the early literature) can be strained out of solution [*Raychoudhury et al.*, 2014; *Sagee et al.*, 2012; *Tosco and Sethi*, 2010].

Many of the above investigators relate straining to wedging; however, wedging is a mode of filtration for larger colloids, whereas straining is entrapment in pore throats too small to pass. Wedging is a mode of attachment (filtration) that involves mass transfer from the bulk fluid to the near surface fluid and eventual contact with two surfaces simultaneously in order to create the adhesive resisting torque that is needed to arrest larger colloids which experience a large drag torque [*Ma et al.*, 2011]. Thus wedged colloids can be much smaller than the pore throats through which they pass [*Johnson et al.*, 2010], and wedging is subject to the same force/torque balance governing colloid attachment to the open surface [*Johnson et al.*, 2007; *Ma et al.*, 2011]. In contrast, straining is purely a matter of colloid size being larger than the pore throat, and as such does not concern the mass transfer of colloids from the bulk fluid to the near surface fluid domain. Instead, straining is a process that cannot be investigated at the single pore scale, and instead requires investigation at the assemblage scale where pore throat size distribution can be determined and compared to colloid size distribution.

While the models developed to incorporate straining at the continuum-scale can accurately reproduce colloid retention behavior when fit to experimental data [*Bradford et al.*, 2003; *Bradford et al.*, 2004; *Flury and Qiu*, 2008; *Shen et al.*, 2008; *Xu et al.*, 2006a], they are subject to the same limitations of inferred mechanisms discussed in Section 3 and elsewhere in the literature [*Johnson et al.*, 2011]. Developing mechanistic methods to predict colloid straining will require an understanding of the pore throat distributions and flow fields. Pore-scale visualization methods such as micro-models and x-ray computed tomography (XCT) are uniquely suited to this purpose.

7.4.4 Opportunities in imaging and x-ray computed microtomography

Flow and transport within porous media are governed by the pore size distribution and the topology; i.e., the way in which pores of different sizes are connected [*Vogel and Roth*, 2001]. Thus, while micromodels, Happel spheres, cubic packings, etc. are useful for studying fundamental colloid transport processes and mechanisms, the idealized or simple pore structures do not represent environmental media. Over the past two decades or so, x-ray computed tomography (XCT) has become a relatively standard approach for extracting grain and pore scale features of unconsolidated porous media (see recent review by Wildenschild and Sheppard [2013]) due to its' ability to 'see inside' of three-dimensional opaque materials. XCT is a non-destructive, non-intrusive technique for acquiring 3D datasets where the fundamental unit, the volume element (voxel), has a value that represents the average x-ray absorption of the material within the voxel. This x-ray absorption value is a function of density, atomic number and the energy of incident x-rays. In this way, it is possible to differentiate between different materials. Therefore, the primary information is simply the voxel gray value (mass linear attenuation, which roughly corresponds to absorbance for SXCMT and CT# for conventional XCT). The major advantage of microtomography over conventional 2D methods (e.g., thin sections, microscopy) is the level of quantitative information that can be derived from a full 3D property map.

While the most common use of XCT in porous media characterization is the segmentation of the volume into solid and void space (which has come to mean the identification of discrete materials in an image; e.g., the binarization of an image into solid and void), XCT can be used to separate and identify more than two phases. Figure 7.3 (left) is a vertical cross-section from a raw XCT image dataset of a partially water-drained column packed with two types of glass beads (75% of the beads (by mass) contained some lead; the other 25% did not have any lead). The presence of lead increases the x-ray absorption of the voxels within those glass beads and makes them distinguishable from the glass beads without lead (note: the voxels with lead show up brighter due to the higher absorption values) and from the water. Figure 7.3 (right) is the

identical cross-section after the phases have been segmented; i.e., each voxel has been uniquely identified as either glass bead with lead (white); glass bead without lead (light gray); water (dark gray); and air (black).
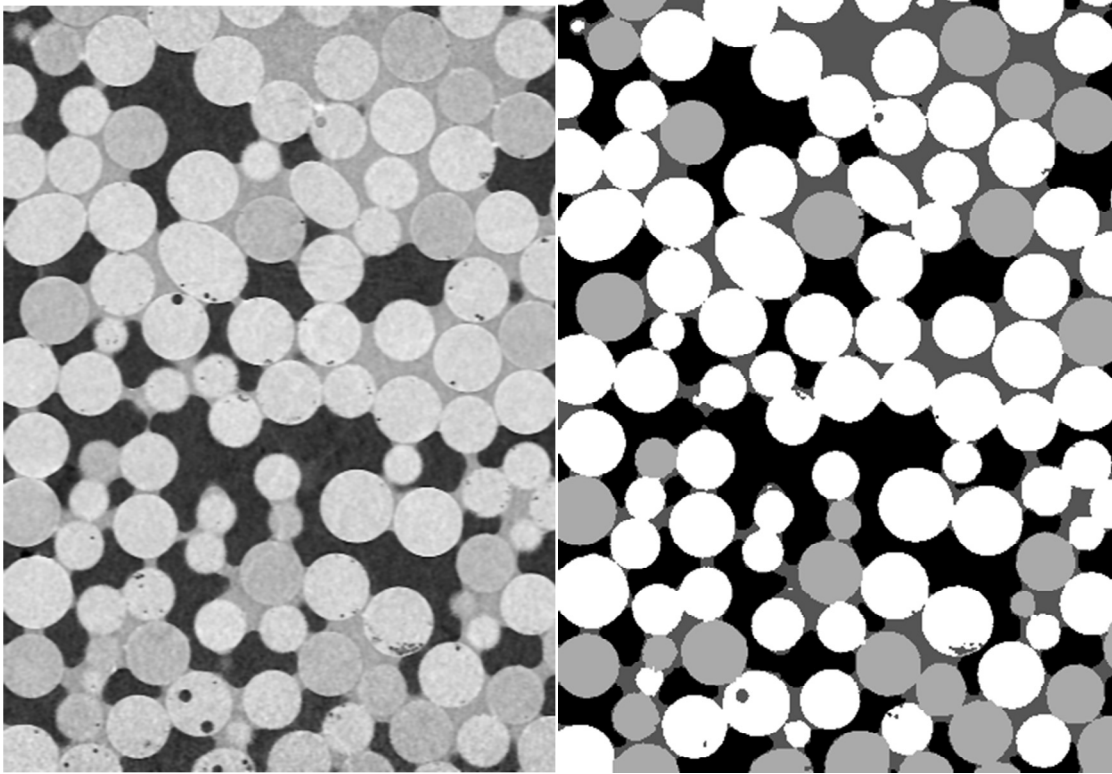

Figure 7.3: Fractionally-wet unsaturated glass bead pack; (left) grayscale XCT cross-section; (right) segmented cross-section where the white represents glass beads containing some lead; light gray: glass beads without lead; dark gray: water; black: air. Imaged at 10.08 μm/voxel. Dimensions: 5.24 mm (vertical) X 3.78 mm (horizontal)

A significant amount of research has gone into quantifying the geometrical and topological properties from XCT datasets and relating those to flow and transport processes [*Herring et al.*, 2015; *Vogel and Roth*, 2001] as well as extracting physically-representative pore network structures, i.e, a direct mapping of the pore bodies, throats and connectivity [*Bhattad et al.*, 2011; *Lindquist et al.*, 1996]. Two specific items to note here: (1) the topological properties of the pore space will have a strong influence on the flow and transport, thus impacting the spatial distribution of colloids as well as their trajectories towards and around collector surfaces; and (2) the direct mapping of the pore structure (e.g., pore body and throat sizes as well as connectivity) provides quantitative

data that can be used to determine whether or not certain colloid transport mechanisms (e.g., straining, discussed in Appendix 7.4.3) might be relevant.

There has been some pore-scale visualization work on straining in both saturated and unsaturated conditions [*Auset and Keller*, 2006; *Bradford et al.*, 2006a; *Crist et al.*, 2004; *Gaillard et al.*, 2007; *Han et al.*, 2006]. However, straining studies have yet to fully incorporate the rich, quantitative data that can be extracted from these methods such as coupling real pore throat distributions with FEM/LBM modeling of the flow field (discussed in Appendix 7.4.3). The type of quantitative data relevant to straining that can be obtained from XCT can be demonstrated using one of the datasets found in Molnar et al. [2015]. In a domain of $3.4 \times 3.4 \times 4.4$ mm^3 imaged at a resolution of 9.87 μm/voxel, the methods described in Thompson et al. [2006] and Bhattad et al. [2011] were used to determine that there were 616 sand grains and the pore network structure consisted of 3,422 unique pore bodies and 17,160 pore throats. The average size (and range) of pore bodies and throats were 62.4 (10.5 – 203) μm and 40.6 (9.87 – 156) μm, respectively. The sizes listed here are the pore and throat inscribed radii, which are defined as the radius of the largest spheres (pores) and circles (throats) that can be drawn within the identified geometries. In addition, the average pore coordination number was 5.1 with a range of 1 – 33 pore connections per pore.

The richness of the XCT datasets and the ability to resolve the pore space, combined with increases in computing power allows for the direct flow modeling at the pore scale in XCT-obtained domains of real pore networks using FEM (Finite Element Modeling), LBM, etc. In particular, the unstructured nature of the FEM allows one to capture the discontinuous and complex nature of the solid/void interface, highly relevant for capturing the near-surface flow field (within nm if necessary), low flow/recirculating regions and stagnation points. While these simulation approaches are now at the point where detailed hydrodynamics and bulk flow properties (e.g., permeability) are representative, there are still challenges to obtaining representative bulk transport properties (e.g. breakthrough curves) due to the complex, time-scale dependent nature of the transport processes (e.g., diffusion (Brownian motion), surface-particle interactions, and gravity) and the number of particles that need to be simulated (thousands if not tens

or hundreds of thousands). Nevertheless, the increasing sophistication of pore-level hydrodynamic modeling is providing critical insights into colloid transport through and around complex structures [*Li et al.*, 2010a; *Li et al.*, 2010b; 2012].

XCT has been successfully used to examine some pore-scale colloid transport details, in particular the spatial location of retained colloids. Gaillard et al. [2007] and Chen et al. [2008] demonstrated the ability to identify the distribution of micrometer-sized colloids (of high x-ray attenuation) in a sandstone and Iltis et al. [2011] mapped the distribution of biofilm in porous media using silver microspheres. Both of these studies utilized micron-sized colloids and, due to their material properties, had high x-ray attenuation coefficients enabling relatively straightforward identification within the systems. Molnar et al. [2014] developed a method that used absorption-edge XCT to extract silver nanoparticle concentrations within individual pores in static and quasi-dynamic (i.e., transport) systems. This approach was then used to assess how relatively immobile (e.g. low velocity) pore space regions near grain-grain contacts could yield deviations between experimentally observed and CFT-predicted retention rates [*Molnar et al.*, 2015]. While the large amount of spatial data of μm-scale nAg concentrations provides powerful statistical measures of the nAg distributions within the pore space, limitations due to X-ray diffraction across the grain/void interface prevents concentration measurements close to grain surfaces (termed 'shadow zone' in Molnar et al. [2014] which, in the system studied, was ~18 microns). The development and application of techniques for eliminating this shadow zone will allow for better estimates of near-surface concentrations and gradients and potentially of the impact of surface heterogeneities.

XCT has also been applied to extract granular properties such as particle size, shape and angularity as well as geomechanically-relevant structural properties such as grain-grain contacts (see review by Moreno-Atanasio et al. [2010]). As mentioned above, the ability to separate the system into void and solid phases allows for detailed hydrodynamic simulations that can be used to better understand the particle trajectories and proximity to the collector surface, locations of straining and wedging.

However, several factors currently limit the use of XCT for fundamental colloid transport studies including: the spatial resolution, sample sizes below that necessary to obtain representative properties, and image contrast. The true spatial resolution of a CT instrument also depends on the sharpness of the imagery [*Ketcham and Carlson*, 2001; *Wildenschild et al.*, 2002]. The spatial resolution of most XCT systems limits the ability to capture small structural/surface features (or heterogeneities) that can influence colloid-surface interactions and retention. While increases in the spatial resolution are possible through the use of higher-resolution XCT systems or other imaging techniques (e.g., SEM, thin sections), the quantitative details extracted may not be representative of the bulk sample and, if not collected directly with (or concurrently with) the XCT data, need to be mapped back to the image data [e.g. *Golab et al.*, 2012]. Quantitative delineation of the mineral phases, which strongly influence the spatial distribution of favorable/unfavorable attachment sites depends on the X-ray attenuation properties of the minerals (as well as the spatial resolution). Fluid phase separation using doping agents is a common approach [e.g. *Al-Raoush and Willson*, 2005; *Porter and Wildenschild*, 2010; *Porter et al.*, 2010; *Prodanović et al.*, 2007; *Schnaar and Brusseau*, 2005]; however, much less work has been done on the spatial distribution of mineralogy. See the recent review paper by Kyle and Ketcham [2015] that discusses the approaches and limitations to mineral identification and quantification (while they focus primarily on ores, this is a very good overview). An interesting but intensive approach that uses the 2D-3D registration of SEM and XCT was developed by a group at the Australian National University [*Golab et al.*, 2012; *Sheppard et al.*, 2014]. In addition to providing additional sub-micron level structural details, this technique allows for the coupling of mineralogy (from the SEM) with the XCT data.

A major limitation of an XCT-based imaging approach is the inability to identify coatings/films on solid surfaces that are thinner than several microns and/or have x-ray absorption values that are similar to the grain. This may limit or prevent direct mapping of transport-relevant heterogeneities onto the grain surface, resulting in the need for indirect "mapping" of chemical heterogeneities.

While XCT is allowing for more detailed pore- and grain-level characterization and the increases in computing power are pushing the simulation details to higher levels, there are still a number challenges/opportunities that can have a major impact on our understanding of colloid transport such as developing robust techniques to, directly or indirectly, extract and map sub-micron heterogeneities. In addition, improvements in the spatial resolution are needed to ensure that the pore structure/topology and mineralogy distribution is representatively captured in complex, environmental media. These features, when combined with improved techniques in quantitatively mapping colloid concentrations and in the modeling of complex pore-level hydrodynamics and colloid transport mechanisms (such as mineral specific surface-particle forces), will greatly improve our understanding of colloid transport in natural systems.

7.5 References

Abudalo, R. A., J. N. Ryan, R. W. Harvey, D. W. Metge, and L. Landkamer (2010), Influence of organic matter on the transport of Cryptosporidium parvum oocysts in a ferric oxyhydroxide-coated quartz sand saturated porous medium, *Water Research*, *44*(4), 1104-1113.

Al-Raoush, R. I., and C. S. Willson (2005), A pore-scale investigation of a multiphase porous media system, *Journal of Contaminant Hydrology*, *77*(1-2), 67-89.

Albinger, O., B. K. Biesemeyer, R. G. Arnold, and B. E. Logan (1994), *Effect of bacterial heterogeneity on adhesion to uniform collectors by monoclonal populations*, 321-326 pp.

Amirbahman, A., and T. M. Olson (1993), Transport of humic matter-coated hematite in packed beds, *Environ. Sci. Technol.*, *27*(13), 2807-2813.

Auset, M., and A. A. Keller (2006), Pore-scale visualization of colloid straining and filtration in saturated porous media using micromodels, *Water Resour. Res.*, *42*(12), W12S02.

Bai, R., and C. Tien (1996), A New Correlation for the Initial Filter Coefficient under Unfavorable Surface Interactions, *Journal of Colloid and Interface Science*, *179*(2), 631-634.

Bai, R., and C. Tien (1999), Particle Deposition under Unfavorable Surface Interactions, *Journal of Colloid and Interface Science*, *218*(2), 488-499.

Baygents, J. C., J. R. Glynn, O. Albinger, B. K. Biesemeyer, K. L. Ogden, and R. G. Arnold (1998), Variation of Surface Charge Density in Monoclonal Bacterial Populations: Implications for Transport through Porous Media, *Environ. Sci. Technol.*, *32*(11), 1596-1603.

Bendersky, M., and J. M. Davis (2011), DLVO interaction of colloidal particles with topographically and chemically heterogeneous surfaces, *Journal of Colloid and Interface Science*, *353*(1), 87-97.

Bergendahl, J., and D. Grasso (2000), Prediction of colloid detachment in a model porous media: hydrodynamics, *Chemical Engineering Science*, *55*(9), 1523-1532.

Berkowitz, B., A. Cortis, M. Dentz, and H. Scher (2006), Modeling non-Fickian transport in geological formations as a continuous time random walk, *Rev. Geophys.*, *44*(2), 49.

Bhattacharjee, S., C.-H. Ko, and M. Elimelech (1998), DLVO Interaction between Rough Surfaces, *Langmuir*, *14*(12), 3365-3375.

Bhattad, P., C. S. Willson, and K. E. Thompson (2011), Effect of Network Structure on Characterization and Flow Modeling Using X-ray Micro-Tomography Images of Granular and Fibrous Porous Media, *Transp Porous Med*, *90*(2), 363-391.

Bolster, C. H., A. L. Mills, G. M. Hornberger, and J. S. Herman (1999), Spatial distribution of deposited bacteria following Miscible Displacement Experiments in intact cores, *Water Resour. Res.*, *35*(6), 1797-1807.

Bolster, C. H., A. L. Mills, G. Hornberger, and J. Herman (2000), Effect of Intra-Population Variability on the Long-Distance Transport of Bacteria, *Ground Water*, *38*(3), 370-375.

Bradford, S. A., S. R. Yates, M. Bettahar, and J. Simunek (2002), Physical factors affecting the transport and fate of colloids in saturated porous media, *Water Resour. Res.*, *38*(12).

Bradford, S. A., J. Simunek, M. Bettahar, M. T. van Genuchten, and S. R. Yates (2003), Modeling Colloid Attachment, Straining, and Exclusion in Saturated Porous Media, *Environ. Sci. Technol.*, *37*(10), 2242-2250.

Bradford, S. A., M. Bettahar, J. Simunek, and M. T. van Genuchten (2004), Straining and attachment of colloids in physically heterogeneous porous media, *Vadose Zone J.*, *3*(2), 384-394.

Bradford, S. A., J. Simunek, M. Bettahar, Y. F. Tadassa, M. T. van Genuchten, and S. R. Yates (2005), Straining of colloids at textural interfaces, *Water Resour. Res.*, *41*(10), n/a-n/a.

Bradford, S. A., J. Simunek, and S. L. Walker (2006a), Transport and straining of E. coli O157:H7 in saturated porous media, *Water Resour. Res.*, *42*(12), W12S12.

Bradford, S. A., J. Simunek, M. Bettahar, M. T. van Genuchten, and S. R. Yates (2006b), Significance of straining in colloid deposition: Evidence and implications, *Water Resour. Res.*, *42*(12), W12S15.

Bradford, S. A., and M. Bettahar (2006), Concentration dependent transport of colloids in saturated porous media, *Journal of Contaminant Hydrology*, *82*(1–2), 99-117.

Bradford, S. A., S. Torkzaban, and A. Wiegmann (2011), Pore-Scale Simulations to Determine the Applied Hydrodynamic Torque and Colloid Immobilization, *Vadose Zone J.*, *10*(1), 252-261.

Bradford, S. A., S. Torkzaban, and A. Shapiro (2013), A Theoretical Analysis of Colloid Attachment and Straining in Chemically Heterogeneous Porous Media, *Langmuir*, *29*(23), 6944-6952.

Cardenas, M. B. (2008), Three-dimensional vortices in single pores and their effects on transport, *Geophysical Research Letters*, *35*(18), L18402.

Chang, Y.-I., W.-Y. Cheng, and H.-C. Chan (2009), A proposed correlation equation for predicting filter coefficient under unfavorable deposition conditions, *Separation and Purification Technology*, *65*(3), 248-250.

Chen, C., A. I. Packman, and J.-F. Gaillard (2008), Pore-scale analysis of permeability reduction resulting from colloid deposition, *Geophys. Res. Lett.*, *35*(7), L07404.

Chen, J. Y., C. H. Ko, S. Bhattacharjee, and M. Elimelech (2001), Role of spatial distribution of porous medium surface charge heterogeneity in colloid transport, *Colloid Surf. A-Physicochem. Eng. Asp.*, *191*(1-2), 3-15.

Chowdhury, I., Y. Hong, R. J. Honda, and S. L. Walker (2011), Mechanisms of TiO2 nanoparticle transport in porous media: Role of solution chemistry, nanoparticle concentration, and flowrate, *Journal of Colloid and Interface Science*, *360*(2), 548-555.

Crist, J. T., J. F. McCarthy, Y. Zevi, P. Baveye, J. A. Throop, and T. S. Steenhuis (2004), Pore-Scale Visualization of Colloid Transport and Retention in Partly Saturated Porous Media, *Vadose Zone J.*, *3*(2), 444-450.

DiCarlo, D. A., L. D. Seale, K. Ham, and C. S. Willson (2010), Tomographic measurements of pore filling at infiltration fronts, *Adv. Water Resour.*, *33*(4), 485-492.

Drelich, J., and Y. U. Wang (2011), Charge heterogeneity of surfaces: Mapping and effects on surface forces, *Advances in Colloid and Interface Science*, *165*(2), 91-101.

Du, Y. C., C. Y. Shen, H. Y. Zhang, and Y. F. Huang (2013), Effects of Flow Velocity and Nonionic Surfactant on Colloid Straining in Saturated Porous Media Under Unfavorable Conditions, *Transp Porous Med*, *98*(1), 193-208.

Duffadar, R., and J. M. Davis (2007), Interaction of micrometer-scale particles with nanotextured surfaces in shear flow, *Journal of Colloid and Interface Science*, *308*(1), 20-29.

Duffadar, R., S. Kalasin, J. M. Davis, and M. M. Santore (2009), The impact of nanoscale chemical features on micron-scale adhesion: Crossover from heterogeneity-dominated to mean-field behavior, *Journal of Colloid and Interface Science*, *337*(2), 396-407.

Elimelech, M., and C. R. Omelia (1990), KINETICS OF DEPOSITION OF COLLOIDAL PARTICLES IN POROUS-MEDIA, *Environ. Sci. Technol.*, *24*(10), 1528-1536.

Elimelech, M. (1992), Predicting collision efficiencies of colloidal particles in porous media, *Water Research*, *26*(1), 1-8.

Elimelech, M., M. Nagai, C.-H. Ko, and J. N. Ryan (2000), Relative Insignificance of Mineral Grain Zeta Potential to Colloid Transport in Geochemically Heterogeneous Porous Media, *Environ. Sci. Technol.*, *34*(11), 2143-2148.

Flury, M., and H. Qiu (2008), Modeling Colloid-Facilitated Contaminant Transport in the Vadose Zone, *Vadose Zone J.*, *7*(2), 682-697.

Foppen, J. W., A. Mporokoso, and J. F. Schijven (2005), Determining straining of Escherichia coli from breakthrough curves, *Journal of Contaminant Hydrology*, *76*(3–4), 191-210.

Foppen, J. W., Y. Liem, and J. Schijven (2008), Effect of humic acid on the attachment of Escherichia coli in columns of goethite-coated sand, *Water Research*, *42*(1–2), 211-219.

Franchi, A., and C. R. O'Melia (2003), Effects of Natural Organic Matter and Solution Chemistry on the Deposition and Reentrainment of Colloids in Porous Media, *Environ. Sci. Technol.*, *37*(6), 1122-1129.

Gaillard, J.-F., C. Chen, S. H. Stonedahl, B. L. T. Lau, D. T. Keane, and A. I. Packman (2007), Imaging of colloidal deposits in granular porous media by X-ray difference micro-tomography, *Geophys. Res. Lett.*, *34*(18), L18404.

Golab, A., R. Romeyn, H. Averdunk, M. Knackstedt, and T. J. Senden (2012), 3D characterisation of potential CO2 reservoir and seal rocks, *Australian Journal of Earth Sciences*, *60*(1), 111-123.

Gu, B., J. Schmitt, Z. Chen, L. Liang, and J. F. McCarthy (1995), Adsorption and desorption of different organic matter fractions on iron oxide, *Geochimica et Cosmochimica Acta*, *59*(2), 219-229.

Haggerty, R., and S. M. Gorelick (1995), Multiple-Rate Mass Transfer for Modeling Diffusion and Surface Reactions in Media with Pore-Scale Heterogeneity, *Water Resour. Res.*, *31*(10), 2383-2400.

Haggerty, R., S. A. McKenna, and L. C. Meigs (2000), On the late-time behavior of tracer test breakthrough curves, *Water Resour. Res.*, *36*(12), 3467-3479.

Hahn, M. W., and C. R. O'Melia (2004), Deposition and reentrainment of Brownian particles in porous media under unfavorable chemical conditions: Some concepts and applications, *Environ. Sci. Technol.*, *38*(1), 210-220.

Han, J., Y. Jin, and C. S. Willson (2006), Virus retention and transport in chemically heterogeneous porous media under saturated and unsaturated flow conditions, *Environ. Sci. Technol.*, *40*(5), 1547-1555.

Harvey, R. W., N. E. Kinner, A. Bunn, D. Macdonald, and D. Metge (1995), Transport behavior of groundwater protozoa and protozoan-sized microspheres in sandy aquifer sediments, *Applied and Environmental Microbiology*, *61*(1), 209-217.

Hendry, M. J., J. R. Lawrence, and P. Maloszewski (1997), The Role of Sorption in the Transport of Klebsiella oxytoca Through Saturated Silica Sand, *Ground Water*, *35*(4), 574-584.

Herring, A. L., L. Andersson, S. Schlüter, A. Sheppard, and D. Wildenschild (2015), Efficiently engineering pore-scale processes: The role of force dominance and topology during nonwetting phase trapping in porous media, *Adv. Water Resour.*, *79*(0), 91-102.

Herzig, J. P., D. M. Leclerc, and P. L. Goff (1970), Flow of Suspensions through Porous Media—Application to Deep Filtration, *Industrial & Engineering Chemistry*, *62*(5), 8-35.

Hoek, E. M. V., and G. K. Agarwal (2006), Extended DLVO interactions between spherical particles and rough surfaces, *Journal of Colloid and Interface Science*, *298*(1), 50-58.

Iltis, G. C., R. T. Armstrong, D. P. Jansik, B. D. Wood, and D. Wildenschild (2011), Imaging biofilm architecture within porous media using synchrotron-based X-ray computed microtomography, *Water Resour. Res.*, *47*(2).

Israelachvili, J. N. (2011), 15 - Solvation, Structural, and Hydration Forces, in *Intermolecular and Surface Forces (Third Edition)*, edited by J. N. Israelachvili, pp. 341-380, Academic Press, San Diego.

Jiang, X., M. Tong, R. Lu, and H. Kim (2012a), Transport and deposition of ZnO nanoparticles in saturated porous media, *Colloids and Surfaces A: Physicochemical and Engineering Aspects*, *401*(0), 29-37.

Jiang, X., M. Tong, and H. Kim (2012b), Influence of natural organic matter on the transport and deposition of zinc oxide nanoparticles in saturated porous media, *Journal of Colloid and Interface Science*, *386*(1), 34-43.

Johnson, K. L., K. Kendall, and A. D. Roberts (1971), *Surface Energy and the Contact of Elastic Solids*, 301-313 pp.

Johnson, P. R., N. Sun, and M. Elimelech (1996), Colloid transport in geochemically heterogeneous porous media: Modeling and measurements, *Environ. Sci. Technol.*, *30*(11), 3284-3293.

Johnson, W. P., and B. E. Logan (1996), Enhanced transport of bacteria in porous media by sediment-phase and aqueous-phase natural organic matter, *Water Research*, *30*(4), 923-931.

Johnson, W. P., X. Li, and G. Yal (2007), Colloid Retention in Porous Media: Mechanistic Confirmation of Wedging and Retention in Zones of Flow Stagnation, *Environ. Sci. Technol.*, *41*(4), 1279-1287.

Johnson, W. P., X. Li, M. Tong, and H. Ma (2009), Comment on "Transport and fate of bacteria in porous media: Coupled effects of chemical conditions and pore space geometry" by Saeed Torkzaban et al, *Water Resour. Res.*, *45*(9), W09603.

Johnson, W. P., E. Pazmino, and H. L. Ma (2010), Direct observations of colloid retention in granular media in the presence of energy barriers, and implications for inferred mechanisms from indirect observations, *Water Research*, *44*(4), 1158-1169.

Johnson, W. P., H. Ma, and E. Pazmino (2011), Straining Credibility: A General Comment Regarding Common Arguments Used to Infer Straining As the Mechanism of Colloid Retention in Porous Media, *Environ. Sci. Technol.*, *45*(9), 3831-3832.

Johnson, W. P., and M. Hilpert (2013), Upscaling colloid transport and retention under unfavorable conditions: Linking mass transfer to pore and grain topology, *Water Resour. Res.*, *49*(9), 5328-5341.

Ketcham, R. A., and W. D. Carlson (2001), Acquisition, optimization and interpretation of X-ray computed tomographic imagery: applications to the geosciences, *Computers & Geosciences*, *27*(4), 381-400.

Kyle, J. R., and R. A. Ketcham (2015), Application of high resolution X-ray computed tomography to mineral deposit origin, evaluation, and processing, *Ore Geology Reviews*, *65, Part 4*(0), 821-839.

Li, X. Q., T. D. Scheibe, and W. P. Johnson (2004), Apparent Decreases in Colloid Deposition Rate Coefficients with Distance of Transport under Unfavorable Deposition Conditions: A General Phenomenon, *Environ. Sci. Technol.*, *38*(21), 5616-5625.

Li, X. Q., Z. L. Li, and D. X. Zhang (2010a), Role of Low Flow and Backward Flow Zones on Colloid Transport in Pore Structures Derived from Real Porous Media, *Environ. Sci. Technol.*, *44*(13), 4936-4942.

Li, Z., D. X. Zhang, and X. Li (2010b), Tracking Colloid Transport in Porous Media Using Discrete Flow Fields and Sensitivity of Simulated Colloid Deposition to Space Discretization, *Environ. Sci. Technol.*, *44*(4), 1274-1280.

Li, Z., D. X. Zhang, and X. Li (2012), Tracking colloid transport in real pore structures: Comparisons with correlation equations and experimental observations, *Water Resour. Res.*, *48*(5), W05533.

Liang, Y., S. A. Bradford, J. Simunek, H. Vereecken, and E. Klumpp (2013), Sensitivity of the transport and retention of stabilized silver nanoparticles to physicochemical factors, *Water Research*, *47*(7), 2572-2582.

Lindquist, W. B., S. M. Lee, D. A. Coker, K. W. Jones, and P. Spanne (1996), Medial axis analysis of void structure in three-dimensional tomographic images of porous media, *Journal of Geophysical Research-Solid Earth*, *101*(B4), 8297-8310.

Litton, G. M., and T. M. Olson (1993), Colloid deposition rates on silica bed media and artifacts related to collector surface preparation methods, *Environ. Sci. Technol.*, *27*(1), 185-193.

Liu, X. Y., D. M. O'Carroll, E. J. Petersen, Q. G. Huang, and C. L. Anderson (2009a), Mobility of Multiwalled Carbon Nanotubes in Porous Media, *Environ. Sci. Technol.*, *43*(21), 8153-8158.

Liu, Y., D. Janjaroen, M. S. Kuhlenschmidt, T. B. Kuhlenschmidt, and T. H. Nguyen (2009b), Deposition of Cryptosporidium parvum Oocysts on Natural Organic Matter Surfaces: Microscopic Evidence for Secondary Minimum Deposition in a Radial Stagnation Point Flow Cell, *Langmuir*, *25*(3), 1594-1605.

Logan, B., D. Jewett, R. Arnold, E. Bouwer, and C. O'Melia (1995), Clarification of Clean-Bed Filtration Models, *Journal of Environmental Engineering*, *121*(12), 869-873.

Loveland, J. P., S. Bhattacharjee, J. N. Ryan, and M. Elimelech (2003), Colloid transport in a geochemically heterogeneous porous medium: aquifer tank experiment and modeling, *Journal of Contaminant Hydrology*, *65*(3-4), 161-182.

Ma, H., J. Pedel, P. Fife, and W. P. Johnson (2009), Hemispheres-in-Cell Geometry to Predict Colloid Deposition in Porous Media, *Environ. Sci. Technol.*, *43*(22), 8573-8579.

Ma, H., E. Pazmino, and W. P. Johnson (2011), Surface Heterogeneity on Hemispheres-in-Cell Model Yields All Experimentally-Observed Non-Straining Colloid Retention Mechanisms in Porous Media in the Presence of Energy Barriers, *Langmuir*, *27*(24), 14982-14994.

Ma, H., M. Hradisky, and W. P. Johnson (2013), Extending Applicability of Correlation Equations to Predict Colloidal Retention in Porous Media at Low Fluid Velocity, *Environ. Sci. Technol.*, *47*(5), 2272-2278.

Matthess, G., A. Pekdeger, and P. McCarty (1985), Survival and transport of pathogenic bacteria and viruses in ground water, in *Environ. Sci. Technol.*, edited, pp. 472-482, Wiley-Interscience.

McDowell-Boyer, L. M., J. R. Hunt, and N. Sitar (1986), Particle transport through porous media, *Water Resour. Res.*, *22*(13), 1901-1921.

Molnar, I. L., D. M. O'Carroll, and J. I. Gerhard (2011), Impact of surfactant-induced wettability alterations on DNAPL invasion in quartz and iron oxide-coated sand systems, *Journal of Contaminant Hydrology*, *119*(1-4), 1-12.

Molnar, I. L., C. S. Willson, D. M. O'Carroll, M. L. Rivers, and J. I. Gerhard (2014), Method for Obtaining Silver Nanoparticle Concentrations within a Porous Medium via Synchrotron X-ray Computed Microtomography, *Environ. Sci. Technol.*, *48*(2), 1114-1122.

Molnar, I. L., J. I. Gerhard, C. S. Willson, and D. M. O'Carroll (2015), The impact of immobile zones on the transport and retention of nanoparticles in porous media, *Water Resour. Res.*

Morales, V. L., W. Zhang, B. Gao, L. W. Lion, J. J. Bisogni Jr, B. A. McDonough, and T. S. Steenhuis (2011), Impact of dissolved organic matter on colloid transport in the vadose zone: Deterministic approximation of transport deposition coefficients from polymeric coating characteristics, *Water Research*, *45*(4), 1691-1701.

Moreno-Atanasio, R., R. A. Williams, and X. Jia (2010), Combining X-ray microtomography with computer simulation for analysis of granular and porous materials, *Particuology*, *8*(2), 81-99.

Mosley, L. M., K. A. Hunter, and W. A. Ducker (2003), Forces between Colloid Particles in Natural Waters, *Environ. Sci. Technol.*, *37*(15), 3303-3308.

Mylon, S. E., K. L. Chen, and M. Elimelech (2004), Influence of Natural Organic Matter and Ionic Composition on the Kinetics and Structure of Hematite Colloid

Aggregation: Implications to Iron Depletion in Estuaries, *Langmuir*, *20*(21), 9000-9006.

Nelson, K. E., and T. R. Ginn (2011), New collector efficiency equation for colloid filtration in both natural and engineered flow conditions, *Water Resour. Res.*, *47*, 17.

Paraskeva, C. A., V. N. Burganos, and A. C. Payatakes (1991), THREE-DIMENSIONAL TRAJECTORY ANALYSIS OF PARTICLE DEPOSITION IN CONSTRICTED TUBES, *Chemical Engineering Communications*, *108*(1), 23-48.

Pazmino, E. F., J. Trauscht, and W. P. Johnson (2014a), Release of Colloids from Primary Minimum Contact under Unfavorable Conditions by Perturbations in Ionic Strength and Flow Rate, *Environ. Sci. Technol.*, *48*(16), 9227-9235.

Pazmino, E. F., J. Trauscht, B. Dame, and W. P. Johnson (2014b), Power Law Size-Distributed Heterogeneity Explains Colloid Retention on Soda Lime Glass in the Presence of Energy Barriers, *Langmuir*, *30*(19), 5412-5421.

Pelley, A. J., and N. Tufenkji (2008), Effect of particle size and natural organic matter on the migration of nano- and microscale latex particles in saturated porous media, *Journal of Colloid and Interface Science*, *321*(1), 74-83.

Pieper, A. P., J. N. Ryan, R. W. Harvey, G. L. Amy, T. H. Illangasekare, and D. W. Metge (1997), Transport and Recovery of Bacteriophage PRD1 in a Sand and Gravel Aquifer: Effect of Sewage-Derived Organic Matter, *Environ. Sci. Technol.*, *31*(4), 1163-1170.

Porter, M. L., and D. Wildenschild (2010), Image analysis algorithms for estimating porous media multiphase flow variables from computed microtomography data: a validation study, *Comput Geosci*, *14*(1), 15-30.

Porter, M. L., D. Wildenschild, G. Grant, and J. I. Gerhard (2010), Measurement and prediction of the relationship between capillary pressure, saturation, and interfacial area in a NAPL-water-glass bead system, *Water Resour. Res.*, *46*(8), n/a-n/a.

Porubcan, A. A., and S. Xu (2011), Colloid straining within saturated heterogeneous porous media, *Water Research*, *45*(4), 1796-1806.

Prodanović, M., W. B. Lindquist, and R. S. Seright (2007), 3D image-based characterization of fluid displacement in a Berea core, *Adv. Water Resour.*, *30*(2), 214-226.

Rajagopalan, R., and C. Tien (1976), TRAJECTORY ANALYSIS OF DEEP-BED FILTRATION WITH SPHERE-IN-CELL POROUS-MEDIA MODEL, *Aiche J.*, *22*(3), 523-533.

Raychoudhury, T., N. Tufenkji, and S. Ghoshal (2014), Straining of polyelectrolyte-stabilized nanoscale zero valent iron particles during transport through granular porous media, *Water Research*, *50*(0), 80-89.

Ryan, J. N., and M. Elimelech (1996), Colloid mobilization and transport in groundwater, *Colloids and Surfaces A: Physicochemical and Engineering Aspects*, *107*(0), 1-56.

Sagee, O., I. Dror, and B. Berkowitz (2012), Transport of silver nanoparticles (AgNPs) in soil, *Chemosphere*, *88*(5), 670-675.

Sakthivadivel, R. (1966), *Theory and mechanism of filtration of non-colloidal fines through a porous medium*, University of California. Hydraulic Engineering Laboratory.

Sakthivadivel, R. (1969), *Clogging of a granular porous medium by sediment*, Hydraulic Engineering Laboratory, College of Engineering, University of California.

Sang, W., V. L. Morales, W. Zhang, C. R. Stoof, B. Gao, A. L. Schatz, Y. Zhang, and T. S. Steenhuis (2013), Quantification of Colloid Retention and Release by Straining and Energy Minima in Variably Saturated Porous Media, *Environ. Sci. Technol.*, *47*(15), 8256-8264.

Scheibe, T. D., Z. S. Hou, B. J. Palmer, and A. M. Tartakovsky (2013), Pore-scale simulation of intragranular diffusion: Effects of incomplete mixing on macroscopic manifestations, *Water Resour. Res.*, *49*(7), 4277-4294.

Schijven, J. F., W. Hoogenboezem, M. Hassanizadeh, and J. H. Peters (1999), Modeling removal of bacteriophages MS2 and PRD1 by dune recharge at Castricum, Netherlands, *Water Resour. Res.*, *35*(4), 1101-1111.

Schnaar, G., and M. L. Brusseau (2005), Pore-scale characterization of organic immiscible-liquid morphology in natural porous media using synchrotron X-ray microtomography, *Environ. Sci. Technol.*, *39*(21), 8403-8410.

Shellenberger, K., and B. E. Logan (2002), Effect of Molecular Scale Roughness of Glass Beads on Colloidal and Bacterial Deposition, *Environ. Sci. Technol.*, *36*(2), 184-189.

Shen, C., B. Li, Y. Huang, and Y. Jin (2007), Kinetics of Coupled Primary- and Secondary-Minimum Deposition of Colloids under Unfavorable Chemical Conditions, *Environ. Sci. Technol.*, *41*(20), 6976-6982.

Shen, C., Y. Huang, B. Li, and Y. Jin (2008), Effects of solution chemistry on straining of colloids in porous media under unfavorable conditions, *Water Resour. Res.*, *44*(5), W05419.

Shen, C., V. Lazouskaya, H. Zhang, B. Li, Y. Jin, and Y. Huang (2013), Influence of surface chemical heterogeneity on attachment and detachment of microparticles, *Colloids and Surfaces A: Physicochemical and Engineering Aspects*, *433*(0), 14-29.

Sheppard, A., et al. (2014), Techniques in helical scanning, dynamic imaging and image segmentation for improved quantitative analysis with X-ray micro-CT, *Nuclear Instruments and Methods in Physics Research Section B: Beam Interactions with Materials and Atoms*, *324*(0), 49-56.

Simoni, S. F., H. Harms, T. N. P. Bosma, and A. J. B. Zehnder (1998), Population Heterogeneity Affects Transport of Bacteria through Sand Columns at Low Flow Rates, *Environ. Sci. Technol.*, *32*(14), 2100-2105.

Song, L., P. R. Johnson, and M. Elimelech (1994), Kinetics of Colloid Deposition onto Heterogeneously Charged Surfaces in Porous Media, *Environ. Sci. Technol.*, *28*(6), 1164-1171.

Taboada-Serrano, P., V. Vithayaveroj, S. Yiacoumi, and C. Tsouris (2005), Surface Charge Heterogeneities Measured by Atomic Force Microscopy†, *Environ. Sci. Technol.*, *39*(17), 6352-6360.

Thompson, K. E., C. S. Willson, and W. L. Zhang (2006), Quantitative computer reconstruction of particulate materials from microtomography images, *Powder Technology*, *163*(3), 169-182.

Tong, M., and W. P. Johnson (2006), Excess Colloid Retention in Porous Media as a Function of Colloid Size, Fluid Velocity, and Grain Angularity, *Environ. Sci. Technol.*, *40*(24), 7725-7731.

Tong, M., and W. P. Johnson (2007), Colloid Population Heterogeneity Drives Hyperexponential Deviation from Classic Filtration Theory, *Environ. Sci. Technol.*, *41*(2), 493-499.

Torkzaban, S., S. A. Bradford, and S. L. Walker (2007), Resolving the coupled effects of hydrodynamics and DLVO forces on colloid attachment in porous media, *Langmuir*, *23*(19), 9652-9660.

Torkzaban, S., S. S. Tazehkand, S. L. Walker, and S. A. Bradford (2008), Transport and fate of bacteria in porous media: Coupled effects of chemical conditions and pore space geometry, *Water Resour. Res.*, *44*(4).

Tosco, T., A. Tiraferri, and R. Sethi (2009), Ionic Strength Dependent Transport of Microparticles in Saturated Porous Media: Modeling Mobilization and Immobilization Phenomena under Transient Chemical Conditions, *Environ. Sci. Technol.*, *43*(12), 4425-4431.

Tosco, T., and R. Sethi (2010), Transport of Non-Newtonian Suspensions of Highly Concentrated Micro- And Nanoscale Iron Particles in Porous Media: A Modeling Approach, *Environ. Sci. Technol.*, *44*(23), 9062-9068.

Tufenkji, N., and M. Elimelech (2004), Deviation from the classical colloid filtration theory in the presence of repulsive DLVO interactions, *Langmuir*, *20*(25), 10818-10828.

Tufenkji, N., G. F. Miller, J. N. Ryan, R. W. Harvey, and M. Elimelech (2004), Transport of Cryptosporidium Oocysts in Porous Media: Role of Straining and Physicochemical Filtration†, *Environ. Sci. Technol.*, *38*(22), 5932-5938.

Tufenkji, N., and M. Elimelech (2005a), Breakdown of colloid filtration theory: Role of the secondary energy minimum and surface charge heterogeneities, *Langmuir*, *21*(3), 841-852.

Tufenkji, N., and M. Elimelech (2005b), Spatial Distributions of Cryptosporidium Oocysts in Porous Media: Evidence for Dual Mode Deposition, *Environ. Sci. Technol.*, *39*(10), 3620-3629.

Vogel, H. J., and K. Roth (2001), Quantitative morphology and network representation of soil pore structure, *Adv. Water Resour.*, *24*(3–4), 233-242.

Wang, D., S. A. Bradford, R. W. Harvey, B. Gao, L. Cang, and D. Zhou (2012), Humic Acid Facilitates the Transport of ARS-Labeled Hydroxyapatite Nanoparticles in Iron Oxyhydroxide-Coated Sand, *Environ. Sci. Technol.*, *46*(5), 2738-2745.

Wang, D., L. Ge, J. He, W. Zhang, D. P. Jaisi, and D. Zhou (2014), Hyperexponential and nonmonotonic retention of polyvinylpyrrolidone-coated silver nanoparticles in an Ultisol, *Journal of Contaminant Hydrology*, *164*(0), 35-48.

Wildenschild, D., C. M. P. Vaz, M. L. Rivers, D. Rikard, and B. S. B. Christensen (2002), Using X-ray computed tomography in hydrology: systems, resolutions, and limitations, *Journal of Hydrology*, *267*(3–4), 285-297.

Wildenschild, D., and A. P. Sheppard (2013), X-ray imaging and analysis techniques for quantifying pore-scale structure and processes in subsurface porous medium systems, *Adv. Water Resour.*, *51*(0), 217-246.

Xu, S., B. Gao, and J. E. Saiers (2006a), Straining of colloidal particles in saturated porous media, *Water Resour. Res.*, *42*(12), n/a-n/a.

Xu, S., Q. Liao, and J. E. Saiers (2008), Straining of Nonspherical Colloids in Saturated Porous Media, *Environ. Sci. Technol.*, *42*(3), 771-778.

Xu, S., and J. E. Saiers (2009), Colloid straining within water-saturated porous media: Effects of colloid size nonuniformity, *Water Resour. Res.*, *45*(5), n/a-n/a.

Xu, W., S. C. Ayirala, and D. N. Rao (2006b), Wettability alterations due to crude oil composition and an anionic surfactant in petroleum reservoirs, *Journal of Adhesion Science and Technology*, *20*(7), 693-704.

8 Appendix B: Supplementary Material for "A Method for Obtaining Silver Nanoparticle Concentrations Within a Porous Medium via Synchrotron X-Ray Computed Microtomography"

8.1 Determination of the nanoparticle synthesis yield

A 30mL 0.1M $AgNO_3$ solution was mixed with a 30mL 1.5% solution of sodium carboxymethylcellulose 90k and titrated with nitric acid to dissolve any Ag/CMC90k complexes. This solution was then stirred continuously while 30mL of a 0.4M $NaBH_4$/1.5% CMC90k solution was added dropwise to reduce the Ag^+_{aq} to silver nanoparticles. A jet black solution formed immediately, indicating that high concentrations of silver nanoparticles had been created. The formation of silver nanoparticles was confirmed by testing for the absorption peak typical of silver nanoparticles (~400nm) in a UV/Vis Spectrophotometer. Because of the high concentrations of nanoparticles, a small amount of the solution had to be diluted by approximately an order of magnitude to get a reading from the UV/Vis Spectrophotometer. Even after dilution, the synthesized solution was found to have a strong absorption peak at 400nm (see Figure 8.1, Initial Solution), confirming that silver nanoparticles had been formed during the addition of $NaBH_4$.

The undiluted solution was then passed through an Amicon 8400 ultrafiltration unit (Millipore) with a cellulose filter (reported as 1 kDa, Millipore). Prior to use, the ultrafiltration unit was thoroughly cleaned with nitric acid and rinsed with deionized water. Nitrogen gas was used to pressurize the ultrafiltration cell and pressure was maintained between 35-60 psi throughout the filtration process. The filtrate was collected in a dark bottle to prevent photoreduction of silver onto the bottle walls. The filtrate was also tested for the presence of the nanosilver plasmon peak via a UV/Vis Spectrophotometer and was found to have no peak in the range of 300-450nm (see Figure 8.1, Filtrate), indicating that all nanoparticles had been retained by the 1 kDa filter.
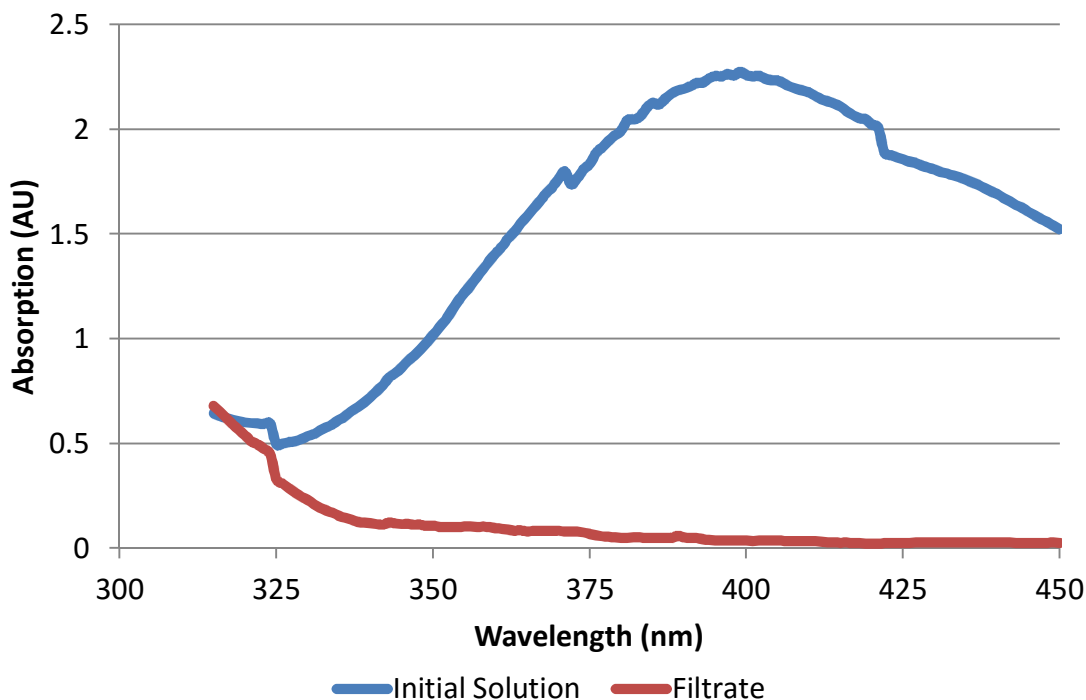
Figure 8.1: UV/Vis Specrophotometer analysis for the silver nanoparticle solution before and after passing through a 1 kDa cellulose filter. The lack of a plasmon peak at 390nm for the filtrate indicates that all silver nanoparticles were removed by the filter.

Both the filtrate and initial solution were then tested for total silver via ICP-OES, after first dissolving each in HNO_3. The results of this test confirmed our initial assumption, that the majority of silver had been reduced.

The concentration of silver in the initial solution was 2.2 g/L (+/- 0.0075). The concentration of silver in the collected filtrate was 0.052g/L (+/- 0.00039). This test confirms that 98% of $AgNO_3$ had been converted to nanosilver and retained by the 1 kDa filter.

A follow up experiment was conducted to quantify the amount of Ag^+ retained by the 1kDa filter. A 0.1M $AgNO_3$ standard was diluted to 3.6 g/L (our target nanoparticle concentration) with a 1.5% CMC90k solution. This solution was passed through the Amicon 8400 ultrafiltration unit with a 1 kDa cellulose filter. The filtrate and initial solutions were tested for total silver in a manner similar to the previous experiment. The initial concentration of silver was 3.6 g/L (+/- 0.016). The concentration of silver in the

filtrate was 3.4 g/L (+/- 0.019). This indicates that 6.4% (+/- 0.94) of Ag^+ had been retained by the 1 kDa cellulose filter.

8.2 Derivation of Equation 3.1

Beer's law is typically written as [*Skoog et al.*, 2007]:

$$A = -log_{10}\left[\frac{I}{I_o}\right] = \propto lc \qquad\qquad 8.1$$

where A is the voxel linear attenuation, I_o and I are the intensity of the incident and transmitted radiation respectively, $\propto$ is the mass attenuation coefficient of the sample, l is the length of the voxel (ie. image resolution) and c is the concentration of the absorbing compound within the voxel. If the voxel contains n absorbing compounds, eq. 8.1 may be rewritten as:

$$A_{sample} = l[(\propto c)_1 + (\propto c)_2 + .. \ (\propto c)_n] \qquad\qquad 8.2$$

However, it is possible to isolate Ag within SXCMT datasets by exploiting the element's mass attenuation K-edge which is unique to each element. Imaging just above and below Ag's K-edge yields a series of datasets for which differences in mass attenuation coefficients can be mostly ascribed to Ag's changing mass attenuation coefficient. More specifically, by subtracting a below-Ag-edge voxel from its corresponding above-Ag-edge voxel, the concentration of Ag in that voxel can be isolated. Assuming water and Ag are the only major x-ray attenuating compounds within the pore space, the above-edge/below-edge subtraction takes on the following form:

$$\Delta A = l\left[\left((\propto_a - \propto_b)c\right)_{silver} + \left((\propto_a - \propto_b)\rho\right)_{water}\right] \qquad\qquad 8.3$$

Subscripts a and b in eq. 8.3 denote the above-edge and below-edge mass attenuation coefficients taken from the NIST database [*M.J. Berger et al.*, 2010]. Equation 8.3 can be rearranged to solve for C_{silver} where ρ_{water} is assumed to be the density of water at room temperature:

$$c_{silver} = \frac{\frac{\Delta A}{l} - [(\propto_a - \propto_b)\rho]_{water}}{(\propto_a - \propto_b)_{silver}}$$

<div align="right">8.4</div>

It was determined that Sodium Carboxymethylcellulose 90k could be excluded from the derivation of eq. 8.4 due to its relatively low concentration (1%) and small difference between the above-edge and below-edge mass attenuation coefficients. The exclusion of CMC90k from eq. 8.4 changes the SXCMT-determined silver concentration by less than 0.05% and was thus excluded.

If imaging at 2 energies (ie. 25.614 keV and 25.414 keV) then eq. 8.4 can be applied to every voxel in the pore-network. However, based upon previous studies employing SXCMT for elemental quantification [*Barnett et al.*, 2010; *Ham et al.*, 2004] it was hypothesized that a higher quality concentration map could be obtained by over-determining the silver concentration at each voxel. Over-determination was completed by 1) collecting multiple above-below edge energy pairs (25.9-25.4 keV, 25.8-25.4 keV, 25.6-25.4 keV), 2) applying eq. 8.4 to each of the energy pairs and 3) averaging the resultant concentration maps. The 25.9-25.4 keV energy pair had a minimal impact on the quality of the averaged L-O concentration map and was excluded from L-PM imaging. The final imaging procedure used the other 2 energy pairs. The improvements associated with using 2 energy pairs as opposed to 1 are discussed further in the Accuracy section.

8.3 Number of nanoparticles per voxel calculation

$$V_{voxel=}1147.73\ \frac{\mu m^3}{voxel}$$

$$C_{Ag} = 3.6\ \frac{g}{L} = 0.0036\ \frac{g}{cm^3}$$

$$\rho_{Ag} = 10.49\ \frac{g}{cm^3}$$

$$\frac{V_{Ag}}{cm^3} = \frac{0.0036\ \frac{g}{cm^3}}{10.49\ \frac{g}{cm^3}} = 0.000343\ \frac{cm^3 Ag}{cm^3}$$

$$1 cm^3 = 10^{12} \mu m^3$$

$$1\ cm^3 = \frac{10^{12}\ \mu m^3}{1147.73\ \frac{\mu m^3}{voxel}} = 8.7\ \times 10^8\ \text{voxels}$$

$$\frac{V_{Ag}}{voxel} = \frac{0.000343\ \text{cm}^3 \text{of Ag}}{8.7 \times 10^8\ \frac{\text{voxels}}{\text{cm}^3}} = 3.94\ \times 10^{-13}\ \frac{\text{cm}^3\text{Ag}}{\text{voxel}}$$

$$\frac{Mass_{Ag}}{voxel} = 3.94 \times 10^{-13}\ \frac{\text{cm}^3\text{Ag}}{\text{voxel}} \times 10.49\ \frac{\text{g Ag}}{\text{cm}^3} = 4.13 \times 10^{-12}\ \frac{\text{g Ag}}{\text{voxel}}$$

Therefore in every voxel in the 3.6 g/L L-PM dataset there are approximately 4.13x10^{-12} g of silver.

Assuming nanoparticle are spherical with a diameter of 27.5 nm:

$$V_{nanoparticle} = \frac{4}{3}\pi\left(\frac{27.5}{2}\right)^3 = 10889 nm^3 = 1.09 \times 10^{-17} cm^3$$

$$\frac{\text{\# nanoparticles}}{\text{voxel}} = \frac{3.94\ \times 10^{-13}\ \frac{\text{cm}^3\text{Ag}}{\text{voxel}}}{1.09 \times 10^{-17}\ \frac{\text{cm}^3\text{Ag}}{\text{nanoparticle}}} = 3.6 \times 10^4\ \text{nanoparticles}$$

Therefore each voxel in the 3.6g/L L-PM dataset has approximately 3.6×10^4 nanoparticles. Repeating these calculations for the 1.2 and 2.2 g/L L-PM datasets yield approximately 1.2×10^4 and 2.2×10^4 nanoparticles per voxel.
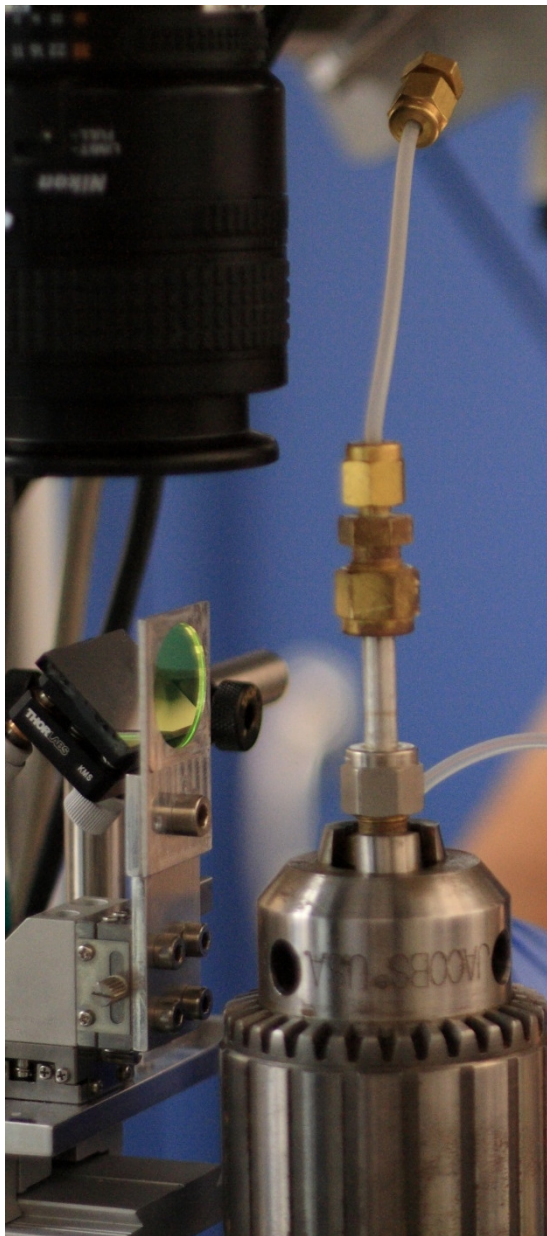

Figure 8.2 A photo of a glass bead/silver nanoparticle column in the imaging hutch at the GSECARS 13-BM-D beamline at the Advanced Photon Source, Argonne National Lab.

Table 8.1: Overview of segmentation and pore-network consistency between images

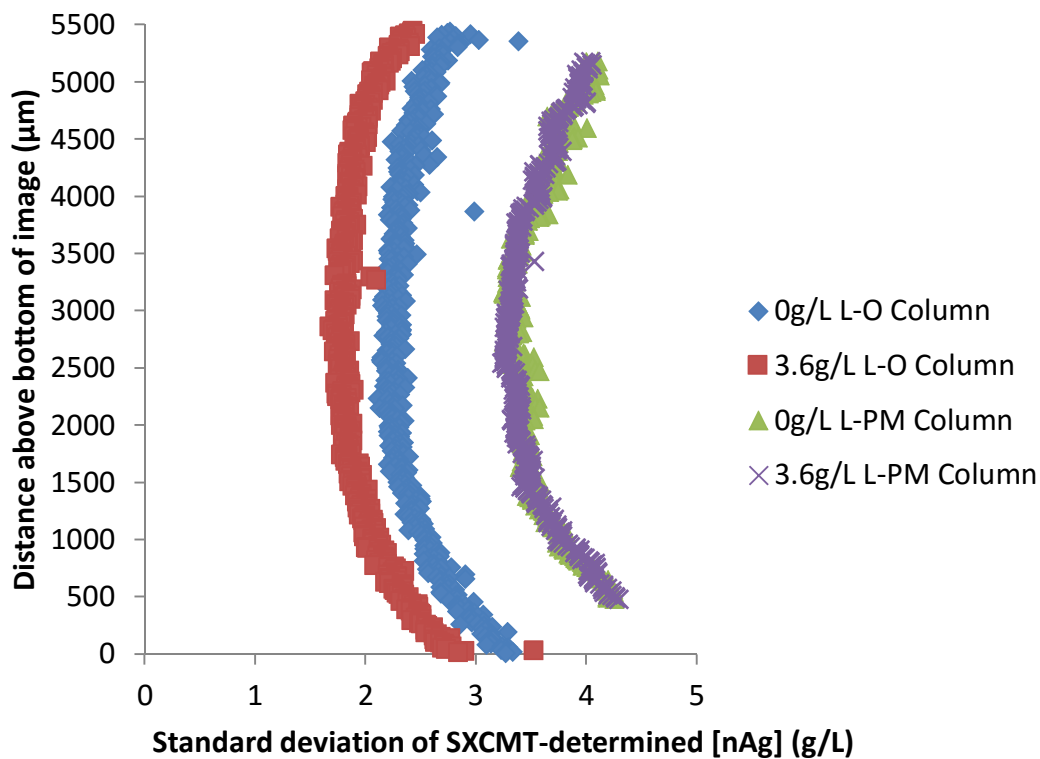| L-PM/IL-PM Sample	# grains	Average grain inscribed radius (µm)	Porosity (%)	# pores	Average pore inscribed radius (µm)	Standard deviation of pore inscribed radii (µm)
0 g/L	1111	165.6	38.2	4878	69.5	29.1
1.2 g/L	1095	167.7	38.3	4628	70.8	29.0
2.3 g/L	1084	170.2	38.2	4677	69.9	28.5
3.6 g/L	1138	164.1	38.6	4812	68.8	31.1
2 PV	1128	164.0	38.2	4864	68.8	29.7
4 PV	1116	165.0	38.2	4799	68.8	29.6
6 PV	1133	163.7	38.0	4873	68.4	29.5
8 PV	1141	163.0	38.0	4933	68.	29.5
10 PV	1114	165.5	38.0	4777	69.0	29.2
12 PV	1124	164.9	37.9	4864	68.5	29.5
16 PV	1119	165.2	38.1	4845	68.8	30.3
18 PV	1118	165.3	38.1	4837	68.9	30.0

Figure 8.3: The standard deviation of SXCMT-determined [nAg] as a function of height for both L-O and L-PM columns with known concentrations of silver nanoparticles. Each data point represents the standard deviation for 1 horizontal slice. Low photon counts at the top and bottom of the collected images causes an increase in noise. The silver concentrations were calculated from images captured at 25.414, 25.614 and 25.814 keV.
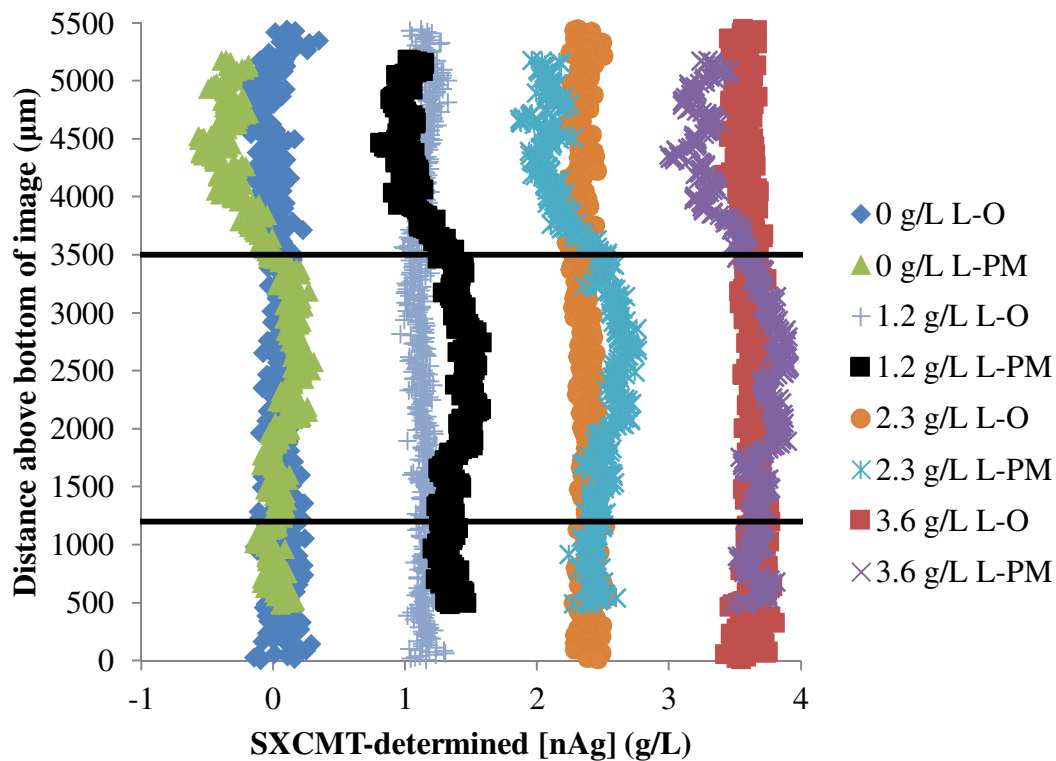
Figure 8.4: SXCMT-determined [nAg] as a function of height for both L-O and L-PM columns with known concentrations of silver nanoparticles. The size of the 95% confidence interval is smaller than the data point icons and has thus been excluded. The horizontal black bars indicate the top boundaries of the subvolume used in the uncertainty calculations.
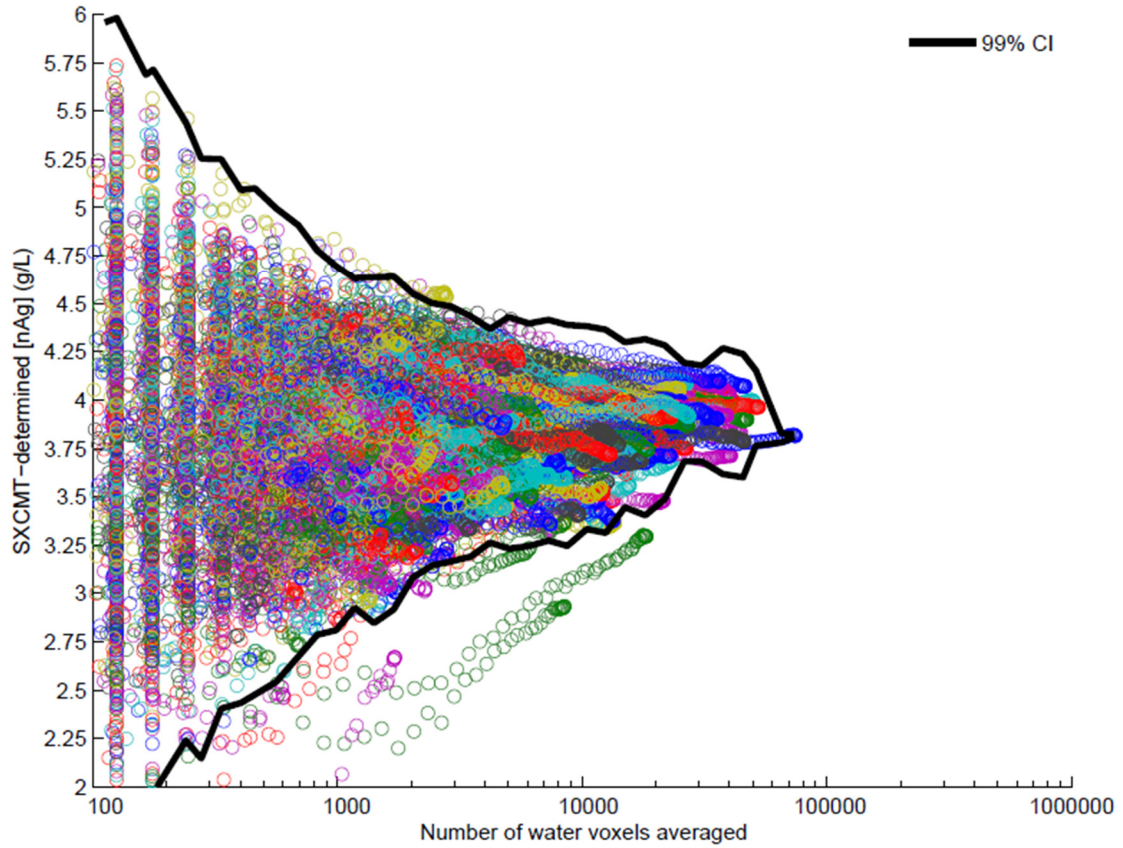
Figure 8.5a: SXCMT-determined [nAg] vs. number of water voxels averaged for three-dimensional subvolumes. Each circle represents a subvolume average with no subvolumes greater than a single pore. The black lines represent the 99% confidence interval using the back-calculated σ_p values.
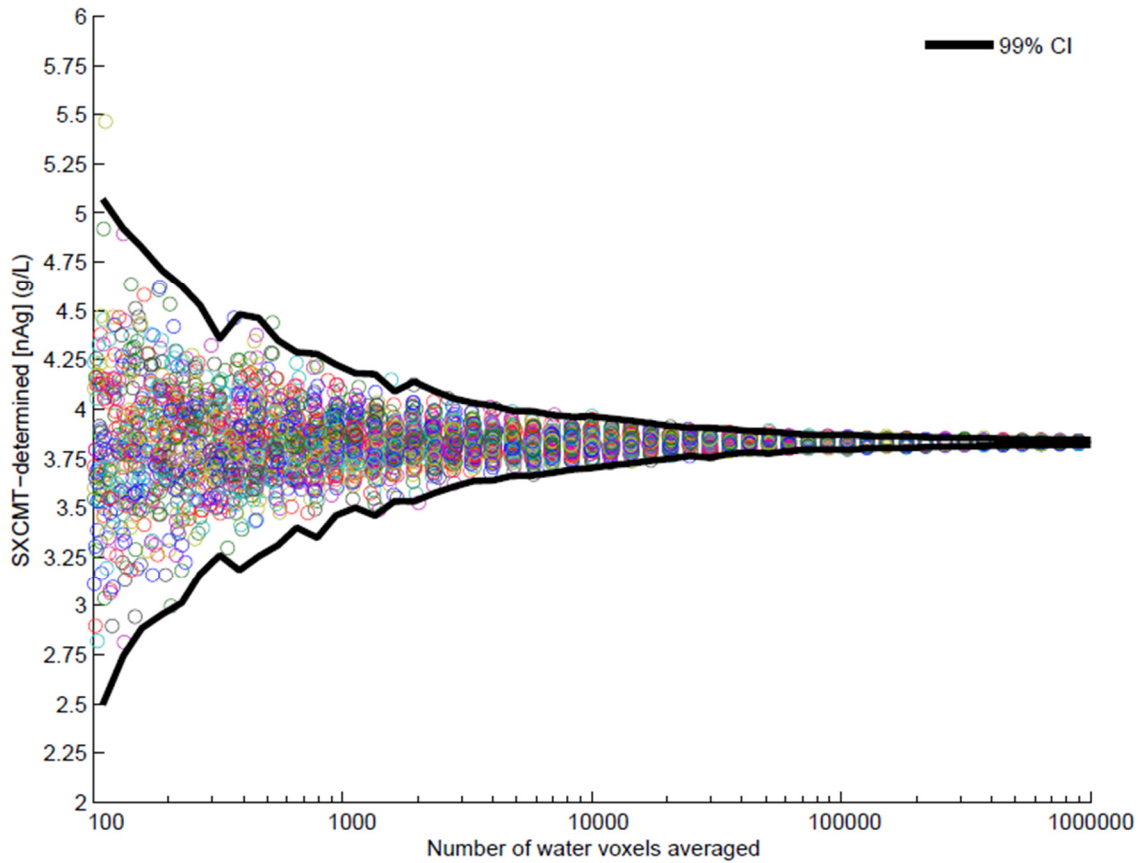
Figure 8.5b: SXCMT-determined [nAg] vs. number of water voxels for a random distribution of water voxels within the 3.6g/L L-PM image. All voxels with a distance of < 15.70 μm to the nearest grain surface were not included in the average. Each circle represents a random sample of size 30-1,000,000 voxels within the subvolume. The error bars represent the 99% confidence interval using a back-calculated σp.
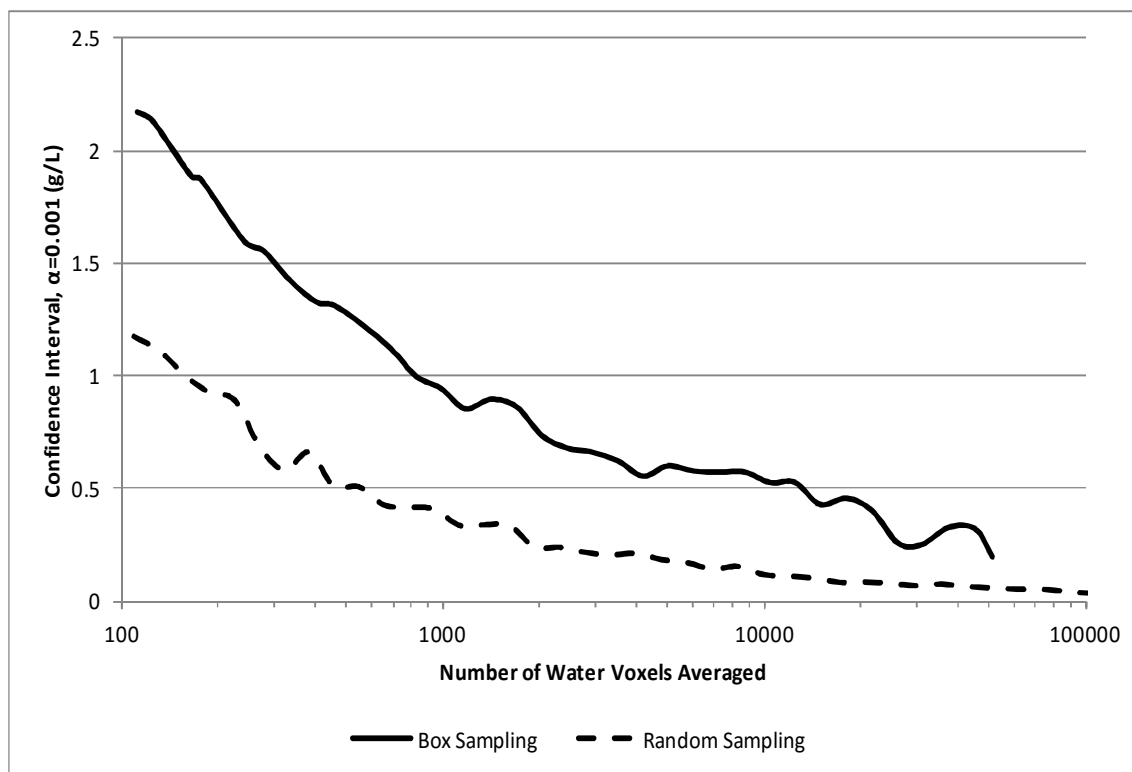
Figure 8.6: The size of the 99% confidence intervals depicted in Figures 8.5a and 8.5b using the back-calculated σp values.

8.4   References

Barnett, H. A., K. Ham, J. T. Scorsone, and L. G. Butler (2010), Synchrotron X-ray Tomography for 3D Chemical Distribution Measurement of a Flame Retardant and Synergist in a Fiberglass-Reinforced Polymer Blend, *Journal of Physical Chemistry B*, *114*(1), 2-9.

Ham, K., H. Jin, R. Al-Raoush, X. G. Xie, C. S. Willson, G. R. Byerly, L. S. Simeral, M. L. Rivers, R. L. Kurtz, and L. G. Butler (2004), Three-dimensional chemical analysis with synchrotron tomography at multiple x-ray energies: Brominated aromatic flame retardant and antimony oxide in polystyrene, *Chemistry of Materials*, *16*(21), 4032-4042.

M.J. Berger, J.H. Hubbell, S.M. Seltzer, J. Chang, J.S. Coursey, R. Sukumar, D.S. Zucker, and K. Olsen (2010), NIST XCOM: Photon Cross Sections Database, edited.

Skoog, D. A., F. J. Holler, and S. R. Crouch (2007), *Principles of Instrumental Analysis*, Thomson Brooks/Cole.

9   Appendix C: Supplementary Material for "The impact of immobile zones on the transport and retention of nanoparticles in porous media"

9.1   nAg/Iron Oxide interactions and batch experimental details

Care was taken to ensure that no Ag mass was lost during ICP analysis, the effluent sample vials were thoroughly rinsed with 68-70% HNO_3 to ensure that no mass was lost to the glassware and the solutions were never diluted below 2% HNO_3. These precautions were deemed appropriate as they lead to excellent Ag mass recovery (Ag in effluent + Ag in sand ÷ Ag injected) for the two quartz experiments (100%) and excellent volume recovery for all three experiments (volume of effluent samples ÷ total injected volume). However, in the iron oxide experiment only 86.3% of the Ag mass was recovered. The 13.7% Ag residual (residual = 100% - recovered percentage) in the iron oxide experiment is hypothesized to have been retained in the iron oxide sand but was non-digestible by concentrated nitric acid.

One possible cause of the 13.7% residual remaining on the iron oxide sand is that trace amounts of Cl^- from the iron oxide coating treatment (using $FeCl_3$) could have formed silver chloride, a compound insoluble in nitric acid [*Jones et al.*, 1984] despite thoroughly rinsing the sand after coating. Another possible explanation is that nitric acid digestion may not dissolve Ag from some mineral structures [*Jones et al.*, 1984] so a reaction between the nAg and the iron oxide coating (predominantly hematite and goethite [*Molnar et al.*, 2011]) could yield an non-digestable compound. Currently there is very little literature on chemical interactions between nAg and iron oxide surfaces. The few transport studies that have examined transport of nAg through iron oxide-containing media [*El Badawy et al.*, 2013; *Lin et al.*, 2011; *Neukum et al.*, 2014] did not digest their sands in nitric acid or report directly measure retained nAg. Reinforcing the hypothesis that the iron oxide's 13.7% non-digestible Ag is retained in the sand is a study that examined the aging of nAg in natural soils [*Coutris et al.*, 2012] and noted unrecoverable

residuals on the soils of up to 86% for un-coated nAg and approximately 10% for citrate-coated nAg.

A simplified batch experiment conducted in triplicate confirmed that poor mass recovery was not due to experimental error. The batch experiments were conducted under conditions similar to the SXCMT experimental conditions, freshly synthesized silver nanoparticles were mixed with iron oxide for the period of time equal to the SXCMT experimental nAg injection time. The nAg solution was drained and replaced with a CMC90k solution, controlled to an ionic strength of 0.12M with $NaNO_3$.This solution was mixed for a period of time equivalent to 1 PV injection and 1 SXCMT image. The sand was drained again and replaced with a volume of CMC90k solution equivalent to the total volume of CMC90k solution used during the elution phase of the SXCMT experiments. This mixture was left to sit for a period of time equal to the total imaging + flushing time during the SXCMT experimental elution phase. Following this, the sand was drained again and each drained sample was digested in 68-70% nitric acid and analyzed in a manner similar to that described in the ICP-determination section. The iron oxide sand was also digested in 68-70% nitric acid and analyzed in a similar manner.

Silver mass recovery from each of the batch experiments was consistently 93% suggesting that there is some interaction between the iron oxide surface and nAg particle rendering the nAg non-digestable in 68-70% HNO_3. Given the consistency of these results, the reported concentration of deposited nAg on the iron oxide sand reported in this thesis is the ICP-determined concentration from the acid-digestion solution + the residual.
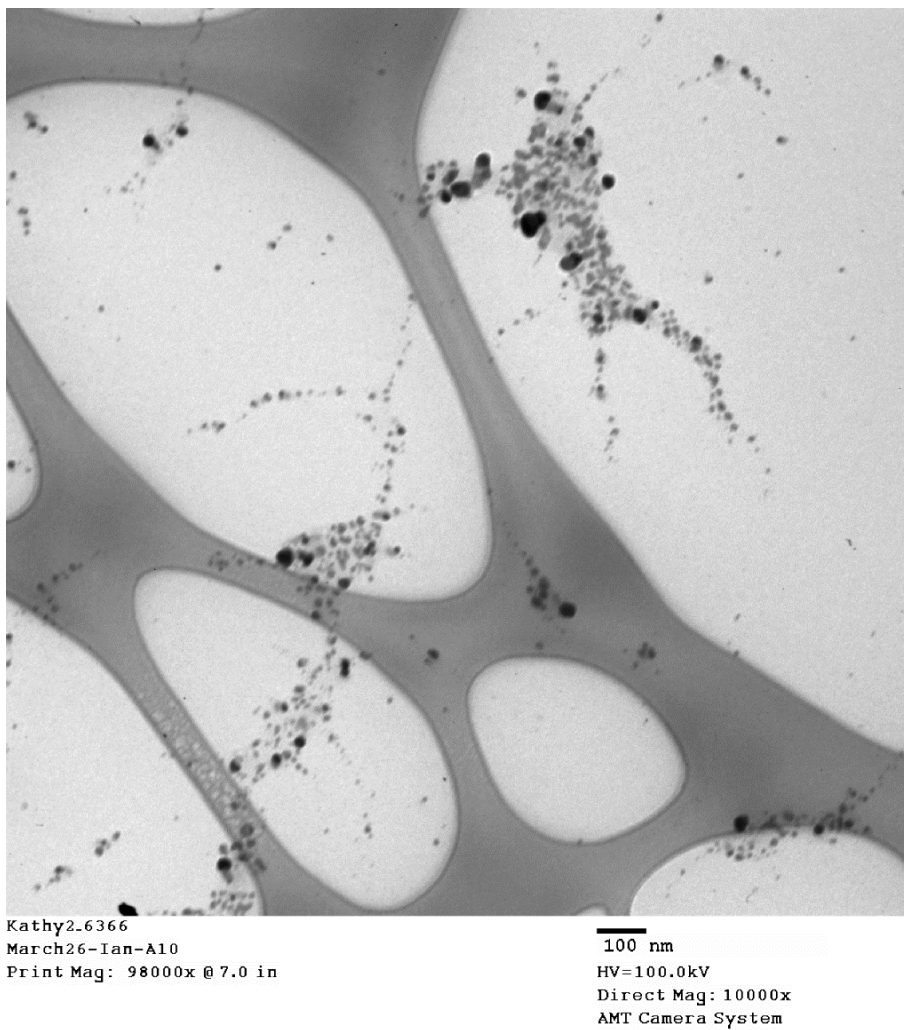
Kathy2_6366
March26-Ian-A10
Print Mag: 98000x @ 7.0 in

100 nm
HV=100.0kV
Direct Mag: 10000x
AMT Camera System

Figure 9.1: A TEM image of a silver nanoparticle solution synthesized using the described synthesis method.
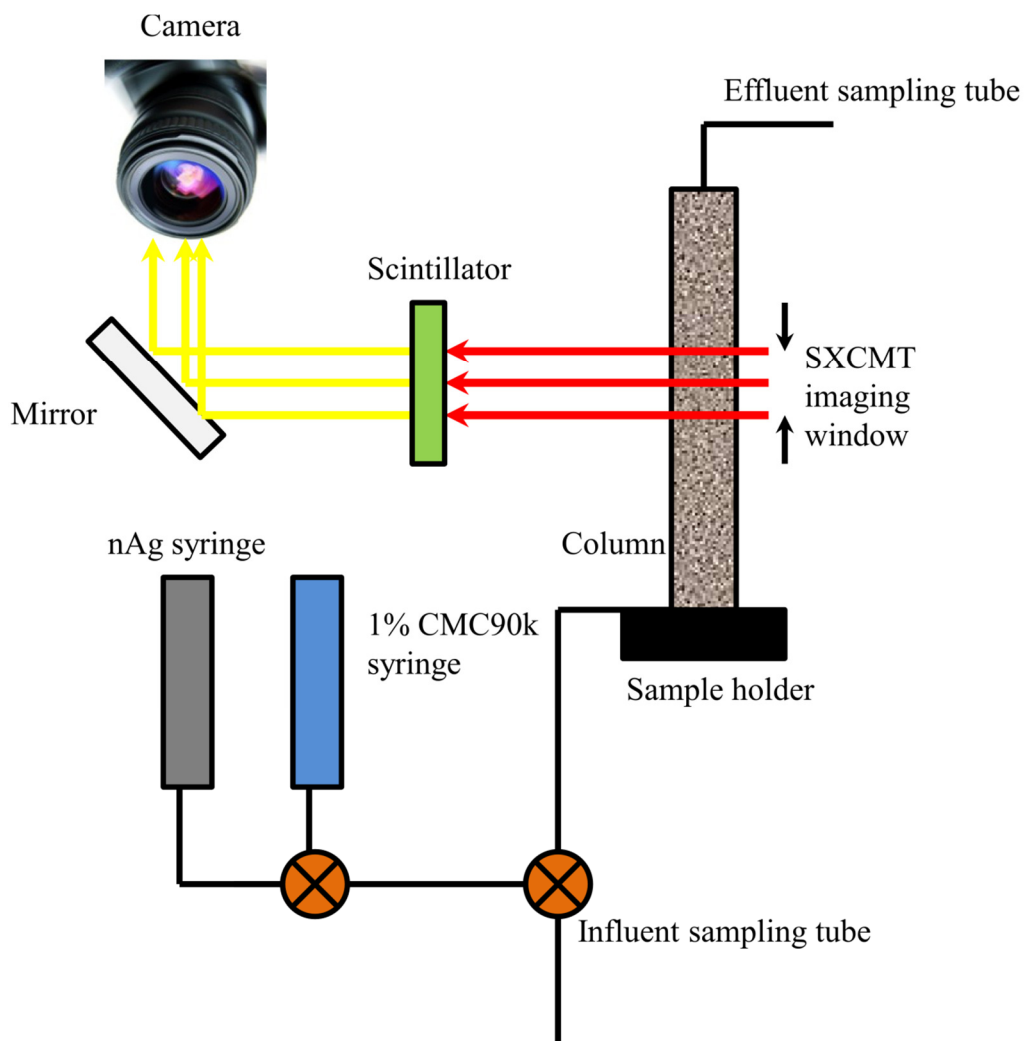
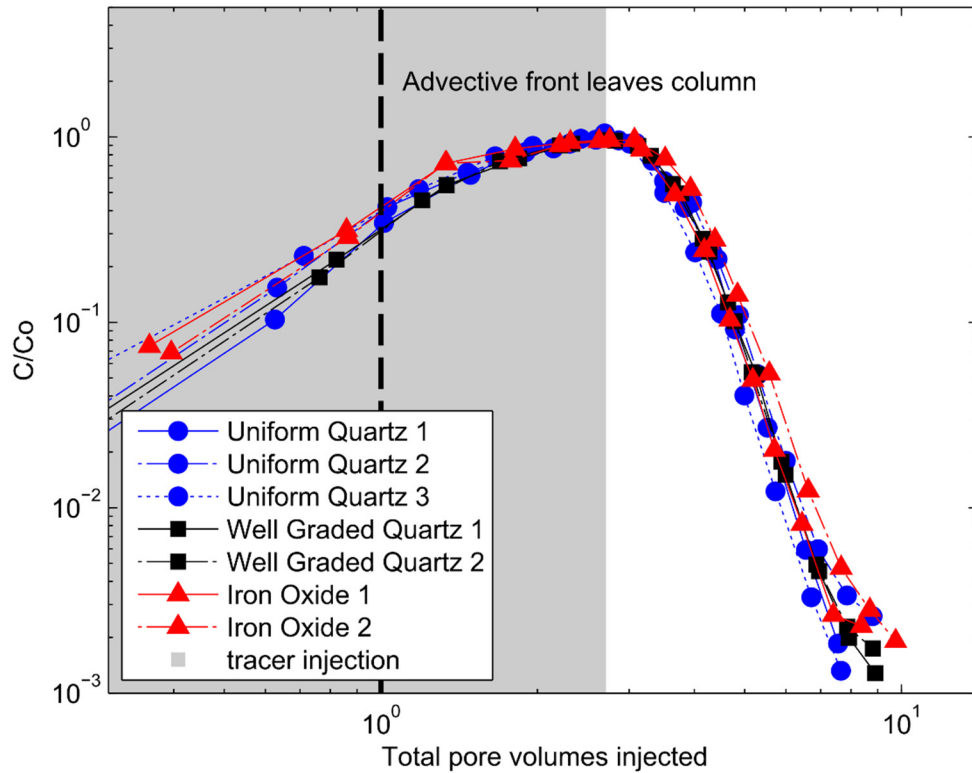**Figure 9.2: Schematic of the experimental set-up employed for each column.**

Figure 9.3: Tracer test C/Co breakthrough curves a log-log scale to emphasize extended tailing in the samples. The grey box represents the nAg injection period and the white background represents the elution. The vertical dotted line indicates when the advective front reached the top of the column. The experiment number (e.g., Uniform Quartz 1, 2 etc..) is used to denote the repeated experiments performed for each sand type.
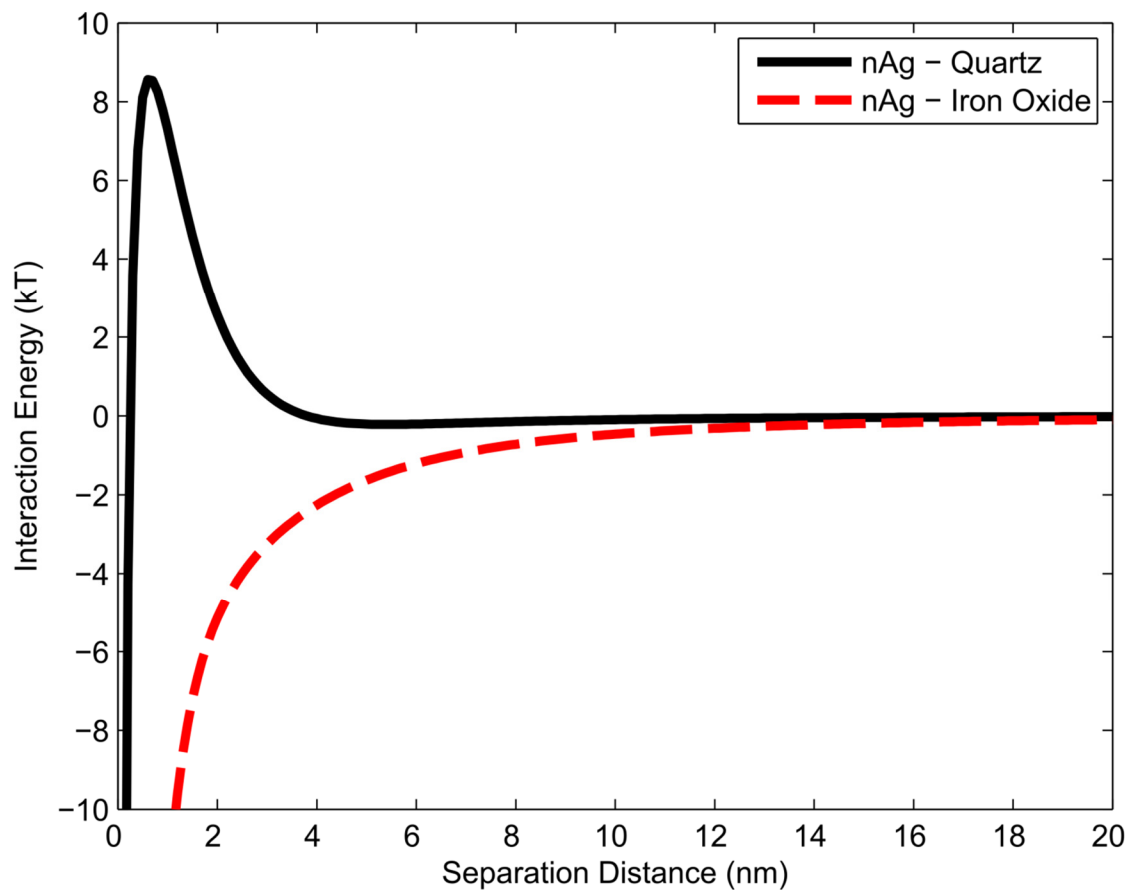
Figure 9.4: Standard DLVO interaction energy profiles for iron oxide sand (dashed red line) and quartz (solid black line) interacting with silver nanoparticles.

9.2 Overview of the dataset analysis procedure:

1. The below K-edge subvolume (25.414 keV) was subtracted from the 3 above K-edge subvolumes (25.614,25.714 and 25.814 keV) to create 3 difference images.

2. A modified form of Beer's Law was applied to each of the 3 difference images to convert the voxel values of x-ray linear mass attenuation to calculated silver nanoparticle concentration. The modified Beer's law [see Molnar et al. 2014, Equation 1] assumes that water and silver are the only x-ray absorbing compounds in solution so the voxel value of x-ray linear mass attenuation is linearly correlated to experimental silver nanoparticle concentration. However the ratio of silver nanoparticle concentration calculated from the modified Beer's law to the experimental concentration is not 1:1 so the term 'SXCMT-determined [nAg]' is employed throughout this paper to differentiate between SXCMT-determined and experimentally-determined [nAg].

3. The 3 SXCMT-determined [nAg] datasets were averaged together. All pore-space voxels <17.3μm away from a grain surface were discarded due to a 'shadow zone' effect caused by x-ray refraction at grain/pore interfaces. All voxels 17 - 25μm away from a grain surface considered only SXCMT-determined [nAg] from the 25.614 keV energy dataset due to observations that the size of the 'shadow zone' was energy dependent. All voxels > 25μm away from the grain surface considered all 3 above K-edge datasets.

4. A calibration curve from the Molnar et al [2014] L-PM datasets ('improved' L-PM calibration curve) was applied to correct the raw SXCMT-determined [nAg] voxel values. All SXCMT-determined [nAg] values reported in the results and discussion section are the calibrated values obtained in this step

9.3   References

Coutris, C., E. J. Joner, and D. H. Oughton (2012), Aging and soil organic matter content affect the fate of silver nanoparticles in soil, *Science of The Total Environment*, *420*(0), 327-333.

El Badawy, A. M., A. Aly Hassan, K. G. Scheckel, M. T. Suidan, and T. M. Tolaymat (2013), Key Factors Controlling the Transport of Silver Nanoparticles in Porous Media, *Environ. Sci. Technol.*

Jones, K. C., P. J. Peterson, and B. E. Davies (1984), Extraction of silver from soils and its determination by atomic absorption spectrometry, *Geoderma*, *33*(2), 157-168.

Lin, S. H., Y. W. Cheng, Y. Bobcombe, K. L. Jones, J. Liu, and M. R. Wiesner (2011), Deposition of Silver Nanoparticles in Geochemically Heterogeneous Porous Media: Predicting Affinity from Surface Composition Analysis, *Environ. Sci. Technol.*, *45*(12), 5209-5215.

Molnar, I. L., D. M. O'Carroll, and J. I. Gerhard (2011), Impact of surfactant-induced wettability alterations on DNAPL invasion in quartz and iron oxide-coated sand systems, *Journal of Contaminant Hydrology*, *119*(1-4), 1-12.

Molnar, I. L., C. S. Willson, D. M. O'Carroll, M. L. Rivers, and J. I. Gerhard (2014), Method for Obtaining Silver Nanoparticle Concentrations within a Porous Medium via Synchrotron X-ray Computed Microtomography, *Environ. Sci. Technol.*, *48*(2), 1114-1122.

Neukum, C., A. Braun, and R. Azzam (2014), Transport of stabilized engineered silver (Ag) nanoparticles through porous sandstones, *Journal of Contaminant Hydrology*, *158*(0), 1-13.

10 Appendix D: Supplementary Material for "The impact of pore geometry and fluid velocity on the transport of nanoparticles in porous media"

10.1 Overview of the algorithm for finding the closest grain surface

1. A unique positive identifier was assigned to each grain within the SXCMT sub-volume. Every voxel within a single grain possessed the same unique identifier.

2. Every voxel within the pore space of the SXCMT sub-volume was assigned an identifier value of -1.

3. The algorithm, written and executed in Matlab, then started moving through the pore space voxels on a voxel-by-voxel basis (i.e. the closest and second closest grain surfaces were found for the first voxel, then the algorithm moved on to the second voxel etc…). It took approximately 3 hours to complete the full analysis on 1 dataset measuring 350×350×450 voxels in size.

4. To find the closest grain surface to the pore space voxel of interest (VOI), the algorithm first searched all adjacent voxels that shared either a face, corner or edge with the VOI (i.e., it searched within a box surrounding the VOI). Each adjacent voxel was checked to see if it possessed a negative (pore space) or positive (grain) identifier. It was assumed that the closest voxel with a positive identifier existed on the surface of a grain.

5. If no positive identifier was found, the search box expanded by 1 voxel in every direction. This process was repeated with progressively larger search boxes until a positive identifier was discovered.

6. Once a voxel with a positive identifier was discovered, the distance between that voxel's centroid and the VOI's centroid was measured via the Pythagorean theorem. By measuring the distance between voxel centroids adjacent voxels which share a face will have a distance equal to the resolution of the voxel. If multiple voxels with positive identifiers were discovered, all distances were measured and the shortest distance was chosen.

7. Once a voxel with a positive identifier was discovered, the search box expanded once more and all voxels within the box were checked to ensure that no voxel with a positive identifier was closer than the previously identified closest voxel. This final search box expansion was because a corner voxel in a smaller box might be further away from the VOI than the face voxel of a larger box.

8. To find the distance to the second closest grain surface, steps 4 to 6 were repeated until a voxel with a different positive identifier was discovered.

9. Once the closest and second closest grain surfaces were discovered for the VOI, the algorithm moved on to the next pore space voxel and repeated the same procedure.
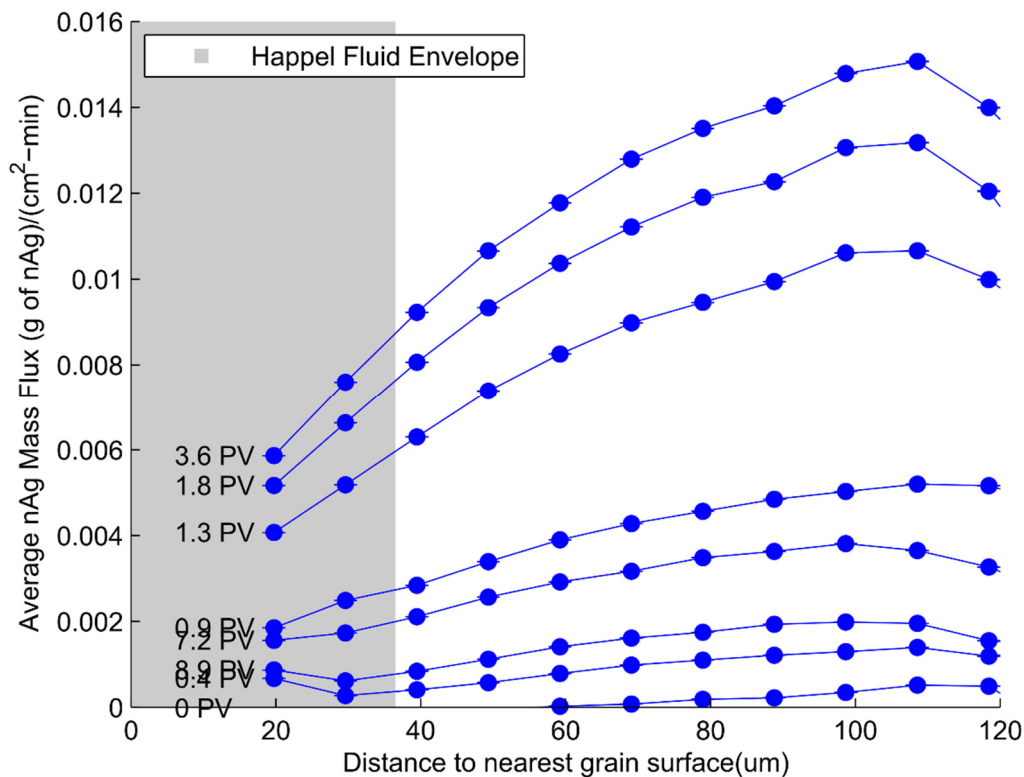

Figure 10.1: The estimated nAg mass flux rate (nAg mass flow per unit area) as a function of distance from the nearest grain surface for each imaged time-step\SXCMT-PV. The gray box represents the thickness *r* of the Happel Sphere-in-Cell fluid envelope. To avoid cluttering the figure, 'PV' is used instead of 'SXCMT-PV's'.

11 Appendix D: Reproduction Licenses

11.1 Chapter 2

This Agreement between Ian Molnar ("You") and John Wiley and Sons ("John Wiley and Sons") consists of your license details and the terms and conditions provided by John Wiley and Sons and Copyright Clearance Center.

License Number	3738481006666
License date	Oct 29, 2015
Licensed Content Publisher	John Wiley and Sons
Licensed Content Publication	Water Resources Research
Licensed Content Title	Predicting colloid transport through saturated porous media: A critical review
Licensed Content Author	Ian L. Molnar,William P. Johnson,Jason I. Gerhard,Clinton S. Willson,Denis M. O'Carroll
Licensed Content Date	Sep 2, 2015
Licensed Content Pages	42
Type of Use	Dissertation/Thesis
Requestor type	Author of this Wiley article
Format	Print and electronic
Portion	Full article
Will you be translating?	No
Title of your thesis / dissertation	EMPLOYING SYNCHROTRON X-RAY COMPUTED MICROTOMOGRAPHY TO STUDY SILVER NANOPARTICLE TRANSPORT THROUGH SOIL
Expected completion date	Dec 2015
Expected size (number of pages)	300

11.2 Chapter 3

Title: Method for Obtaining Silver Nanoparticle Concentrations within a Porous Medium via Synchrotron X-ray Computed Microtomography

Author: Ian L. Molnar, Clinton S. Willson, Denis M. O'Carroll, et al

Publication: Environmental Science & Technology

Publisher: American Chemical Society

Date: Jan 1, 2014

Copyright © 2014, American Chemical Society

PERMISSION/LICENSE IS GRANTED FOR YOUR ORDER AT NO CHARGE

This type of permission/license, instead of the standard Terms & Conditions, is sent to you because no fee is being charged for your order. Please note the following:

- Permission is granted for your request in both print and electronic formats, and translations.
- If figures and/or tables were requested, they may be adapted or used in part.
- Please print this page for your records and send a copy of it to your publisher/graduate school.
- Appropriate credit for the requested material should be given as follows: "Reprinted (adapted) with permission from (COMPLETE REFERENCE CITATION). Copyright (YEAR) American Chemical Society." Insert appropriate information in place of the capitalized words.
- One-time permission is granted only for the use specified in your request. No additional uses are granted (such as derivative works or other editions). For any other uses, please submit a new request.

11.3 Chapter 4

This Agreement between Ian Molnar ("You") and John Wiley and Sons ("John Wiley and Sons") consists of your license details and the terms and conditions provided by John Wiley and Sons and Copyright Clearance Center.

License Number	3738481006666
License date	Oct 29, 2015
Licensed Content Publisher	John Wiley and Sons
Licensed Content Publication	Water Resources Research
Licensed Content Title	Predicting colloid transport through saturated porous media: A critical review
Licensed Content Author	Ian L. Molnar,William P. Johnson,Jason I. Gerhard,Clinton S. Willson,Denis M. O'Carroll
Licensed Content Date	Sep 2, 2015
Licensed Content Pages	42
Type of Use	Dissertation/Thesis
Requestor type	Author of this Wiley article
Format	Print and electronic
Portion	Full article
Will you be translating?	No
Title of your thesis / dissertation	EMPLOYING SYNCHROTRON X-RAY COMPUTED MICROTOMOGRAPHY TO STUDY SILVER NANOPARTICLE TRANSPORT THROUGH SOIL
Expected completion date	Dec 2015
Expected size (number of pages)	300

Curriculum Vitae

Name: Ian Molnar

Post-secondary Education and Degrees: University of Western Ontario
London, Ontario, Canada
2010 – 2015 Ph.D.

The University of Western Ontario
London, Ontario, Canada
2007 – 2009 M.E.Sc

The University of Western Ontario
London, Ontario, Canada
2003-2007 B.E.Sc

Honours and Awards: The John Booker Award
Geotechnical Research Centre
2013

The L.G. Soderman Award
Geotechnical Research Centre
2012

Walkerton Clean Water Centre Award
Walkerton Clean Water Centre
2010

The R.M. Quigley Award
Geotechnical Research Centre
2008

Related Work Experience   Limited Duties Lecturer (CEE 3386a, CEE4465a)
The University of Western Ontario
2015

Teaching Assistant
The University of Western Ontario
2007 – 2013

Publications:

a. Articles published or accepted in refereed journals

Molnar, I. L.; W.P. Johnson; J.I. Gerhard; C.S. Willson, and O'Carroll D.M., (2015), Predicting colloid transport through saturated porous media: A critical review [Special issue, 50th Anniversary of Water Resources Research], *Water Resources Research*, *51* (Invited contribution)

Molnar, I.L.; Gerhard, J.I.; Willson, C.S. and O'Carroll, D.M., (2015), The impact of immobile zones on the transport and retention of nanoparticles in porous media. *Water Resources Research.* doi:10.1002/2015WR017167

Molnar, I.L.; Willson, C.S.; O'Carroll, D.M.; Rivers, M.L. and Gerhard, J.I., (2014), Method for Obtaining Silver Nanoparticle Concentrations within a Porous Medium via Synchrotron X-ray Computed Microtomography. *Environmental Science and Technology, 48*, (2), 1114-1122.

Molnar, I.L.; O'Carroll, D.M. and Gerhard, J.I., (2011), Impact of surfactant-induced wettability alterations on DNAPL invasion in quartz and iron oxide-coated sand systems. *Journal of Contaminant Hydrology 119*, (1-4), 1-12.

b. Non-refereed contributions

Molnar, I.L.*; O'Carroll, D.M.; Gerhard, J.I. and Willson C.S., (2015), Silver Nanoparticle Transport Through Soil: Illuminating the Pore-Scale Processes. American Geophysical Union Fall Meeting. San Francisco, California.

Molnar, I.L.*; O'Carroll, D.M.; Gerhard, J.I. and Willson C.S., (2014), From Pore to Core: Do Engineered Nanoparticles Violate Upscaling Assumptions? A Microtomographic Investigation. American Geophysical Union Fall Meeting. San Francisco, California.

Molnar I.L.*; O'Carroll, D.M.; Gerhard, J.I. and Willson C.S., (2014), The Influence of Favorable/Unfavorable Deposition Conditions on the Pore Space Distribution of Silver Nanoparticles. 6th International Conference on Porous Media - Interpore. Milwaukee, Wisconsin.

Molnar, I.L. *; Willson, C.S.; O'Carroll, D.M. and Gerhard, J.I., (2013), The Influence of Pore Network Geometry on Silver Nanoparticle Transport through Soil. American Geophysical Union Fall Meeting. San Francisco, California.

Molnar, I.L. *; O'Carroll, D.M.; Gerhard, J.I. and Willson, C.S., (2013), Exploring the Use of Synchrotron Radiation to Image Silver Nanoparticles in a Porous Media. Symposium for New Research in Groundwater Science. London, Ontario.

Molnar, I.L. *; Gerhard, J.I.; O'Carroll, D.M. and Willson, C.S., (2012), Imaging the Transport of Silver Nanoparticles Through Soil With Synchrotron X-ray Microtomography. American Geophysical Union Fall Meeting, San Francisco, California.

Molnar, I.L. *; Willson, C.S.; O'Carroll, D.M. and Gerhard, J.I., (2012), Employing Synchrotron X-Ray Microtomography to Study Silver Nanoparticle Transport Through Soils. 2012 International Association of Hydrologeologists Congress, Niagara Falls, Ontario.

Molnar, I.L. *; O'Carroll, D.M.; Gerhard, J.I. and Willson, C.S., (2012), Investigating Silver Nanoparticle Transport in Soil via Synchrotron X-Ray Microtomography. 2012 Goldschmidt Conference, Montreal, Quebec.

Molnar, I.L. *; O'Caroll D.M.; Gerhard, J.I. and Willson, C.S., (2011), Exploring the Use of Synchrotron Radiation to Image Silver Nanoparticles in a Porous Media. American Geophysical Union Fall Meeting. San Francisco, California.

Molnar, I.L. *; O'Caroll D.M.; Gerhard, J.I. and Willson, C.S., (2010), Impact of mineral isoelectric point on subsurface/NAPL wettability. American Geophysical Union Fall Meeting. San Francisco, California.

Molnar, I.L. *; O'Carroll, D.M. and Gerhard, J.I., (2009)*,* The Wettability of a Multi-Component DNAPL on Quartz and Iron Oxide Sands. American Geophysical Union Joint Assembly. Toronto, Ontario.

Molnar, I.L.*; Gerhard, J.I.; O'Carroll, D.M., (2008), The Effect of Surfactants on PCE Migration and Wettability. Symposium for NAPLs Research & Groundwater Studies. London, Ontario.

Molnar, I.L.*, Jasim, S.Y.; Ndiongue S. et al. (2007), Pilot Study to Investigate the Removal of Bacteria, Turbidity and Organics using a Reverse Osmosis Package Plant. Ontario Water Works Association Conference. Blue Mountain, Ontario.

* indicates the presenting author